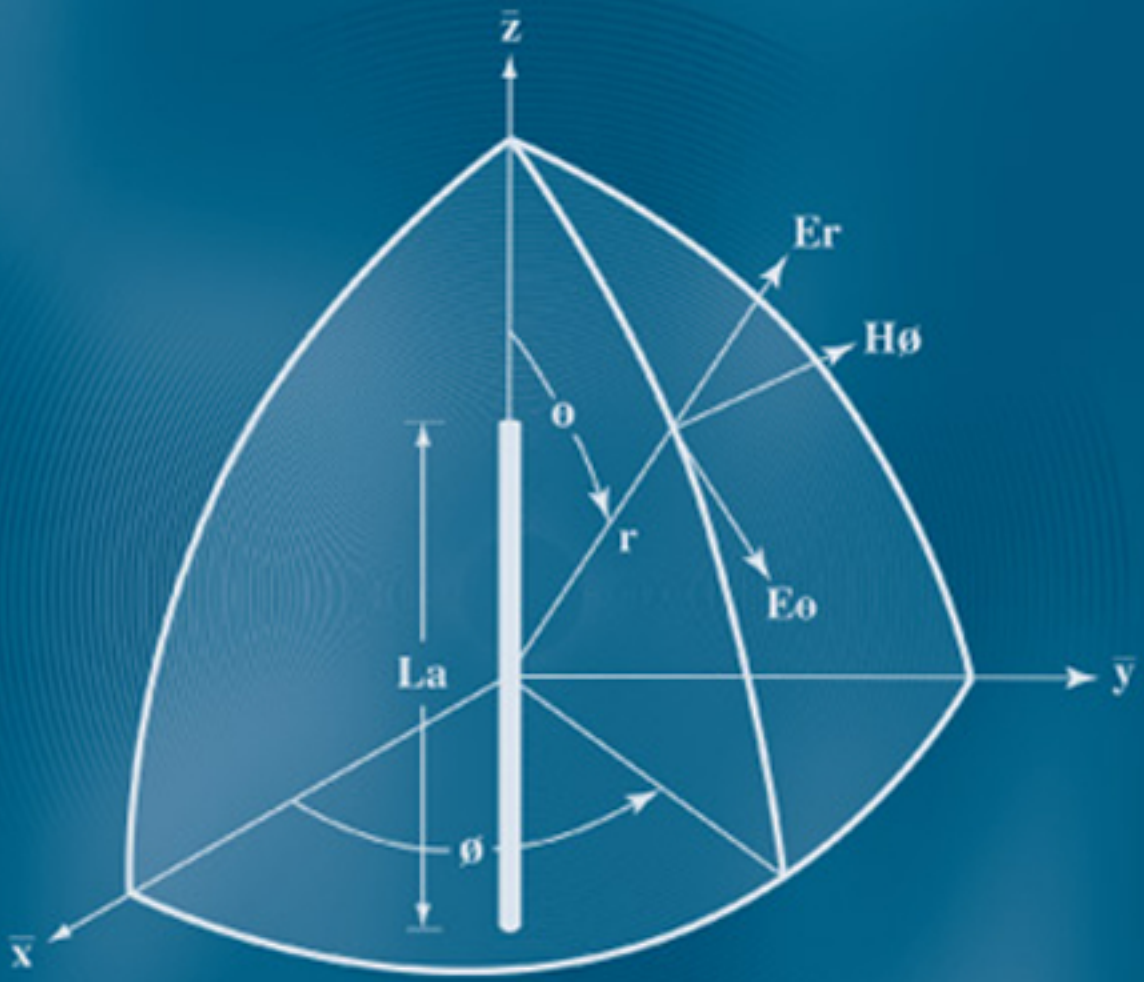

Analysis of Radome-Enclosed Antennas second edition

Dennis J. Kozakoff

CD-ROM INCLUDED

Analysis of Radome-Enclosed Antennas

Second Edition

For a listing of related Artech House in the,
Antennas and Propagation Series
turn to the back of this book.

Analysis of Radome-Enclosed Antennas

Second Edition

Dennis J. Kozakoff

ARTECH
HOUSE
BOSTON | LONDON
artechhouse.com

Library of Congress Cataloging-in-Publication Data
A catalog record for this book is available from the U.S. Library of Congress.

British Library Cataloguing in Publication Data
A catalogue record for this book is available from the British Library.

Cover design by Greg Lamb

ISBN 13: 978-1-59693-441-2

685 Canton Street
Norwood, MA 02062

Disclaimer:
This eBook does not include the ancillary media that was packaged with the original printed version of the book.

10 9 8 7 6 5 4 3 2 1

Contents

Foreword

The advancement of military platforms to meet new mission requirements continues to place new demands on the design process for all components and structures, including composite radomes. Radome design is uniquely challenging in that the performance parameters are generally in direct conflict with each other and the design must be iterated until all competing parameters are optimally satisfied. The design process is a compromise between electrical transparency and mechanical strength. There are many dielectric material options, each with their unique properties, including electrical properties, mechanical properties, environmental resistance, and cost. Finally, the radome design must be evaluated from a manufacturing standpoint.

The tools and analysis methods used for radome design continually evolve to address these competing engineering aspects of radome design. The need for these evolutions has been accelerated by the increasingly challenging requirements of next generation manned and unmanned platforms. New platforms require increased RF transparency, low observability, frequency selective surfaces, reduced weight, and improved structural efficiency.

Advancements in computer hardware and software algorithms have enabled significant improvements in the radome design process. The increased power of modern computers allows a radome designer to evaluate designs in a manner that was not previously possible, such as designs with frequency selective materials, low observable treatments, or metamaterials. Previous approaches to radome design required the designer to create custom algorithms for specific geometries to predict performance. Due to the error associated with this approach, extensive radome hardware iterations were required to validate and finalize the design, which is costly and time-consuming.

Today there are extremely powerful electromagnetic simulation packages that are used for all types of electromagnetic problems, including radomes. These tools are commercially available and use many different mathematical approaches to analyzing radomes and predicting performance. These programs operate using the finite-difference time-domain, method of moments, physical optics, or finite element method, depending on the circumstances of the design.

This book presents many new and useful insights into design and analysis of modern radomes of different shapes and requirements. Supporting new radome specifications requires the ability to execute a quick and accurate modeling of the radome early in the design stage. The information presented will enable improvements in the accuracy, cost, and timeliness of the radome design and development process.

Mike Stasiowski
Senior Antenna Engineer
Cobham Defense Systems, Sensor Systems
Baltimore, MD
November 2009

Preface

If you are reading this book, you probably fit into one of the following occupational profiles:

- An engineer, physicist, or scientist with a career interest in antennas, radomes, or electromagnetic theory;
- A program manager in government or industry with the job of buying, specifying, or evaluating a radome that is being procured or has already been installed.
- A technician who must test radomes. This book describes test techniques and equipment required.

If one of these occupational profiles describes you, then this book should target your needs. If you are just reading this book for general interest, you too should be able to learn much about radomes.

Objectives

The ultimate goal of this book is to help you develop your own advanced software techniques for radome analysis. To accomplish this goal you will be led systematically through the building blocks and individual computational steps that must be solved on the way to achieving your ultimate goal.

If you read and study this book thoroughly, you should be able to:

- Define a radome, describe how it works, tell the history of its development, and understand the fundamental mathematical tools.
- Develop a knowledge of the approaches to analyzing the effects of a radome on an various enclosed antenna types and with different radome shapes.
- Understand how radome materials and wall construction affect radome performance.
- Have a knowledge of radome test techniques and equipments.
- Be aware of environmental factors that can degrade radome performance and how to minimize the possible deleterious effects.
- Understand and use the computer software accompanying this book.
- Have an ability to develop your own customized computer software.

Skills and Hardware That You Will Need

Although radome analysis does not require that you have the math skills of a Ph.D., you do need to understand the fundamental equations presented in this book. In addition, you need to be PC-literate and have minimal programming skills.

The state-of-the-art of PC hardware has increased incredibly since the first edition. Today you can run sophisticated radome modeling programs on your PC that in years past would have required a mainframe computer. The following computer hardware is recommended in order to run the software programs:

- A desktop or laptop computer with an XP, XP Professional, or Visio operating system;
- A minimum of 1.5-GHz clock speed;
- A minimum of 2 GB of RAM computer;
- A 32-bit or 64-bit PC.

The programming of various examples in this book use the Power Basic programming language, a very simple yet highly sophisticated programming language. It is extremely easy to learn and the coding can easily be transferred into other programming languages such as Fortran, Pascal, or C++. More information about this programming language can be found on the Internet at www.powerbasic.com.

The software accompanying this book is on the CD-ROM and in compiled form; the compiled software execution time is very short.

The computer software that is provided with the book is on a CD and is comprised of two seperate programs that run on a PC computer:

1. Program WALL computes the transmission loss of an electromagnetic wave propagating through a flat multilayer dielectric composite comprised of 1 to 5 layers of different types of dielectric materials;
2. Program To-Radome computes the transmission loss and boresight error (BSE) performance of a general three-dimentional tangent ogive (TO) shaped radome where the user can vary the radome geometry and wall layers in order to achieve best performance.

In use, program WALL can be used to obtain the least transmission loss for various composite designs, and program TO-Radome can be used to determine the best composite design's performance when in a radome geometrical shape. The transmission performance for a flat composite sample can be different from the results when that composite design is used in a three-dimensional radome geometry. However, program WALL is useful to obtain a ballpark wall design; that wall design can be empirically iterated when using program TO-Radome in order to optimize performance.

What You Can Expect from Radome Analysis

Radome analysis is somewhat of an art as a science. You cannot guarantee that your solution to a given problem will be exact. The approach to analysis used in this book uses many approximations. The accuracy of the dielectric wall data that you apply (thickness, dielectric constant, and loss tangent) will constrain overall computational accuracy. In addition, the effect of tolerances on these parameters is many times difficult to model. However, you can expect a good ballpark estimate of radome performance estimates. The approaches and the examples shown are believed to be correct by the author and are believed to yield a reasonable ballpark solution when applied.

The radome analysis herein consists of selecting a fundamental approach to solving the problem and then dividing the overall problem into many smaller problems or software modules. The particular approaches that can be applied are discussed in the book and include possibilities such as Method of Moment (MOM) and Plane Wave Spectra (PWS). However, either Geometric Optics (GO) or Physical Optics (PO) computational ray trace approaches are the most straightforward techniques and easiest to apply. The GO technique works well when the antenna size is large in terms of wavelengths and the PO technique works well when the antenna size is small in terms of wavelengths. Both techniques make extensive use of ray tracing and vector mathematics.

Organization of the Book

This book contains four sections:

- Part I, Background and Fundamentals, covers the history, overview of radome materials and wall constructions, the relevant mathematical tools, and antenna fundamentals.
- Part II, Radome Analysis Techniques, is an overview of electromagnetic theory and radome modeling methodology.
- Part III, Computer Implementation, discusses software programming approaches to achieve the modeling on a PC.
- Part IV, Specifying Performance, Testing, and Degradations, is a new section for this edition.

Acknowledgments

For this second edition I am indebted to other key personnel from various companies for contributing data and providing valuable insights into the current needs of the radome development community and the state of the art in radome design, fabrication, and testing technology.

One of the greatest single contributors was Ben MacKenzie, the director of technology and engineering at Saint Gobain Performance Plastics (previously Norton Radomes), in Norton, Ohio, who recently retired after 30 years of working on advanced radome development. Formerly, Mr. MacKenzie chaired the subcommittee that set the first internationally accepted standards of radomes for civil aircraft (RTCA document DO-213, Minimum Performance Standards for Nose Mounted Radomes). In 2005 he received the Exceptional Public Service Medal from NASA for his significant contributions to aviation radome development.

I would also like to thank Mike Stasiowski, senior antenna engineer at Cobham Sensor Systems, for writing the Foreword. Dave Moorehouse, general manager of Cobham Senior Systems, was encouraging and provided a number of photographs. Clint Lackey and Dr. Lance Griffiths, general manager and radome design engineer, respectively, of MFG Galileo Composites and Tim O'Conner and John Phillips, RF engineer and vice president of engineering, respectively, of Cobham SATCOM provided valuable photos. Dave Stressing, engineering manager, aerospace, of Saint Gobain Performance Plastics provided input on environmental effects on radomes and associated photos. Dr. Jeff Fordham and Jan Kendell, vice president of marketing and director of product marketing, respectively, of MI Technologies provided photographs of radome near field and compact range test instrumentation. John Aubin, vice president

and chief technology officer of Orbit FR, provided several photographs of radomes in testing. I would like to add a special thanks to the numerous suppliers and manufacturers that have provided product information and/or characterization data that was used herein.

I would like to recognize Dennis Kozakoff, Jr., vice president of USDigiComm Corporation, who contributed artwork, photographs, and other computational data for use by the radome design community as it appears in this book. This book could not have been completed without the help of my wife, Ruth Kozakoff, who not only typed the original manuscript, but was also a great source of encouragement and inspiration throughout the process.

Part I
Background and Fundamentals

1

Overview of Radome Phenomenology

A radome, an acronym coined from radar dome, is a cover or structure placed over an antenna that protects the antenna from its physical environment. Ideally, the radome is radio frequency (RF) transparent so that it does not degrade the electrical performance of the enclosed antenna in any way.

Today, radomes find wide applications in ground, maritime, terrestrial (ground), vehicular, aircraft, and missile electronic systems. For example, a radome-enclosed air traffic control radar antenna is shown in Figure 1.1 and a radome-enclosed missile guidance antenna shown in Figure 1.2.

1.1 History of Radome Development

Before the use of radomes, slow-speed aircraft in early World War II carried VHF radars that used externally mounted Yagi or dipole-array antennas. With the advent of microwave radar on higher-speed aircraft, a means of protecting the antennas from the physical flight environment became necessary.

There was even a greater need for protecting airborne antennas when microwave radar first appeared in the United States in 1940. Initially, Sperry Rand Corporation tested an experimental unit, suspended in the open bomb bay of a B-18 aircraft [1]. At about the same time, the introduction of the high-power microwave magnetron from England spawned the rapid development of both military and civilian radars.

The first reported aircraft radomes used simple, thin-wall designs. In 1941, the first in-flight radome was a hemispherical nose radome fabricated from Plexiglas. It protected an experimental S-band, Western Electric radar flown in a B-18A aircraft, shown in Figure 1.3. Beginning in 1943, production

Figure 1.1 Radome-enclosed air traffic control radar antenna at an airport. (Photo courtesy of USDigiComm Corporation.)

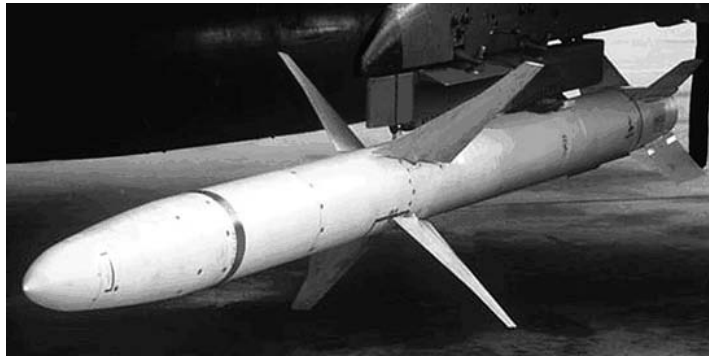

Figure 1.2 Radome-enclosed missile guidance antenna. (Photo courtesy of USAF National Museum.)

airborne radars used plywood radomes that were 0.25 inch thick [2]. In this period, plywood radomes also appeared on U.S. Navy PT boats and blimps, as well as in ground installations.

Because plywood has moisture absorption problems and does not easily bend into doubly curved shapes, new radome construction techniques and materials were necessary. For instance, in 1944 the MIT Radiation Laboratory developed the three-layer A-sandwich, which used dense skins and a low-density core material. Fiberglass skins and polystyrene fiber core materials were common during this era [3].

Figure 1.3 Photograph of a B-18A aircraft. (Photo courtesy of USDigiComm Corporation.)

However, since World War II, radome materials have continued to develop in two main areas: ceramics, used primarily for hyper velocity missile radomes, and high-strength organic materials for sandwich composite radomes.

Today, the most modern of aircraft radomes use sandwich-wall construction. Figure 1.4 shows a modern aircraft with a radar nose radome designed with a sandwich wall construction.

Advanced computerized design analysis techniques have also appeared as the result of electronic performance requirements for new avionics and radars. The distribution of radome technology data through the various symposia is the primary force advancing computerized design analysis techniques. The most well known of these symposia was probably the biennial Electromagnetic Window Symposium held at the Georgia Institute of Technology in Atlanta, Georgia.

1.2 Radome-Antenna Interaction

Over recent decades, the rapid growth in the use of the electromagnetic spectrum has led to many improvements in the performance of the antennas associated with electromagnetic sensors or communications electronics. Two examples of these improvements are dual-polarized ultrawideband antenna systems for improved radar performance and very low sidelobe antennas for use in

Figure 1.4 Radome-enclosed radar antenna on the nose of a modern aircraft. (Photograph courtesy of USAF National Museum.)

SATCOM communications equipment which must meet very stringent, far-out sidelobe requirements.

The antennas associated with these equipments require far more stringent radome performances than their predecessors because the antenna performance can be altered by radome effects that include, but are not limited to:

1. Introduction of a boresight error (BSE) and boresight error slope (BSES);
2. Introduction of a registration error;
3. Increased antenna sidelobe levels;
4. Increased depolarization or the folding of energy from one polarization sense to the other;
5. Increase in antenna voltage standing wave ratio (VSWR);
6. Introduction of an insertion loss due to the presence of the radome.

1.2.1 Boresight Error (BSE) and Boresight Error Slope (BSES)

BSE is a bending of the angle of arrival of a received signal relative to its actual angle of arrival or line of sight. This phenomenon stems primarily from distortions of the electromagnetic wavefront as it propagates through a dielectric

radome wall. BSES is defined as the rate of change of BSE as a function of the antenna scan angle within the radome.

For a radome-enclosed missile monopulse antenna, BSE depends on frequency, polarization, and antenna orientation. Radome BSE directly affects the miss distance of a missile flying a pursuit guidance trajectory. Radome BSES also impacts the miss distance (or guidance accuracy) of a missile flying a proportional or modern guidance law trajectory [4].

Radome BSES can cause severe degradation for modern guidance systems and classical proportional navigation systems. Missile guidance system designers often use computer and/or hardware in-the-loop (HWIL) simulations to determine the relationship between a missile terminal miss distance versus the BSES of the radome. The desired guidance accuracy will dictate a maximum allowable BSES.

In production, the radome manufacturing tolerance affects the BSES characteristics of the radome. As a result of the computer and/or HWIL simulations discussed earlier, the maximum allowable BSES is often used to specify the required manufacturing tolerances of the radome [5].

1.2.2 Registration Error

Registration error is the difference in uplink frequency and downlink frequency BSE in the case of radome-enclosed SATCOM antennas. It is important that this parameter be sufficiently small to assure that both the transmit beam and receive beam peaks are coaligned on the same satellite.

1.2.3 Antenna Sidelobe Degradation

Antenna sidelobes generally increase when an antenna is placed within a radome. This increase occurs because of distortion and wall transmission effects as a wavefront propagates through a radome wall. The state of the art of low-sidelobe-level antennas has progressed to the point where the radome is the main source of clutter, resulting from increased sidelobes [6].

1.2.4 Depolarization

Radome depolarization is a folding of energy from the primary antenna polarization to the other sense. For instance, assume that the antenna is receiving a right-hand circularly polarized (RHCP) signal. After the received signal propagates through the radome wall, part of the energy is converted into a left-hand circularly polarized (LHCP) signal. This phenomenon occurs as a result of the radome wall curvature and the difference in complex transmission coefficient between orthogonal polarized vectors.

Depolarization can be a big problem, particularly with satellite communications (SATCOM) ground terminals that utilize frequency reuse, such as the typical SATCOM on a ship shown in Figure 1.5. Here two independent signals are transmitted or received within the same frequency channel, but in opposite polarization senses.

1.2.5 Antenna Voltage Standing Wave Ratio (VSWR)

The antenna VSWR can greatly increase from RF power reflected from the inner radome wall surface. The VSWR increase from this radome reflected power will represent an additional gain/loss that can be critical to, for example, SATCOM communications systems.

1.2.6 Introduction of an Insertion Loss Due to the Presence of the Radome

Lastly, radome insertion loss is a reduction in signal strength as the electromagnetic wave propagates through the dielectric radome wall. Part of the loss occurs as a reflection at the air/dielectric interface. The remainder of the loss occurs from dissipation within the dielectric layers. The *material loss tangent* or $\tan\delta$ is a measure of these dissipative losses.

1.3 Significance of Parameters in Radome Performance

The particular application decides which radome-induced effects are of greatest concern. Table 1.1 gives an overview of the most typical radome degradations that are most important to the design engineer in various sensor or electronics applications.

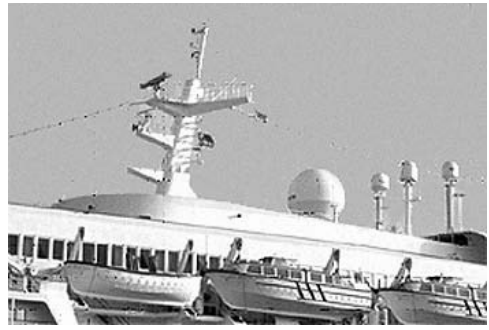

Figure 1.5 Radome-enclosed SATCOM antennas on a ship. (Photo courtesy of USDigiComm Corporation.)

Table 1.1
Most Important Radome Degradations in Various Applications

Application	Radome Loss Increase	Antenna Sidelobe Increase	Radome Depolarization	BSE Increase	BSES Increase	Antenna VSWR Increase
Ground/Sea						
Weather radars	X	X	X			X
Air defense radars	X	X	X	X	—	X
Marine radars	X	X	X	X	—	X
Gun fire control radars	X	X	—	X	X	X
Microwave communications	X	—	—	—	—	X
Ground and marine SATCOM	X	X	X	—	—	X
GPS/satellite navigation	X	—	X	—	—	—
Airborne						
Weather radars	X	X	X	—	—	X
Ground imaging radar	X	X	—	—	—	X
Radar altimeters	X	X	—	—	—	X
Radar beacons/TCAS	X	—	—	—	—	X
Aircraft fire control radars	X	X	—	X	X	X
Airborne SATCOM	X	X	X	—	—	X
Microwave air-to-ground communications	X	—	—	—	—	—
Missiles/Munitions						
Radar guidance	X	X	X	X	X	X
Passive antiradiation homing	X	X	—	—	—	—
Passive radiometric imaging	X	—	—	—	—	—

Early methods of radome evaluation used to determine the severity of these degradations were cumbersome and approximate, relying primarily on the

use of the nomograph [7]. With the arrival of the computer, modern mathematical approaches began to appear, featuring better computational accuracy [8].

For high-accuracy radome performance computations, the efficiency of the calculation determines its limitation as a design tool. Therefore, the combination of accuracy and efficiency must be a goal in any radome-antenna analysis approach.

In addition, the radome design community faces increased computer run times for analysis of new millimeter wave (very short wavelength) radar systems. The increased run time is due to the fact that sample spacings are typically a half wavelength over the antenna aperture in order to avoid computational errors that occur when grating lobes come into real space. This additional run time adds impetus to the search for more efficient methods of performing millimeter-wave radome analysis.

Fortunately, computational approaches that would have required a mainframe a few years ago can now utilize the low-cost, high-performance personal computer (PC). The goal of this book is to provide you with working tools amenable to PC modeling so that you can quantify the radome-induced parameters of interest in a particular application.

1.4 Radome Technology Advances Since the First Edition

Since the first edition of this book, the greatest advances in radome technology probably have been in the use of metamaterials or frequency selective layers within the radome wall composite. A brief discussion of these advances appears in the following.

1.4.1 Use of Metamaterials

Metamaterials are unique materials possessing characteristics opposite to those of naturally occurring materials. They exhibit unusual electrical properties such as a reversal of Snell's law. A *metamaterial* is a material that gains its properties from its structure rather than directly from its composition. The term was coined in 1999 by Rodger M. Walser of the University of Texas at Austin [9], who defined metamaterials as macroscopic composites having a manmade, three-dimensional, periodic cellular architecture designed to produce an optimized combination not available in nature. In simple terms, it is a manmade composite material that exhibits a negative index of refraction. Additional information about metamaterials appears in [10].

The design of an antenna radome using such metamaterials can enhance antenna gain. Research by Liu et al. [11] used multilayered structures composed of two materials with left-handed materials having an average index of refraction

close to zero and air. Liu et al.'s analysis showed a beamwidth reduction of 37.5% and an antenna gain increase of about 6 dBi.

Work by Metz [12] used metamaterials to create a biconcave lens architecture for focusing the microwaves transmitted by the antenna, in which the sidelobes of the antenna were greatly reduced. This suggests that such materials may have a role in minimizing the effects of sidelobe degradation, which is very important to radome-enclosed SATCOM antennas.

Metamaterials have also been used to compensate for the effects of radome BSE [13]. In one compensation technique comprised of a two-layer radome, an inner metamaterial layer of a negative index of refraction material is used with an outer layer of a conventional radome dielectric material having a positive index of refraction material. The thickness of the two materials and their respective refractive indices are adjusted so that a beam of electromagnetic energy passing through the radome is effectively not refracted.

1.4.2 Frequency Selective Radomes

Under many circumstances it is desirable to add frequency selectivity to a radome to prevent coupling from nearby transmit antennas that may interfere with the electronics. For instance, a radome-enclosed IRIDIUM antenna receiving relatively weak satellite signals may be interfered with by a high-power transmitter on the same platform. What might be employed is a frequency selective surface on the IRIDIUM radome providing a bandpass performance at the IRIDIUM frequency, and/or a band reject frequency selective surface on the IRIDIUM radome providing a band reject performance at the interfering transmit frequency that may be overloading the IRIDIUM receiver.

The frequency selective surface (FSS) layer is generally arranged on the surface of the radome wall composite, and a discussion of design techniques appear in [14–17]. However, there is no reason why the FSS layer cannot be arranged on the inner surface of the radome wall composite or even embedded within the wall. FSS surfaces usually consist of arrays of etched antenna elements of some kind and can be designed to either reflect or transmit electromagnetic waves with a frequency discrimination. The simplest of these are conducting strips (or conducting slots in a metal ground plane), which can be represented in computer modeling by reactive equivalent components. Reactive components can also be identified in other, more complicated elements such as square loops or slots and Jerusalem cross geometries. For FSS band transmission behavior, these elements mostly take the form of slot geometries in a conducting radome wall layer.

For a monolithic wall radome, Purinton [18] has investigated the possibility of embedding a wire mesh or screen into the radome material itself. The inductance can be arranged to offset the capacitance of the radome dielectric

material. By proper design, a radome can be built that will pass only a single band of frequencies centered on any desired operating radar frequency. Wu [19] has developed an approach to obtain a multiple bandpass FSS performance.

1.4.3 Concealed Radomes

Zoning regulations, land developer/subdivision covenants, and other legal restrictions have sometimes created problems for telecom companies installing sensitive microwave and SATCOM antennas of various types within certain

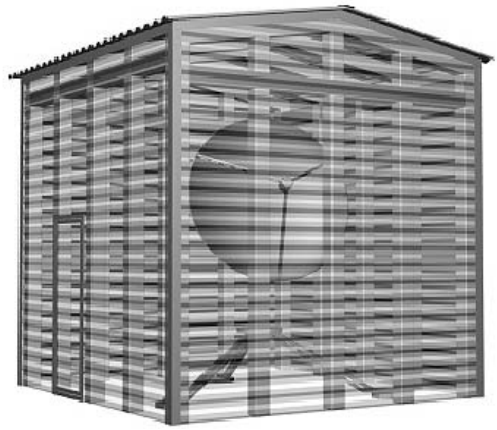

(a)

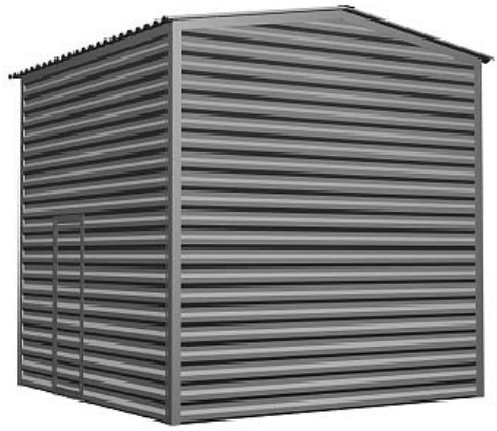

(b)

Figure 1.6 (a, b) Microwave antenna within an RF transparent structure. (Photo courtesy of ConcealFab Corporation.)

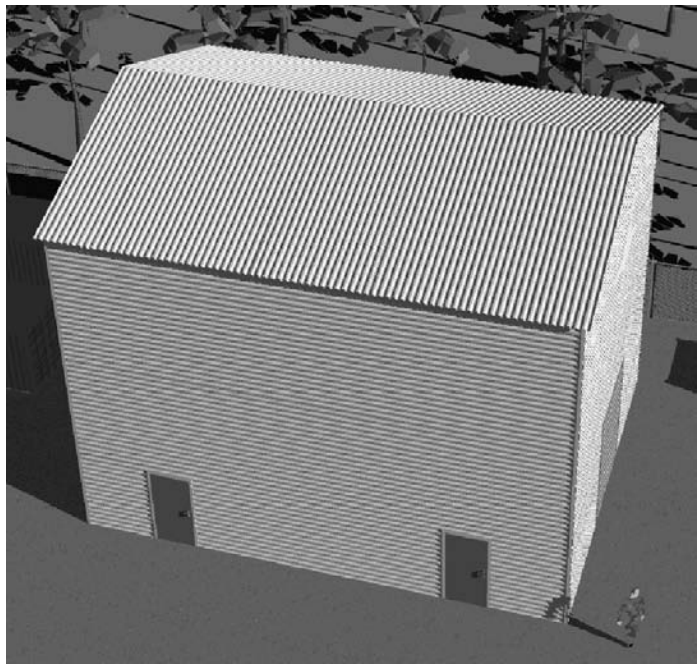

Figure 1.7 Very large microwave antenna within an RF transparent structure. (Photo courtesy of ConcealFab Corporation.)

urban areas. Unique cost-effective RF transparent structures have been recently designed and engineered out of innovative structural shapes and constructed from plastic materials that will last a lifetime [20]. These structures are lightweight and blend into virtually any environment and can be fabricated to resemble virtually any building configuration, as shown in Figure 1.6, which encloses a small microwave antenna. The concept is scalable to any antenna size as illustrated for a very large antenna in Figure 1.7.

References

[1] Tice, T. E., "Techniques for Airborne Radome Design," AFATL-TR-66-391, Air Force Avionics Laboratory, AFSC, Wright Patterson AFB, Ohio, December 1966.

[2] Baxter, J. P., *Scientists Against Time*, Boston, MA: Little, Brown and Company, 1952.

[3] Eggleston, W., *Scientists at War*, Toronto, Canada: Hunter Rose Company, Ltd., 1950.

[4] Johnson, R. C., "Seeker Antennas," Ch. 38 in *Antenna Engineering Handbook*, 3rd ed., New York: McGraw-Hill, 1992.

[5] Yueh, W. R., "Adaptive Estimation Scheme of Radome Error Calibration," *Proceedings of the 22nd IEEE Conference on Decision and Control*, Vol. 8, No. 5, 1983, pp. 666–669.

[6] Rulf, B., "Problems of Radome Design for Modern Airborne Radar," *Microwave Journal*, Vol. 28, No. 5, May 1995, pp. 265–271.

[7] Kaplun, V. A., "Nomograms for Determining the Parameters of Plane Dielectric Layers of Various Structure with Optimum Radio Characteristics," *Radiotechnika I Electronika* (Russian), Part 2, Vol. 20, No. 9, 1965, pp. 81–88.

[8] Bagby, J., "Desktop Computer Aided Design of Aircraft Radomes," *IEEE MIDCON 1988 Conference Record*, Western Periodicals Company, N. Hollywood, CA, 1988, pp. 258–261.

[9] Walser, R. M., *Introduction to Complex Mediums for Electromagnetics and Optics,* W. S. Weiglhofer and A. Lakhtakia, (eds.), Bellingham, WA: SPIE Press, 2003.

[10] Smith, D. R., et al, "Composite Medium with Simultaneously Negative Permeability and Permittivity," *Physical Review Letters*, Vol. 84, No. 18, May 2000.

[11] Liu, H. -N., et al., "Design of Antenna Radome Composed of Metamaterials for High Gain," *IEEE Antennas and Propagation Society International Symposium 2006*, July 9–14, 2006, pp. 19–22.

[12] Metz, C., "Phased Array Metamaterial Antenna System," U.S. Patent, October 2005, http://patft.uspto.gov/netacgi/nph-Parser?Sect2=PTO1&Sect2=HITOFF&p=1&u=%2Fnetahtml%2FPTO%2Fsearch-bool.html&r=1&f=G&l=50&d=PALL&RefSrch=yes&Query=PN%2F6958729-h0#h0http://patft.uspto.gov/netacgi/nph-Parser?Sect2=PTO1&Sect2=HITOFF&p=1&u=%2Fnetahtml%2FPTO%2Fsearch-bool.html&r=1&f=G&l=50&d=PALL&RefSrch=yes&Query=PN%2F6958729-h2#h26,958,729.

[13] Schultz, S. M., D. L. Barker, and H. A. Schmitt, "Radome Compensation Using Matched Negative Index or Refraction Materials," U.S. Patent 6,788,273, September 2004.

[14] Parker, E. A., "The Gentleman's Guide to Frequency Selective Surfaces," *17th Q.M.W. Antenna Symposium*, London, Electronic Engineering Laboratories, University of Kent, April 1991

[15] Munk, B. A., *Frequency Selective Surfaces*, New York: John Wiley & Sons, 2000.

[16] Vardaxoglou, J. C., *Frequency Selective Surface: Analysis and Design*, Electronic & Electrical Engineering Series, Taunton, Somerset, England: Research Studies Press, 1997.

[17] Wang, Z. L., et al., "Frequency-Selective Surface for Microwave Power Transmission," *IEEE Transactions on Microwave Theory and Techniques*, Vol. 47, No. 10, October 1999, pp. 2039–2042.

[18] Purinton, D. L., "Radome Wire Grid Having Low Pass Frequency Characteristics," U.S. Patent 3,961,333, 1976.

[19] Wu, T. -K., "Multi-Band Frequency Selective Surface with Double-Square-Loop Patch Elements," Jet Propulsion Laboratory, NTRS: 2006-12-25, Document ID: 20060037676, available through National Technology Transfer Center (NTTC), Wheeling, WV, 1995.

[20] http://www.concealfab.com.

2

Basic Principles and Conventions

This chapter provides a reference and review of topics used in the modeling of radome-covered antennas. The topics covered in this chapter are:

- Vector mathematics;
- Electromagnetic theory;
- Matrices;
- Coordinate systems and antenna pointing gimbals.

These topics are not treated rigorously, but rather in a top-level summary. If you are well versed in these subjects, you may wish to skip most of this chapter. However, you should review Section 2.4, which defines reference conventions used in later mathematical modeling.

2.1 Vector Mathematics

A Cartesian coordinate system is used where a vector is represented as the sum of three vectors parallel to Cartesian coordinate axes, with the components of given by a_x, a_y, a_z. For this purpose, we associate with that coordinate system three mutually perpendicular unit vectors ($\bar{x}$, $\bar{y}$, $\bar{z}$), which have the positive directions of the three-coordinate axes. Accordingly, the vector can be represented as

$$\bar{A} = a_x \bar{x} + a_y \bar{y} + a_z \bar{z} \tag{2.1}$$

Figure 2.1 illustrates the three unit vectors $\bar{x}, \bar{y}, \bar{z}$ when the origin is chosen as their common initial point and vector $\overline{A}$ in this coordinate system. In a like manner, another vector may be defined as

$$\overline{B} = b_x \bar{x} + b_y \bar{y} + b_z \bar{z} \tag{2.2}$$

The dot and scalar cross products of vectors $\overline{A}$ and $\overline{B}$ are both scalar quantities expressed in terms of the angle ψ between the two vectors [1].

$$\overline{A} \cdot \overline{B} = AB \cos\psi \tag{2.3}$$

$$\left|\overline{A} \times \overline{B}\right| = AB \sin\psi \tag{2.4}$$

where the magnitude of these two vectors are expressed by the following two formulas:

$$A = \sqrt{a_x^2 + a_y^2 + a_z^2} \tag{2.5}$$

$$B = \sqrt{b_x^2 + b_y^2 + b_z^2} \tag{2.6}$$

However, the vector cross product of vectors $\overline{A}$ and $\overline{B}$ results in another vector, which can be defined as:

$$\overline{C} = \overline{A} \times \overline{B} \tag{2.7}$$

This is illustrated in Figure 2.2.

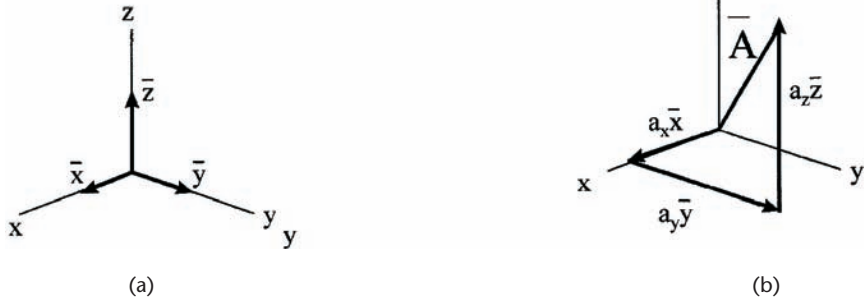

Figure 2.1 (a) The unit vectors $\bar{x}, \bar{y}, \bar{z}$ and (b) representation of vector $\overline{A}$.

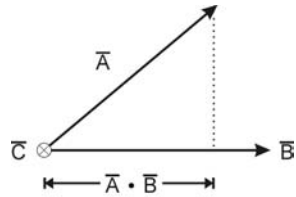

Figure 2.2 Dot and cross products of vectors *A* and *B*.

This vector is orthogonal to the plane in which vectors $\overline{A}$ and $\overline{B}$ lie, and its sense is determined by the right-hand rule. In a matrix form, it is given by [2]:

$$\overline{C} = \begin{bmatrix} \bar{x} & \bar{y} & \bar{z} \\ a_x & a_y & a_z \\ b_x & b_y & b_z \end{bmatrix} \tag{2.8}$$

or, expanding the matrix

$$\overline{C} = \left(a_y b_z - b_y a_z\right)\bar{x} + \left(a_z b_x - b_z a_x\right)\bar{y} + \left(a_x b_y - b_x a_y\right)\bar{z} \tag{2.9}$$

Other vector manipulations that are worth mentioning include the following:

- The *distributive law* for scalar multiplication [3]:

$$\overline{A} \cdot \left(\overline{B} + \overline{C}\right) = \overline{A} \cdot \overline{B} + \overline{A} \cdot \overline{C} \tag{2.10}$$

- The *distributive law* for vector multiplication:

$$\overline{A} \times \left(\overline{B} + \overline{C}\right) = \overline{A} \times \overline{B} + \overline{A} \times \overline{C} \tag{2.11}$$

- The *scalar and vector triple products,* respectively:

$$\overline{A} \cdot \left(\overline{B} \times \overline{C}\right) = \left(\overline{A} \times \overline{B}\right) \cdot \overline{C} = \overline{C} \cdot \left(\overline{A} \times \overline{B}\right) + \overline{B} \cdot \left(\overline{C} \times \overline{A}\right) \tag{2.12}$$

$$\overline{A} \times \left(\overline{B} \times \overline{C}\right) = \left(\overline{A} \cdot \overline{C}\right)\overline{B} - \left(\overline{A} \cdot \overline{B}\right)\overline{C} \tag{2.13}$$

Finally, some relationships important in electromagnetic theory are as follows:

- The *curl* of a vector:

$$\nabla \times \overline{A} = \begin{bmatrix} \overline{x} & \overline{y} & \overline{z} \\ \dfrac{\partial}{\partial x} & \dfrac{\partial}{\partial y} & \dfrac{\partial}{\partial z} \\ a_x & a_y & a_z \end{bmatrix} \tag{2.14}$$

- The *divergence* of a vector:

$$\nabla \cdot \overline{A} = \frac{\partial a_x}{\partial x} + \frac{\partial a_y}{\partial y} + \frac{\partial a_z}{\partial z} \tag{2.15}$$

- The *curl of the curl* of a vector:

$$\nabla \times \left(\nabla \times \overline{A}\right) = \nabla\left(\nabla \cdot \overline{A}\right) - \nabla^2 \overline{A} \tag{2.16}$$

2.2 Electromagnetic Theory

The development of the wave equation begins with Maxwell's relationships for the electric and magnetic field quantities applicable to a charge and an impressed current free region.

$$\nabla \cdot \overline{D} = 0 \tag{2.17}$$

$$\nabla \cdot \overline{B} = 0 \tag{2.18}$$

$$\nabla \times \overline{E} = -\mu \frac{\partial \overline{H}}{\partial t} \tag{2.19}$$

$$\nabla \times \overline{H} = \varepsilon \frac{\partial \overline{E}}{\partial t} \tag{2.20}$$

along with the *auxiliary relations:*

$$B = \mu H \tag{2.21}$$

$$D = \varepsilon E \tag{2.22}$$

The preceding differential equations are the fundamental Maxwell relationships, written in a rationalized meter, kilogram, seconds (mks) system of units. In this system, we have

E = electric intensity (V/m);

D = electric displacement (C/m^2);

H = magnetic intensity (A/m);

B = magnetic induction (Wb/m);

$\mu = \mu_r \mu_o$ = permeability or magnetic inductive capacity of medium (H/m);

μ_r = relative permeability (dimensionless);

$\mu_o = 4\pi \times 10^{-7} = 1.257 \times 10\text{-}6$ H/m;

ε = permittivity or electric inductive capacity of medium (F/m);

ε_r = relative permittivity or relative dielectric constant (dimensionless);

$\varepsilon_o = 8.854 \times 10^{-12}$ F/m.

Note that the permittivity is a complex number:

$$\varepsilon = \varepsilon' - j\varepsilon'' \tag{2.23}$$

where ε' is the real part of ε in farads per meter and ε'' is the imaginary part of ε also in farads per meter.

Assuming a time harmonic field of the form e^{jwt}, a solution is required for the wave equation developed from Maxwell's equations

$$\nabla^2 \overline{E} = -k^2 \overline{E} \tag{2.24}$$

A solution to this differential equation for a wave propagating in the z-direction takes the form e^{-jkt}, where k is the wave number. The wave number is complex for waves propagating through a typical dielectric radome material:

$$jk = j\omega\sqrt{\mu(\varepsilon' - j\varepsilon'')} = j\omega\sqrt{\omega\varepsilon'\left(1 - j\frac{\varepsilon''}{\varepsilon'}\right)} \tag{2.25}$$

In (2.25), it is convenient to introduce the concept of a dielectric material loss tangent:

$$\tan\delta = \frac{\varepsilon''}{\varepsilon'} \tag{2.26}$$

This concept allows the wave number to be broken into real and imaginary parts [4]:

$$\alpha = \omega\sqrt{\frac{\mu\varepsilon'}{2}\left[\sqrt{1+(\tan\delta)^2}-1\right]} \tag{2.27}$$

$$\beta = \omega\sqrt{\frac{\omega\varepsilon'}{2}\left[\sqrt{1+(\tan\delta)^2}+1\right]} \tag{2.28}$$

Using this notation, the wave propagating through the dielectric in the z-direction then takes the more convenient form:

$$E = E_o e^{-jkz} = E_o e^{-\alpha z} e^{-j\beta z} \tag{2.29}$$

In this equation, α is known as the attenuation constant and β is known as the phase constant. An electromagnetic wave is then both attenuated and phase shifted as it propagates through a dielectric medium.

For a wave propagating in the z-direction, valid solutions to the wave equation are orthogonal signal sets E_x, H_y or E_y, H_x, which are related by the wave impedance of the medium:

$$\frac{E_x}{H_y} = \frac{E_y}{H_x} = \eta \tag{2.30}$$

In terms of the definition of polarization of the wave, note the following:

- The polarization is *linear* when only E_x or E_y exists or when both components exist simultaneously but are in phase.
- The polarization is *elliptical* when two components exist, are unequal in amplitude, and are out of phase with each other.
- The polarization is said to be *circular* when two components exist and are equal in amplitude and the phase is a +90° or −90° difference.

Because of the modeling used in later sections of this book, an electromagnetic wave incident on a dielectric medium must be quantified into two orthogonal components. These components are defined as parallel and

perpendicular to the plane formed by a vector in the direction of propagation and a vector normal to the surface of the radome at the incidence point.

The convention used for parallel and perpendicular wave components for a wave propagating from free space and an incident on a dielectric medium is illustrated in Figure 2.3.

2.3 Matrices

Matrix algebra is a powerful mathematical tool in connection with linear equations and transformations [5].

An $\mathbf{m} \times \mathbf{n}$ matrix is an ordered set of **mn** quantities, arranged in a rectangular array of **m** rows and n columns. If $\mathbf{m} = \mathbf{n}$, the array is a square matrix of order **n**. A matrix having only one column is called a *column matrix* or *column vector*.

The following are useful relationships for $\mathbf{m} \times \mathbf{n}$ matrices $[F]$, $[G]$, $[J]$, and arbitrary constants u and v:

$$[F]+[G]=[G]+[F] \tag{2.31}$$

$$u(v[F])=(uv)[F] \tag{2.32}$$

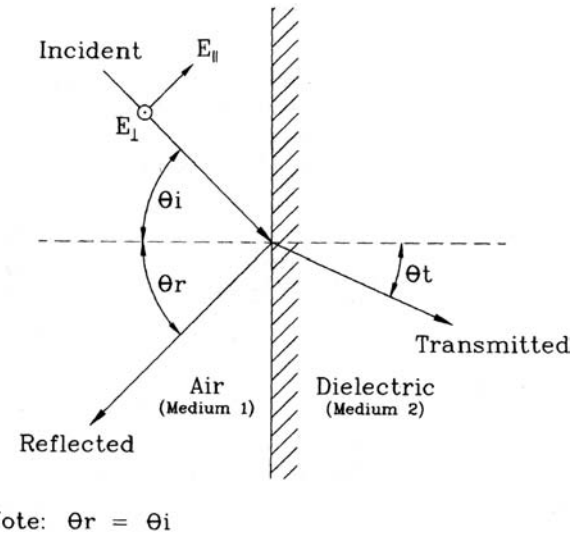

Figure 2.3 Illustration of parallel and perpendicular wave components.

$$(u+v)[F]=u[F]+v[F] \tag{2.33}$$

$$[F]+([G]+[J])=([F]+[G]+[J]) \tag{2.34}$$

$$u([F]+[G])=u[F]+u[G] \tag{2.35}$$

If we have an $\mathbf{m}\times\mathbf{n}$ matrix $[G]$ and an $\mathbf{n}\times\mathbf{p}$ matrix $[J]$, the product of $[G]$ and $[J]$ is an $\mathbf{m}\times\mathbf{p}$ matrix given by

$$[F]=[G][J] \tag{2.36}$$

We can only multiply two matrices if the number of columns of the first factor is equal to the number of rows in the second.

The set of relations given in (2.36) can be solved for $[J]$ via Cramer's rule [6] in order to obtain an inverse transformation

$$[G]^{-1}[G][J]=[J]=[G]^{-1}[F] \tag{2.37}$$

where the identity matrix is defined via

$$[I]=[G]^{-1}[G] \tag{2.38}$$

We will now demonstrate the inverse transformation. Consider $[G]$ represented by:

$$[G]=\begin{bmatrix} g_{11} & g_{12} & g_{13} \\ g_{21} & g_{22} & g_{23} \\ g_{31} & g_{32} & g_{33} \end{bmatrix} \tag{2.39}$$

The first step in the process is to form the transpose of $[G]$

$$[G]^{T}=\begin{bmatrix} g_{11} & g_{21} & g_{31} \\ g_{12} & g_{22} & g_{32} \\ g_{13} & g_{23} & g_{33} \end{bmatrix} \tag{2.40}$$

To get the inverse of [G], we now replace the elements of the transpose matrix by their corresponding cofactors and divide by the determinant of [G] [6]:

$$[G]^{-1} = \frac{\begin{bmatrix} g_{22}g_{33} - g_{23}g_{32} & g_{13}g_{32} - g_{12}g_{33} & g_{12}g_{23} - g_{13}g_{22} \\ g_{23}g_{31} - g_{21}g_{33} & g_{11}g_{33} - g_{13}g_{31} & g_{13}g_{21} - g_{11}g_{23} \\ g_{21}g_{32} - g_{22}g_{31} & g_{12}g_{31} - g_{11}g_{32} & g_{11}g_{22} - g_{12}g_{21} \end{bmatrix}}{|G|} \quad (2.41)$$

2.4 Coordinate Systems and Gimbal Relationships

The mathematics applied to mechanically pointing an antenna within a fixed radome requires that we establish a coordinate system in which to solve the problem. It will be necessary to transform the location of an arbitrary point on the antenna face into radome coordinates after all gimbal angular rotations. For many problems the derivation of the desired transformations begins by definition of a standard spherical coordinate system that relates θ, φ gimbal rotations into the standard two-axis antenna azimuth (AZ) and elevation (EL) rotations. These are illustrated in Figure 2.4 for two popular types of antenna pointing gimbals, specifically, elevation over azimuth (EL/AZ) gimbals or azimuth over elevation (AZ/EL) gimbals.

A definition of these gimbal rotation parameters are:

- *Elevation angle* (EL) = the angle between the antenna centerline and its projection onto the *z-x* plane of the local coordinate system, often termed the elevation component of the look angle;
- *Azimuth angle* (AZ) = the angle between the projection of the antenna centerline onto the *x-y* plane and the boresight, often termed the azimuth component of the look angle.

In missile or aircraft applications, the reference Cartesian coordinate system used throughout this book is generally placed at the geometric center of the radome base in the *y-z* plane, as illustrated in Figure 2.4. The gimbal location $P_g(x_g, 0, 0)$ within the radome represents the center of gimbal rotations. Note that Δ_a, Δ_b are independent azimuth and elevation rotation offsets from $P_g(x_g, 0, 0)$. Figure 2.5 is a photograph of a waveguide type missile-seeker antenna, mounted on an AZ/EL antenna gimbal.

The mathematical development can be simplified by sequentially performing the following steps:

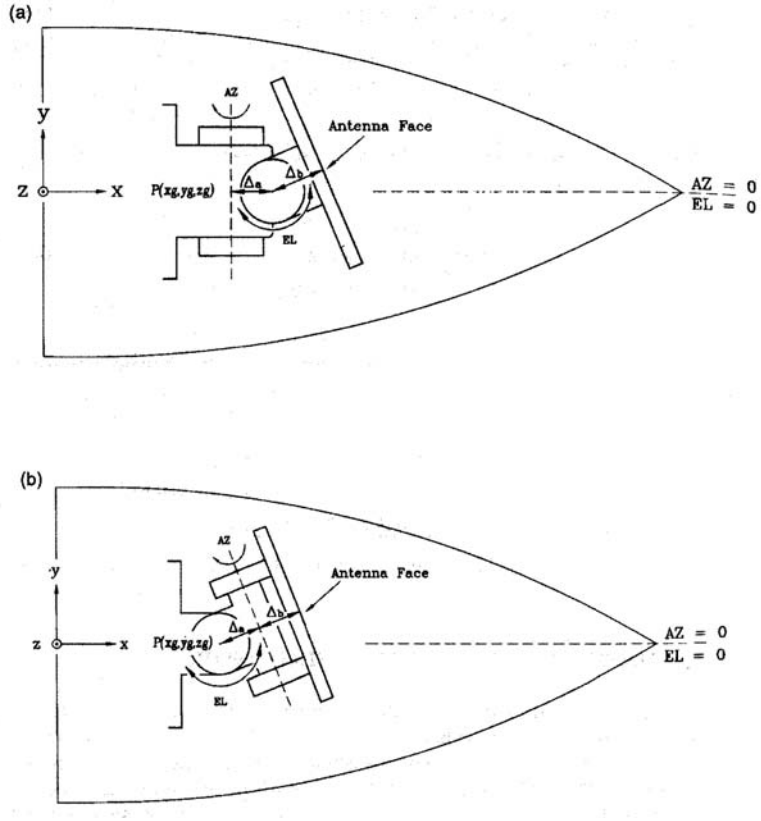

Figure 2.4 (a) EL/AZ gimbal and (b) AZ/EL gimbal.

- With a Cartesian coordinate system placed at the antenna center, compute the transformation that results from angular rotations.
- Transform results to a Cartesian coordinate system placed at center of a gimbal rotation, taking into account the rotational offsets.
- Linearly transform the results to true radome coordinates with the coordinate system located at the base of the radome.

Consider the following development. With a coordinate system placed at the antenna center, as illustrated in Figure 2.6, the transformation of any point on the antenna aperture $P_a(x', y', z')$ is:

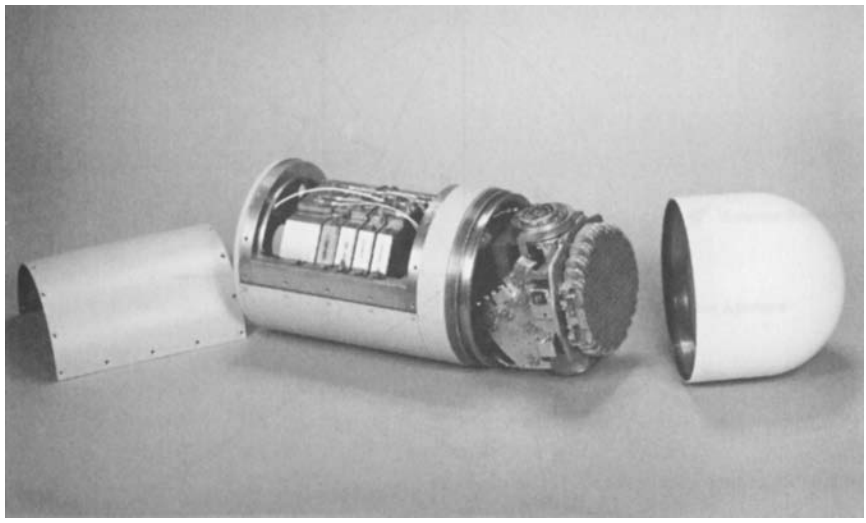

Figure 2.5 AZ/EL gimbaled waveguide antenna. (Photo courtesy of Lockheed Martin Corporation.)

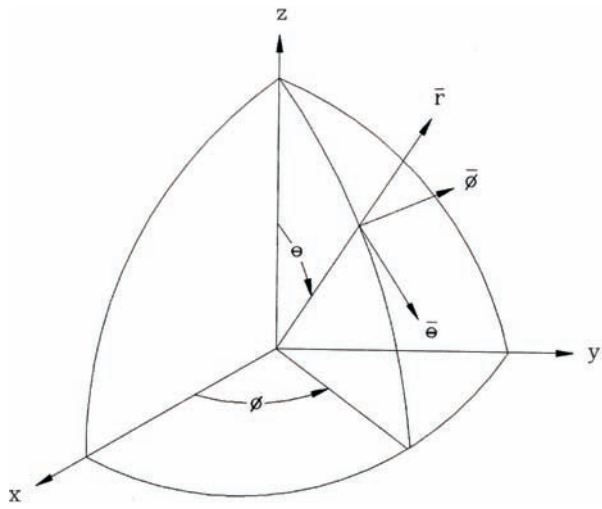

Figure 2.6 Reference spherical coordinate system.

$$\begin{bmatrix} x \\ y \\ z \end{bmatrix} = \begin{bmatrix} \sin\theta\cos\phi & -\sin\theta & -\cos\theta\cos\phi \\ \sin\theta\sin\phi & \cos\phi & -\cos\theta\sin\phi \\ \cos\theta & 0 & \sin\theta \end{bmatrix} \begin{bmatrix} x' \\ y' \\ z' \end{bmatrix} \tag{2.42}$$

If we let $\psi = 90° - \theta$, then this becomes

$$\begin{bmatrix} x \\ y \\ z \end{bmatrix} = \begin{bmatrix} \cos\psi\cos\phi & -\sin\phi & -\sin\psi\cos\phi \\ \cos\psi\sin\phi & \cos\phi & -\sin\psi\sin\phi \\ \sin\psi & 0 & \cos\psi \end{bmatrix} \begin{bmatrix} x' \\ y' \\ z' \end{bmatrix} \tag{2.43}$$

The coordinate system space is illustrated in Figure 2.7 for the elevation over azimuth (EL/AZ) antenna gimbal case and illustrated in Figure 2.8 for the azimuth over elevation (AZ/EL) antenna gimbal case.

For the EL/AZ antenna gimbal case, we can now incorporate translations due to the offsets from the gimbal point. We do this by first applying the elevation gimbal rotation with $x' = \Delta_b$, $\psi = 0$ and $\phi = EL$. Next, the azimuth offset, Δ_a, and then the azimuth gimbal rotation is applied by letting $\phi = 0$ and $\psi = AZ$. We then obtain for the transformation [personal communication with Rich Matyskiela, AEL Industries, Lansdale, Pennsylvania, 1994]:

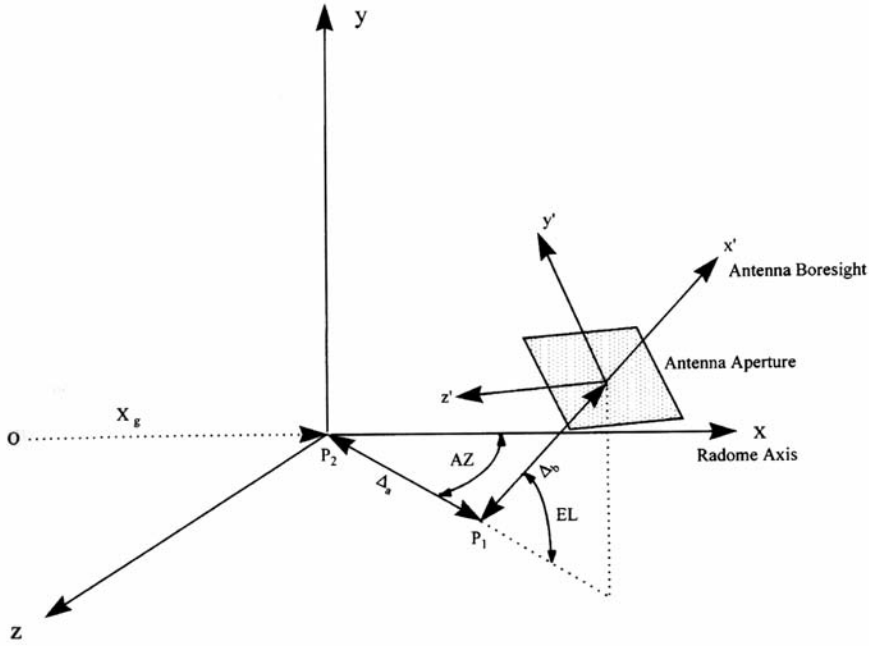

Figure 2.7 EL/AZ coordinate system.

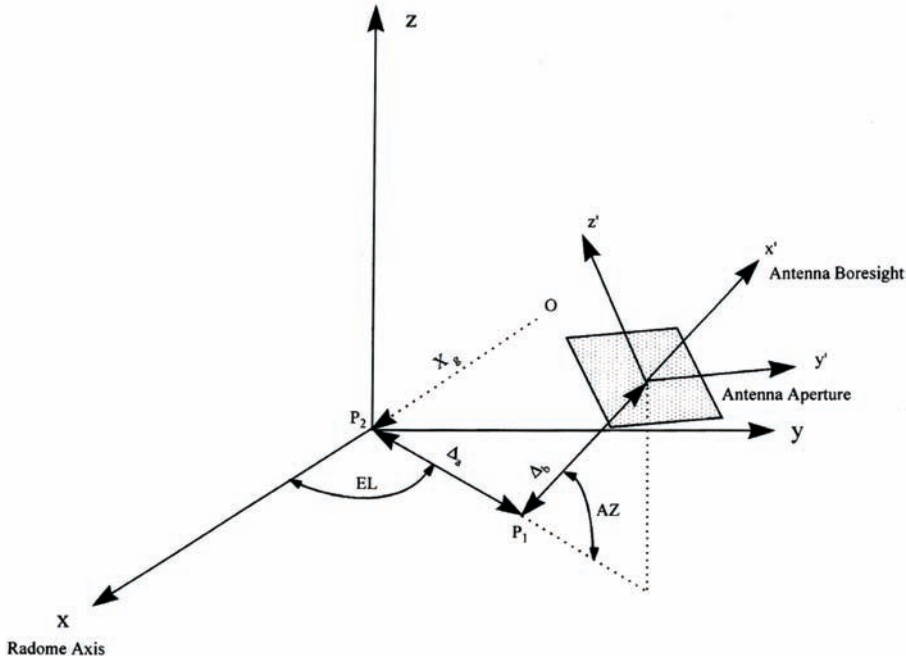

Figure 2.8 AZ/EL coordinate system.

$$\begin{bmatrix} x \\ y \\ z \end{bmatrix} = \begin{bmatrix} \cos AZ & 0 & -\sin AZ \\ 0 & 1 & 0 \\ \sin AZ & 0 & \cos AZ \end{bmatrix} \begin{bmatrix} \cos EL & -\sin EL & 0 \\ \sin EL & \cos EL & 0 \\ 0 & 0 & 1 \end{bmatrix} \begin{bmatrix} \Delta_b \\ y' \\ z' \end{bmatrix} + \begin{bmatrix} \Delta_a \\ 0 \\ 0 \end{bmatrix} \quad (2.44)$$

Performing the indicated matrix multiplications, and adding a translation for the initial gimbal location $P_g(x_g, 0, 0)$, we obtain the final result:

$$\begin{bmatrix} x \\ y \\ z \end{bmatrix} = \begin{bmatrix} \cos AZ \cos EL & -\cos AZ \sin EL & -\sin AZ \\ \sin EL & \cos EL & 0 \\ \sin AZ \cos EL & -\sin AZ \sin EL & \cos AZ \end{bmatrix} \begin{bmatrix} \Delta_b \\ y' \\ z' \end{bmatrix} + \begin{bmatrix} \Delta_a \cos AZ \\ 0 \\ \Delta_a \sin AZ \end{bmatrix} + \begin{bmatrix} x_g \\ 0 \\ 0 \end{bmatrix} \quad (2.45)$$

Similarly, for an AZ/EL gimbal, the matrix solution in (2.46) includes the same translations for the rotational offsets and the initial gimbal location:

$$\begin{bmatrix} x \\ y \\ z \end{bmatrix} = \begin{bmatrix} \cos EL \cos AZ & -\sin EL & -\cos EL \sin AZ \\ \sin EL \cos AZ & \cos EL & -\sin EL \sin AZ \\ \sin AZ & 0 & \cos AZ \end{bmatrix} \begin{bmatrix} \Delta_b \\ y' \\ z' \end{bmatrix} + \begin{bmatrix} \Delta_a \cos EL \\ \Delta_a \sin EL \\ 0 \end{bmatrix} + \begin{bmatrix} x_g \\ 0 \\ 0 \end{bmatrix} \tag{2.46}$$

In computer modeling of radome-enclosed gimbaled antenna cases discussed later in this book, we will use these latter two expressions extensively.

2.5 Specialized Antenna Pointing Gimbals

We consider gimbals in radome analysis for the mathematical transformation between the commanded antenna azimuth (AZ) and elevation (EL) angle pointing and the coordinates of rotated points on the antenna aperture.

Gimbal mountings for antennas have been made in many different configurations such as Figure 2.9. For dynamic situations that require the motion of the platform on which the radome enclosed antenna is mounted to be isolated from the antenna pointing gimbal within the radome, the easiest and most straightforward approach is to provide a separate set of gimbals to isolate the standard EL/AZ or AZ/EL antenna gimbals within the radome from the platform motion [7].

For rapid platform directional changes, it is important that the accuracy, stability, and stiffness of the positioner be acceptable under worst-case dynamic

Figure 2.9 Specialized antenna gimbal that is neither AZ/EL or EL/AZ. (Photo courtesy of K. Guerin and E. Bannon of Carnegie Mellon University.)

and environmental conditions. The positioning accuracy is determined by how precisely the positioner can move to a defined point as well as how stable and stiff the positioner is in maintaining that position. The speed of movement is based on how quickly the positioner can move from one angular position to another.

Numerous more sophisticated gimbal approaches have been developed to combine antenna pointing and platform isolation within a single device. For instance, in a patent, Speicher describes a gimbal assembly in which the outer gimbal member is an arcuate yoke mounted on rollers to rotate about one axis and the inner gimbal member is a platform pivotally mounted in the yoke to rotate about a second orthogonal axis. Two motors are connected through a differential drive system to rotate either gimbal member selectively or both together in any combination of motions [8].

In a patent by Vucevic [9] a stabilized platform that is suitable for stabilizing the boresight of a communications antenna is provided with a pendulous mounting that holds the structure erect. A pair of gyroscopes gives active control of the attitude of the platform and is coupled to the platform via a gear arrangement. When the platform is rotated rapidly (to unravel feed cables or to permit overhead tracking of the antenna), the gyroscopes experience a much lesser degree of movement that is determined by the gearing ratio, so that the gyroscopes are not destabilized.

Many other approaches are possible [10–12]. In the following sections we consider three cases in which specialized antenna pointing gimbals may be required: marine SATCOM, vehicular SATCOM, and airborne applications.

2.5.1 Maritime SATCOM

In previous years shipboard satellite communications (SATCOM) systems were limited to only C-band terminals for the transfer of high-speed data and most used circularly polarized satellite transponders. In some instances the satellite link used a linear transponder, but the terminal operator was then required to lease both polarizations, which essentially doubled the cost of the bandwidth being leased [13]. Currently, Inmarsat and mini-VSAT are two state-of-the-art services for maritime communications. A disadvantage of VSAT is the requirement for stabilized antenna systems because VSAT communications often operate at Ku-bands in contrast to the low-frequency L-band used by Inmarsat. Because the beam is much narrower at this frequency band, it is even more important to keep the antenna locked closely onto the satellite signal considering the dynamic roll, pitch, and yaw motion of the vessel.

Loss in the gain in the use of marine SATCOM antennas is due to both pointing errors and polarization misalignment. Many of the current generation of ship terminals use EL/AZ-type pedestals that require specialized design to get

Figure 2.10 Stabilized gimbal marine SATCOM antenna. (Photo courtesy of Cobham SATCOM.)

rid of the keyhole effect when the satellite is directly overhead, as shown in Figure 2.10. A patent by Kiryu et al. [14] used a two-gyro reference gimbal to stabilize a marine SATCOM antenna against the pitch and roll effects of the ship's motion in the sea. Some other commercially available antenna gimbals are up to four axis stabilized and use fiber optic laser gyro references. The gyros are connected to servo motors located on each antenna axis to constantly adjust the direction of the antenna.

Varley et al. [15] researched the application of SATCOM earth terminal techniques to unmanned, maritime-based platforms. Varley et al. traded off parameters related to platform physical constraints to assess the most appropriate SATCOM solution to various marine platform applications.

2.5.2 Vehicular Applications

Vehicular applications include, but are not limited to, ground-to-air radar and microwave communications. The increasing need for timely information has led to the recent development of mobile SATCOM terminals to provide wideband communications on the move while even traversing rough off-road terrain at moderate speeds. The motion of the antenna platform complicates the pointing problem and must be accounted for in mobile SATCOM applications. High-performance antenna positioner systems that are commercially available provide inertially stabilized platforms for antenna pointing within fractions of a degree and may operate in either an open or a closed-loop fashion [16]. Some systems that have been successful in achieving these goals used a 6 degree of freedom (6 DOF) motion table in order to stabilize the SATCOM antenna [17]. A typical radome-enclosed vehicular antenna is shown in Figure 2.11.

SATCOM communications on the move that operate at Ku-band (11 to 14 GHz) play a significant role in both military and civilian communications systems. To limit interference to adjacent satellites, regulatory and standards

Figure 2.11 Vehicular radome-enclosed antenna. (Photo courtesy of USDigiComm Corporation.)

bodies have established strict limits on the effective isotropic radiated power (EIRP) in the antenna off-axis direction [18]. Vehicular SATCOM systems that operate at millimeter-wave frequencies are even more difficult to keep pointed toward the satellite because of much narrower antenna beamwidths. One possibility is to use closed loop auto acquisition and tracking to keep the antenna pointed under dynamic conditions. However, a consequence of using auto track gimbals on a moving vehicle is that the registration error (the difference between the transmit and receive frequency band BSE) must be suitably close so that both the peaks of the transmit and receive antenna beams are coaligned on the same satellite. To achieve this, the stiffness and stability of the positioner must be suitable for extreme environmental conditions.

2.5.3 Airborne Applications

Airborne applications include, but are not limited to, SATCOM and air-to-ground microwave communications. In a patent by Holandsworth and Cantrell [19] the line of sight of an airborne radar antenna is stabilized from the pitch and roll motions of the aircraft by mounting the antenna on a three degree of freedom gimbal system. The gimbal system is comprised of a first gimbal mounted for rotation about the aircraft Z-axis (azimuth) for pointing the antenna along the intended line of sight, a second gimbal mounted on the first gimbal for rotating up and down with respect to the azimuth gimbal, and a third gimbal mounted on the second gimbal to which the antenna is connected to provide rotation to align antenna polarization relative to inertial ground.

Pointing and scanning control algorithms for a two-axis gimbal, inertially stabilized, airborne antenna system are described in [20]. Satisfactory performance is demonstrated in the presence of aircraft maneuvers, with some (expected) degradation for the very-near-zenith antenna states. The antenna scanning algorithm presented is adaptive in its scan rate (to avoid scan

distortions due to the azimuth rate limiting imposed by the physical antenna system), is simple to implement, and properly accounts for aircraft maneuvering to maintain circular scanning trajectories in inertial space.

In a U.S. Army report a pedestal and gimbal assembly related to missile semiactive radar seekers supported three gyroscopes and functions as a reference platform to relate airframe attitude. This is mechanized by utilizing the 2 degree of freedom gimbal for pitch and yaw and controlling the missile body roll axis for the third degree of freedom. Structure of the positioning system includes a pedestal having an inner gimbal assembly with a support for mounting the antenna assembly and the gyros. A yaw torque motor assembly is carried by the inner gimbal and is provided with a pair of output shafts for supporting the inner gimbal and controlling the yaw movement thereof. A pitch motor is housed in the pedestal and includes a drive pinion and a drive shaft. The drive pinion is connected to the drive shaft. The drive pinion and yaw motor operates to control the pitch movement of the antenna assembly [19].

References

[1] Sokolnikoff, I. S., and R. M. Redheffer, *Mathematics of Physics and Modern Engineering,* New York: McGraw-Hill, 1958.

[2] Kreyszig, E., *Advanced Engineering Mathematics,* New York: John Wiley & Sons, 1965.

[3] *Reference Data for Radio Engineers,* 5th ed., New York: Howard W. Sams & Company, Inc., 1974.

[4] Ramo, S., J. R. Whinnery, and T. Van Duzer, *Fields and Waves in Communications Electronics,* 2nd ed., New York: John Wiley & Sons, 1984.

[5] Franklin, P., *Functions of Complex Variables,* Englewood Cliffs, NJ: Prentice Hall, 1958.

[6] Pipes, L. A., and L. R. Harville, *Applied Mathematics for Engineers and Physicists,* New York: McGraw-Hill, 1970.

[7] Storaasli, A., "Multi-Axis Positioner with Base-Mounted Actuators," U.S. Patent 5,875,685, March 1999.

[8] Speicher, J., "Differential Drive Rolling Arc Gimbal," U.S. Patent 4,282,529, August 1981.

[9] Vucevic, S., "Stabilized Platform Arrangement," U.S. Patent, 4,696,196, September 1987.

[10] Fujimoto, K., and J. R. James, *Mobile Antenna Systems Handbook,* 2nd ed., Artech House, Norwood, MA, 2001.

[11] Lawrence, E. G., and W. H. Warner, *Dynamics*, 3rd ed., Courier Dover Publications, 2001.

[12] Biezad, D. L., *Integrated Navigation and Guidance Systems*, AIAA, 1999.

[13] Cavalier, M., *Marine Stabilized Multiband Antenna Terminal*, Overwatch Systems Ltd. Publication, 2002.

[14] Kiryu, R., et al., "Gyro Stabilization Platform for Scanning Antenna," U.S. Patent 4,442,435, April 1984.

[15] Varley, R. F., R. Kolar, and S. Smith, "SATCOM for Marine Based Unmanned Systems," *Oceans 02 MTS/IEEE*, Vol. 2, October 2002, pp. 645–653.

[16] Marsh, E., "Inertially Stabilized Platforms for SATCOM On-the-Move Applications," Masters Thesis, Massachusetts Institute of Technology Cambridge Department of Aeronautics and Astronautics, June 2008.

[17] Nazari, S., K. Brittain, and D. Haessig, "Rapid Prototyping and Test of a C4ISR Ku-Band Antenna Pointing and Stabilization System for Communications On-the-Move," *Military Communications Conference (MILCOM 2005)*, October 2005, pp. 1528–1534.

[18] Weerackody, V., and L. Gonzalez, "Motion Induced Antenna Pointing Errors in Satellite Communications On-the-Move Systems," *Information Sciences and Systems, 2006 40th Annual Conference*, March 2006, pp. 961–966.

[19] Holandsworth, P., and C. Cantrell, "Orientation Stabilization by Software Simulated Stabilized Platform," U.S. Patent 5,202,695, April 1993.

[20] Karabinis, P. D., R. G. Egri, and C. L. Bennett, "Antenna Pointing and Scanning Control for a Two Axis Gimbal System in the Presence of Platform Motion," *Military Communications Conference (MILCOM88)*, San Diego, CA, October 23–26, 1988, Vol. 3, pp. 793–799.

Selected Bibliography

Estlick, R. J., and O. E. Swenson, *Pedestal and Gimbal Assembly*, U.S. Army Report ADD007965, April 1980.

Hirsch, H. L., and D. C. Grove, *Practical Simulation of Radar Antennas and Radomes,* Norwood, MA: Artech House, 1987.

3

Antenna Fundamentals

In this chapter, we will discuss the radiation patterns of an antenna, which follow from the solution of Maxwell's equations. The solution is subject to boundary conditions at both the radiator and at infinity distance. Many antenna types are too complicated for direct solution. Fortunately, we can make approximations to arrive at a simplified solution.

We will examine a variety of radiators, including aperture and spiral antennas. For these antennas, we can use Huygens' principle to help us analyze the problem. Huygens' principle states that each elemental portion of the wave in the aperture can be considered as a source of waves in space.

This chapter focuses primarily on the antenna and its radiation patterns, but please keep in mind that this chapter serves only as background material. The main focus of this book is the impact of the *radome* on the antenna radiation patterns.

3.1 Directivity and Gain

Diffraction theory shows that, for an antenna without a radome, the minimum angle within which radiation can be concentrated by an antenna is [1]:

$$\theta_o = \frac{1}{(L_a/\lambda)} \tag{3.1}$$

where

θ_0 is the half-power beamwidth in radians;

L_a is the length of the antenna;

λ is the wavelength.

In evaluating an antenna's radiating characteristics, we only need to consider the electromagnetic field at a great distance from the antenna. In this far-field region, the antenna's power radiation pattern varies only with angles and not with range.

The directive properties of an antenna are expressed as the radiation intensity function, $P(\theta, \phi)$, where θ is the elevation angle and ϕ is the azimuth angle in a standard spherical coordinate system centered on the antenna, as illustrated in Figure 3.1. Accordingly, the directive power gain function, G_D, is related to the maximum value of the effective power radiated per unit solid angle at the antenna beam peak, P_{max}, and the total radiated power, P_t, by [2]:

$$G_D = \frac{P_{\max}}{P_t/4\pi} = \frac{4\pi P(0,0)}{\int_0^{2\pi}\int_0^{\pi} P(\theta,\phi)\sin\theta\, d\theta\, d\phi} \tag{3.2}$$

This equation makes two assumptions:

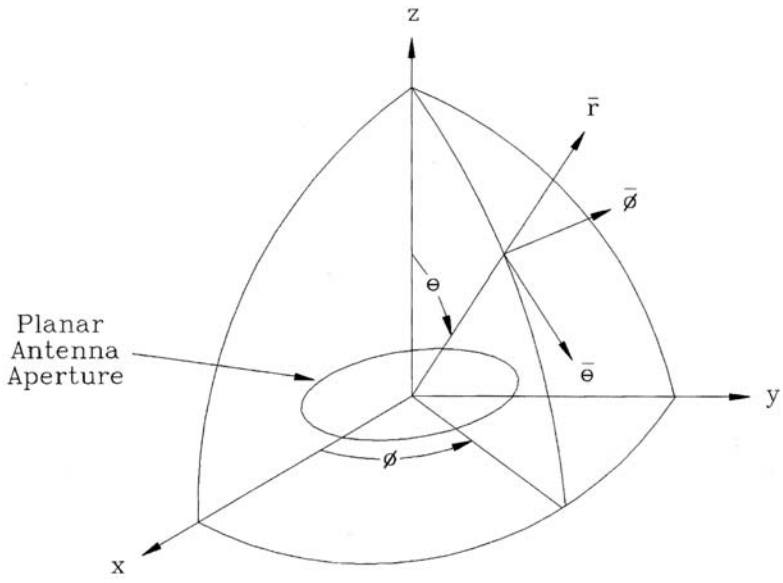

Figure 3.1 Spherical coordinate system centered on antenna aperture.

- We integrate the term in the denominator in all directions of space about the antenna.
- The maximum radiation is in the direction $\theta = 0, \phi = 0$.

For an antenna with 100% radiation efficiency, we relate the antenna directivity to the half-power antenna beamwidths in each principal plane, θ_0 and ϕ_0, respectively, by

$$G_D = \frac{4\pi}{\theta_0 \phi_0} \tag{3.3}$$

where both half power beamwidths are in radians.

For any physically realizable antenna, the radiation efficiency is less than 100% because of ohmic losses within the antenna structure. We relate the power gain of any antenna to antenna radiation efficiency, η_a, via

$$G = \eta_a G_D \tag{3.4}$$

For aperture antennas, the directive gain and power gain are related to the physical aperture area and effective aperture area, A and A_{eff}, by

$$G_D = \frac{4\pi A}{\lambda^2} \tag{3.5}$$

$$G = \frac{4\pi A_{eff}}{\lambda^2} \tag{3.6}$$

From the last three expressions, we can derive a formula for antenna efficiency, based on the effective area

$$\eta_a = \frac{A_{eff}}{A} \tag{3.7}$$

Since the antenna radiation efficiency is equal to or less than unity, we can conclude that the effective antenna area is always equal to or less than its physical area. The amount of power that a receiving antenna can gather from an incident plane electromagnetic wavefront is generally less than the power impinging on its physical area due to internal losses.

3.2 Radiation from Current Elements

By its nature, computer modeling of antennas requires antenna aperture currents to be sampled at discrete points as along a continuous distribution. In the following equations, we have assumed a sinusoidally time-varying current of constant frequency, which means that a time factor of $e^{j\omega t}$ is relevant but has not been included.

Consider the far-field radiation patterns for a *z*-directed infinitesimal current element of amplitude I_o and length h, as depicted in Figure 3.2. For this infinitesimal dipole, the electromagnetic field components at distance r from the dipole are [3, 4]:

$$H_\phi = \frac{I_0 h}{2\pi} e^{-jkr}\left(\frac{jk}{r} + \frac{1}{r^2}\right)\sin\theta \tag{3.8}$$

$$E_r = \frac{I_0 h}{2\pi} e^{-jkr}\left(\frac{1}{j\omega\varepsilon r^3} + \frac{\eta}{r^2}\right)\cos\theta \tag{3.9}$$

$$E_\theta = \frac{I_0 h}{2\pi} e^{-jkr}\left(\frac{j\omega \mathrm{m}}{r} + \frac{1}{j\omega\varepsilon r^3} + \frac{\eta}{r^2}\right)\sin\theta \tag{3.10}$$

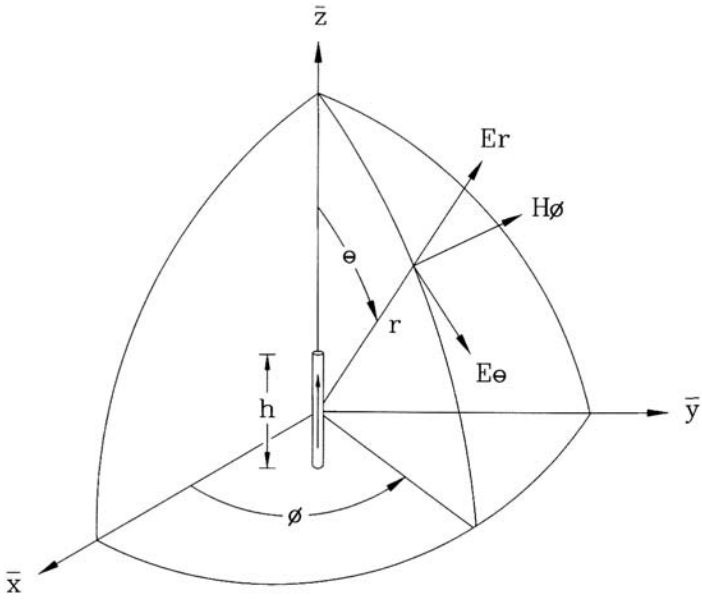

Figure 3.2 *Z*-directed current element.

where E is in volts per meter, H is in amperes per meter, and η is the wave impedance in ohms given by:

$$\eta = \sqrt{\frac{\mu}{\varepsilon}} \tag{3.11}$$

For most problems of interest, it is only necessary to know the field components if r is very much greater than a wavelength. For this condition, we may ignore the r^2 and r^3 terms in the above expressions. Under the condition where we can do this, the only remaining significant electromagnetic field components are:

$$H_\phi \approx \frac{I_0 h}{2\pi}\left(\frac{jk}{r}\right)\sin\theta \tag{3.12}$$

$$E_\theta \approx \frac{I_0 h}{2\pi}\left(\frac{j\omega\mu}{r}\right)\sin\theta \tag{3.13}$$

From (3.12) and (3.13), the free-space wave impedance (in air or vacuum) in the far field is derived as the ratio

$$\eta_0 = \frac{E_\theta}{H_\phi} = \sqrt{\frac{\mu_0}{\varepsilon_0}} = 120\pi \tag{3.14}$$

At a fixed distance, the variation of the electromagnetic field components only contains a sinusoidal variation with a maximum value in the direction orthogonal to the dipole. When modeling an antenna aperture as an ensemble of dipole radiators, we have to account for this variation of the dipole element pattern.

3.3 Antenna Array Factor

An antenna element radiates an electric field with two polarization components:

$$E = E_\theta(\theta,\phi)\bar{\theta} + E_\phi(\theta,\phi)\bar{\phi} \tag{3.15}$$

where E_θ and E_ϕ are the two complex electric field components that have a common phase center and $\bar{\theta}$ and $\bar{\phi}$ are unit vectors in the θ and ϕ directions, respectively.

Assume an array of N antenna elements, where N is an integer equal to or greater than two. The total pattern is obtained by adding the electric fields radiated from each, as in:

$$E = \sum_{n=1}^{N} \left[E_{\theta i}(\theta,\phi)\bar{\theta} + E_{\phi i}(\theta,\phi)\bar{\phi} \right] e^{-jkr_i} \tag{3.16}$$

We make various approximations in this equation. For instance, we ignore mutual coupling changes in the dipole patterns due to nearby antennas, and only the isolated element patterns are used. If the antennas all have identical element patterns, then we can separate (3.16) into a product [4]:

$$E = \left[E_{\theta}(\theta,\phi)\bar{\theta} + E_{\phi}(\theta,\phi)\bar{\phi} \right] \sum_{n=1}^{N} I_i e^{-jkr_i} \tag{3.17}$$

where E_θ and E_ϕ are the normalized patterns of the electric field from a single element with unity current and I_i are the relative current weights of the ith element and generally include amplitude and phase terms originating in the feed distribution. The (θ, ϕ) notation indicates that both of the electric field components have a θ and ϕ dependence.

Equation (3.17) is a powerful notion since it divides the far-field radiation pattern into an element pattern factor and an array factor. (The element pattern is the left-side expression, and the array factor is the right-side expression.) In the analysis of a radome-enclosed antenna, we will primarily be interested in the impact of a radome on the antenna array factor. We will compare the array factor with the radome and the array factor without the radome.

3.4 Linear Aperture Distributions

Assume that an antenna is transmitting and that it is a z-directed current element with a total array length L_a and centered at $z = 0$, as illustrated in Figure 3.3. If the distribution of the radiating current is continuous, the electric and magnetic fields are [5]

$$E_{\theta} = \left(j\omega\mu \frac{e^{-jkr_o}}{4\pi r_o} \sin\theta \right) \int_{\frac{-L_a}{2}}^{\frac{L_a}{2}} I(z) e^{j\frac{2\pi z}{\lambda}\cos\theta} dz \tag{3.18}$$

and

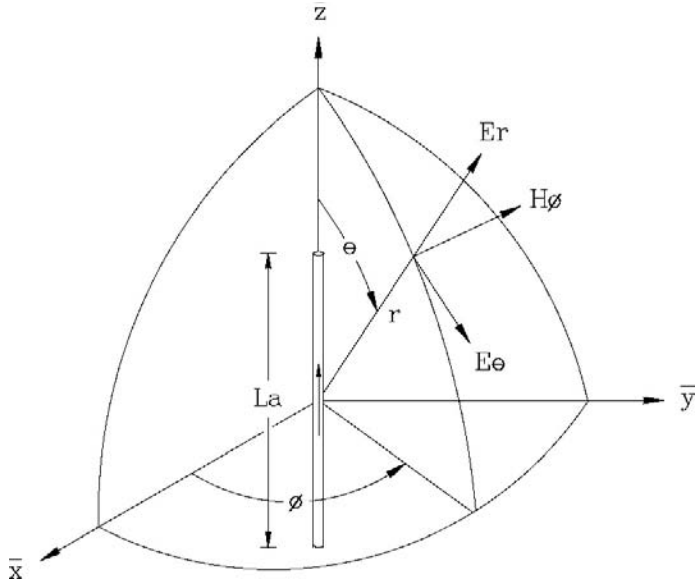

Figure 3.3 *Z*-directed line source current distribution.

$$H_{\phi} = \eta E_{\theta} \tag{3.19}$$

In (3.18), the integration is over the physical length of the antenna and $I(z)$ is the complex current as a function of z. The array factor is the right side of the expression and is the Fourier transform of the relative current aperture field distribution.

$$E_{\theta}^{AF} = \int_{\frac{-L_a}{2}}^{\frac{L_a}{2}} I(z) e^{j\frac{2\pi z}{\lambda}\cos\theta} dz \tag{3.20}$$

We define the aperture distribution as the current amplitude and phase across the antenna aperture. Controlling the aperture distribution: (1) permits sidelobe reduction and (2) allows the synthesis of desired antenna beam shapes or the control of antenna beam pointing direction (as with a phased array antenna.)

If the line source has a uniform distribution, $I(z) = 1$, and the far-field radiation pattern is obtained by carrying out the integration indicated in (3.20), then

$$E_{\theta}^{AF} = \frac{\sin\left(\frac{\pi L_a \cos\theta}{\lambda}\right)}{\frac{\pi L_a \cos\theta}{\lambda}} \tag{3.21}$$

This directivity pattern is significant because it has the highest directivity of all known aperture distributions. However, it has relatively high (−13.2 dB) first sidelobe levels. Figure 3.4 illustrates the computed antenna pattern for a line distribution that is 0.1m long at 10 GHz. In the case of radars, high sidelobes are undesirable because of increased ground clutter reception. High sidelobes are also undesirable in satellite communications because it can result in adjacent satellite interference.

We can reduce antenna sidelobes via tapered antenna aperture current distributions, but only at the expense of increased half-power beamwidth. For instance, consider a cosine aperture current line distribution

$$I(z) = \cos\left[\frac{\pi z}{L_a}\right] \tag{3.22}$$

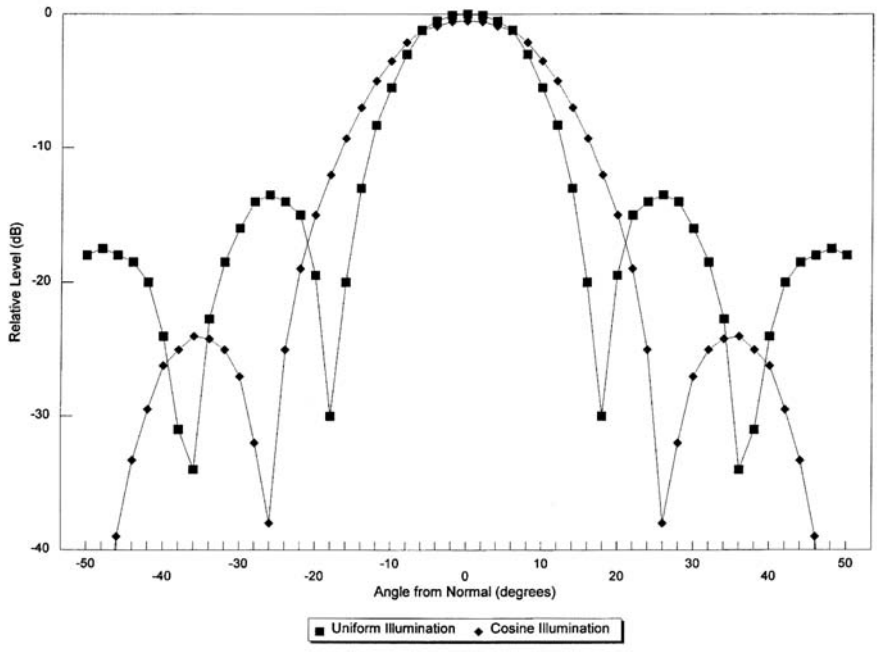

Figure 3.4 Line source antenna patterns (L_a = 0.1m long, f = 10 GHz).

Note that the maximum for this current distribution in (3.22) is at the center of the current element at $z = 0$ and that the vertically oriented current element extends from $z = -L_a/2$ to $z = +L_a/2$. Substituting this into (3.20) and carrying out the integration, we obtain

$$E_{\theta}^{AF} = \frac{1}{2}\left[\frac{\sin\left(\frac{\pi L_a}{\lambda}\cos\theta + \frac{\pi}{2}\right)}{\left(\frac{\pi L_a}{\lambda}\cos\theta + \frac{\pi}{2}\right)} + \frac{\sin\left(\frac{\pi L_a}{\lambda}\cos\theta - \frac{\pi}{2}\right)}{\left(\frac{\pi L_a}{\lambda}\cos\theta - \frac{\pi}{2}\right)}\right] \tag{3.23}$$

We show this pattern also in Figure 3.4 for an antenna that is 0.1m long at 10 GHz. It has −23.5-dB sidelobes, but a greater half-power beamwidth than the uniform distribution case. Other antenna aperture distributions that we can apply to this vertical current element for low sidelobe levels include a cosine raised to a power

$$I(z) = \cos^n\left(\frac{\pi z}{L_a}\right) \tag{3.24}$$

in which n is a power equal to or greater than 0 and need not be an integer. The maximum for this current distribution in (3.24) is at the center of the current element at $z = 0$, and the vertically oriented current element extends from $z = -L_a/2$ to $z = +L_a/2$. Also, $n = 0$ reduces to the uniform illumination case.

A parabolic distribution on a pedestal is defined by the following formula:

$$I(z) = p + [1 - p]\left(1 - \frac{z^2}{(0.5L_a)^2}\right) \tag{3.25}$$

In this equation p is the pedestal parameter and is equal to or less than unity.

The maximum for this current distribution in (3.25) is also at the center of the current element at $z = 0$, and the vertically oriented current element extends from $z = -L_a/2$ to $z = +L_a/2$.

For all these distributions, Table 3.1 summarizes the relative gain to the uniform distribution case, the half-power beamwidth, and the first sidelobe levels.

A combination of simpler forms can approximate many other distributions. For example, to find the directivity pattern of a cosine raised to a power on a pedestal having the form, use the following:

Table 3.1
Line Source Pattern Characteristics

Distribution	Relative Gain (dB)	Half-Power Beamwidth HPBW (°)	First Null Position (°)	First Sidelobe Level (dB)
Uniform	**0**	**51/(*L*/λ)**	**57.3/(*L*/λ)**	**–13.2**
$\cos^n$, *where:*				
$n=1$	–0.92	68.75/(*L*/λ)	85.94/(*L*/λ)	–23
$n=2$	–1.76	83.08/(*L*/λ)	114.59/(*L*/λ)	–32
$n=3$	–2.4	95.11/(*L*/λ)	143.23/(*L*/λ)	–40
$n=4$	–2.88	110.58/(*L*/λ)	171.89/(*L*/λ)	–48
Parabolic, where:				
$p=0.8$	–0.03	52.71/(*L*/λ)	60.73/(*L*/λ)	–15.8
$p=0.5$	–0.13	55.58/(*L*/λ)	65.32/(*L*/λ)	–17.1
$p=0.0$	–0.79	65.89/(*L*/λ)	81.93/(*L*/λ)	–20.6

$$I(z) = p + [1 - p]\cos^n\left[\frac{\pi z}{L_a}\right] \tag{3.26}$$

The resulting pattern is the superposition of the pattern obtained for a uniform distribution (this corresponds to the pedestal) and the pattern obtained for a cosine raised to the *n*th power. For instance, for a cosine-squared distribution on a pedestal, the directivity pattern is

$$E_\theta^{AF} = pL_a \frac{\sin\left(\frac{\pi L_a \cos\theta}{\lambda}\right)}{\frac{\pi L_a \cos\theta}{\lambda}} + 1(1-p)\frac{L_a}{2}\frac{\sin\left(\frac{\pi L_a \cos\theta}{\lambda}\right)}{\frac{\pi L_a \cos\theta}{\lambda}}\frac{\pi^2}{\pi^2 - \left(\frac{\pi L_a \cos\theta}{\lambda}\right)^2} \tag{3.27}$$

In a computerized analysis of radome-enclosed antennas, the antenna aperture is generally sampled in discrete increments in accordance with the Nyquist criteria. These criteria are analogous to the criteria for keeping grating

lobes out of real space, as in the case of a phased array antenna. These grating lobes would corrupt antenna pattern data and result in computational errors.

The criterion for determining the maximum sample spacing so that the nearest grating lobe is on the edge of real space corresponds to the condition [6]:

$$\frac{d}{\lambda} \leq \frac{1}{1+\sin\theta_o} \tag{3.28}$$

where d/λ_o is the sample to sample spacing in wavelengths at the operating frequency and θ_o is the direction of maximum radiation. (Most of the antennas to be addressed in this book have a maximum radiation lobe normal to the antenna aperture surface.) A sample spacing of a half wavelength is guaranteed to keep grating lobes out of real space, which will contribute to computational errors.

Assume that there are N samples with d_z being the interval between samples, such that $L_a = Nd_z$. On this basis, the array factor corresponding to (3.20) will reduce to:

$$E_\theta^{AF} = \sum_{n=1}^{N} I_n e^{jkz_n \cos\theta} \tag{3.29}$$

where I_n represents the sampled aperture distribution weighting at the nth point and is generally a complex quantity and z_n is the z-coordinate location of the nth point where $z_n = nd_z$.

3.5 Two-Dimensional Distributions

A method similar to that used for the line source can find the far-field radiation directivity pattern for a two-dimensional aperture. However, the Fourier transform is taken over two dimensions instead of one dimension. For instance, assume that the aperture distribution is in the y-z plane. The array factor is now given by

$$E_\theta^{AF} = \iint I(y,z) e^{jk\sin\theta(x\cos\phi + y\sin\phi)} dydz \tag{3.30}$$

This integral can treat circular apertures by defining the appropriate illumination function, $I(y, z)$. Note that $I(y, z)$ must be zero outside of the circular antenna aperture. To illustrate the use of this integral, consider a circular aperture of diameter D_a centered at the origin with a parabolic distribution raised to a power n having the form:

$$I(y,z) = \left[1 - \frac{y^2 + z^2}{(D_a/2)^2}\right]^n \tag{3.31}$$

Table 3.2 shows the far-field pattern characteristics. Note that the condition for $n = 0$ corresponds to a uniformly illuminated circular aperture and has −17.6-dB first sidelobe levels. The condition for $n = 1$ corresponds to a circular aperture parabolic distribution and has reduced sidelobes to −24.6 dB.

A planar aperture two-dimensional transform separates into one-dimensional transforms when the aperture distribution involves a product where each factor depends on only one coordinate [2], that is, it is product separable of the form

$$I(y,z) = I(y)I(z) \tag{3.32}$$

In this equation, we define the net radiation pattern as the product of the principal plane patterns obtained from line source distributions $I(y)$ and $I(z)$, respectively. However, if the aperture distribution is not separable, we must evaluate a two-dimensional integral numerically.

From Maxwell's equations, Appendix A develops a formulation for the far-field radiation patterns of an ensemble of infinitesimal current elements, equally spaced d_y apart in the y-plane and d_z apart in the z-plane, thus forming a rectangular grid, as illustrated in Figure 3.5. The numerical summation has given the resulting array factor [5]:

$$E_\theta^{AF} = \sum_{m=1}^{M}\sum_{n=1}^{N} I_{mn}\, e^{jk \sin\theta\left(md_x \cos\phi + nd_y \sin\phi\right)} \tag{3.33}$$

The m index pertains to the y-coordinate, and the n index pertains to the z-coordinate.

Table 3.2
Circular Aperture Pattern Characteristics

n	Relative Gain (dB)	Half-Power Beamwidth HPBW (°)	First Null Position (°)	First Sidelobe Level (dB)
0	0	58.44/(D/λ)	sin-1[1.22/(D/λ)]	–17.6
1	–1.25	72.77/(D/λ)	sin-1[1.63/(D/λ)]	–24.6
2	–2.52	84.22/(D/λ)	sin-1[2.03/(D/λ)]	–30.6

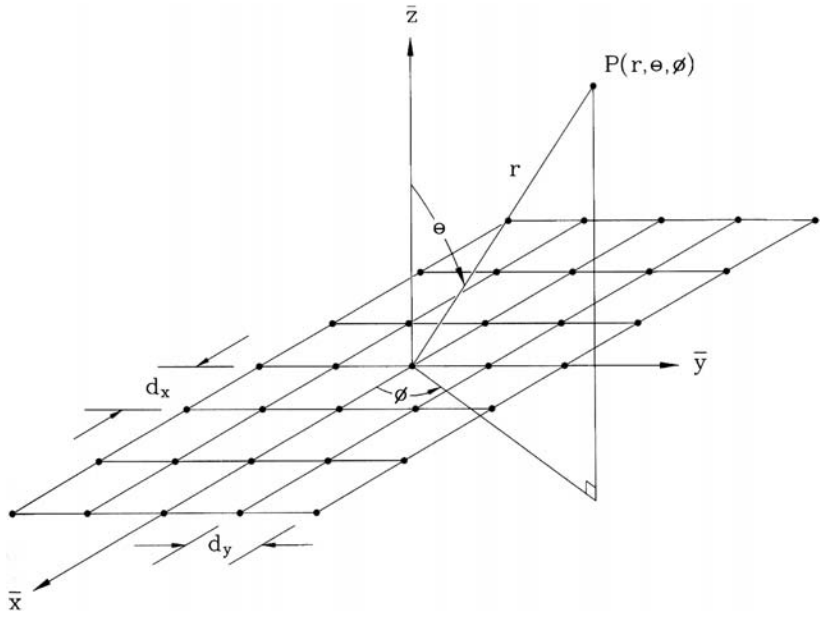

Figure 3.5 Aperture modeled as an ensemble of *z*-directed infinitesimal current elements in an *x-y* plane.

The weighting coefficient, I_{mn}, usually is a complex quantity. As with the continuous aperture distributions, by a proper choice of the I_{mn} coefficients, the boundary of the antenna aperture can be modeled as square, rectangular, elliptical, or circular. For circular, we often assume that we can subdivide the array into four symmetrical quadrants, resulting in excitations that will give sum and difference antenna patterns.

If this aperture distribution can be described as a product of two current distributions where each factor depends on only one coordinate, $I_{mn} = I_m I_n$, then the function is product separable, as indicated in the discussion of (3.33). The net radiation pattern is the product of the principal plane patterns obtained from I_m and I_n, respectively.

$$E_\theta^{AF} = \sum_{m=1}^{M} I_m e^{jkmd_x \sin\theta \cos\phi} \sum_{n=1}^{N} I_n e^{jknd_y \sin\theta \cos\phi} \tag{3.34}$$

Here I_m and I_n are complex coefficients that represent the antenna current distributions along the *x*- and *y*-axes. Some times these may conveniently correspond to the physical location of radiating elements on a planar antenna aperture. For instance, the location of slots on the flat plate waveguide antenna array is shown in Figure 3.6.

Figure 3.6 Waveguide flat plate antenna. (Photo courtesy of Hughes Missile Systems Division.)

3.6 Spiral Antennas

Spiral antennas have frequency-independent radiation patterns and are used in radome-enclosed direction finding (DF) systems on aircraft, antiradiation homing (ARH) missile guidance systems, and broadband surveillance systems. An overview of the historical development of these antennas appears in [7–11].

We generally fabricate planar spiral antennas on a printed circuit (PC) board. To obtain a unidirectional pattern, a lossless cavity is placed on one side of the spiral. This cavity limits the frequency-independent pattern bandwidth to

about an octave. Hamel and Scherer [12] have found that an absorber-lined cavity can extend a spiral operation to a decade bandwidth.

A two-arm (or log-spiral) antenna, shown in Figure 3.7, is frequency independent because angles entirely describe the antennas shape, which make it invariant to a change of scale [11, 13, 14]. The radius function can be found from the formula

$$\rho = \rho_0 e^{\alpha\psi} \tag{3.35}$$

where a is the expansion coefficient. We rotate the curve of the equation 180° around the origin to define the second arm of the spiral.

We may analyze the planar spiral structure as a strip radiator with currents flowing along the arms. The inner part of the spirals serves as a nonradiating transmission line, carrying the current out to the active region, which is a narrow circumferential ring where antenna radiation takes place. The active regions where radiation takes place correspond to circumferences of $m\lambda$ in diameter, where m is an integer equal to or greater than unity and is referred to as the *mode* of the radiation.

Hand rules determine the sense of the circular polarization. For instance, pointing your thumb away from the spiral, let the fingers roll in the direction of the increasing spiral radius. The hand that must be used determines the polarization sense. For instance, if you must use your right hand in order for your fingers to roll in the direction of increasing spiral radius, then the spiral antenna is of the right-hand circular polarization (RHCP) sense.

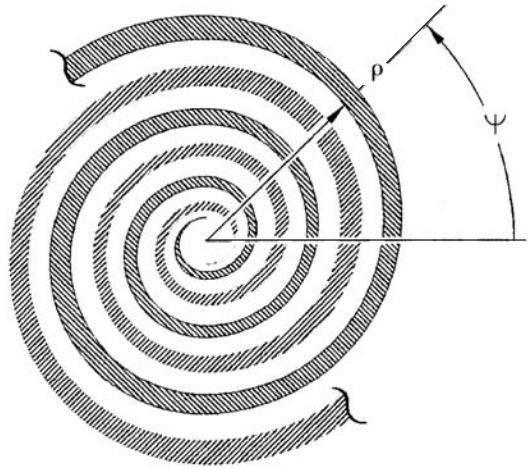

Figure 3.7 Equiangular spiral antenna geometry.

The Archimedean spiral antenna has constant spacing between adjacent arms, as illustrated in Figure 3.8. It is only frequency independent over a typical decade-bandwidth frequency range [15]. However, in order to obtain this complete bandwidth, it requires lossy material on the ends of the arms to eliminate end reflections [16].

The Archimedean spiral has a radius function that increases uniformly with the angle Φ according to

$$\rho = \rho_o + \alpha\psi \tag{3.36}$$

For sufficiently large spiral antennas that support higher-order modes, the currents in these modes vary as $e^{jm\psi}$ with ψ varying from 0 to 2π. All modes for which $m > 1$ have a null on boresight. For bandwidths less than 3:1 for a two-arm spiral, the 3λ diameter ring cannot exist, so that only the principal $m = 1$ mode exists. For greater electrical bandwidths, the control of radiation in the higher-order modes can be controlled by spiral design methods; an excellent discussion appears in Corzine and Mosko [17].

With four-arm spirals, it is possible to simultaneously excite and isolate both the mode 1 and mode 2 responses, which appear much like a monopulse antenna sum and difference pattern. We model the spiral by replacing the aperture with two concentric current rings and their proper phase distributions. The mode 1 and mode 2 radiation patterns are shown in Figure 3.9. A phasing technique to obtain these modes is shown in Schuchardt and Kozakoff [18], as illustrated in Figure 3.10. Each of these modes is rotationally symmetric about the

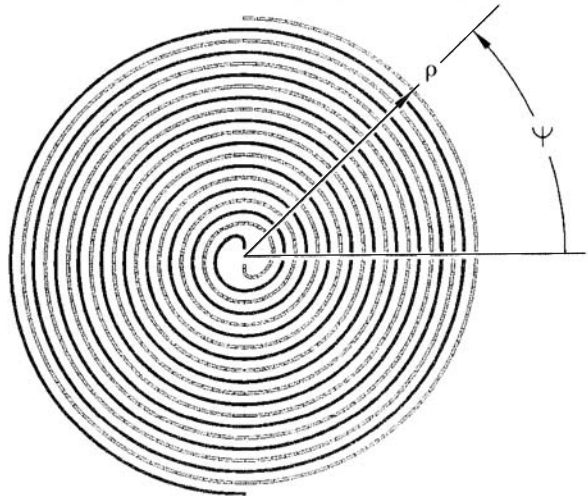

Figure 3.8 Archimedean spiral antenna geometry.

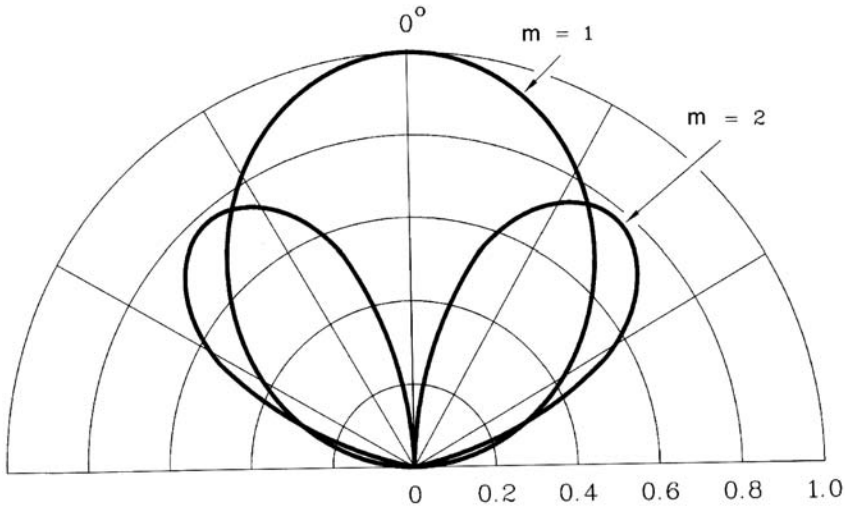

Figure 3.9 Radiation patterns for four-arm multimode spiral.

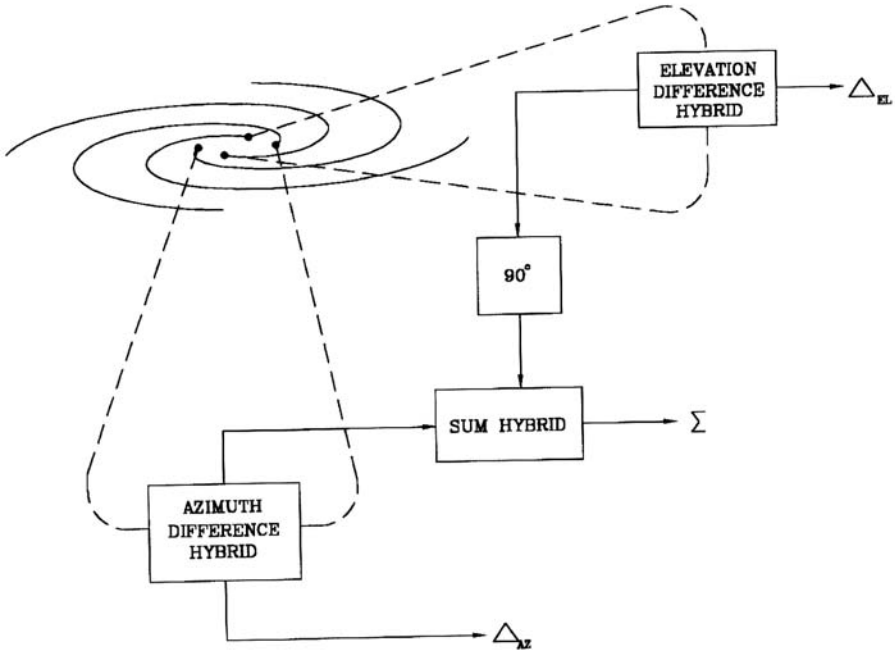

Figure 3.10 Monopulse circuit for four-arm spiral.

z-axis, and the field is pure circular polarization, with the polarization sense determined by the spiral winding.

For all planar spiral antennas operating in the principal ($m = 1$) mode, the antenna must have an outer circumference of 1.25 wavelengths at the lowest operating frequency. This circumference insures good antenna patterns and impedance match when the antenna is operating at lowest frequency.

References

[1] Silver, S., *Microwave Antenna Theory and Design*, New York: McGraw-Hill, 1949.

[2] Jasik, H., "Fundamentals of Antennas," Ch. 1 in *Antenna Engineering Handbook*, 3rd ed., R. C. Johnson, (ed.), New York: McGraw-Hill, 1993.

[3] Eibert, T. F., and J. L. Volakis, "Fundamentals of Antennas, Arrays, and Mobile Communications," Ch. 1 in *Antenna Engineering Handbook*, 4th ed., J. Volakis, (ed.), New York: McGraw-Hill, 2007.

[4] Milligan, T. A., *Modern Antenna Design,* 1st ed., New York: McGraw-Hill, 1986.

[5] Johnson, R. C., "Fundamentals of Antennas," and "Arrays of Discrete Elements," Chs. 2 and 3 in *Antenna Engineering*, 3rd ed., R. C. Johnson, (ed.), New York: McGraw-Hill, 1993.

[6] Mailloux, R. J., *Phased Array Antenna Handbook*, Norwood, MA: Artech House, 1994.

[7] Jordan, E. C., et al., "Developments in Broadband Antennas," *IEEE Spectrum*, Vol. 1, April 1964, pp. 58–71.

[8] Wang, J. J. H., and V. K. Tripp, "Design of Multi-Octave Spiral-Mode Microstrip Antennas," *IEEE Transactions on Antennas and Propagation*, Vol. 39, No. 3, March 1991, pp. 332–335.

[9] Cubley, H. D., and H. S. Hayre, "Radiation Field of Spiral Antennas Employing Multimode Slow Wave Techniques," *IEEE Transactions on Antennas and Propagation*, Vol. AP-19, January 1971, pp. 126–128.

[10] Dyson, J. D., "The Characteristics and Design of the Conical Spiral Antennas," *IEEE Transactions on Antennas and Propagation,* Vol. AP-13, July 1965, pp. 488–499.

[11] Deschamps, G. A., and J. D. Dyson, "The Logarithmic Spiral in a Single-Aperture Multi-Mode Antenna System," *IEEE Transactions on Antennas and Propagation*, Vol. AP-19, January 1971, pp. 90–95.

[12] Du Hamel, R. H., and J. P. Scherer, "Frequency Independent Antennas," Ch.14 in *Antenna Engineering Handbook*, 2nd ed., R. C. Johnson and H. Jasik (eds), New York: McGraw-Hill, 1984.

[13] Rumsey, V. H., "Frequency Independent Antennas," *IRE National Convention Record*, Part 1, 1957, pp. 114–118.

[14] Dyson, J. D., "The Equiangular Spiral," *IRE Transactions on Antennas and Propagation*, Vol. AP-7, No. 2, April 1959, pp. 181–187.

[15] Turner, E. M., "Spiral Slot Antenna," U.S. Patent 2,863,145, December 1958.

[16] Rudge, A. W., et al., *The Handbook of Antenna Design*, 2nd ed., London, England: Peter Peregrinus Ltd, on behalf of the Institution of Electrical Engineers (UK), 1986.

[17] Corzine, R. G., and J. A. Mosko, *Four Arm Spiral Antennas*, Norwood, MA: Artech House, 1990.

[18] Schuchardt, J. M., and D. J. Kozakoff, "Seeker Antennas," Ch. 46, *Antenna Engineering Handbook*, 4th ed., J. Volakis, (ed.), New York: McGraw-Hill, 2007.

4

Radome Dielectric Materials

In analyzing radome electrical performance, it is important to evaluate the electrical properties of possible radome wall materials at various wavelengths. The primary electrical properties of candidate materials are the relative dielectric constant and the loss tangent of the candidate materials at the operational frequencies of the radome.

The structural (aeromechanical) and environmental requirements determine other parameters for a candidate radome material and include:

- Mechanical properties, such as flexural moduli, strength, and hardness;
- Material density;
- Water absorption;
- Rain erosion (particle impact) resistance;
- The variation of both the mechanical and electrical parameters of the material due to temperature variations.

This chapter focuses on the electrical properties of selected radome wall materials as they influence the electrical design of a radome. Mechanical and physical data for candidate materials are readily available in many sources, such as the biannual Proceedings of the Symposium on Electromagnetic Windows [1–9]. A survey of the properties of many avionics radome materials was published in a NATO funded report [10], a survey of ceramics materials appear in [11], a review of moldable organic (plastic) materials is found in a USAF publication [12], and an electromagnetic window material data handbook was prepared by the IIT Research Institute and Purdue University [13] that addresses

the multispectral performance of candidate materials. Lastly, since the first edition of this book, Burks has published some updated radome material data in [14].

4.1 Organic Materials

Most civilian/military aircraft, ground vehicles, and fixed terrestrial radomes use organic radome wall materials. Organic radome materials are useful at maximum service temperatures below 1,000°F (the maximum temperature dependent on the material chosen); at temperatures above the service temperature, both the mechanical and electrical parameters rapidly degrade to unacceptable values.

Radome wall construction is typically one of the following categories:

- Solid (*monolithic*), generally made of resins incorporating reinforcements such as chopped glass fibers;
- Sandwich design, consisting of alternating high-density (high relative dielectric constant) and low-density (low relative dielectric constant) materials.

4.1.1 Monolithic Radomes

Many radomes, particularly of the electrically thin wall variety, use a single-layer wall material and are termed monolithic wall radomes. Monolithic radomes often incorporate some type of fiber reinforcement in order to enhance the mechanical properties of the resin material. For this case, we obtain the resulting relative dielectric constant of the mixture from

$$\varepsilon_m = \frac{V_R \log \varepsilon_R + V_F \log \varepsilon_F}{V_R + V_F} \tag{4.1}$$

where

ε_m = relative dielectric constant of mixture;

ε_R = relative dielectric constant of the resin;

ε_F = relative dielectric constant of reinforcement fibers;

V_R = volume of the dielectric resin;

V_F = volume of reinforcement fibers.

Equation (4.1) assumes that the mixture is uniform and isotropic.

Occasionally, particularly at millimeter-wave bands, monolithic radomes are used without reinforcement. Table 4.1 shows the dielectric properties of several of these materials [15, 16].

The fabrication method for small monolithic wall radomes includes compound or injection molding, and even possibly machining. Fabrication of larger monolithic wall radomes might use a wet layup on a mandrel of the desired radome shape.

4.1.2 Sandwich Radomes

Throughout the microwave spectrum, sandwich radomes that include low-density core materials and higher-density skin materials are popular because sandwich radomes are more broadband than monolithic radomes and also have a higher strength-to-weight ratio.

4.1.2.1 Prepreg Materials

The more dense layers typically are fabricated from a fiber-reinforced resin system. Table 4.2 shows the approximate dielectric properties of some popular fiber reinforcement and resin systems [10, 11; personal communication with Ben MacKenzie, Saint Gobain Performance Plastics (formerly Norton Performance Plastics), Ravenna, Ohio, 1996].

The radome designer must consider both the electrical and mechanical properties in selecting a reinforcement. Some of these properties are listed here:

- S-glass, a silica-alumina-magnesia composite, is a high-strength glass where the reinforcement fibers' tensile strength is maintained to 650°C.
- E-glass contains alumina-borosilicate and is low-cost. Compared with S-glass, it shows a greater reduction of tensile strength at 650°C.

Table 4.1
Approximate Dielectric Properties of Some Common Plastics

Material	Relative Permittivity, X-Band	Loss Tangent, X-Band	Relative Permittivity, Ka-Band	Loss Tangent, Ka-Band
Rexolite	2.54	0.0005	2.6	0.002
Nylon	3.03–3.21	0.014–0.02	3.6	0.02
Teflon	2.1	0.0003	2.08–2.10	0.0006–0.001
Polystyrene	2.55	0.0004	2.54	0.00053–0.001
IparPlexiglass	2.59	0.015	2.61	0.02
Polyethylene	2.25	0.0004	2.28	0.007

Table 4.2
Approximate Dielectric Properties of Selected Fiber and Resin Systems (X-Band Data)

Material Category	Reinforcement or Resin	Relative Permittivity	Loss Tangent
Reinforcement			
	E-glass	6.06	0.004
	S-glass	5.2	0.007
	D-glass	4	0.005
	Polyethylene (Spectra)	2.25	0.0004
	Kevlar	4.1	0.02
	Quartz	3.8	0.0001
Resin			
	Polyester	2.95	0.007
	Bismaleimide	3.32	0.004
	Polybutadiene	3.83	0.015
	Epoxy	3.6	0.04
	Polyimide	3.1	0.0055
	Polycyanate	2.86	0.005

- D-glass was developed for radome applications and has a lower dielectric constant and loss tangent that the other glass fibers. However, it is lower in strength and higher in cost.
- Spectra consists of ultra-high-strength polyethylene fibers. It is lightweight with high-impact resistance, low water pickup, and excellent electrical properties for a low-loss radome.
- Quartz has a high silica content, resulting in a low dielectric constant and a small loss tangent. It is higher in cost, but offers a lower loss potential than a polyethylene radome.
- Kevlar is useful for high-strength applications. However, its loss tangent is higher.

When integrating a reinforcement with a resin, the overall electrical properties depend on the ratio of a resin to reinforcement. A mix formula similar to (4.1) must determine the resulting electrical properties. Table 4.3 shows the approximate dielectric properties of selected prepreg laminates available in the industry [10, 11; personal communication with Ben MacKenzie, Saint Gobain

Table 4.3
Approximate Dielectric Properties of Selected Laminates (X-Band Data)

Reinforcement	Resin	Relative Permittivity	Loss Tangent
E-glass	Epoxy	4.4	0.016
	Polyester	4.15	0.015
	Polyimide	4.7	0.014
D-glass	Polycyanate	3.45	0.009
Polyethylene (Spectra)	Epoxy	2.8	0.004
	Polyester	2.52	0.007
	Polycyanate	2.65	0.003
Kevlar	Polyester	3.5	0.05
Quartz	Epoxy	3.12	0.011
	Polyester	3.6	0.012
	Polyimide	3.34	0.005
	Polycyanate	3.23	0.006
	Polybutadiene	3.1	0.003
	Bismaleimide	3.35	0.009

Performance Plastics (formerly Norton Performance Plastics), Ravenna, Ohio, 1996].

The sheet prepreg laminate comes with precise and uniform resin content through the wall. Thus, tolerances can be controlled to a desired thickness more accurately than with the wet-layup approach. Prepreg material is commercially available in commonly used discrete thicknesses that are multiples of one ply (i.e., about 11 mils per ply). Special-order plies are available in a nonstandard thickness of a half ply (i.e., 5.5 mils for a half ply).

Note that in radome electrical design, it will be shown that the least thickness dense layers (least number of plies) results in the best bandwidth and the least radome losses. Marine, terrestrial, or vehicular sandwich radomes could use as few as one ply for the dense layers. However, for aircraft applications the number of plies required is dictated by the aeromechanical environment. Very slow-moving aircraft or unmanned air vehicles (UAVs) might use as few as one or two plies. Commercial jet aircraft may use three or four plies for the dense layers of aircraft sandwich radomes.

4.1.2.2 Core Materials

Honeycomb and foam are both extremely lightweight and strong materials that are commonly used for the low-density layer of sandwich radomes.

Reinforced plastic honeycomb materials as illustrated in Figure 4.1 are available in a variety of wall resins and reinforcements that operate over a wide temperature range. Nomex honeycomb has been the leading structural honeycomb core in the aerospace industry. Nomex operates to 350°F, is an aramid honeycomb core material, and has a relative dielectric constant on the order of 1.1 and a loss tangent less than 0.005 [36]. Korex honeycomb is available in small cell sizes and low densities like the honeycomb of Nomex aramid. We reinforce it with high modulus aramid fibers and a phenolic resin. However, stiffness in shears and compression of the core are about double those of the aramid cores. Korex electrical properties are the same as Nomex.

Standard glass-reinforced honeycombs with phenolic resins operate to 350°F. These honeycombs have a relative dielectric constant on the order of 1.35 and a loss tangent of 0.001. Anisotropy of honeycomb cores can become a problem at millimeter-wave frequencies. Many other honeycomb materials are available for higher-temperature operation, such as glass reinforcement with a polyimide resin system, which operates to 500°F.

Dielectric foam materials have also been used for the low-density layers of sandwich radomes as a substitute for honeycomb materials previously discussed. At microwave frequencies either may be used with essentially no difference in performance. However, at millimeter-wave frequencies many radome designers have found that waveguide type behavior of the honeycomb cells results in deteriorated performance of a sandwich radome from the theoretically predicted

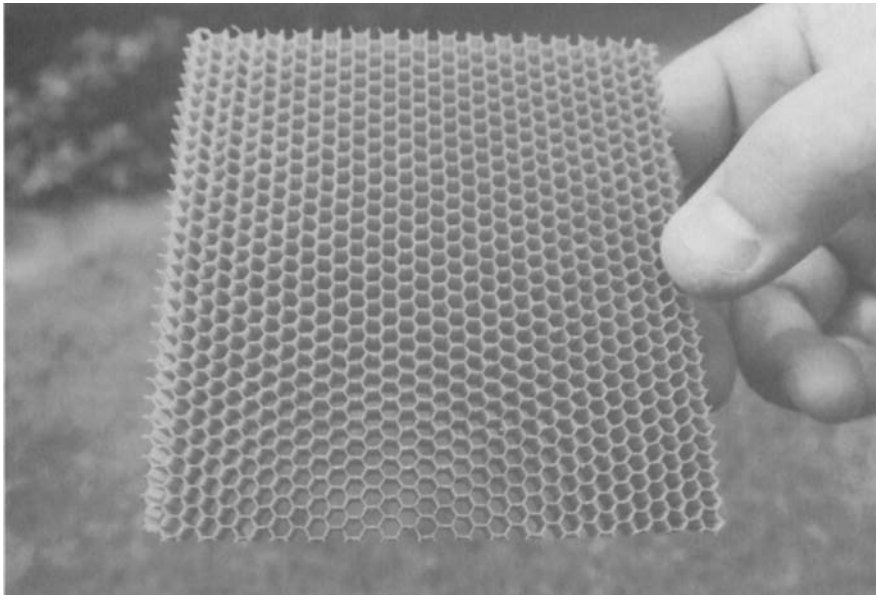

Figure 4.1 Phenolic honeycomb core material photo.

performance; foam type materials eliminate this problem. Foam materials used for the low-density layers of a sandwich radome have been used sucessfully at millimeter wave frequencies to over 100 GHz. One product marketed under the trade name Divinycell has been popular with radome designers in many applications.

Commonly, polyurethane foams have been used as a core material for sandwich radomes. The flexibility and toughness of the foam are dependent on its density. However, those typically used for radomes are in the range of 0.21 to 0.5 g/cm^3. This corresponds to relative dielectric constants ranging from about 1.05 to 1.30 and loss tangents ranging from 0.0005 to 0.001, respectively [17].

4.1.2.3 Fabrication Methods

To fabricate sandwich radomes, the most common method uses the wet layup or uses prepreg materials. The wet layup was one of the earliest methods for fabrication of multilayer wall radome structures. The technique involves laying down plies of the reinforcement fabric that are wetted with a liquid resin to the desired inner skin thickness shown in Figure 4.2 in a female mold of the desired radome shape shown in Figure 4.3. We then insert a low-density core layer (typically a honeycomb) that is precut to a desired thickness. The process is repeated with alternate layers of the resin reinforced fabric and low-density cores until the

Figure 4.2 Ply cutter arrangement. (Photo courtesy of Cobham Sensor Systems.)

Figure 4.3 Female radome mold fixture. (Photo courtesy of Cobham Sensor Systems.)

desired number of layers and total thickness is obtained. Note that using a female mold in the final resin-reinforced fabric plies represents the innermost radome layer.

When the layup is completed, a plastic (vacuum) bag is placed over the complete layup, thereby sealing the mold. The plastic bag is connected to a vacuum pump that evacuates the air between the bag and the layup. The complete mold is then inserted in an autoclave to cure the sandwich under heat and pressure; a typical autoclave used for this purpose is shown in Figure 4.4. By this fabrication process, the tolerance on skins is typically plus or minus 1 mil on each ply of the dense layers.

The state-of-the-art method of sandwich radome fabrication uses prepreg materials that are resin-preimpregnated fabric-reinforced laminates. The methodology is near identical to the wet layup; however, resins do not have to be applied since the material is preimpregnated with resins. The fabrication tolerance using prepreg materials is very good compared to the wet layup method.

4.2 Inorganic Materials

The mechanical strength of most organic wall materials deteriorates at 250°C, and even the best can only survive for a short time at 500°C [18]. Therefore,

Figure 4.4 Autoclaves. (Photo courtesy of Cobham Sensor Systems.)

high-temperature applications, such as hypersonic missiles, often use nonorganic (ceramic) type radome materials. Table 4.4 lists representative values for nonorganic radome materials.

Most of these materials have suitable electrical properties for high-velocity radome applications, such as missiles. For instance, alumina (aluminum oxide) and Pyroceram and Rayceram (both cordierite) have been widely used for flight vehicles operating at and below about Mach 4. They are hard and have fair rain erosion resistance, but are difficult to grind to shape. Pyroceram has a higher dielectric constant than either Rayceram or alumina, which implies tighter mechanical tolerances in manufacture.

Many ceramic materials have a high thermal expansion and are susceptible to thermal shock resulting from rapidly forming temperature gradients during flight. Shock causes the dome to fracture, particularly if the radome is under a mechanical loading. For instance, a 400°C differential may result in failure due to the thermal shock for an alumina radome [11]. Therefore, the radome designer must take care in material selection.

Slip cast fused silica (SCFS), a form of silicon oxide, is suited for high-temperature applications. It has good electrical properties, low cost, and a thermal expansion coefficient less than either alumina or cordierite materials, which

Table 4.4
Dielectric Properties of Selected Ceramic Materials (X-Band Data)

Materials	Relative Permittivity	Loss Tangent
Alumina	9.4–9.6	0.0001–0.0002
Boron nitride	4.2–4.6	0.0001–0.0003
Beryllia	4.2	0.0005
Borosilicate glass	4.5	0.0008
Pyroceram	5.54–5.65	0.0002
Rayceram	4.70–4.85	0.0002
Slip cast fused silica (SCFS)	3.30–3.42	0.0004
Woven (3D) quartz	3.05–3.1	0.001–0.005
Silicon nitride (HPSN)	7.8–8.0	0.002–0.004
Silicon nitride (RSSN)	5.6	0.0005–0.001
Nitro-oxyceram	5.2	0.002
Reinforced Celsian	6.74	0.0009

improves its thermal shock capability. It has been used on reentry vehicles at over Mach 8 velocities.

A high-temperature resin was developed for use in quartz-based 3D composites and in chopped fiber-filled molding compounds [19]. This 3D quartz has good thermal shock resistance and finds application for hypersonic missiles or reentry antenna windows. Structures fabricated from this material have been tested at over 1,900°C with a negligible change in transmission.

A radome designer must be concerned by the variation of a dielectric constant and loss tangent with increasing temperatures since the loss tangent of the material must be kept low to achieve high radome transmissivity. Figure 4.5 shows representative data for SCFS, Pyroceram, and Rayceram. As with the dielectric constant, the loss tangent also increases with increasing temperature. The variation of these properties with temperature can result in disastrous results in the antenna performance if not accounted for in a particular radome application, for instance, thermally increased transmission loss to an unacceptable level or thermally increased BSE or BSES, which might result in an unstable guidance system. Figure 4.6 is a photo of thin wall ceramic radomes.

Researchers at the Georgia Institute of Technology have evaluated silicon nitride [20] and found it to have good electrical properties, mechanical strength, and high rain erosion and thermal shock resistance. They have investigated it in two forms:

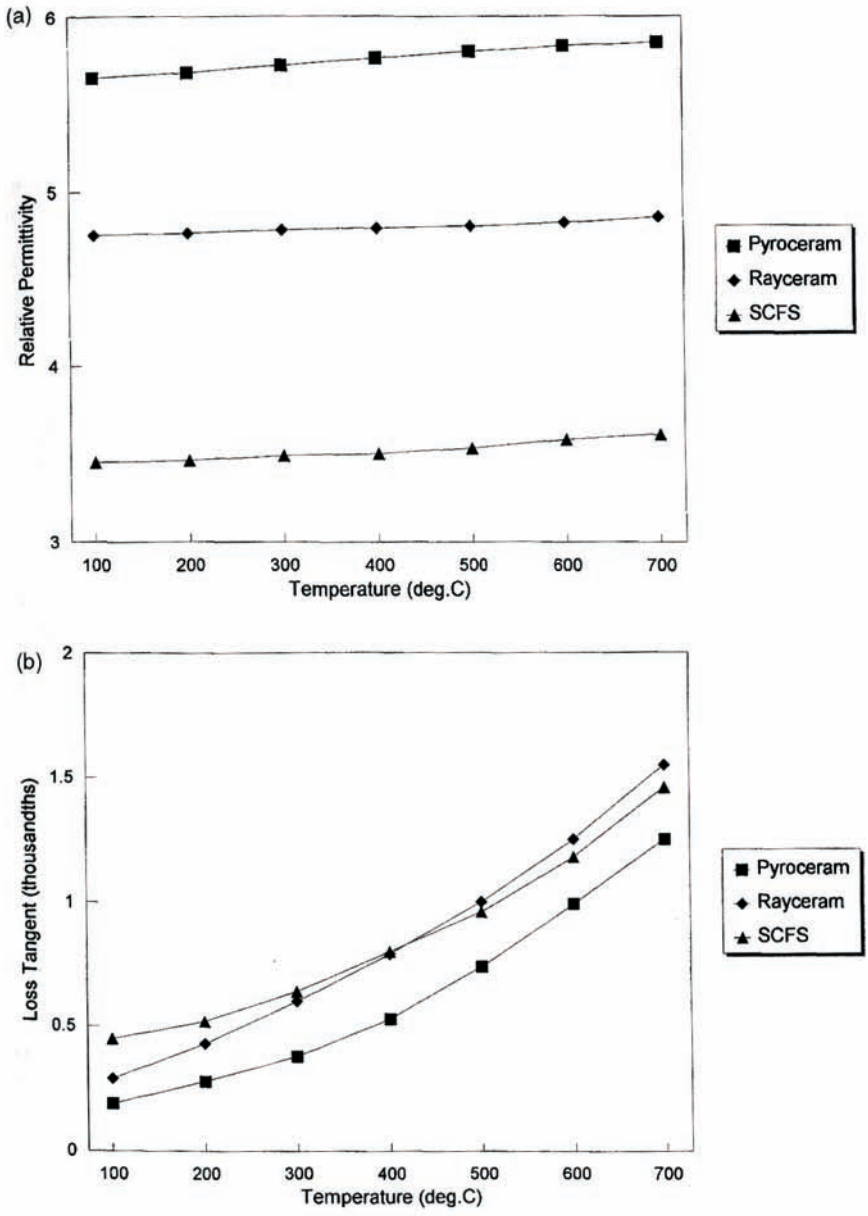

Figure 4.5 Slip cast fused silica (SCFS), Rayceram, and Pyroceram variations of electrical properties with temperature: (a) relative permittivity and (b) loss tangent.

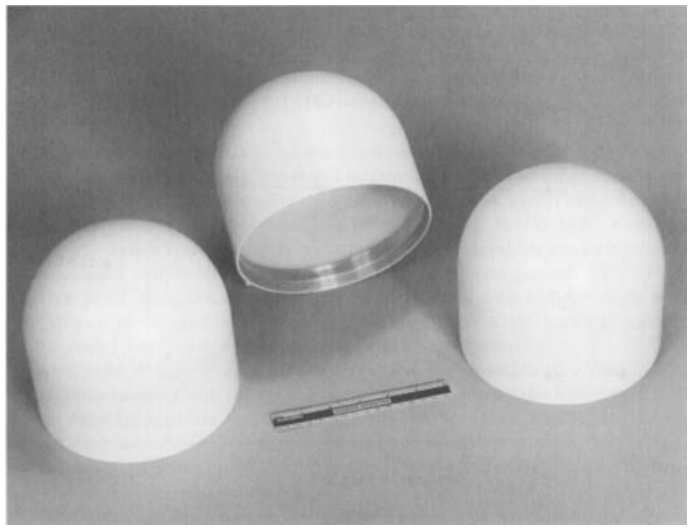

Figure 4.6 Thin wall ceramic radomes. (Photo courtesy of Lockheed Martin Electronics and Missile Systems.)

- Reaction sintered silicon nitride (RSSN) is formed by reaction of silicon with nitrogen in which a flame spray molds silicon powder to shape.
- Hot pressed silicon nitride (HPSN) forms from the reaction of silicon with nitrogen to form a powder that can be hot pressed. HPSN is a more dense material than RSSN.

Although silicon nitride generated great interest during the 1980s, to date, only very small radomes have been produced, with some fabrication problems still unresolved.

Several advanced ceramic composites have been researched for applications where high-temperature microwave transparency must be combined with good strength and all-weather capability [21]. These composites are:

- Nitro-oxyceram, a family of composite materials fabricated from a mixture of silicon nitride, boron nitride, and silica. These materials are fabricated by hot pressing or hot isostatic processing.
- Celsian, a high-purity barium aluminosilicate. This material exhibits mechanical strength that is typically six times greater than silica with a much higher rain erosion resistance.

Measured permittivity data for a number of other ceramic materials was published in [22, 23].

4.3 Dual Mode (RF/IR) Materials

Many modern military sensors use dual-mode operation for improved target recognition capability. While most of these sensors currently use individual sensor windows for the infrared (IR) and for the RF (microwave or millimeter waves) ranges, increasingly users are interested in consolidating both sensors, which permits a single electromagnetic window for both.

Typical IR sensors generally operate in either the near-IR (0.45- to 1.2-micron wavelengths), the mid-IR (3- to 5-micron wavelengths), or the far-IR (8- to 12-microns wavelength) ranges. These wavelengths generally correspond to atmospheric windows where propagation losses are acceptable.

4.3.1 Nonorganic Dual-Mode Materials

Table 4.5 shows the IR transmittance ranges versus the wavelength for many optical materials. Variations in transmittance of a given material occur because of: (1) manufacturing process differences among suppliers, (2) material impurities, and (3) crystalline structure differences.

The candidates in the list of optical materials become fewer when both of the following requirements for the radome are considered:

- A small loss tangent, that is, preferably $\tan \alpha < 0.01$ in the microwave/millimeter-wave band of interest;
- If for an airborne application, the thermal and mechanical requirements for the flight regime.

Selection factors are dependent on the application and include mechanical strength, hardness, coefficients of expansion, thermal shock resistance, temperature range of operation, and stability of permittivity (or refractive index) with temperature. Another concern of currently available optics materials is poor thermal shock resistance.

Researchers at the Georgia Institute of Technology conducted studies of the potential of zinc selenide (ZnSe) and zinc sulfide (ZnS) for optical windows [24]. Texas Instruments (TI) has investigated gallium arsenide (GaAs) as a potential dual-mode material [25]. GaAs is much harder and more resistant to rain erosion than either ZnS or ZnSe. General Electric (GE) has researched chemically deposited silicon nitride as a dual-mode window [26]. GTE Laboratories has also done studies of transparent polycrystalline yttria for IR

Table 4.5
Transmission Ranges Versus Wavelength for Selected Optical Materials

Material	**Transmission Wavelengths**	
	Minimum (Microns)	Maximum (Microns)
Lithium fluoride(LiF)	0.11	6.0
Magnesium fluoride (MgF_2)	0.12	7.0
Calcium fluoride (CaF_2)	0.13	8.0
Barium fluoride (MgF_2)	0.14	12.0
Quartz (SiO_2)	0.15	3.0
UV fused silica (SiO_2)	0.16	2.5
IR fused silica (SiO_2)	0.22	3.3
Glass (BK-7)	0.40	1.4
Silicon (Si)	0.45	7.0
Germanium (Ge)	0.18	12.0
Zinc sulfide (ZnS)	0.40	13.0
Gallium arsenide (GaAs)	1.00	14.0
Sodium chloride (NaCl)	0.18	16.0
Zinc selenide (ZnSe)	0.60	28.0
Potassium chloride (KCl)	0.19	20.0
Potassium bromide (KBr)	0.21	25.0
Cadmium telluride (CdTe)	1.00	25.0
Silver chloride (AgCl)	0.40	29.0
Silver bromide (AgBr)	0.45	35.0
Thallium bromoiodide (KRS-5)	0.60	39.0
Cesium bromide (CaBr)	0.22	50.0
Cesium iodide (CeI)	0.25	60.0

applications [27]. Domes could be isostatically pressed and sintered, which is an economical fabrication process. Also, GTE Laboratories report near net shape sintering, which should reduce the cost of grinding and polishing.

The Office of Naval Research (ONR) conducted a study that identified about 30 ceramic materials suitable for dual-mode windows [28]. These include:

- Mullite;
- Germanium mullite;

- Boron aluminate;
- Zinc germanate;
- Thorium germinate;
- Pollucite;
- Hafnium titanate;
- Calcium lanthanum sulfide.

In recent years, several new mid-range IR materials have become available, including lanthana-strengthened Yittria (LSY). The physical and electrical properties of these new materials are reported in [29].

The fabrication process produces LSY in near net shape. The process consists of pressing LSY into the final shape using an isopress mold. The compacted powder is then placed in a high-temperature furnace where it is fired at over 2,100°C. The rest of the process consists of sintering, annealing, and grinding and polishing. At Ka-band, LSY has a relative permittivity of 11.2 and a loss tangent of 0.0005. Its high-end infrared cutoff at 7.5 microns is considerably higher than that of other mid-range materials. At IR wavelengths, scattering within the crystalline structure is also a major loss factor. Only ceramic windows are possible for mid- and far-IR bands. However, in the near-IR band, there are many viable organic materials.

4.3.2 Organic Dual-Mode Materials

With organic electromagnetic windows, previous studies have shown that the OH-molecular bond is responsible for severe absorption resonances that fall within the mid- and far-IR bands of interest [30]. These absorption resonances exclude the possibility of using many organic window materials.

However, many plastic materials that provide good radome performance in the microwave and millimeter-wave ranges also offer high transparency in the near-IR range. Nevertheless, compared with ceramics, the lower physical strengths and lower range of potential operating temperatures limit the use of these materials to subsonic aircraft, ground vehicles, or fixed terrestrial applications.

Many organic dual-mode materials exist that give excellent transmission in the near-IR range. These include the following [31]:

- *Polymethyl methacrylate (acrylic)* is the most commonly used plastic and has $\varepsilon_r = 2.22$. It is moderately priced, easily molded, and machinable. It has an effective combination of transmission, scratch resistance, wavelength stability, and resistance to water absorption. Acrylic materials

that transmit in the UV range without noticeable aging are also available.

- Methylpentene is optically similar to acrylic, with a relative permittivity of $\varepsilon_r = 2.15$. It is tough and has a chemical resistance, a high temperature resistance, and excellent electrical properties.
- *Polystyrene (styrene)* has a relative permittivity of $\varepsilon_r = 2.53$. It is a low-cost material with excellent molding properties. Methyl methacrylate styrene (NAS) is a copolymer material consisting of 70% acrylic and 30% styrene. The relative permittivity can vary from $\varepsilon_r = 2.35$ to 2.45, depending on the blend. The material can be machined and polished, molds easily, and is considered stable. Styrene acrylonitrile (SAN) is also an acrylic styrene copolymer with $\varepsilon_r = 2.5$. The material is thermally stable and molds well, but has a tendency to yellow.
- *Polycarbonate* maintains its physical strength over a temperature range of −135°C to +120°C, making it suitable for airborne applications. Its relative permittivity is approximately $\varepsilon_r = 2.52$. The material is more difficult to mold than either acrylic or styrene, and is not easily machined or polished due to its high ductility. The major advantage is its high impact resistance, which makes it the preferred material where durability is important. Its cost is significantly high among optical plastics.
- *Nylon* has a relative permittivity of $\varepsilon_r = 2.4$ to 2.9. It is used in applications requiring a combination of transparency and resistance to a wide range of solvents and chemicals. It displays excellent electrical properties with strength and stiffness. Moisture absorption is high; therefore, dimensional stability is low. Nylon's high-flow characteristics and melt stability allow easy processing and the ability to fill thin wall sections. It is one of the more expensive optical plastics.

4.4 Effect of Radome Material on Antenna Performance

Radome losses have the following effects on the enclosed antenna system: (1) reduction of the main beam antenna gain due to the transmission loss, (2) an increase in the antenna noise temperature because of the resistive losses of the radome, and (3) a decrease in the G/T ratio of the system due to both (1) and (2). This is particularly important to radome-enclosed satellite communications (SATCOM) receiving systems since it effectively decreases the dynamic range of the receive system.

In this section we will consider the details of these degradations.

4.4.1 Receiver Noise

It is customary to model a receiver system as noiseless, but account for the noise at the output by a noise factor F where the noise factor is a dimensionless quantity. The noise can be of a thermal origin (thermal noise) or it can be from other noise-generating processes. Most of these other processes generate noise whose spectrum and probability distributions are similar to that of thermal noise. To consider how we model the effects of noise in a receiver, consider a single receiver subsystem stage illustrated in Figure 4.7(a). Using the well-known laws of black body radiation, the total noise at the output of this single-stage electronic subsystem is [32, 33]:

$$P_{no} = k_b T_o BGF \tag{4.2}$$

where

G = subsystem power gain (dimensionless);

B = noise bandwidth of the system (Hz);

k_b = Boltzmann's constant = 1.38×10^{-23} w-s/K;

T_o = ambient temperature = 290K.

The quantity $K_b T_o B$ is the actual thermally generated noise power referenced to the input port of the subsystem. Given that the noise figure is the noise factor expressed in decibels:

$$NF = 10\log(F) \tag{4.3}$$

we can express the noise factor in terms of the noise figure

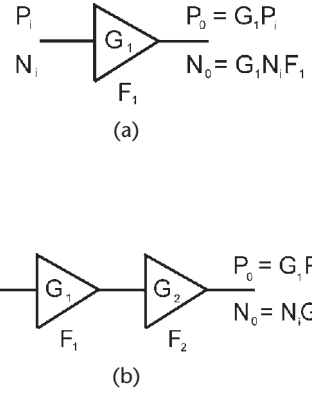

Figure 4.7 Representation of noisy receiver stages: (a) single stage and (b) two stages in cascade.

$$F = 10^{NF/10} \tag{4.4}$$

Alternatively, we can account for subsystem generated noise via a noise-free termination at a temperature T_e. The total noise at the output of the single-stage subsystem is then

$$P_{no} = k_b T_e BG \tag{4.5}$$

from which we see that the equivalent noise temperature is related to the noise factor via

$$T_e = T_o F \tag{4.6}$$

This equivalent noise temperature would produce the same noise power at the output.

Note consider two cascaded receiver subsystems illustrated in Figure 4.7(b). Assuming that the bandwidth of the two cascaded stages is the same ($B_1 = B_2 = B$), then the total thermal noise at the output of the second stage can be shown to be:

$$P_{no} = k_b T_o BG_1 G_2 \left(F_1 + \frac{(F_2 - 1)}{G_1} \right) = k_b T_o BG_1 G_2 F_e \tag{4.7}$$

with the equivalent noise factor

$$F_e = F_1 + \frac{F_2 - 1}{G_1} \tag{4.8}$$

The equivalent noise factor is approximately equal to the noise factor of the first stage if the gain of the first stage is at least 10. This result is particularly relevant in low-noise receiving systems where the first stage is usually a low-noise amplifier (LNA) and the second stage is representative of the microwave receiver; here $F_e \approx F_{LNA}$. In SATCOM systems, the noise factor of the LNA therefore sets the noise factor for the entire receive system. The state of the art in the C-band LNAs is less than 10K.

Finally, the effective noise temperature may be defined in terms of the system noise factor as in [34, 35]:

$$T_e = T_o \left(F_1 + \frac{(F_2 - 1)}{G_1} \right) \tag{4.9}$$

Note that the above expressions only apply for a particular terminating impedance at the receiver input. If another value were used, the noise temperature expressions change. Many microwave receiver systems use 50-ohm coaxial transmission lines, and antennas are matched for the 50-ohm receiver load impedance.

4.4.2 Noise Temperature Without Radome

For an antenna connected to a receiver, the system noise temperature is approximately

$$T_{sys} = T_a + T_e \tag{4.10}$$

Here, T_a is the antenna noise temperature and is the noise power seen at the output terminals of the antenna. The term T_e represents the noise temperature of the receiver electronics representative of the noise generated by its nonideal components and is approximately equal to the noise temperature of the LNA as previously discussed.

Consider that the receiver G/T is the figure of merit at the receiver antenna and is:

$$G/T = G_a - 10\log(T_a + T_e) \tag{4.11}$$

4.4.3 Noise Temperature with Radome

Placed over an antenna, a radome having a power loss L_{dB} can seriously degrade the receive system noise temperature. Consider a radome enclosed antenna illustrated in Figure 4.8. The noise is the total of internally and externally generated noise. The main contributors to the total system noise temperature are given in the following equation:

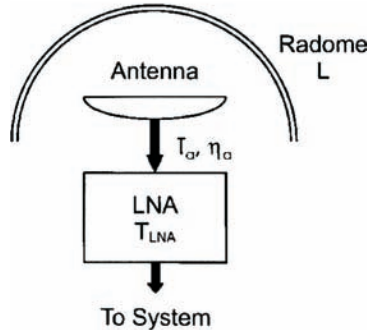

Figure 4.8 Satellite receiving antenna enclosed in a radome of loss L_r.

$$T_{sys} = T_a L_r + 290(1 - L_r) + T_e$$

where

T_{sys} = system noise temperature in degrees K;

T_a = Antenna noise temperature in degrees K;

T_e = Electronics noise temperature in degrees K;

and the radome loss factor is related to the radome loss in decibels (L_{dB}) via

$$L_r = 10^{Ldb/10}$$

Note that $L_r = 1$ for a lossless radome. The noise temperature introduced by the radome loss is the temperature you would have to thermally heat the radome if it were lossless in order to get the same noise power contribution. The antenna noise temperature T_a can be computed from the antenna's radiation pattern and its surrounding environment. A zenith-pointing satellite antenna may have an antenna temperature in the order of 10K due to the low cosmic (galactic) sky temperature.

The G/T ratio is then:

$$G/T = G_a - 10\log(T_a L_r + 290(1 - L_r) + T_e)$$

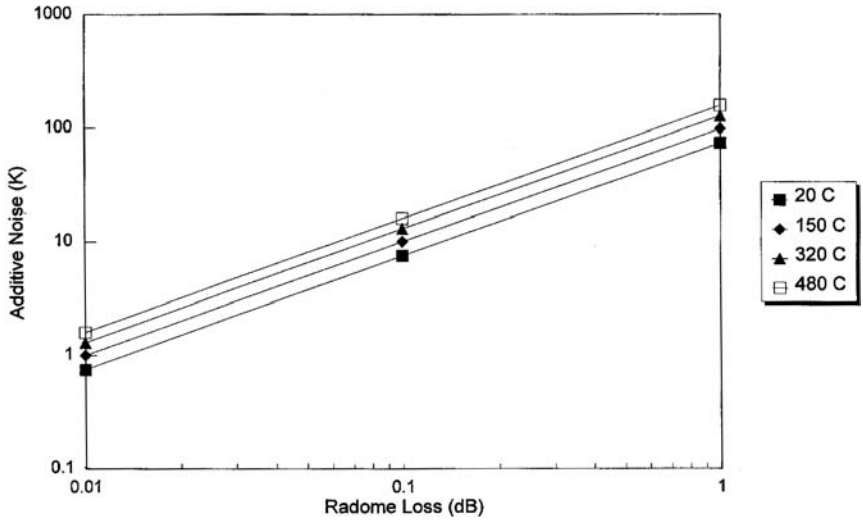

Figure 4.9 Additive system noise due to a heated lossy radome.

For a low-noise system, Figure 4.9 shows the additive system noise temperature due to both the radome loss and its physical temperature. These data show that at ambient temperatures, the radome loss can be a large contributor to system noise temperature. For instance, every –0.1 dB of radome loss can degrade system noise temperature in the order of 10K. Also, note that missile radomes operating at very high physical temperatures may further degrade the sensitivity of radome-enclosed receiving systems. Radomes wetted by rain have also been found to exhibit increased system noise temperature degradation [34]. To minimize this effect, Teflon was investigated as a hydrophobic coating [35].

Figure 4.10 SATCOM radome in a maritime application. (Photo courtesy of Cobham SATCOM.)

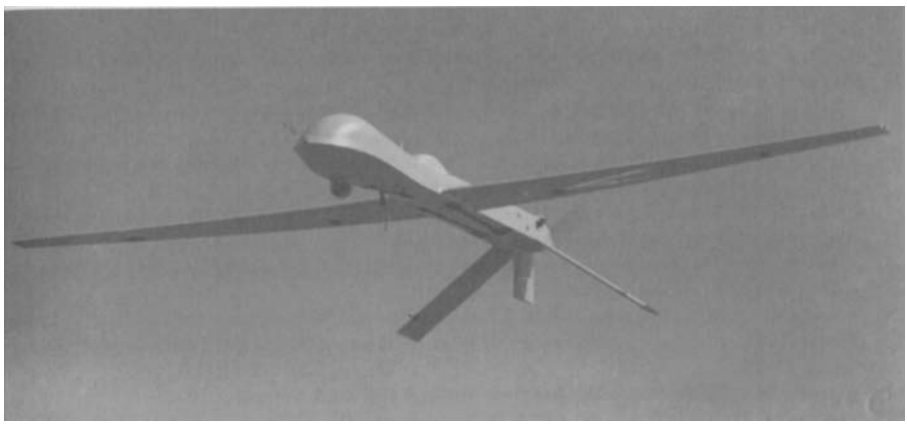

Figure 4.11 SATCOM antenna in a UAV application. (Photo courtesy of General Atomics Aeronautical Systems.)

The effectiveness of various commercially available hydrophobic coatings is listed in [29].

To illustrate several radome applications in which these considerations apply, Figure 4.10 shows a shipboard radomes placed over several SATCOM antennas, and Figure 4.11 shows a SATCOM radome installed on a small aircraft.

References

[1] Bassett, H. L., and J. M. Newton, (eds.), *Proceedings of the 13th Symposium on Electromagnetic Windows*, Georgia Institute of Technology, Atlanta, GA, September 1976.

[2] Harris, J. N., (ed.), *Proceedings of the 14th Symposium on Electromagnetic Windows*, Georgia Institute of Technology, Atlanta, GA, June 1978.

[3] Bassett, H. L., and G. K. Huddleston, (eds.), *Proceedings of the 15th Symposium on Electromagnetic Windows*, Georgia Institute of Technology, Atlanta, GA, June 1980.

[4] Huddleston, G. K., (ed.), *Proceedings of the 16th Symposium on Electromagnetic Windows*, Georgia Institute of Technology, Atlanta, GA, June 1982.

[5] Bassett, H. L., (ed.), *Proceedings of the 17th Symposium on Electromagnetic Windows*, Georgia Institute of Technology, Atlanta, GA, July 1984.

[6] Harris, J. N., (ed.), *Proceedings of the 18th Symposium on Electromagnetic Windows*, Georgia Institute of Technology, Atlanta, GA, September 1986.

[7] Handley, J. C., (ed.), *Proceedings of the 19th Symposium on Electromagnetic Windows*, Georgia Institute of Technology, Atlanta, GA, September 1988.

[8] Ohlinger, W. L., (ed.), *Proceedings of the 20th Symposium on Electromagnetic Windows*, Georgia Institute of Technology, Atlanta, GA, September 1992.

[9] Handley, J. C., (ed.), *Proceedings of the 21st Symposium on Electromagnetic Windows*, Georgia Institute of Technology, Atlanta, GA, January 1995.

[10] Cary, R. H., *Avionics Radome Materials*, North Atlantic Treaty Organization (NATO) Report AGARD-AR-75, London, Technical Editing and Reproduction Ltd., 1974.

[11] Walton, J. D., *Radome Engineering Handbook*, New York: Marcel Dekker, 1970.

[12] Ossin, A., et al., *Millimeter Wavelength Radomes*, Report AFML-TR-79-4076, Wright Patterson Air Force Base, OH, AF Materials Laboratory, 1979.

[13] Gibson, C. C., R. H. Bogaard, and D. L. Taylor, "The EM Window Material Database: A Progress Report," *Proceedings of the 21st Symposium on Electromagnetic Windows*, Georgia Institute of Technology, Atlanta, GA, January 1995.

[14] Burkes, D. G., "Radomes," Ch. 53 in *Antenna Engineering Handbook*, 4th ed., J. L. Volakis, (ed.), New York: McGraw-Hill, 2007.

[15] Skolnik, M. I., *Radar Handbook,* New York, McGraw-Hill, 1970.

[16] Newton, J. M., D. J. Kozakoff, and J. M. Schuchardt, "Methods of Dielectric Material Characterization at Millimeter Wavelengths," *Proceedings of the 15th Symposium on Electromagnetic Windows*, Georgia Institute of Technology, Atlanta, GA, June 1980.

[17] Rudge, A. W., et al., *The Handbook of Antenna Design*, IEEE Electromagnetic Waves Series, London: Peter Peregrinus Ltd., 1986.

[18] Coy, T. N., "Hot Pressed Silicon Nitride," *Proceedings of the 11th Symposium on Electromagnetics Windows*, Georgia Institute of Technology, Atlanta, GA, 1972.

[19] Favaloro, M. R., "A Dielectric Composite Material for Advanced Radome and Antenna Window Applications," *Proceedings of the 20th Symposium on Electromagnetic Windows*, Georgia Institute of Technology, Atlanta, GA, September 1992.

[20] Walton, J. D., "Reaction Sintered Silicon Nitride," *Proceedings of the 11th Symposium on Electromagnetics Windows*, Georgia Institute of Technology, Atlanta, GA, 1972.

[21] Wright, J. M., J. F. Meyers, and E. E. Ritchie, "Advanced Ceramic Composites for Hypersonic Radome Applications," *Proceedings of the 20th Symposium on Electromagnetic Windows*, Georgia Institute of Technology, Atlanta, GA, September 1992.

[22] Sheppard, A. P., A. McSweeney, and K. H. Breeden, "Submillimeter Wave Material Properties and Techniques," *Proceedings of the Symposium on Submillimeter Waves*, Polytechnic Institute of Brooklyn, NY, 1970.

[23] Nickel, H. U., and R. Heidinger, "A Survey of Vacuum Windows for High Energy Millimeter Wave Systems in Fusion Experiments," *Proceedings of the 20th Symposium on Electromagnetic Windows*, Georgia Institute of Technology, Atlanta, GA, September 1992.

[24] Papis, J., B. DiBeneditto, and A. Swanson, "Low Cost Zinc Selenide and Zinc Sulfide for FLIR Optics," *Proceedings of the 13th Symposium on Electromagnetic Windows*, Georgia Institute of Technology, Atlanta, GA, 1976.

[25] Purinton, D., "GaAs IR-RF Window Material," *Proceedings of the 13th Symposium on Electromagnetic Windows*, Georgia Institute of Technology, Atlanta, GA, 1976.

[26] Tanzilli, R. A., J. J. Gebhardt, and J. O. Hanson, "Potential of Chemically Vapor Deposited Silicon Nitride as a Multimode EM Window," *Proceedings of the 14th Symposium on Electromagnetic Windows*, Georgia Institute of Technology, Atlanta, GA, 1978.

[27] Rhodes, W. H., "Transparent Polycrytalline Yttria for IR Applications," *Proceedings of the 16th Symposium on Electromagnetic Windows*, Georgia Institute of Technology, Atlanta, GA, 1982.

[28] Musikant, S., et al., "Advanced Optical Ceramics," *Proceedings of the 15th Symposium on Electromagnetic Windows*, Georgia Institute of Technology, Atlanta, GA, 1976.

[29] Rhodes, W. H., et al., "Lanthana Strengthened Yttria as a Mid-Range Infrared Window Material," *Proceedings of the 20th Symposium on Electromagnetic Windows*, Georgia Institute of Technology, Atlanta, GA, September 1992.

[30] Townes, C. H., and A. L. Shawlow, *Microwave Spectroscopy*, New York: McGraw-Hill, 1965.

[31] Tribastone, C., and C. Teyssier, "Designing Plastic Optics for Manufacturing," *Photonics Spectra Magazine*, January 1991.

[32] Skolnik, M. I., *Introduction to Radar Systems*, 2nd ed., New York: McGraw-Hill, 1980.

[33] Ulaby, F. T., R. K. Moore, and A. K. Fung, *Microwave Remote Sensing: Volume 1,* Dedham, MA: Artech House, 1981.

[34] Dijk, J., and A. C. A. Van der Vorst, "Depolarization and Noise Properties of Wet Antenna Radomes," *AGARD Proceedings*, No.159, Paris, France, October 1974.

[35] Siller, C. A., "Preliminary Testing of Teflon as a Hydrophobic Coating for Microwave Radomes," *IEEE Transactions on Antennas and Propagation*, Vol. AP-27, No. 4, July 1979.

[36] "Hexweb HRH10 Aramid Fiber/Phenolic Honeycomb Product Data Sheet," Hexcel Composites, Dublin, CA, 2008.

Part II
Radome Analysis Techniques

5

Dielectric Wall Constructions

The aim of this chapter is to introduce the reader to the most common radome wall constructions. Some radome walls, called monolithic radome walls, are comprised of a single type of dielectric material. The term "sandwich" is applied to radomes of any multilayer wall construction in which the layers differ in dielectric constant. All these can be mathematically modeled by the boundary value problem solution presented in Section 5.1. Other less common radome walls such as serrated or grooved walls [1, 2] are not treated here.

5.1 Mathematical Formulation for Radome Wall Transmission

The analysis of microwave transmission and reflection for a flat multilayer lamination can be achieved via a boundary value solution of the N-layer dielectric wall depicted in Figure 5.1 for forward and reverse propagating waves (E^+ and E^-, respectively), where the solution takes the form [3, 4]:

$$\begin{bmatrix} E_0^+ \\ E_0^- \end{bmatrix} = \left[\prod_{i=1}^{N} \frac{1}{T_i} \begin{pmatrix} e^{j\gamma_i t_i} & R_i e^{-j\gamma_i t_i} \\ R_i e^{+j\gamma_i t_i} & e^{-j\gamma_i t_i} \end{pmatrix} \right] \frac{1}{T_{N+1}} \begin{bmatrix} 1 & R_{N+1} \\ R_{N+1} & 1 \end{bmatrix} \begin{bmatrix} E_{N+1}^+ \\ 0 \end{bmatrix} \tag{5.1}$$

where

t_i = layer thickness of ith layer.

R_i, T_i = Fresnel reflection and transmission coefficients, respectively, at the interface between the $(i-1)$th and ith layers; see Appendix C for methods to compute these.

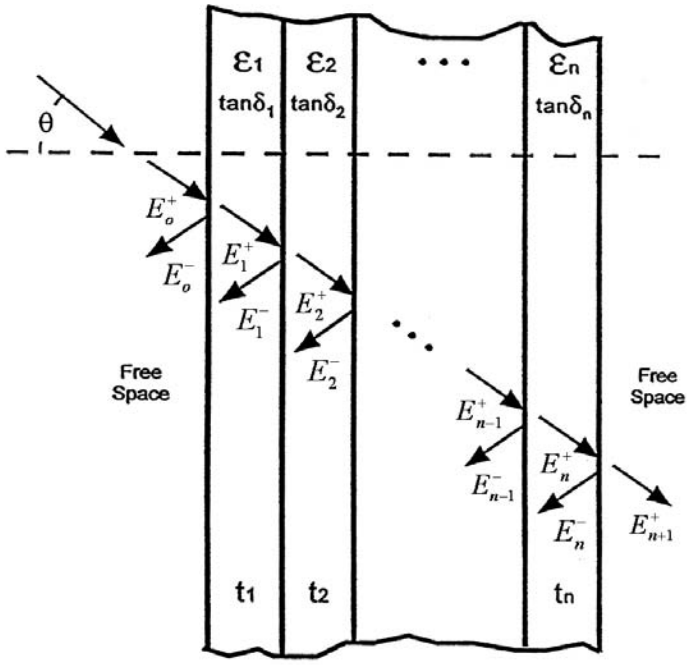

Figure 5.1 *N*-layer dielectric wall boundary value problem.

γ_i = propagation constant within the ith layer normal to the boundary given by:

$$\gamma_i = k_o \sqrt{\varepsilon_{ri}} \cos\theta_i \tag{5.2}$$

in which ε_{ri} is the relative permittivity of the ith layer (a complex quantity), k_o is the wave number in free space, and θ_i is the ray angle within the ith layer measured with respect to the surface normal.

The ray angle as it penetrates into the very first layer can be found from the well-known Snell's law:

$$\frac{\sin\theta_1}{\sin\theta_o} = \frac{\sqrt{\varepsilon_{ro}}}{\sqrt{\varepsilon_{r1}}} \tag{5.3}$$

or

$$\theta_1 = \sin^{-1}\left(\frac{\sqrt{\varepsilon_{ro}}}{\sqrt{\varepsilon_{r1}}}\sin\theta_o\right) \tag{5.4}$$

Similarly, the angle in each layer can be found from the angle in the previous layer via:

$$\theta_i = \sin^{-1}\left(\frac{\sqrt{\varepsilon_{r(i-1)}}}{\sqrt{\varepsilon_{ri}}}\sin\theta_{i-1}\right) \tag{5.5}$$

Note that the dielectric loss is accounted for by a loss tangent term for the dielectric material:

$$\varepsilon_{ri} = \varepsilon'_{ri}\left(1 - j\tan\delta\right) \tag{5.6}$$

where ε'_{ri} is the real part of the relative permittivity for the ith layer. Alternatively one could modify the previous equations to include a conductivity term.

By carrying out the matrix multiplication in (5.1) and gathering terms together, the equation can then be manipulated to take the form:

$$\begin{bmatrix} E_0^+ \\ E_0^- \end{bmatrix} = \begin{bmatrix} A_{11} & A_{12} \\ A_{21} & A_{22} \end{bmatrix} \begin{bmatrix} E_{N+1}^+ \\ 0 \end{bmatrix} \tag{5.7}$$

5.1.1 Transmission Coefficients for Linear Polarization

From (5.7) the final result is obtained for voltage reflection coefficient:

$$R_w = \frac{A_{21}}{A_{11}} \tag{5.8}$$

Likewise, the transmission voltage coefficient is given by

$$T_w = \frac{1}{A_{11}} \tag{5.9}$$

Note that both the reflection coefficient and the transmission coefficient are complex and can be expressed in terms of its magnitude and the insertion phase delay (IPD) angle. For instance, the transmission coefficient may be expressed:

$$T_w = |T_w| \angle IPD \tag{5.10}$$

Engineers working in radome design often use the term *radome transmission efficiency* for:

$$|T_w|^2 \tag{5.11}$$

In Appendix 5A a computer software listing is provided for the preceding matrix solution for a multilayer wall transmission coefficient. The software coding was formulated in POWER BASIC [5].

5.1.2 Transmission Coefficients for Circular Polarization

Transmission coefficients for circular polarized waves are computed from the following formulas

$$T_{w-copol} = \frac{T_{w\perp} - T_{w\parallel} \sin \Delta_{IPD} + T_{w\perp} \cos \Delta_{IPD}}{2} \tag{5.12}$$

$$T_{w-xpol} = \frac{T_{w\perp} - T_{w\parallel} \sin \Delta_{IPD} - T_{w\perp} \cos \Delta_{IPD}}{2} \tag{5.13}$$

In which

$T_{w\parallel}$ and $T_{w\perp}$ = parallel and perpendicular polarization transmission coefficients, respectively;

$\Delta_{IPD} = (IPD_{\perp} - IPD_{\parallel})$ = the difference between the perpendicular and the parallel insertion phase delay values.

These co- and cross-polarized transmission coefficient expressions are useful to calculate the effects of radome depolarization on antenna performance.

5.1.3 Transmission for Elliptical Polarization

In some cases we transmit or receive a circular polarized signal, but the effect of the polarization is to attenuate or phase delay one of the two orthogonal components from the other resulting in the polarization ellipse shown in Figure 5.2. The axial ratio, AR, is defined as the ratio of the magnitudes of the major and minor axes of the polarization ellipse:

$$AR = \frac{b}{a} \tag{5.14}$$

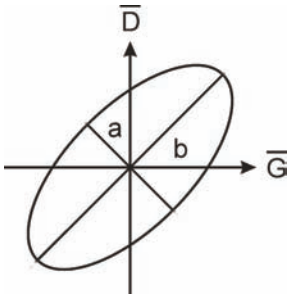

Figure 5.2 Polarization ellipse.

or often expressed in decibels

$$AR_{\text{dB}} = 20\log(AR) \tag{5.15}$$

Let $\overline{D}$ be a unit vector perpendicular to the plane defined by the propagation vector and the surface normal in propagating through the radome wall, and let $\overline{G}$ be a unit vector parallel to the plane defined by the propagation vector and the surface normal in propagating through the radome wall. A circular polarized signal propagating through the radome wall would be modified as:

$$E_t = T_{w\parallel} e^{jIPD\parallel} \overline{G} + T_{w\perp} e^{jIPD\perp} \overline{D} \tag{5.16}$$

We can calculate the AR in propagating through the wall by defining:

$$g_1 = T_{w\parallel} \cos IPD_{\parallel} - T_{w\perp} \sin\left(\frac{\pi}{2} + IPD_{\perp}\right) \tag{5.17}$$

$$g_2 = T_{w\parallel} \sin IPD_{\parallel} + T_{w\perp} \cos\left(\frac{\pi}{2} + IPD_{\perp}\right) \tag{5.18}$$

$$g_3 = T_{w\parallel} \cos IPD_{\parallel} + T_{w\perp} \sin\left(\frac{\pi}{2} + IPD_{\perp}\right) \tag{5.19}$$

$$g_4 = T_{w\parallel} \sin IPD_{\parallel} - T_{w\perp} \cos\left(\frac{\pi}{2} + IPD_{\perp}\right) \tag{5.20}$$

Now let

$$Y = \sqrt{g_1^2 + g_1^2} \tag{5.21}$$

$$Z = \sqrt{g_3^2 + g_4^2} \tag{5.22}$$

From which,

$$a = \frac{\sqrt{Y + Z}}{2} \tag{5.23}$$

$$b = \frac{\sqrt{-Y + Z}}{2} \tag{5.24}$$

From which we get the final result:

$$AR = \frac{b}{a} \tag{5.25}$$

$$AR_{\text{dB}} = 20\log(AR) \tag{5.26}$$

5.2 Radome Types, Classes, and Styles Definition

Radomes for use on flight vehicles (aircraft or missiles), surface vehicles and fixed ground installations are classified into various categories according to MIL-R-7705B [6]. These categories are determined by the specific radome use and wall construction.

There are six types of radomes as identified in the following sections.

5.2.1 Radome Type Definitions

There are six types of radome definitions:

- *Type I* radomes are low frequency radomes and used at frequencies at or below 2.0 GHz.
- *Type II* radomes are directional guidance radomes having specified directional accuracy requirements. These include boresight error (BSE), boresight error slope (BSES), antenna pattern distortion, and antenna sidelobe degradation.
- *Type III* radomes are narrowband radomes with an operational bandwidth less than 10%.

- *Type IV* radomes are multiple frequency band radomes used at two or more narrow frequency bands.
- *Type V* radomes are broadband radomes generally providing an operational bandwidth between 0.100 GHz and 0.667 GHz.
- *Type VI* radomes are very broadband radomes that provide an operational bandwidth greater than 0.667 GHz.

5.2.2 Radome Class Definitions

In addition to the type, the referenced MIL specification defines classes of radomes according to the general application. These are: Class I (flight vehicles), Class II (surface vehicles), and Class III (fixed ground installations).

5.2.3 Radome Style Definitions

Radome styles are defined according to the dielectric wall construction. There are five basic styles described here.

- *Style a* radomes are half-wave wall solid (monolithic) radomes.
- *Style b* radomes are thin-wall monolithic structures with a wall thickness equal to or less than 0.1λ wavelengths at the highest operating frequency.
- *Style c* radomes are also called A-sandwich multilayer walls. These consist of three layers: two high-density skins and a low-density core material. The dielectric constant of the skins is greater than the dielectric constant of the core material.
- *Style d* radomes are multilayer walled structures having five or more dielectric layers. These have an odd number of high-density skin layers and an even number of low-density core layers. The dielectric constants of the skins are greater than the dielectric constants of the core materials. As the number of layers is increased, the broadband frequency performance is improved.
- *Style e* radomes are defined herein as all possible radome wall construction not fitting into styles a through d. These include the B-sandwich and others. The B-sandwich is similar to the A-sandwich except it consists of two low-density skins and a high-density core material. The dielectric constant of the skins is less than the dielectric constant of the core material.

5.3 Wall Style Electrical Performance

This section examines design criteria and typical transmission performance of the various radome wall styles previously defined. Some of the most commonly used radome walls are illustrated in Figure 5.3.

5.3.1 Half-Wave Wall Radomes (Style a)

The characteristics of a half-wave wall are dependent on the interactions at the two air-dielectric interfaces and are inherently narrow banded with typically 5% bandwidth achievable with performance specifications consistent with normal radome applications. An example radome is shown in Figure 5.4. Wall thicknesses that are multiples of a half-wavelength have an even narrower operational bandwidth. Another disadvantage of the monolithic half-wave walled radomes is weight.

For the half-wave wall radome, the wall thickness for lowest transmission loss is a function of incidence angle and wavelength of the electromagnetic radiation and the wall material dielectric constant. This relationship can be expressed as follows:

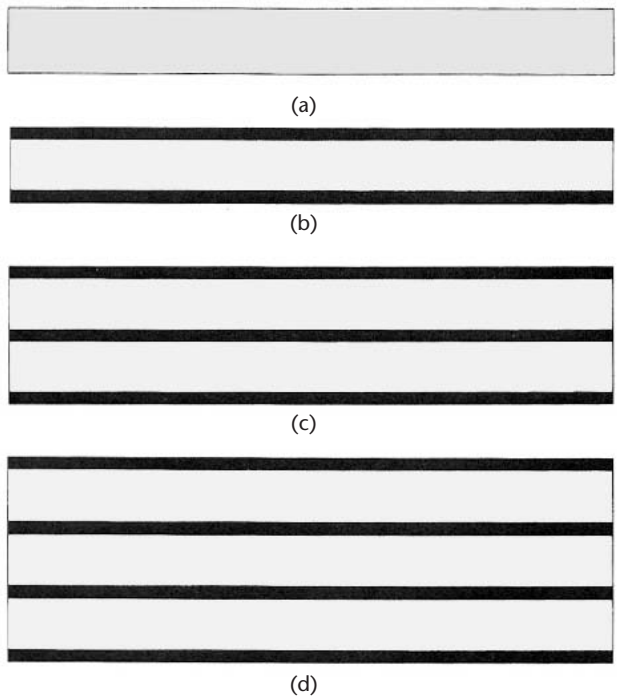

Figure 5.3 (a–d) Illustration of the most common sandwich radome walls.

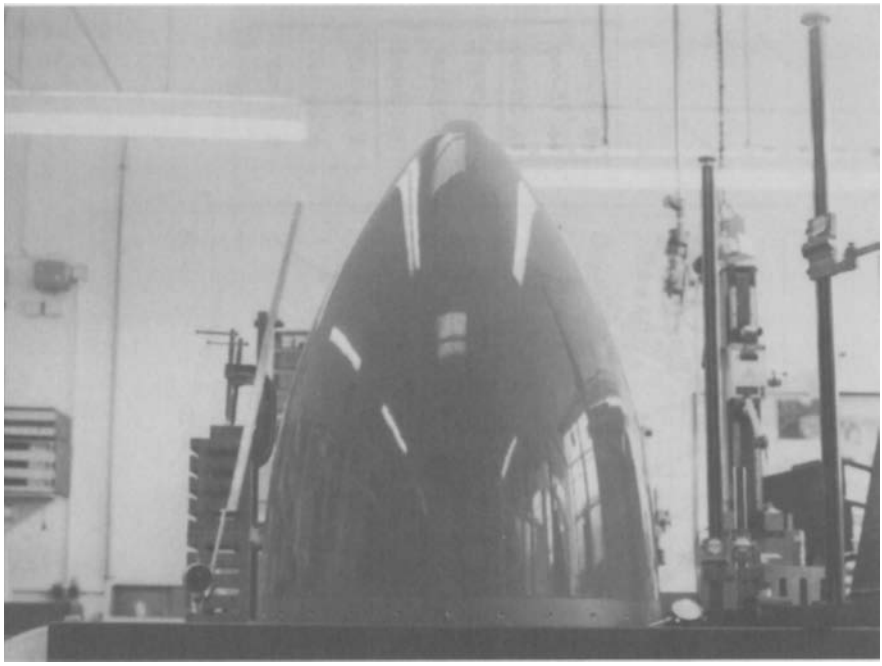

Figure 5.4 High performance monolithic radomes in production at British Aerospace. (Photo courtesy of British Aerospace.)

$$t = \frac{m\lambda}{2\sqrt{\varepsilon_r - \sin^2\theta}} \tag{5.27}$$

Here, λ is the wavelength of radiation and m is the wall order (an integer >= 1).

The voltage transmission coefficient for a monolithic half-wave wall with a thickness of 0.8255 cm is shown in Figures 5.5 and 5.6 for perpendicular and parallel polarizations, respectively. The material had a relative dielectric constant of 4 and a loss tangent of 0.015. The parallel polarization data, in particular, demonstrates zero front face reflection at the Brewster angle given by

$$\theta_B = \tan^{-1}\left(\sqrt{\varepsilon}\right) \tag{5.28}$$

At the Brewster angle, transmission loss through the material is due entirely to ohmic loss. The loss increases with the increasing value of a material loss tangent.

The use of multiple half-wave higher-order (i.e., $m > 1$) wall designs is not normally considered unless the realization of structural integrity is not possible

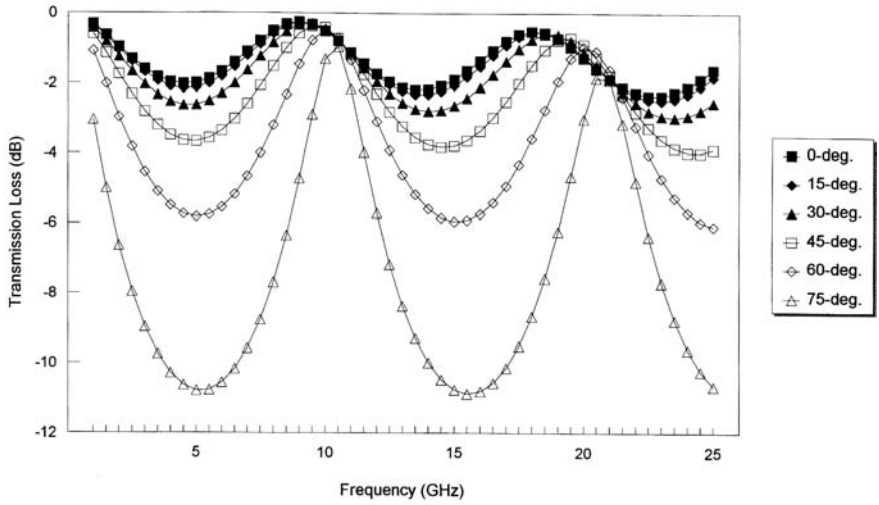

Figure 5.5 Half-wave wall transmission, perpendicular polarization ($t = 0.8255$ cm, $\varepsilon_r = 4$, $\tan\delta = 0.015$).

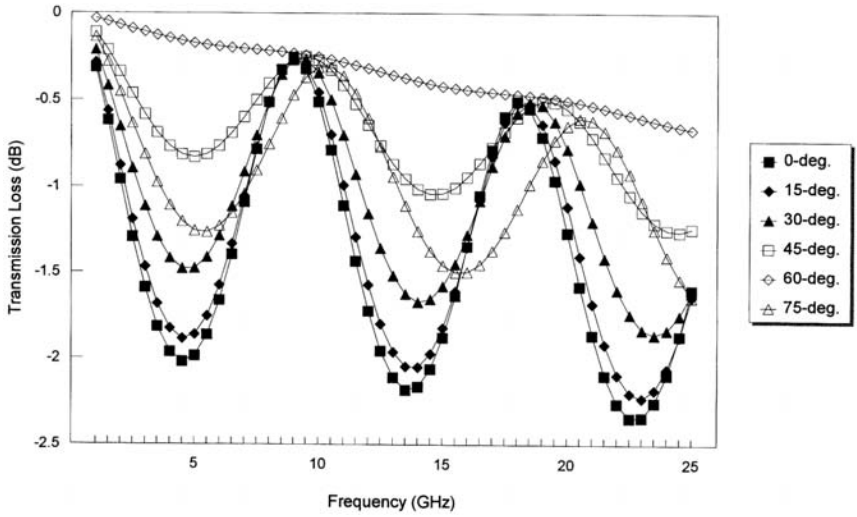

Figure 5.6 Half-wave wall transmission, parallel polarization ($t = 0.8255$ cm, $\varepsilon_r = 4$, $\tan\delta = 0.015$).

by any other means [7]. The penalties for higher-order monolithic walls are reduced bandwidth and increased radome boresight error (BSE) and radome boresight error slope (BSES).

5.3.2 Thin Walled Radomes (Style b)

The thin wall radome essentially behaves like a lowpass filter below the frequency for which it is 0.05 wavelength in thickness [8]. It is particularly useful for transmission incidence angles ranging from 0° through 70° measured from the surface normal [9]. Typical transmission performance data for a material with relative dielectric constant = 4 and a loss tangent = 0.015 are shown in Figures 5.7 and 5.8 for perpendicular and parallel polarizations, respectively. Often, very thin wall radome structures are implemented as protective covers over telecom antenna apertures as illustrated in Figure 5.9. The thin wall radome finds little aircraft or missile applications above X-band since significant mechanical stresses are to be encountered [10].

5.3.3 A Sandwich Radome (Style c)

An A-sandwich wall consists of two more dense dielectric skins separated by a less dense core having a lower relative dielectric constant than the skins. In aircraft radomes, for instance, A-sandwich constructions generally utilize electrically thin plastic skins and cores made of a fiberglass or phenolic honeycomb or

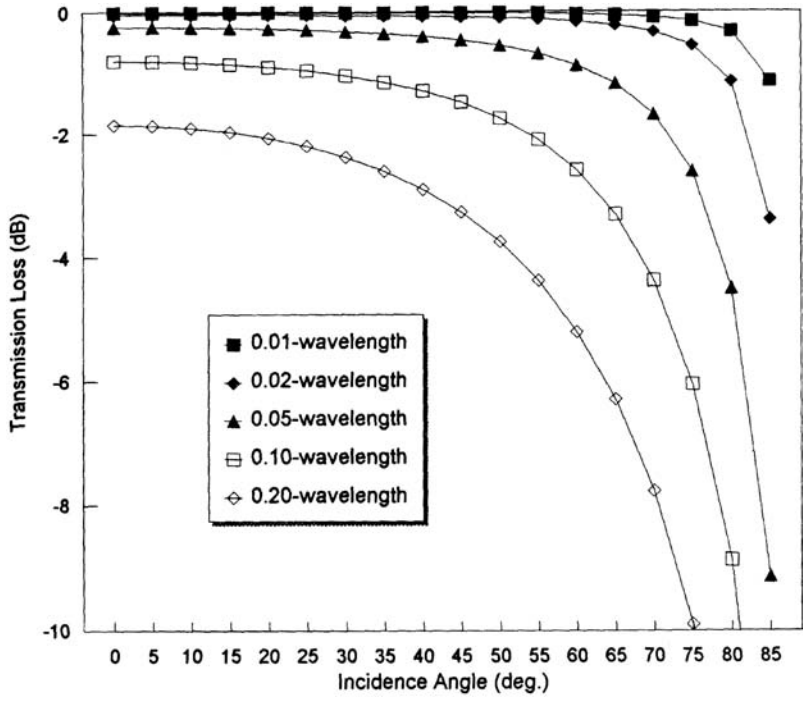

Figure 5.7 Thin wall transmission, perpendicular polarization ($\varepsilon_r = 4$, $\tan\delta = 0.015$).

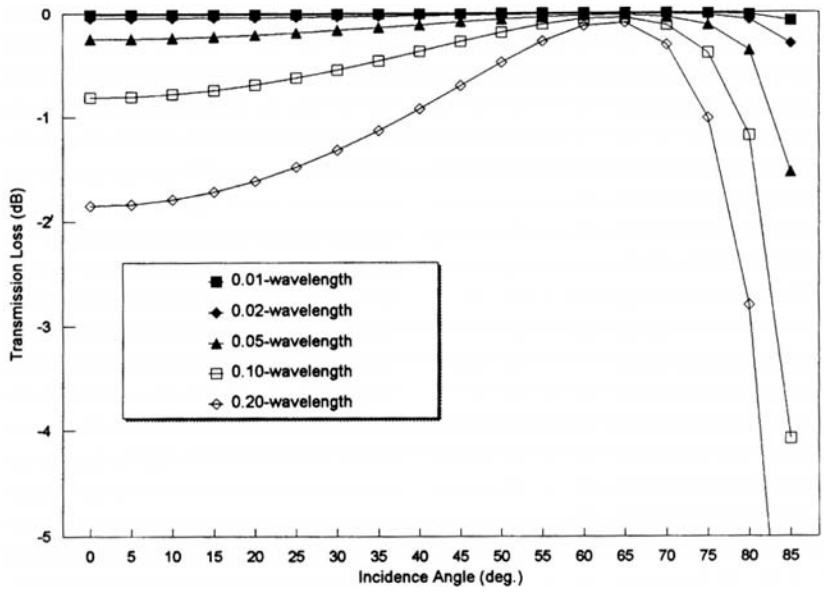

Figure 5.8 Thin wall transmission, parallel polarization ($\varepsilon_r = 4$, $\tan\delta = 0.015$).

else a lightweight plastic foam material. The skins are normally 0.0762 cm or greater in order to provide sufficient structural properties. The A-sandwich wall designs provide high strength-to-weight ratios and good electrical performance at low incidence angles. At higher incidence angles typical of streamlined high fineness ratio (i.e., length-to-diameter ratio) radomes, the performance is poor. As a result, A-sandwich radomes are only used on a low fineness ratio (subsonic) aircraft or fixed applications where near hemispherical shapes may be utilized. These radomes present low incidence angles.

To demonstrate a typical A-sandwich performance, consider a sandwich with 0.0762-cm quartz polycyanate skins ($\varepsilon_r = 3.23$, $\tan\delta = 0.016$) and a 1.016-cm phenolic honeycomb core ($\varepsilon_r = 1.10$, $\tan\delta = 0.001$). The wall transmission versus frequency data are shown for perpendicular and parallel polarizations in Figures 5.10 and 5.11, respectively.

5.3.4 Multilayer Radomes (Style d)

Multilayer or sandwich radome wall designs having five or more layers were developed in answer to the need for increased operating bandwidth and reduced weight. Sandwich walls are more flexible in design than monolithic walls because of their greater degrees of freedom. For instance, multiple frequency or broadband operation is more easily accommodated. The primary disadvantage is that at higher angles of incidence, sandwich wall radomes have greater insertion

Figure 5.9 Photograph of thin wall radome covers over horn antenna apertures. (Photo courtesy of USDigiComm Corporation.)

phase delays (IPDs) than monolithic walled radomes. This results in higher BSE and BSES.

The C-sandwich wall consists of a double A-sandwich design. It offers a greater operating bandwidth than the A-sandwich. Also, when properly designed, the C-sandwich provides a reasonably good performance even at elevated incidence angles. A representative C-sandwich with 0.0762-cm quartz

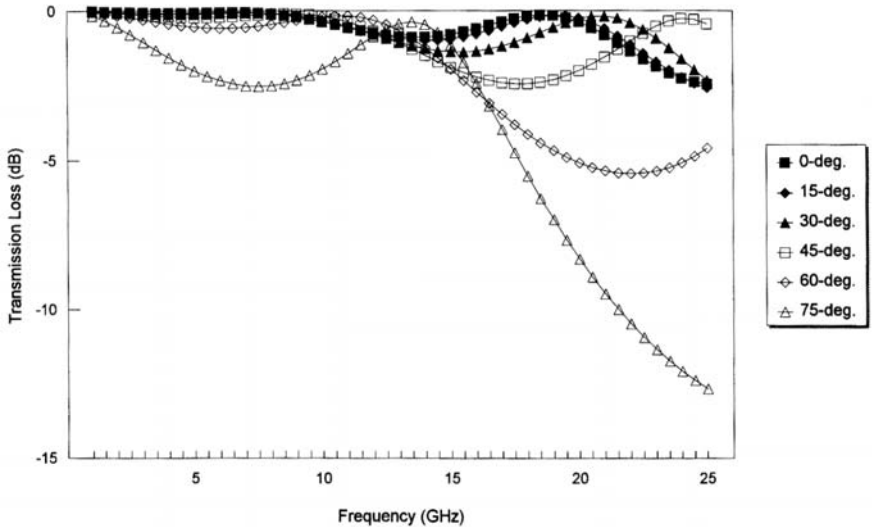

Figure 5.10 An A-sandwich transmission, perpendicular polarization (skins: $t = 0.0762$ cm, $\varepsilon_r = 3.23$, $\tan\delta = 0.016$, cores: $t = 1.016$ cm, $\varepsilon_r = 1.1$, $\tan\delta = 0.001$).

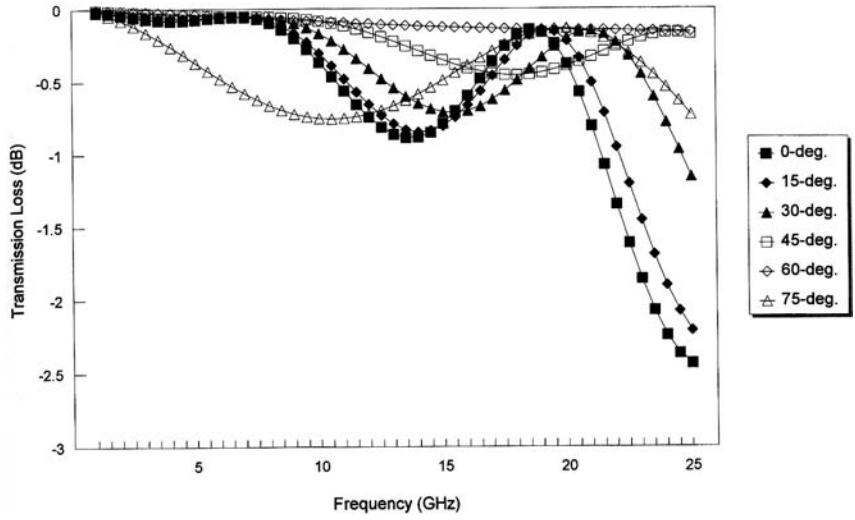

Figure 5.11 An A-sandwich transmission, parallel polarization (skins: $t = 0.0762$ cm, $\varepsilon_r = 3.23$, $\tan\delta = 0.016$, cores: $t = 1.016$ cm, $\varepsilon_r = 1.1$, $\tan\delta = 0.001$).

polycyanate skins and 0.5842-cm phenolic honeycomb cores was considered. Computed transmission data versus frequency are shown in Figures 5.12 and 5.13 for perpendicular and parallel polarizations, respectively. A photograph of a typical C-sandwich radome is shown in Figure 5.14.

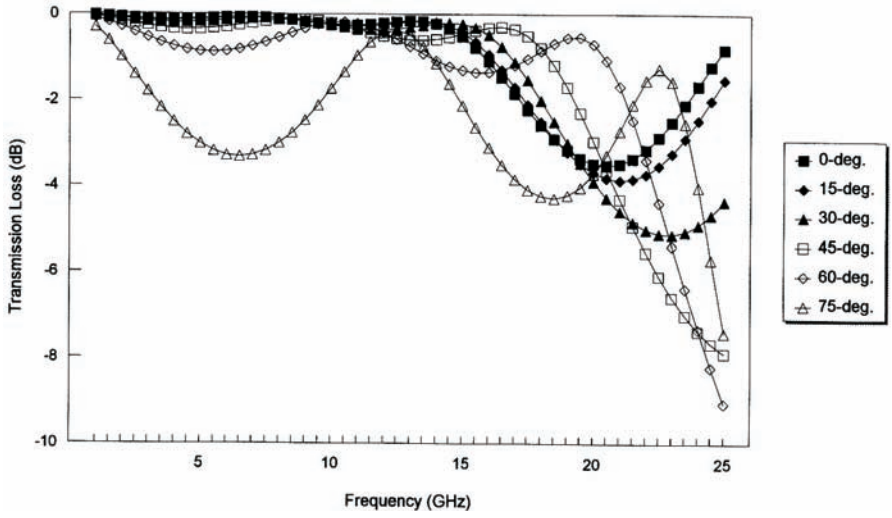

Figure 5.12 A C-sandwich wall transmission, perpendicular polarization (skins: $t = 0.0762$ cm, $\varepsilon_r = 3.23$, $\tan\delta = 0.016$, cores: $t = 0.5842$ cm, $\varepsilon_r = 1.1$, tand = 0.001).

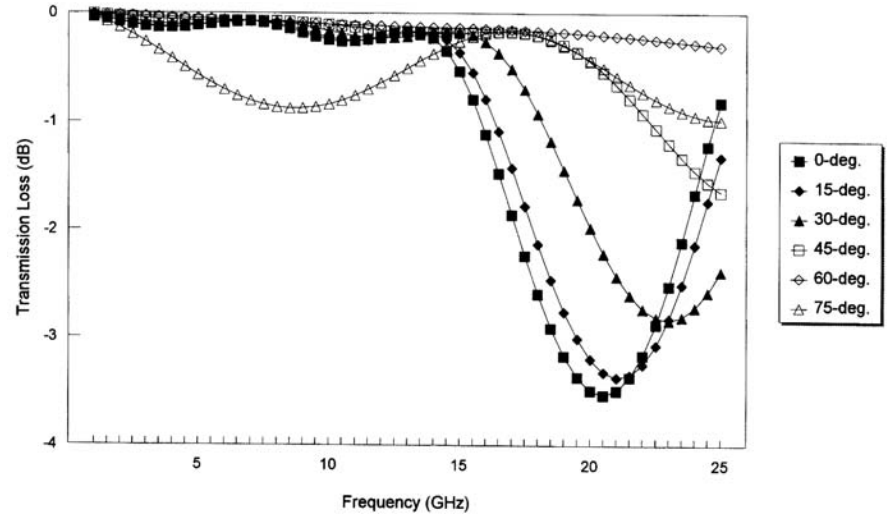

Figure 5.13 A C-sandwich wall transmission, parallel polarization (skins: $t = 0.0762$ cm, $\varepsilon_r = 3.23$, $\tan\delta = 0.016$, cores: $t = 0.5842$ cm, $\varepsilon_r = 1.1$, tand = 0.001).

A greater number of layers most often increases the transmission bandwidth. For instance, the five-layer (C-sandwich) wall design was modified to a seven-layer system. Here, the quartz polycyanate skins are 0.0762 cm, but phenolic honeycomb cores were reduced to 0.3302 cm. The computed transmission versus frequency data are shown in Figures 5.15 and 5.16 for perpendicular and

Figure 5.14 Photograph of an experimental broadband C-sandwich radome.

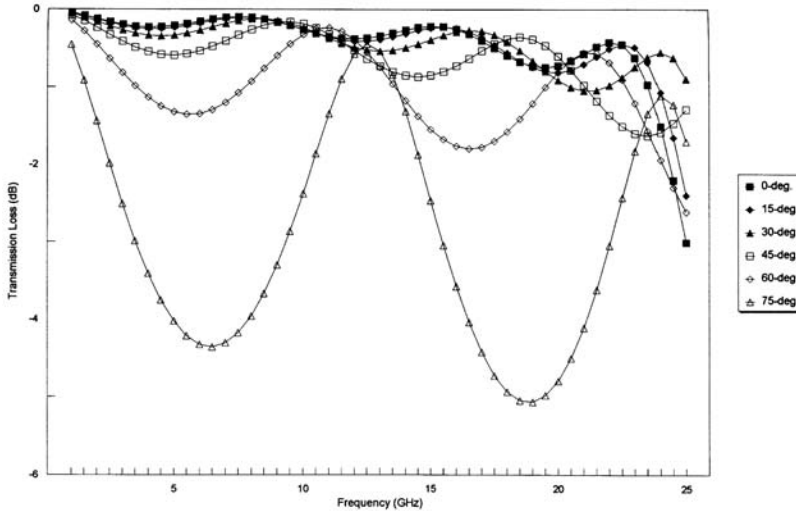

Figure 5.15 Seven-layer wall transmission, perpendicular polarization (skins: $t = 0.0762$ cm, $\varepsilon_r = 3.23$, $\tan\delta = 0.016$, cores: $t = 0.3302$ cm, $\varepsilon_r = 1.1$, $\tan\delta = 0.001$).

parallel polarizations, respectively. Comparing these data to the previous C-sandwich data, considerable improvement in transmission bandwidth is observed.

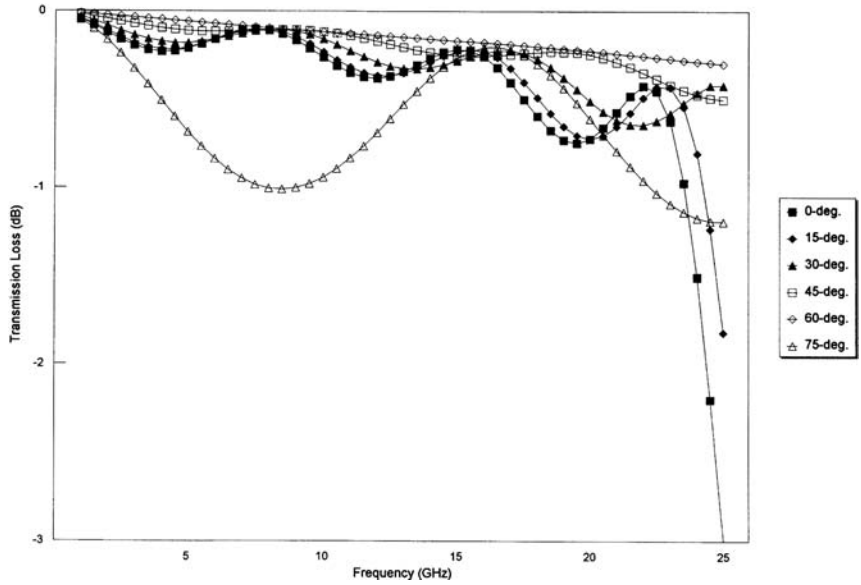

Figure 5.16 Seven-layer wall transmission, parallel polarization (skins: t = 0.0762 cm, ε_r = 3.23, tanδ = 0.016, cores: t = 0.3302 cm, ε_r = 1.1, tanδ = 0.001).

5.3.5 B-Sandwich Radomes (Style e)

A B-sandwich wall is similar to the A-sandwich wall. However, it has less dense dielectric skins separated by a denser (higher dielectric constant) core. The use of B-sandwich wall radomes have been primarily constrained to terrestrial and marine applications as opposed to flight vehicles because of structural problems associated with low-density dielectric skins such as rain erosion and structural problems. In a 1999 patent, MacKenzie [11] considered a multilayer aircraft radome wall design where the outermost layers were low density (with many of the same physical limitations as the B-sandwich wall discussed here). Such structures were found to exhibit superior broadband performance and millimeter-wave performance. MacKenzie also invented a retractable radome that could only be used on aircraft landing and which might have applications for the B-sandwich as well as his multilayer wall design with low-density outermost skin applications [12]; structural demands on the radome are minimal at the lower aircraft landing speed.

References

[1] Bodnar, D. G., and H. L. Bassett, "Analysis of an Isotropic Dielectric Radome," *IEEE Transactions on Antennas and Propagation*, Vol. AP-23, No. 6, November 1975.

[2] Yost, D. J., L. B. Weckesser and R. C. Mallalieu, "Technology Survey of Radomes for Anti-Air Missiles," FS-80-022, John Hopkins Applied Physics Laboratory, Baltimore, MD, 1980.

[3] Collin, R. G., *Field Theory of Guided Waves*, New York: McGraw-Hill, 1960.

[4] Orfanidis, S. J., "Electromagnetic Waves and Antennas," Rutgers University, NJ, 2009.

[5] www.powerbasic.com.

[6] *Military Specification: General Specification for Radomes*, MIL-R-7705 B, January 12, 1975.

[7] Tornani, O., *Radomes, Advanced Design*, North Atlantic Treaty Organization (NATO) Report AGARD-AR-53, prepared by Advisory Group for Aerospace Research and Development, Neuilly Sur Seine, France, 1973.

[8] Rudge, A. W., G. A. E. Crone, and J. Summers, "Radome Design and Performance," *Conference Proceedings of Military Microwaves*, IEE (UK), TK6867.C65, 1980.

[9] Cary, R. H. J., "Design of Multi-Band Radomes," *Proceedings of the IEE Conference on Aerospace Antennas (UK)*, IEE Publication No. 77, TL694.A6C57, 1971.

[10] Tice, T. E., *Techniques for Airborne Radome Design*, USAF Report AFATL-TR-66-391, 1966.

[11] MacKenzie, B., "Radome Wall Design Having Broadband and Millimeter Wave Characteristics," U.S. Patent 5,408,244, April 1995.

[12] MacKenzie, B., "Retractable. Forward Looking Radome for Aircraft," U.S. Patent 5,969,686, October 1999.

Appendix 5A: Program WALL Computer Software Listing

```
     COMPILE EXE
     FUNCTION PBMAIN
     '_____________________________________________
     'GLOBAL VARIABLES NEEDED FOR PROGRAM WALL
      GLOBAL wavenumber, ER(), LTAN(), THK(), GAMMA, FREQ, DRAD, Tm(),
Tp() AS DOUBLE
      GLOBAL Rtotmag(), Rtotph(), PI AS DOUBLE
      GLOBAL N, I, J, K AS INTEGER
      DIM ER(1), LTAN(1), THK(1), Tm(2), Tp(2), Rtotmag(2), Rtotph(2)
     '_____________________________________________
     ' DEFINITION OF INPUT VARIABLES:
     ' N = Number of Layers
     ' THK(i) = Thickness of ith layer (inches)
     ' ER(i) = Relative dielectric constant of ith layer
(dimensionless)
     ' LTAN(i)= Loss tangent of ith layer (dimensionless)
     ' FREQ = frequency (GHz)
     ' GAMMA = angle of incidence (degrees)
     ' DEFINITION OF OUTPUT VARIABLES:
     ' Tm(0) = Magnitude of voltage transmission coefficient (perpen-
dicular polarization)
```

```
     ' Tm(1) = Magnitude of voltage transmission coefficient (parallel
polarization)
     ' Tp(0) = Phase of transmission coefficient for perpendicular
polarization (radians)
     ' Tp(1) = Phase of transmission coefficient for parallel polar-
ization (radians)
     ' ————————————————————————————————————————————————
     DRAD = 3.14159265/180
     ' SAMPLE DATA RUN:
      N=3
      THK(1)=0.005: ER(1)=3.4: LTAN(1)=.02
      THK(2)=0.15: ER(2)=3.58: LTAN(2)=.0045
      THK(3)=0.02: ER(3)=3.65: LTAN(3)=0.017
      GAMMA=0
     FOR FREQ=1 TO 10
      wavenumber=0.532*FREQ
      GAMMA=GAMMA*DRAD
      GOSUB WALL
      PRINT FREQ, Tm(0), Tm(1)
      PRINT FREQ, Tp(0)/DRAD, Tp(1)/DRAD
      NEXT FREQ
      GOTO 1000
      '————————————————————————————————————————
     WALL:
      ' THIS SUBROUTINE COMPUTES THE COMPLEX TRANSMISSION COEFFICIENT
THROUGH A MULTI LAYER
     LOCAL Am(), Bm(), Cm(), Ap(), Bp(), Cp(), ANG, delay AS DOUBLE
     LOCAL IW, JW, KW, POL AS INTEGER
     LOCAL R1, R2, E1, E2, R3, E3, tranmag, tranph, SUM, PA, corr AS
DOUBLE
     LOCAL ZM(), zph(), rez(), imz(), emag(), eph() AS DOUBLE
     LOCAL phimag(), phiph(), rephi(), imphi(), magterm(), angterm()
AS DOUBLE
     LOCAL Rmag(), Rph(), reR(), imR(), reT(), imT() AS DOUBLE
     LOCAL xx, yy, MAG, ROOTMAG, ROOTANG, NUMMAG AS DOUBLE
     LOCAL NUMANG, DENMAG, DENANG AS DOUBLE
     DIM Am(10), Bm(10), Cm(10), Ap(10), Bp(10), Cp(10)
     DIM ZM(10), zph(10), rez(10), imz(10), emag(10), eph(10)
     DIM phimag(10), phiph(10), rephi(10), imphi(10), magterm(10),
angterm(10)
     DIM Rmag(10), Rph(10), reR(10), imR(10)
     DIM Tmag(10), Tph(10), reT(10), imT(10)
      FOR POL=0 TO 1
      ZM(0) = 1: zph(0) = 0: rez(0) = 1: imz(0) = 0
      FOR IW = 1 TO N
      xx = ER(IW): yy = ER(IW) * -LTAN(IW)
      GOSUB RECTPOLAR
      emag(IW) = MAG: eph(IW) = ANG
      NEXT IW
      rephi(N + 1) = 0: imphi(N + 1) = 0
      FOR IW = 1 TO N
      xx = ER(IW) - (SIN(GAMMA))^2: yy = ER(IW) * -LTAN(IW)
      GOSUB RECTPOLAR
      GOSUB COMPLEXSR
      magterm(IW) = ROOTMAG: angterm(IW) = ROOTANG
      phimag(IW) = wavenumber * magterm(IW)
      phiph(IW) = angterm(IW)
      MAG = phimag(IW): ANG = phiph(IW)
```

```
GOSUB POLARRECT
rephi(IW) = xx: imphi(IW) = yy
zmag(IW) = COS(GAMMA) / (magterm(IW) + 1E-12)
zph(IW) = -angterm(IW)
MAG = zmag(IW): ANG = zph(IW)
GOSUB POLARRECT
rez(IW) = xx: imz(IW) = yy
IF POL = 1 THEN
zmag(IW) = 1 / ((emag(IW) * zmag(IW)) + 1E-12)
zph(IW) = -(eph(IW) + zph(IW))
MAG = zmag(IW): ANG = zph(IW)
GOSUB POLARRECT
rez(IW) = xx: imz(IW) = yy
END IF
NEXT IW
zmag(N + 1) = 1: zph(N + 1) = 0
rez(N + 1) = 1: imz(N + 1) = 0
FOR IW = 1 TO (N + 1)
xx = rez(IW) - rez(IW - 1): yy = imz(IW) - imz(IW - 1)
GOSUB RECTPOLAR
NUMMAG = MAG: NUMANG = ANG
xx = rez(IW) + rez(IW - 1): yy = imz(IW) + imz(IW - 1)
GOSUB RECTPOLAR
DENMAG = MAG: DENANG = ANG
Rmag(IW) = NUMMAG / DENMAG
Rph(IW) = NUMANG - DENANG
MAG = Rmag(IW): ANG = Rph(IW)
GOSUB POLARRECT
reR(IW) = xx: imR(IW) = yy
reT(IW) = 1 + reR(IW): imT(IW) = imR(IW)
xx = reT(IW): yy = imT(IW)
GOSUB RECTPOLAR
Tmag(IW) = MAG: Tph(IW) = ANG
NEXT IW
Am(1) = EXP(-imphi(1) * THK(1))
Am(4) = 1 / Am(1)
Am(2) = Rmag(1) * Am(4)
Am(3) = Rmag(1) * Am(1)
Ap(1) = rephi(1) * THK(1)
Ap(2) = Rph(1) - Ap(1)
Ap(3) = Rph(1) + Ap(1)
Ap(4) = -Ap(1)
FOR KW = 2 TO N
Bm(1) = EXP(-imphi(KW) * THK(KW))
Bm(4) = 1 / Bm(1)
Bm(2) = Rmag(KW) * Bm(4)
Bm(3) = Rmag(KW) * Bm(1)
Bp(1) = rephi(KW) * THK(KW)
Bp(2) = Rph(KW) - Bp(1)
Bp(3) = Rph(KW) + Bp(1)
Bp(4) = -Bp(1)
GOSUB CMULT
NEXT KW
Bm(1) = 1: Bm(4) = 1
Bm(2) = Rmag(N + 1): Bm(3) = Bm(2)
Bp(1) = 0: Bp(2) = Rph(N + 1)
Bp(3) = Bp(2): Bp(4) = 0
GOSUB CMULT
```

```
tranmag = 1: tranph = 0
FOR JW = 1 TO N + 1
tranmag = tranmag * Tmag(JW)
tranph = tranph + Tph(JW)
NEXT JW
tranmag = 1 / (tranmag + 1E-12)
120 IF tranph > 2 * PI THEN
tranph = tranph - 2 * PI
GOTO 120
END IF
tranph = -tranph
IF POL=0 THEN
Tm(0) = 1 / (tranmag * Am(1))
Tp(0) = ABS(-(tranph + Ap(1)))
Rtotmag(0) = Am(3) / Am(1)
Rtotph(0) = ABS(Ap(3) - Ap(1))
END IF
IF POL=1 THEN
Tm(1)= 1 / (tranmag * Am(1))
Tp(1) = ABS(-(tranph + Ap(1)))
Rtotmag(1) = Am(3) / Am(1)
Rtotph(1) = ABS(Ap(3) - Ap(1))
END IF
NEXT POL
GOTO 101
CMULT:
FOR IW = 1 TO 3 STEP 2
FOR JW = 1 TO 2
R1 = Am(IW) * Bm(JW)
R2 = Am(IW + 1) * Bm(JW + 2)
E1 = Ap(IW) + Bp(JW)
E2 = Ap(IW + 1) + Bp(JW + 2)
R3 = R1 * COS(E1) + R2 * COS(E2)
E3 = R1 * SIN(E1) + R2 * SIN(E2)
Cm(JW + IW - 1) = SQR(R3 * R3 + E3 * E3)
IF (R3 > 0) AND (E3 > 0) THEN
PA = 0
END IF
IF (R3 < 0) THEN
PA = PI
END IF
IF (R3 > 0) AND (E3 < 0) THEN
PA = 2 * PI
END IF
Cp(JW + IW - 1) = (ATN(E3 / (R3 + 1E-12))) + PA
NEXT JW
NEXT IW
FOR IW = 1 TO 4
Am(IW) = Cm(IW): Ap(IW) = Cp(IW)
NEXT IW
RETURN
RECTPOLAR:
MAG = SQR(xx ^ 2 + yy ^ 2)
IF (xx > 0) AND (yy > 0) THEN
corr = 0
END IF
IF (xx < 0) AND (yy < 0) THEN
corr = PI
```

```
 END IF
 IF (xx > 0) AND (yy < 0) THEN
 corr = 0
 END IF
 IF (xx < 0) AND (yy > 0) THEN
 corr = PI
 END IF
 IF (xx > 0) AND (yy = 0) THEN
 corr = 0
 END IF
 IF (xx < 0) AND (yy = 0) THEN
 corr = PI
 END IF
 IF (xx = 0) AND (yy  0) THEN
 corr = 0
 END IF
 IF (xx = 0) AND (yy = 0) THEN
 ANG = 0
 END IF
 ANG = ATN(yy / (xx + 1E-12)) + corr
 RETURN
 POLARRECT:
 xx = MAG * COS(ANG): yy = MAG * SIN(ANG)
 RETURN
 COMPLEXSR:
 ROOTMAG = SQR(MAG): ROOTANG = ANG / 2
 RETURN
101 'CONTINUE
'THE FOLLOWING RETURN IS FOR THE ENTIRE WALL SUBROUTINE
RETURN:
1000 'CONTINUE
END FUNCTION
```

6

Radome Analysis Techniques

This chapter summarizes selected radome analysis techniques used to predict a radome-enclosed antenna's performance. In any analysis technique, the most significant electrical performance parameters of a radome are:

- Boresight error and registration error (if applicable);
- Copolarized and cross-polarized transmission loss;
- Antenna sidelobe-level degradation.

For certain applications, other parameters that might be of concern are the antenna pattern axial ratio (AR) and the antenna voltage standing wave ratio (VSWR) [1].

Ray tracing is a widely used method for describing propagation through a radome wall. When using ray tracing in a receive mode, an incident wavefront is sampled at uniform sample increments, generally a half-wave apart. From each of these sample points, a ray in the direction of the propagation vector is traced through the radome wall and onto the antenna aperture where an integration of these rays produces the antenna receive port voltage. The point at which each of these rays intercepts the outer surface of the radome is known as the *intercept point*.

Ray tracing methods use many approximations, such as the idea of treating the radome wall at each intercept point as a local plane surface and assuming parallelism between the inner and outer radome walls at the intercept point. Several other factors, such as the antenna size and radome curvature (in wavelengths), may influence discrepancies between the measured and predicted

results. Nonetheless, by comparing predicted and measured results, ray tracing has yielded reasonably accurate results. A large part between measured and predicted values often relates to the accuracy of the values used for radome materials (dielectric constant and loss tangent) and thickness tolerances of the various wall layers.

6.1 Background

Early methods of radome electrical design were cumbersome and approximate, relying primarily on the use of nomographs, such as Kaplun [2] and Zamyatin et al. [3]. With the arrival of the microcomputer, computer-aided design of radomes eventually became widespread [4]. The earliest recorded use of a digital computer in radome analysis is believed to be a 1959 paper by Mahan, Bitterli, and Wein [5]. Other early design methods that used computers were described in papers by Tricoles [6, 7].

Although a number of different radome electromagnetic analysis techniques are feasible, this book primarily focuses on the geometric optics (GO) and the physical optics (PO) methods that can be easily implemented on a personal computer (PC). GO treats the electromagnetic propagation as light-like in behavior and, although approximate, is exact only in the limit of zero wavelength (infinite frequency). However, this GO method produces reasonably good results for radome-enclosed antennas as small as about five wavelengths in diameter. GO will not give good results near physical boundaries, but provides useful insights in those cases. We must consider three aspects to fully use GO: ray reflections, polarization, and amplitude variations along the ray path and through reflections [8].

PO is based on Huygens' principle, which has been of fundamental importance to the development of the electromagnetic wave theory. Huygens' principle states that each point on a primary wavefront can be considered as a new source of secondary spherical waves and that a secondary wavefront can be constructed as the envelope of these spherical waves. Thus, a spherical wave from a point source propagates as a spherical wave as illustrated in Figure 6.1(a), while an infinite plane wave continues as a plane wave as depicted in Figure 6.1(b). PO methods are employed in surface integration formulations that produce reasonably good results for radome-enclosed antennas less than a wavelength in diameter.

A comparison between PO and GO solutions can be obtained by considering a uniform plane electromagnetic wave incident on an electrically large and perfectly conducting obstacle shown in Figure 6.2. We want to obtain a solution to the electric field variation at points along the x-axis and at a distance r behind the obstacle. According to Kraus [9], we can apply Huygens' principle to obtain:

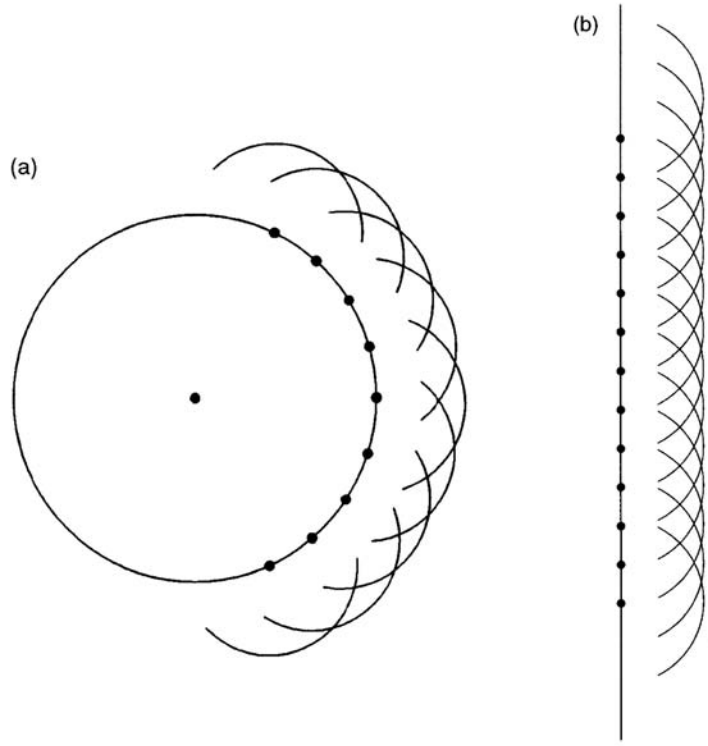

Figure 6.1 Illustration of Huygens' sources: (a) point source and (b) plane wave.

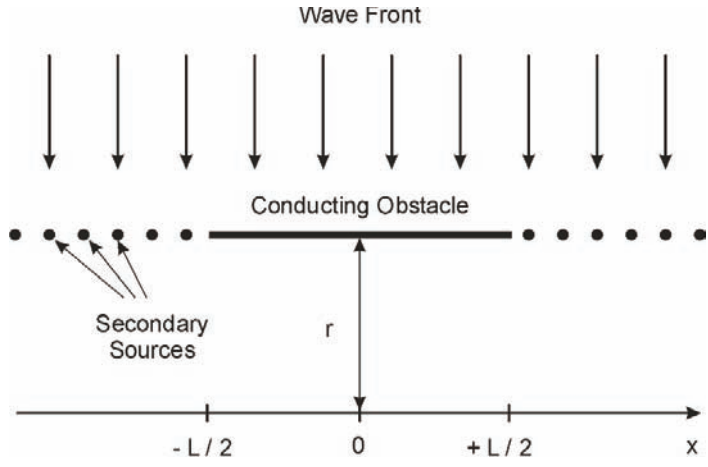

Figure 6.2 Plane wave incident from above onto an electrically large plane object.

$$E^i = \int dE \tag{6.1}$$

where dE is the electric field at point P and the integration is along the x-axis as illustrated in Figure 6.2. We note that in terms of the wave number k, the following holds true:

$$dE = \frac{E_o}{r} e^{-k(r+\delta)} dx \tag{6.2}$$

so that

$$E^i = \frac{E_o}{r} e^{-jkr} \int_{-\infty}^{\infty} e^{-jk\delta} dx \tag{6.3}$$

The PO solution for the power density variation at a distance r below the plane is shown in Figure 6.3. Also depicted is the GO solution wherein it is seen that the conducting obstacle casts a simple shadow, illustrating its light-like behavior. Intuitively, the PO approach is more robust. For instance, assume an incident wavefront on a radome having a conducting rain erosion tip. The GO modeling approach would cast a simple tip shadow onto the antenna aperture. The PO modeling approach is more robust in predicting the actual electromagnetic (EM) fields incident on the antenna aperture.

Section 6.2 discusses the geometric optics method applied by Kilcoyne to develop a two-dimensional ray tracing code for analyzing radomes on a digital computer [10]. Bagby subsequently published a three-dimensional GO method applicable to the desktop computer–aided design of aircraft radomes [11].

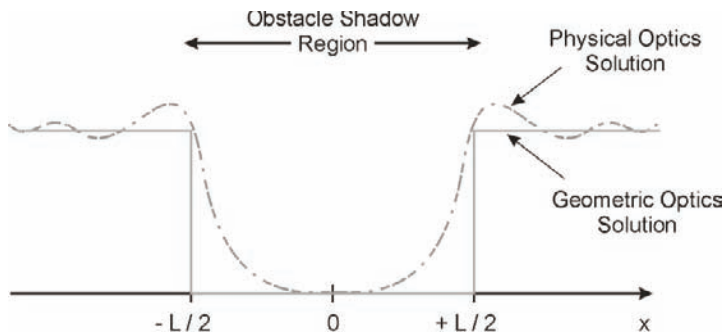

Figure 6.3 Power density variation for the plane wave incident from above onto an electrically large plane object.

Section 6.3 describes physical optics methods, which were developed later and offer more robust radome electromagnetic modeling. Hayward, Rope, and Tricoles [12, 13] adapted PO to a simple receive mode radome surface integration method. Raz et al. [14] and Israel et al. [15] used PO in a transmit formulation that projected the antenna aperture through the radome to an external reference plane. An integration over this reference plane produced the far-field radiation patterns of the radome enclosed antenna.

Section 6.4 describes other methods that can be employed for radome analysis, for instance, the method of moments (MOM) technique reported by Tricoles, Rope, and Hayward [16] and the plane wave spectra (PWS) approach used by Wu and Ruddick [17] and Joy and Huddleston [18].

Section 6.5 discusses sources of computational errors in the modeling. Primarily, these include those error sources pertinent to the GO and PO analysis approaches.

A comparison of the relative accuracy and difficulty of implementation for the techniques discussed in this chapter appear in [12, 13, 19, 20].

6.2 Geometric Optics (GO) Approaches

Most radome analysis approaches based on GO ray tracing have the following characteristics: (1) conceptual simplicity combined with reasonable accuracy, and (2) application in either the transmit or the receive modes.

For radomes large in wavelengths, GO methods produce good boresight error prediction accuracy. Tavis [21] researched both the transmitting and the receiving GO formulations and found identical boresight error prediction with either model. However, the receive approach required a greater computer run time.

According to GO, we can decompose the problem of defining the EM field with a radome over the antenna into two parts:

- Determine the rays that define the phase of the field independently from its amplitude. The ray optic field is a local plane wave field that propagates along trajectories satisfying the laws of geometric optics [22].
- Determine the amplitude that can be carried out by following intensity variations along each ray without regard to the field of other rays [23].

The earliest known approach to radome analysis was an optical one for which the aperture was assumed to be very large compared to a wavelength. A solution for a two-dimensional wedge was reported by Mahan et al. [5], and a

solution for a three-dimensional cone was reported by Mahan and Bone [24]. Both considered a monolithic radome wall and the approach-traced rays from an incident wavefront through the radome walls onto an internal antenna aperture assuming that the refraction effects at the air-dielectric boundaries can be described by Snell's law.

Another early GO transmit formulation modeled the antenna aperture as a collection of sources with arbitrary amplitude and phase. The collection of rays defined an equivalent aperture outside of the radome whose amplitude and phase distributions incorporated the effect of the radome [25]. The Fourier transform of this distribution yielded the far-field radiation pattern of the radome-enclosed antenna. In Einziger and Felson [26], GO ray tracing also accounted for multiple reflections on the concave (inner) radome side and for reflections between its layer boundaries.

6.2.1 GO Receive Mode Calculations

The receiving formulation finds the voltage at the antenna port when a plane wave is incident on a radome-enclosed antenna, as illustrated in Figure 6.4(a). This is sometimes referred to as a *backward ray trace*. The antenna receive port voltage is obtained from the incident fields and the known characteristics of the antenna. Thus, the problem is really one of finding the incident fields at the antenna in the presence of both the radome and the antenna [27]. For monopulse radar antennas, we can derive a quantitative estimate of the radome boresight error from the complex sum and difference antenna patterns computed without and with the radome in place.

Assume an incident plane EM wave coming from an arbitrary but fixed direction, θ and φ. To obtain the received antenna voltage, we integrate the wavefront data over the receive antenna aperture in accordance with the equivalence theorem [6]. This leads to a calculation of the propagation of the EM field to its values on the antenna aperture surface. Accordingly, the received complex voltage at the terminal of the antenna is [13, 28]:

$$\int\int F^a \left(E^i T_w\right) da \tag{6.4}$$

This integration extends over the physical antenna surface area for which F^a has a significant contribution. In addition, E^i is the incident plane wave function, F^a is the complex valued receiving aperture distribution at point on the antenna surface, and T_W is the complex valued radome transmission coefficient a ray intercept point.

Usually, the radome is treated as a local plane at each ray intercept point [29], which leads to small errors in the calculation of T_W. The transmission

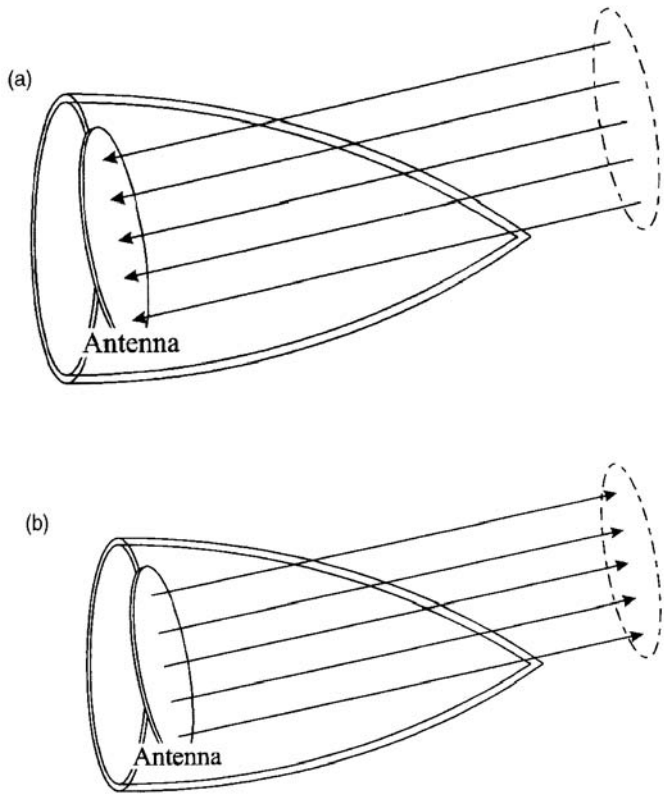

Figure 6.4 Geometric optics (GO) ray trace approaches: (a) receive mode and (b) transmit mode.

characteristics of the radome wall for any given frequency, material type, number of layers, and layer thicknesses also depend on the angle of incident θ (the angle between the propagation vector and the radome surface normal vector at the ray intercept point) and the apparent polarization of the wave E^i with respect to the plane of incidence. $TW_{\parallel}$ is the complex transmission coefficient for field components that line in the incidence plane, and $TW_{\perp}$ is the complex transmission coefficient for field components perpendicular to the incidence plane. We will see in Chapter 7 that E^i is normally decomposed into components that are parallel and perpendicular to the plane of incidence prior to applying the respective transmission coefficients. Subsequently, the wave is reconstructed on the other side of the wall. For all cases, an equivalent transmission coefficient T_W can be defined. The calculation of T_W usually ignores multiple reflections within the radome wall and trapped waves. Tricoles et al. [30] have observed significant errors that occur sometimes by this omission.

The antenna aperture distribution, F^a, can be found from probing the near field at several wavelengths from an actual antenna surface and applying a backward propagation (Fourier transform) technique [12]. Alternatively, it can be probed very close to the antenna aperture with a suitable probe.

6.2.2 GO Transmit Mode Calculations

The transmit mode is illustrated in Figure 6.4(b). The antenna aperture distribution is projected through the radome wall to form an equivalent aperture outside of the radome. However, each ray is modified by the amplitude and phase of its associated radome transmission coefficients, and the modified effective aperture distribution includes the effect of the radome walls. Thus, points forming the modified aperture distribution are related to the actual aperture distribution via:

$$F_{mn}^{a'} = T_w F_{mn}^{a} \tag{6.5}$$

where F_{mn} is the complex valued transmit aperture distribution at the point on the actual antenna aperture and T_W is the complex valued radome transmission coefficient associated with the intercept of the mnth ray at its intercept point. In this case, the equivalent aperture size is identical in size to the actual antenna aperture. Assume that the antenna is in the x-y plane with the z-coordinate corresponding to the radome axis. We can obtain the far-field antenna array pattern from the reference plane distribution by applying the following formula.

$$E_t = \sum_{m=1}^{M} \sum_{n=1}^{N} F_{mn}^{a'} e^{-jk(x_m \sin\theta\cos\phi + y_n \sin\theta\sin\phi)} \tag{6.6}$$

where $x_m = m\,d_x$, $y_n = n\,d_y$, and d_x, d_y are the sample spacing in x- and y-coordinate directions, respectively.

6.3 Physical Optics (PO) Approaches

In analyzing the performance of a radome-enclosed antenna system, physical optics techniques generally offer a higher computational accuracy than geometric optics, due to the assumptions of geometric optics. For instance, GO makes the assumption that the EM wave propagates as a plane wave confined to a cylinder whose cross section the antenna aperture defines. However, in reality the field diverges. Shifflett [31] gives a good overview of the method. In the following sections we attempt to explain some of the variants of PO radome analysis.

6.3.1 PO Receive Mode Calculations

For radomes smaller than about five wavelengths in diameter, the GO approach is too approximate and we must go to PO techniques. Integrating over the radome surface with the Kirchoff-Fresnel integral yields better results to obtain the field at each point on the antenna aperture, as illustrated in Figure 6.5(a). To accomplish this integration, we use an external reference plane to reformulate an incident plane wave as a grid of Huygens' sources, and we then trace rays between that grid and each point on the antenna aperture. Hence:

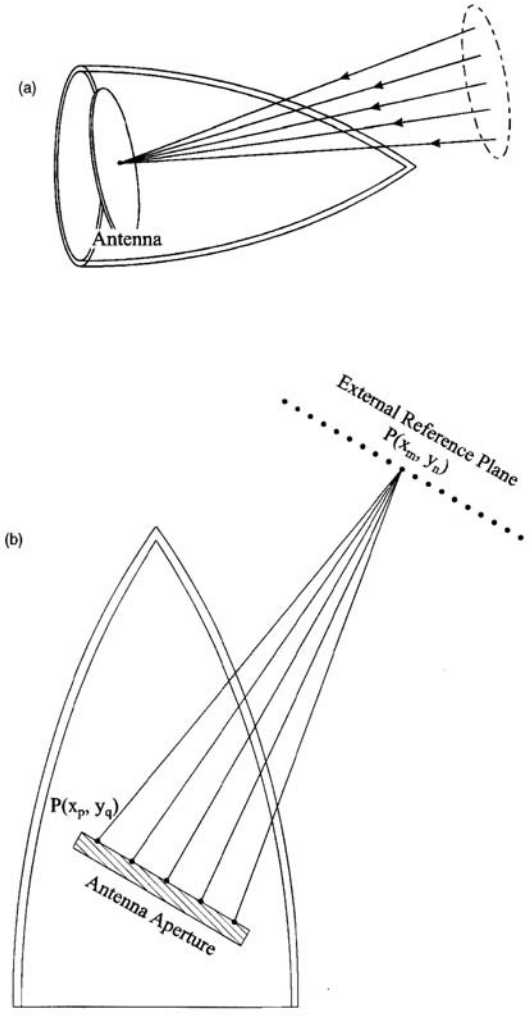

Figure 6.5 Physical optics: (a) receive mode and (b) transmit mode.

$$V_a = \iint F^a \left(\iint E^i T_w \frac{e^{-jkr}}{r} ds \right) da \tag{6.7}$$

The outer integration extends over the antenna surface area for which F^a has a significant contribution, and the inner integration is over the external reference plane where:

E_i = incident plane wave function;

F^a = complex valued receiving aperture distribution at a point on the antenna surface;

T_W = complex valued radome transmission coefficient at a ray intercept point;

k = wave number = $2\pi/\lambda$;

r = the distance from each point on the external reference plane to an antenna aperture point, x_a, y_a, z_a.

The direct ray (GO) and surface integration (PO) methods differ primarily in the computation of the total transmission coefficient. With the PO method, the integration of a bundle of rays through the radome wall, as opposed to a single ray, more densely samples the curvature variation results in a more robust wall transmission model. Both methods use the flat panel approximation to compute wall transmission coefficients at the ray intercept points and ignore both multiple internal reflections and trapped waves. Hayward et al. [12] have compared predicted with measured data for these two receive ray trace methods. Overall, the researchers found that the surface integration was more accurate, especially for radomes that were small in wavelengths.

6.3.2 PO Transmit Mode Calculations

In a physical optics transmit formulation, the following steps occur, which conform better to reality:

- We obtain the antenna near-field distribution on the inner radome surface.
- The transmission coefficients of the radome wall are applied to give the field on the exterior of the radome.
- We make a final transformation to the far field by a Fourier transform technique.

A useful radome analysis technique researched by Raz et al. [14] and Israel et al. [15] uses PO for tracing the field from an antenna aperture through the

radome wall to an external reference plane, where contributions are collected. The geometry is illustrated in Figure 6.5(b).

Assuming that each point on the antenna aperture radiates as a Huygens' source, the complex distribution can be derived for each point on an external reference plane via:

$$F_{mn}^{a'} = \iint F^{a} T_{w} \frac{e^{-jkr}}{r} da \tag{6.8}$$

The integration extends over the physical antenna surface area for which F^a has significant contribution and where

$F_{mn}^{a'}$ = complex valued transmit aperture distribution at a point on the external reference plane surface;

T_W = complex valued radome transmission coefficient at ray intercept point;

k = wave number = $2\pi/\lambda$;

r = the distance from each point on the antenna aperture to a point x_m, y_n on the external reference plane.

Here the area forming the external reference plane should be larger than the physical area of the radome-enclosed antenna. An exact solution corresponds to an infinite external plane, but this is not possible. Typically, we may take it two to four times the physical area of the antenna. The far-field antenna array pattern can be computed from the reference plane distribution as we did in (6.6).

$$E_t = \sum_{m=1}^{M} \sum_{n=1}^{N} F_{mn}^{a'} e^{-jk(x_m \sin\theta\cos\phi + y_n \sin\theta\sin\phi)} \tag{6.9}$$

where $x_m = m\,d_x$, $y_n = n\,d_y$, and d_x, d_y are the sample spacings in x-and y-coordinate directions, respectively.

6.4 Other Approaches

6.4.1 Method of Moments (MOM)

Joy et al. [20] applied a two-dimensional method of moments technique to a tangent ogive radome based on the approach developed by Richmond [28–30]. An integral equation for the electric field was solved by dividing the dielectric into cells that were small enough so that the electric field intensity was approximately uniform in each cell.

Also applying a MOM approach, Tricoles, Rope, and Hayward [32] analyzed the EM fields scattered by a hollow cone, using two formulations. One was based on a scalar Green's function and the other on a tensor Green's function. The two are equivalent, but the procedures differ in the following ways.

- The scalar Green's function method decomposes the cone into circular cylinders and subsequently decomposes the cylinders into angular sectors. The tensor Green's function method decomposes the cone into spheres.
- The number of cells differs because the cell sizes differ.
- Polarization dependence differs.

Tricoles et al. [15] applied this MOM technique to dielectric cylinders of an arbitrary shape. Although sophisticated, the MOM is more difficult to apply to radome modeling than the other methods previously discussed. Very limited validation data appears in the technical literature to compare its accuracy with geometric optics of physical optics methods. However, MOM may give the effects of guided waves or scattering by a radome rain erosion tip.

In 2001, Abdel Moneum et al. [33] developed a hybrid technique for electrically large axisymmetric tangent ogive shaped radomes. The method applies MOM analysis for the wall in the nose region and PO analysis for the remaining wall.

6.4.2 Plane Wave Spectra (PWS)

Paris developed a three-dimensional approach that could find the tangential fields on the outside radome surface due to a horn antenna radiating inside the radome [16]. Wu and Rudduck developed a three-dimensional method that used a plane wave spectrum representation to characterize the antenna [17]. A discrete PWS is a complex vector array obtained from a Fourier transform of the near-field aperture field and represents the radiating antenna properties. If an antenna aperture has M by N sample points, then the PWS contains MN plane waves. The approach is illustrated in Figure 6.6.

Joy and Huddleston expanded on this idea by using a fast Fourier transform (FFT) to speed up the computer calculations when applying a plane wave spectrum approach [18]. PWS is believed to give more accurate results than either the GO or PO approaches discussed earlier. However, PWS requires a considerably greater computer run time and cannot be implemented on a PC.

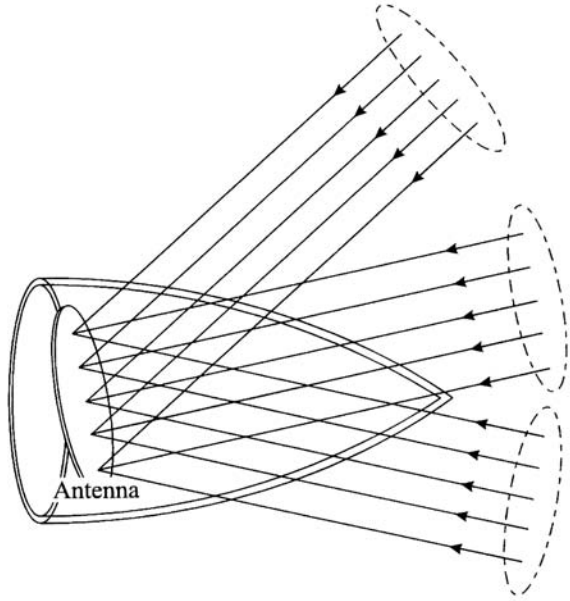

Figure 6.6 Illustration of a plane wave spectra (PWS) approach.

6.4.3 FDTD and Integral Equation Methods

A method for solving the differential form of Maxwell's equations is known as the finite-difference time-domain (FDTD) method. Maloney and Smith [34] present methodology to apply FDTD to model a radome. The method requires defining a grid over the radome and surrounding space and then applying boundary conditions. The technique can be computationally intensive compared to the ray trace methods discussed in this chapter.

For a radome that is large in terms of wavelengths, integral equation methods are also generally impractical because of the enormous computational requirements. However, applying the technique to a two dimensional geometry greatly reduces the computer run time. In [35] Sukharevsky et al. reported on the successful application of the technique to a large fineness ratio two-dimensional radome.

6.5 Sources of Computational Error

Ray trace computational errors have several causes, including:

- Antenna modeling;
- Statistical wall variations;

- Internal wave reflections;
- Rain erosion tip modeling;
- Radome wall modeling.

Table 6.1 gives an assessment of additional factors contributing to radome performance computational accuracy. The internal reflections illustrated in Figures 6.7 and 6.8 are a potentially significant source of computational error. In these figures, a GO receive mode ray trace uses the direct rays incident on the aperture from a specified direction. The insertion voltage transmission coefficients based on a flat panel theory for both the parallel and perpendicular polarizations are used to transform the plane wave fields associated with each ray from their values outside the radome to their values on the antenna aperture. A number of the most significant errors are discussed in the following sections.

6.5.1 Internal Reflections

Sidewall reflections illustrated in Figure 6.7(b) exist when part of the energy incident on a radome is reflected from portions of the wall into the antenna. For most radomes, it is safe to ignore rays that reflect off the radome wall more than once before striking the antenna because these multiple bounces produce insignificant energy. The mathematical modeling describing this error source is shown in Burk, Brand, and Graf [36].

Figure 6.8(a) illustrates antenna scattered energy. Notice that not all the energy striking an antenna is absorbed by the antenna, but depends on the

Table 6.1
Parameters That Influence Prediction Accuracy

Category	Uncertainties
Antenna modeling	Antenna aperture distribution Polarization detail Physical detail
Statistical variations	Thickness variation Dielectric uncertainty and inhomogeneity Loss tangent uncertainty
Internal reflections	Back wall reflections Bulkhead reflections Multiple bounce Flash lobe
Erosion tip modeling	Diffraction

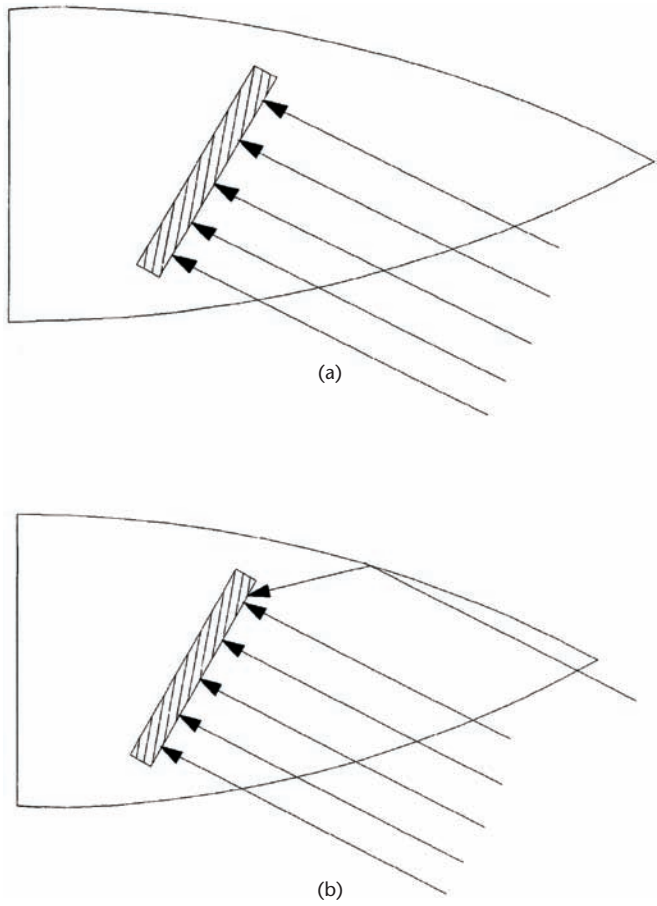

Figure 6.7 Internal ray reflections: (a) no reflections and (b) sidewall reflections.

antenna's aperture distribution. The inverse of the antenna's illumination function often provides an approximation to the energy reflected by the antenna aperture. The antenna scattered energy can bounce off the radome wall one or more times before striking the antenna. Again, rays that reflect off the radome wall more than once before striking the antenna are relatively small and can be ignored.

Many aircraft or missiles have a bulkhead plate between the radome and the vehicle body, as illustrated in Figure 6.8(b). If this bulkhead is not microwave-absorber treated, incoming rays can reflect off this surface and strike the backside of the antenna. The backlobe pattern of the antenna receives the bulkhead reflected energy causing boresight errors. Generally, bulkhead reflections will not have much effect until the angle of incidence of the incoming rays (with respect to the radome axis) becomes large. In actual applications, positioners and

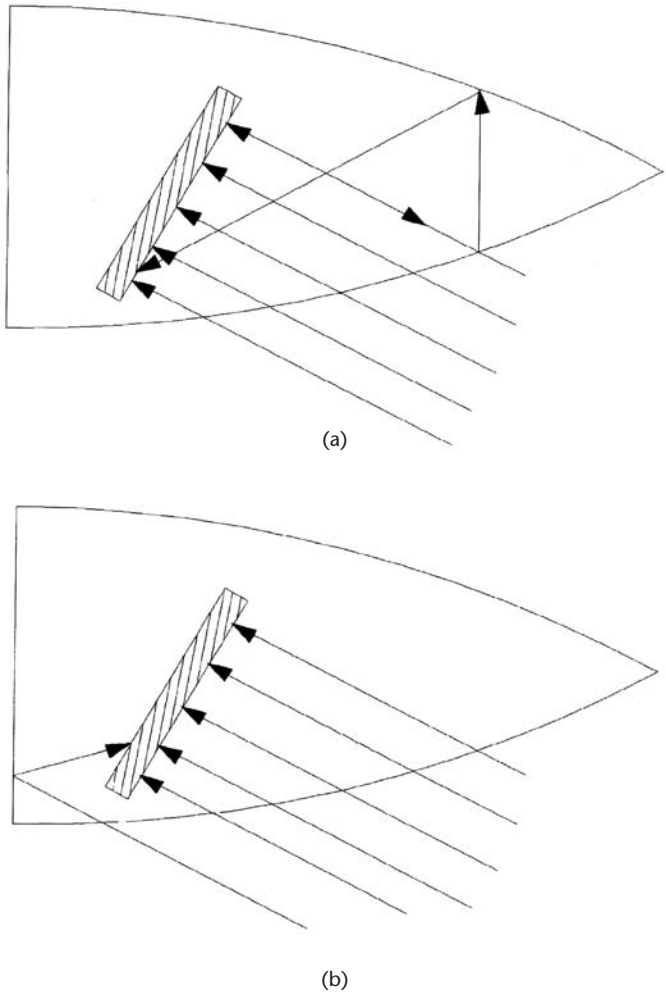

Figure 6.8 Internal ray reflections: (a) antenna scattered energy and (b) bulkhead reflections.

other electronic hardware may block some reflections from reaching the antenna.

To evaluate the typical contribution of each of the ray bounce error contributors, we studied an A-sandwich tangent ogive radome with a fineness ratio of 3. The antenna size was approximately 20 wavelengths at the operating frequency and the polarization was vertical. Using a GO receive mode prediction model, we compared the measured elevation plane boresight error (BSE) data to predicted data in Figure 6.9. For this particular radome, when ignoring all internal reflection error sources, there was reasonably good correlation between

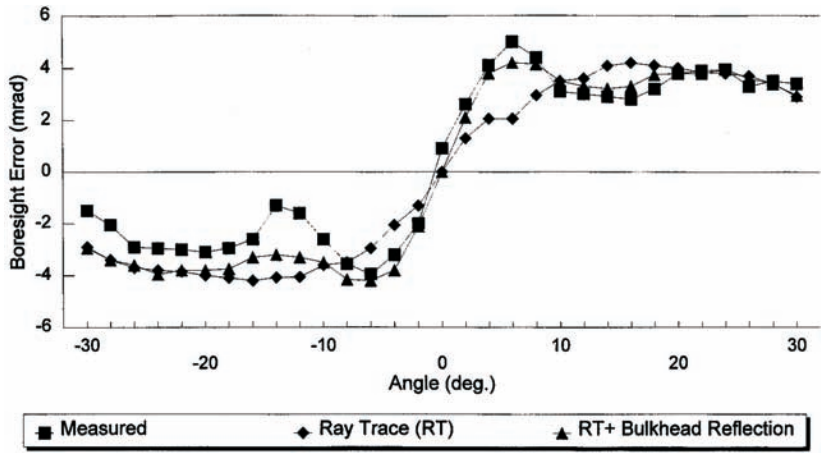

Figure 6.9 Measured and computed BSE of an A-sandwich tangent ogive radome and the effect of bulkhead reflections.

measured and predicted BSE data. The predominant internal reflection error source was found to be bulkhead reflections. The computed BSE data when including this error source is also shown in Figure 6.9.

6.5.2 Wall Model and Statistical Variations

Another source of computational error is the wall transmission model. In all current ray trace solutions, the radome walls are approximated as a local plane at the ray intercept point because most radome shapes are not separable coordinate surfaces, and differential equations cannot be used. The flat panel approximation is not valid for thick, highly curved walls. For spherical radomes, Bloom, Overfelt, and White [37] attempted to compensate the transmission coefficient to account for a wall curvature by the use of a divergence factor (DF). Kozakoff [38] derived a solution applicable to ogive radome shapes. Geometric optics was used to trace the fields from the reference plane through the radome wall to a receiving monopulse antenna, where the wall transmissions on each ray are collected. However, a DF derived from Snell's law for spherical shells accounted for the local wall curvature at each ray intercept point.

Most radome wall models assume that the dielectric and magnetic properties are homogeneous and isotropic with individual layers. This is not always true, and is another potential source of computational error and complication in the modeling. For instance, Kozakoff and Hensel [39] showed that the orientation of structural fibers in reinforced plastic radomes results in anisotropy of the electromagnetic medium that influences the modeling. To solve this type of problem, White and Banks [40] derived the wave equation into three

components to deal with a plane wave transmission and reflection from anisotropic materials. Guided waves were observed to propagate in radome walls by Tricoles [41] and are a potential source of computational error.

According to Ersoy and Ford [42], a radome performance degradation from the theoretical predictions also occurs from radome surface irregularities. Vorobyev [43] has applied statistical methods to manufacturing tolerances (on both the dielectric constant and the wall thickness) and related the manufacturing tolerances to the electrical performance of radomes.

References

[1] Torani, O., *Radomes, Advanced Design*, AGARD Advisory Report No. 53, Advisory Group for Aerospace Research and Development, North Atlantic Treaty Organization (NATO), Neuilly Sur Seine, France, 1953, pp. 111–112.

[2] Kaplun, V. A., "Nomographs for Determining the Parameters of Plane Dielectric Layers of Various Structure with Optimum Radio Characteristics," *Radiotechnika i Electronika* (USSR), Part 2, Vol. 20, No. 9, 1975, pp. 81–88.

[3] Zamyatin, V. I., A. S. Klyuchnikov, and V. I. Shvets, *Antenna Fairings*, Minsk, USSR: V. I. Lenin Belorussian Publishing House, 1980.

[4] Kaplun, V. A., and V. M. Zelenkevich, "Introduction to Computer-Aided Design of Microwave Antenna Radomes," *Radiotechnika i Electronika* (USSR), Vol. 42, No. 2, 1987, pp. 89–93.

[5] Mahan, A. I., C. V. Bitterli, and C. G. Wein, "Far Field Diffraction and Boresight Error Properties of a Two Dimensional Wedge," *Journal of the Optical Society of America*, Vol. 49, No. 6, June 1959, pp. 535–566.

[6] Tricoles, G., "Radiation Patterns and Boresight Error of a Microwave Antenna Enclosed in an Axially Symmetric Dielectric Shell," *Journal of the Optical Society of America*, Vol. 54, No. 9, September 1964, pp. 1094–1101.

[7] Tricoles, G., "Radiation Patterns of a Microwave Antenna Enclosed in a Hollow Dielectric Wedge," *Journal of the Optical Society of America*, Vol. 53, No. 5, May 1963, pp. 545–557.

[8] Milligan, T. A., *Modern Antenna Design*, New York: McGraw-Hill, 1985, pp. 215–216.

[9] Kraus, J. D., *Antennas*, 2nd ed., New York: McGraw-Hill, 1988, pp. 174–189.

[10] Kilcoyne, N. R., "An Approximate Calculation of Radome Boresight Error," *Proceedings of the USAF/Georgia Institute of Technology Symposium on Electromagnetic Windows*, Georgia Institute of Technology, Atlanta, GA, June 1968, pp. 91–111.

[11] Bagby, J., "Desktop Computer Aided Design of Aircraft Radomes," *IEEE MIDCON 88 Conference Record*, Western Periodicals Company, North Hollywood, CA, 1988, pp. 258–261.

[12] Hayward, R. A., E. L. Rope, and G. Tricoles, "Accuracy of Two Methods for Numerical Analysis of Radome Electromagnetic Effects," *Proceedings of the 14th Symposium on Electromagnetic Windows*, Georgia Institute of Technology, Atlanta, GA, 1978, pp. 53–57.

[13] Hayward, R. A., E. L. Rope, and G. Tricoles, "Accuracy of Two Methods for Numerical Analysis of Radome Electromagnetic Effects," *IEEE International Symposium Digest on Antennas and Propagation*, Seattle, WA, June 1979, pp. 598–601.

[14] Raz, S., et al., "Numerical Analysis of Antenna Radome Systems," *Proceedings of the 10th IEEE Convention*, Tel Aviv, Israel, October 1977.

[15] Israel, M., et al., "A Reference Plane Method for Antenna Radome Analysis," *Proceedings of the 15th Symposium on Electromagnetic Windows*, Georgia Institute of Technology, Atlanta, GA, 1980, pp. 34–39.

[16] Tricoles, G., E. L. Rope, and R. A. Hayward, "Analysis of Radomes by the Method of Moments Method," *Proceedings of the 17th Symposium on Electromagnetic Windows*, Georgia Institute of Technology, Atlanta, GA, 1984, pp. 1–8.

[17] Wu, D. C. F., and R. C. Rudduck, "Plane Wave Spectrum Surface Integration Technique for Radome Analysis," *IEEE Transactions on Antennas and Propagation*, AP-22, No.3, May 1974, pp. 497–500.

[18] Joy, E. B., and G. K. Huddleston, *Radome Effects on Ground Mapping Radar*, Final Report on Contract DAAH01-72-C-0598, SF-778 203/0, U.S. Army Missile Command, Huntsville, AL, May 1973.

[19] Huddleston, G. K., H. L. Bassett, and J. M. Newton, *Parametric Investigation of Radome Analysis Methods; Computer Aided Radome Analysis Using Geometric Optics and Lorentz Reciprocity*, Final Report on Contract AFOSR-77-3469, Volumes 1-3, Georgia Institute of Technology, Atlanta, GA, 1981.

[20] Joy, E. B., et al., "Comparison of Radome Electrical Analysis Techniques," *Proceedings of the 15th Symposium on Electromagnetic Windows*, Georgia Institute of Technology, Atlanta, GA, 1980, pp. 29–33.

[21] Tavis, M., *A Three-Dimensional Ray Tracing Method for Calculation of Radome Boresight Error and Antenna Pattern Distortion*, Aerospace Corporation Report, TOR-0059(56860), AD 729811, 1971.

[22] Einziger, P. D., and L. B. Felson, "Ray Analysis of Two-Dimensional Radomes," *IEEE Transactions on Antennas and Propagation*, Vol. AP-31, No. 6, 1983, pp. 870–884.

[23] Deschamps, G. A., "Ray Techniques in Electromagnetics," *Proceedings of the IEEE*, Vol. 60, No. 9, September 1972, pp. 1021–1035.

[24] Mahan, A. I., and L. P. Bone, "Far Field Diffraction and Polarization Properties of a Three Dimensional Hollow, Homogeneous, Isotropic Cone," *Journal of the Optical Society of America*, Vol. 53, No. 5, May 1963, pp. 533–544.

[25] Hayward, R. A., and G. P. Tricoles, "Radome Boresight Error: Numerical Prediction and Physical Interpretation," *IEEE Antennas and Propagation Society (AP-S) Digest*, IEEE Catalog No. 75CH0963-9AP, June 1975, pp. 61–63.

[26] Einziger, P. D., and L. B. Felsen, "Rigorous Asymptotic Analysis of Transmission Through a Curved Dielectric Slab," *IEEE Transactions on Antennas and Propagation*, Vol. AP-31, No. 6, November 1983, pp. 863–869.

[27] Richmond, J. H., "Scattering by Dielectric Cylinders of Arbitrary Cross Sectional Shapes," *IEEE Transactions on Antennas and Propagation*, Vol. AP-13, 1965, pp. 334–341.

[28] Richmond, J. H., *The Calculation of Radome Diffraction Patterns*, Ohio State University, Department of Electrical Engineering Report 1180-13, AD-423660 September 1966.

[29] Richmond, J. H., "TE Wave Scattering by a Dielectric Cylinder of Arbitrary Cross Sectional Shape," *IEEE Transactions on Antennas and Propagation*, Vol. AP-14, 1966, pp. 460–464.

[30] Tricoles, G., E. L. Rope, and R. A. Hayward, *Wave Propagation Through Axially Symmetric Missile Radomes*, Final Report No. R-81-125 on Contract N00019-79-C-0638, AD-A106762/8, 1981.

[31] Shifflett, J. A., CADDRA: A Physical Optics Radar Radome Analysis Code for Arbitrary 3D Geometries," *IEEE Antennas and Propagation Magazine*, Vol. 39, No. 6, 1977, pp. 73–79.

[32] Paris, D. T., "Computer Aided Radome Analysis," *IEEE Transactions on Antennas and Propagation*, Vol. AP-18, No. 1, January 1970, pp. 7–15.

[33] Abdel Moneum, M. A., et al., "Hybrid PO-MOM Analysis of Large Axi-Symmetric Radomes," *IEEE Transactions on Antennas and Propagation*, Vol. 49, No. 12, 2001, pp. 1657–1660.

[34] Maloney, J. G., and G. S. Smith, "Modeling of Antennas," in *Advances in Computational Electrodynamics*, A. Taflove, (ed.), Norwood, MA: Artech House, 1998, pp. 453–456.

[35] Sukharevsky, O. I., S. V. Kukobko, and A. Z. Sazonov, "Volume Integral Equation Analysis of a Two Dimensional Radome with a Sharp Nose," *IEEE Transactions and Propagation*, Vol. 53, No. 4, 2005, pp. 1500–1506.

[36] Ersoy, L., and D. Ford, "RF Performance Degradation Due to Random Radome Surface Irregularities," *AP-S International Symposium Digest, IEEE Antennas and Propagation Society*, 1986, pp. 875–878.

[37] Burks, D. G., J. Brand, and E.R. Graf, "The Equivalent Source Concept Applied to the Analysis of Radome Performance," *Proceedings of Southeastcon '78, Region 3 Conference*, Auburn University, Auburn, AL, April 1978.

[38] Bloom, D. A., P. L. Overfelt, and D. J. White, "Comparison of Spherical Wave Ray Tracing and Exact Boundary Value Solutions for Spherical Radomes," *Proceedings of the 17th Symposium of Electromagnetic Windows*, Georgia Institute of Technology, Atlanta, GA, July 1984.

[39] Kozakoff, D. J., "Geometric Optics Radome Analysis Wall Solution Incorporating the Effects of Wall Curvature," *Proceedings of OE LASE '94 International Symposium*, SPIE, Los Angeles, CA, January 1994.

[40] Kozakoff, D. J., and J. Hensel, "Materials Implications of Millimeter Wave Radome Performance," *Proceedings of the IEEE International Conference on Infrared (IR) and Millimeter Waves*, Miami, FL, December 1981.

[41] Vorobyev, E. A., "Certain Production Criteria for Large Scale Monolithic Antenna Radomes," *Izvestiya vuz Radioteknika* (USSR), Vol. 9, No. 3, 1966, pp. 359–362.

[42] White, D. J., and D. J. Banks, "Plane Wave Transmission and Reflection Coefficients for Anisotropic Sheets of Radome Materials," *Proceedings of the 16th Symposium on Electromagnetic Windows*, Georgia Institute of Technology, Atlanta, GA, June 1982.

[43] Tricoles, G., and E. L. Rope, "Scattering of Microwaves by Dielectric Slabs and Hollow Dielectric Wedges," *Journal of the Optical Society of America*, Vol. 55, No. 11, November 1965, pp. 1479–1498.

Part III
Computer Implementation

7

Ray Trace Approaches

Part III of this book deals with the practical issues of how to apply the ray trace concepts in order to solve actual radome-enclosed antenna problems on a PC.

This chapter will lay the groundwork in ray trace modeling issues that are fundamental to all computerized ray trace techniques. Specifically, you will learn how to apply ray trace modeling to do the following:

- Mathematically model both tangent ogive and other axial symmetric radome shapes;
- Understand the vector concepts utilized in tracing a ray from an arbitrary point on the antenna aperture to find its intercept point with the radome wall;
- Find the unit surface normal vector at the ray intercept point on the radome's surface;
- Determine the angle of incidence with the ray relative to the surface normal vector at the intercept point;
- Learn how to decompose an electromagnetic wave in parallel and perpendicular wave components at the ray intercept in order to properly apply the proper radome wall to parallel or perpendicular transmission coefficients;
- Understand how to recompose the parallel and perpendicular wave components after they propagate through the radome wall.

The organization of this chapter systematically leads you through these issues. Section 7.1 discusses the significance of the radome shape and fineness

ratio on performance with a particular emphasis on the tangent ogive shape. Methods are discussed in order to find the intercept point of an arbitrary ray and the radome wall, the surface normal vector at the intercept point, and the angle of incidence, which is defined as the angle between the propagation vector and the surface normal vector at the intercept point. Section 7.2 discusses hemispherical radome shapes as a subset of the generic tangent ogive shape. Section 7.3 considers any arbitrary radome shape that is rotationally symmetric about the vehicle flight axis. Formulas are derived to find the intercept point of an arbitrary ray and the radome wall, the surface normal vector at the intercept point, and the angle of incidence. Lastly, the computer subroutine listings in the chapter appendices illustrate the techniques and include:

- Program OGIVE (Appendix 7A), which demonstrates the ray trace of an arbitrary vector in a tangent ogive radome in order to compute the intercept point, the surface normal, and the angle of incidence of the propagation vector relative to the surface normal vector;
- Program POLY (Appendix 7B), which is a polynomial regression routine useful for modeling an arbitrary shaped radome having axial symmetry;
- Subroutine ARBITRARY (Appendix 7C), which demonstrates the ray trace of an arbitrary vector in an arbitrary shaped (axially symmetric) radome in order to compute the intercept point, the surface normal, and the angle of incidence of the propagation vector relative to the surface normal vector;
- Subroutine COMPOSE (Appendix 7D), which demonstrates the decomposition of an arbitrary polarized EM ray into components parallel and perpendicular with respect to the plane of incidence, applying the parallel and perpendicular transmission coefficients as the wave propagates through the radome wall and then recombining the components on the emergent side of the wall into an emergent wave.

7.1 Shape Considerations

7.1.1 Rationale for Choosing a Particular Shape

Common radome shapes include, but are not limited to the following:

- Hemisphere;
- Secant ogive;
- Tangent ogive;

- Von Karman;
- Power series.

For all radome shapes discussed in this section, the outside base diameter D_o and length L_o define the fineness ratio, according to the formula

$$F = \frac{L_o}{D_o} \tag{7.1}$$

According to Groutage [1], aerodynamic considerations play a major role in radome design, especially in selecting both shape and materials. Shape determines aerodynamic drag, whereas material choice determines the structural response to aerodynamic heating, dynamic pressures, and rain erosion. The decision to reduce drag generally determines the exact shape of the radome. Unfortunately, the most desirable shapes to reduce drag are not the best from the viewpoint of electrical performance. Chin [2] has provided an excellent overview of radome shapes with complete mathematical descriptions of each.

Weckesser [3] published a comparison of various radome shapes as shown in Figure 7.1, where the radome is assumed to have a fineness ratio of 2.5. The conical and tangent ogive shapes contain the minimum and maximum volumes, respectively. Figure 7.2 illustrates the aerodynamic drag, showing the approximate drag coefficient for the four shapes. The tangent ogive shape has the worst drag, while the secant ogive shape has the best drag.

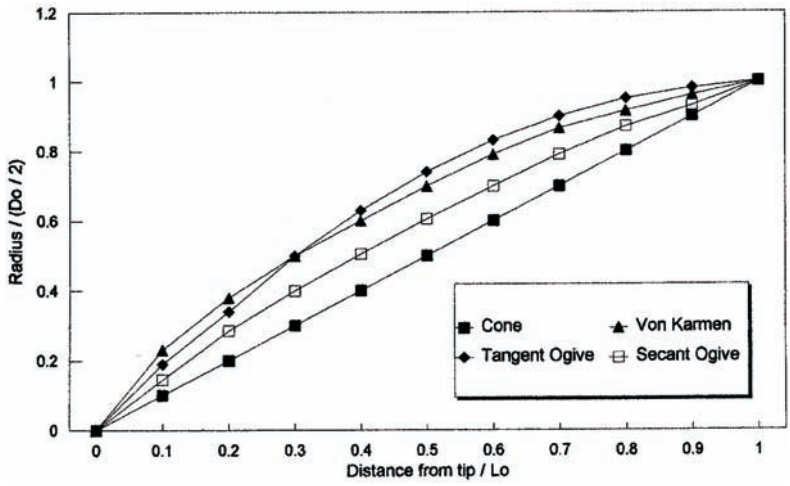

Figure 7.1 A comparison of some common radome shapes [3].

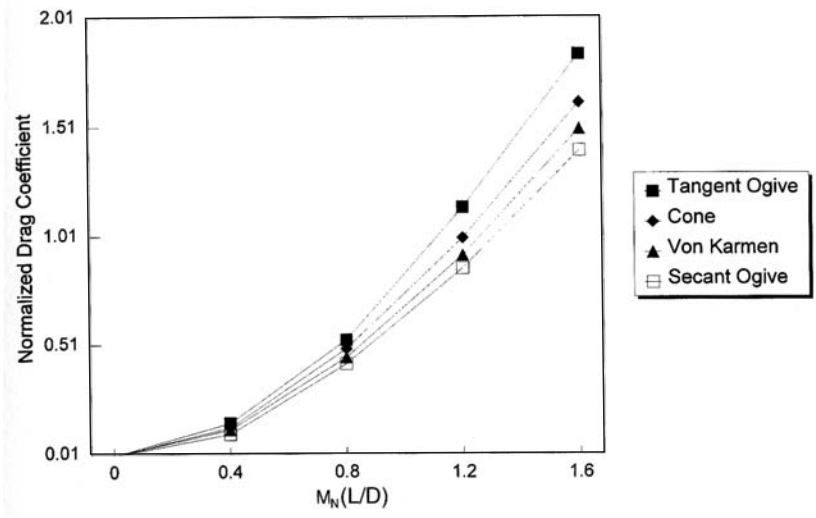

Figure 7.2 Wave drag of common radome shapes (M_N is the Mach number).

Yost, Weckesser, and Mallalieu [4] pointed out that the fineness ratio has a much greater and a pronounced effect on the drag coefficient than shape. For instance, these authors cite a particular missile for which a 28% increase in the fineness ratio decreased the drag coefficient by 35% at Mach 3. The reduction in drag coefficient due to a potential change in shape while keeping the same fineness ratio was very small.

An analytical study by Crowe [5] indicated that, for fineness ratios of less than 2.25, the secant ogive radome causes less BSE than either the Von Karman, the tangent ogive, or the power series radome of the same fineness ratio. However, for larger fineness ratios, the tangent ogive shape is best.

For radome modeling, in this book we have selected the tangent ogive as the most versatile radome shape to approximate most radome geometries in use for the following reasons:

- Representative of many common radomes, ranging from a hemisphere (fineness ratio = 0.5) to very streamlined radomes (fineness ratios >3);
- Relatively easy mathematical modeling;
- Mathematical principles that can be transferred to other radome shapes.

The electrical performance of a radome, in general, degrades very rapidly as the maximum angle of incidence exceeds about 75°. For a tangent ogive shape, Figure 7.3 illustrates the relationship between the maximum incidence angle for an on-axis target and the fineness ratio of the radome. (An on-axis

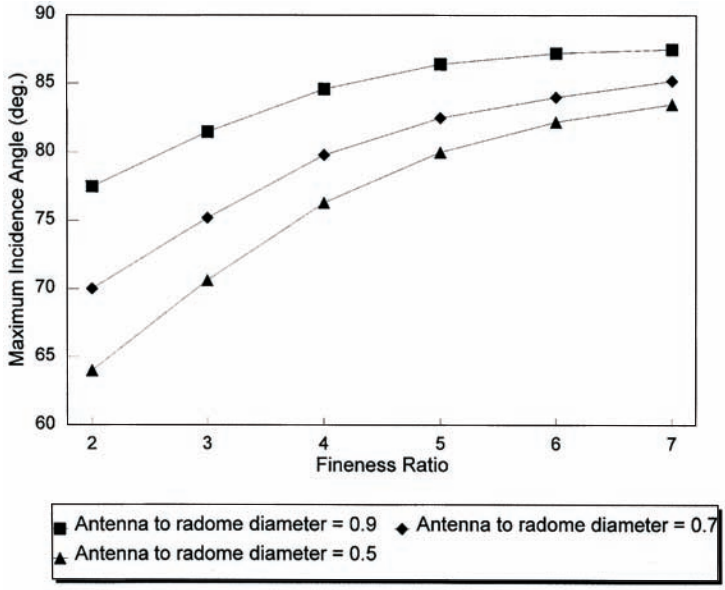

Figure 7.3 Maximum incidence angles for an on-axis antenna pointing in a tangent ogive shape.

target produces the worst-case incidence angles.) From this plot, it is clear that the maximum incidence angle can only be reduced by a decrease in the fineness ratio. From an electrical viewpoint, a hemisphere is most desirable because of its very small incidence angles resulting in small electrical degradations.

Tangent ogive geometries with high fineness ratios are typical of the shapes used for aircraft radomes shown in Figure 7.4 and missile radomes shown in Figure 7.5.

7.1.2 Mathematical Modeling of the Tangent Ogive Shape

Figure 7.6 defines the key parameters needed to mathematically describe a tangent ogive radome shape. Any point on the outside surface must satisfy the following equation:

$$\left(r_p + B\right)^2 + x^2 = R^2 \tag{7.2}$$

where this equation applies for fineness ratios of 0.5 or larger, and

$$R^2 = L_o^2 + B^2 \tag{7.3}$$

Figure 7.4 High fineness ratio tangent ogive radome used in a modern high-speed aircraft. (Photo courtesy of USDigiComm Corporation.)

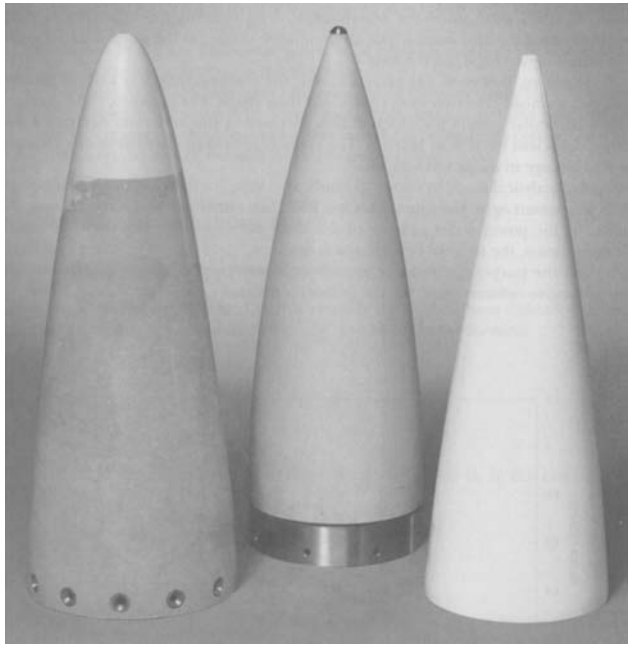

Figure 7.5 Experimental tangent ogive missile radomes. (Photo courtesy of USAF Wright Laboratory Armorment Division.)

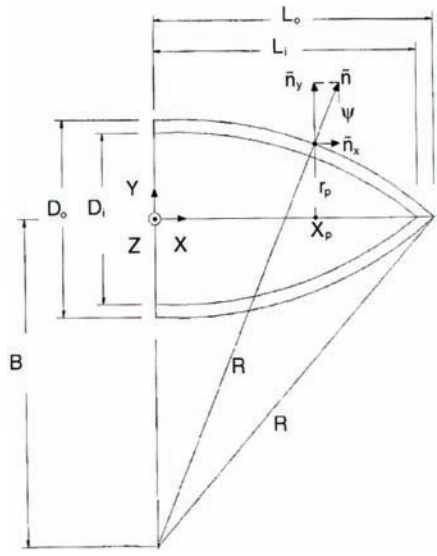

Figure 7.6 Mathematical description of a tangent ogive radome geometry.

$$\frac{D_o}{2} = R - B \tag{7.4}$$

By the simultaneous solution of these two equations, we obtain expressions for the two unknowns in terms of the radome length and diameter, respectively:

$$B = \frac{4L_o^2 - D_o^2}{4D_o} \tag{7.5}$$

$$R = \frac{4L_o^2 - D_o^2}{4D_o} \tag{7.6}$$

Since in the development here in the *x*-axis corresponds to the radome axis, the radome shape is a surface of revolution formed by revolving a tangent ogive shape about the *x*-axis. The cross sections through this three-dimensional shape are circular in the *y*-*z* plane with the radome radius given by the formula:

$$r_p = \sqrt{z_p^2 + y_p^2} \tag{7.7}$$

7.1.3 Determining the Intercept Point of a Ray with the Tangent Ogive Wall

All ray trace analysis methods require the determination of the point of intercept of a ray and the radome surface [6]. Some radome shapes such as the cone lend themselves to an exact solution of the intercept point. Other shapes such as the Von Karman do not [7]. This section discusses three methods of determining the intercept point.

7.1.3.1 Method 1

Huddleston and Baluis [8] introduced a method for finding the intercept point that can apply to the tangent ogive radome geometry. Using this method, the outer radome shape can be represented by samples spaced equally along the radome axis. Any two sample points are sufficient to define a cone with the vertex beyond the tip and opening toward the radome base. Between the sample points, the intersection of an incident ray and the cone approximates the point of intersection with the actual surface. The intersection point is then refined, using additional sample points and a perturbational technique.

7.1.3.2 Method 2

Joy and Ball [9] also reported the development of a ray intercept technique. They specified the radome surface as cylindrical radius values for constant station (z-position) values. This method of radome shape specification is typical of radome shape data available to the radome analyst.

The technique is an interactive algorithm that locally approximates the radome surface as a cone that is tangent to the radome surface at the point of the ray intercept point. Using the interactive algorithm, the analyst can iteratively vary the fineness ratio and the location of the cone axis so that the intersection point of the ray and the cone equals the intersection point of the ray and the radome surface. Convergence is always possible for monotonically concave radome shapes.

7.1.3.3 Method 3

This method of determining the intercept point is, like Method 2, an iterative method. However, it is more general than the two previously discussed methods and is particularly well suited to computer use. It is very practical particularly because of the greatly increased speed of PCs that has occurred since the first edition of this book. This technique uses a generalized ray tracing method for tangent ogive shapes that are treated as surfaces of revolution formed by revolving a single-valued plane curve about the radome axis.

Referring to Figure 7.7, the problem starts with definition of a vector originating at a point $P(x_o, y_o, z_o)$ within the radome and having a propagation

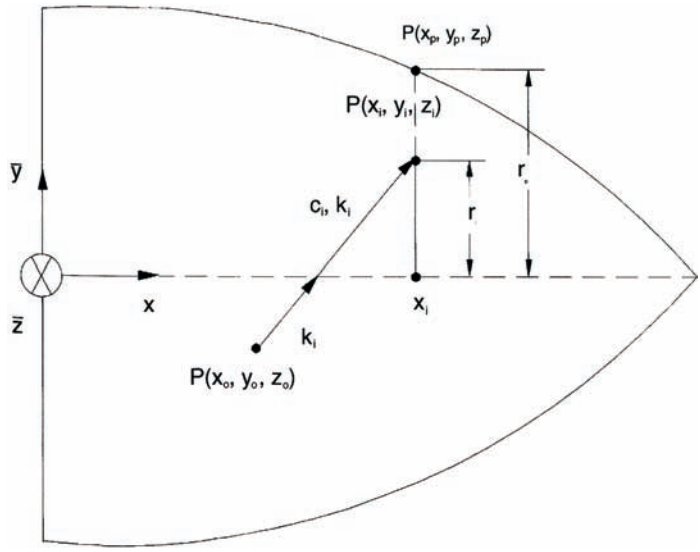

Figure 7.7 Illustration of propagation vector when it is inside a radome.

direction $\bar{k}$. The unit propagation vector emanating from the origin in the azimuth (AZ) and elevation (EL) directions is given by

$$\bar{k} = (\cos EL \cos AZ)\bar{x} - (\sin AZ)\bar{y} - (\sin EL \cos AZ)\bar{z} \tag{7.8}$$

$$\bar{k} = k_x \bar{x} + k_y \bar{y} + k_z \bar{z} \tag{7.9}$$

In which

AZ = azimuth direction and is the same as angle ϕ as used in a standard spherical coordinate system;

EL = elevation direction = $90 - \theta$ where θ was used in a standard spherical coordinate system.

Note that AZ = 0 and EL = 0 correspond to propagation in the $+x$-direction.

Using this definition for the various components of the propagation vector, the coordinates corresponding to the tip of the vector can be expressed as a parametric equation via [10]

$$x_i = x_0 + C_i k_x \tag{7.10}$$

$$y_i = y_0 + C_i k_y \tag{7.11}$$

$$z_i = z_0 + C_i k_z \tag{7.12}$$

where k_x, k_y, k_z are the direction cosines of the line and C_i is a constant. Specifically, there is a unique value of C_i at the intercept point of interest. The point $P(x_o, y_o, z_o)$ is arbitrary in this example, but in actual radome analysis it will correspond to a point on the antenna aperture surface.

As we iteratively vary C_i, we iteratively vary the vector length; we should think of the vector as a ray. The procedure for finding the intersection of this ray with the radome surface consists of varying the parameter C_i until the vector intercepts the radome wall. At the intercept point shown in Figure 7.8, the coordinates of the tip of the vector will correspond to a point on the radome surface. Note that this parameter will fall in the range $0 < C_i < L_o$ where L_o is the radome length.

The process is aided by definition of an error function ERF, which is the distance between this vector and the radome wall:

$$ERF = r_p - r_i = \left(\sqrt{R^2 - x_i^2} - B\right) - \sqrt{z_i^2 + y_i^2} \tag{7.13}$$

Clearly, the value of ERF is positive when the tip of the vector is within the radome, is zero when the tip of the vector strikes the radome wall, and is negative when the tip of the vector is external to the radome wall as seen in Figure 7.9. Figure 7.10 is a flow diagram showing one of the simplest rootfinder

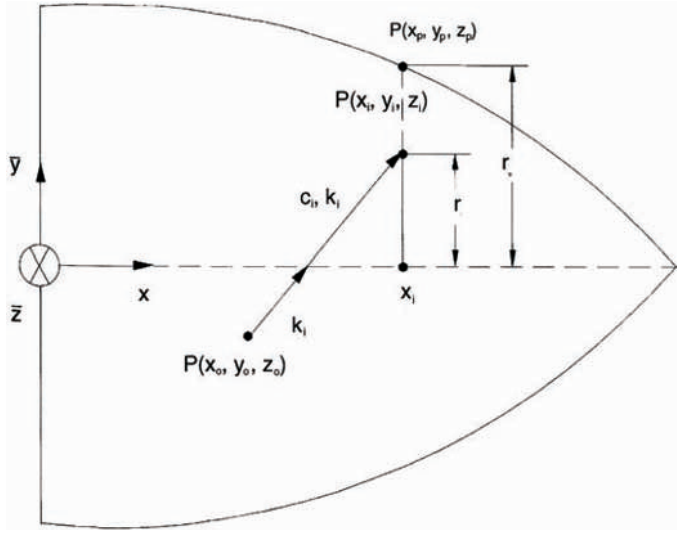

Figure 7.8 Illustration of propagation vector when it intercepts a radome wall.

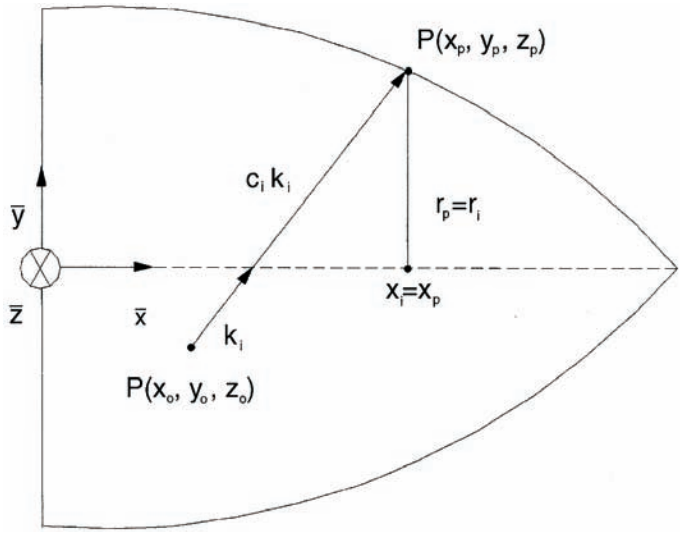

Figure 7.9 Illustration of propagation vector when it is outside the radome.

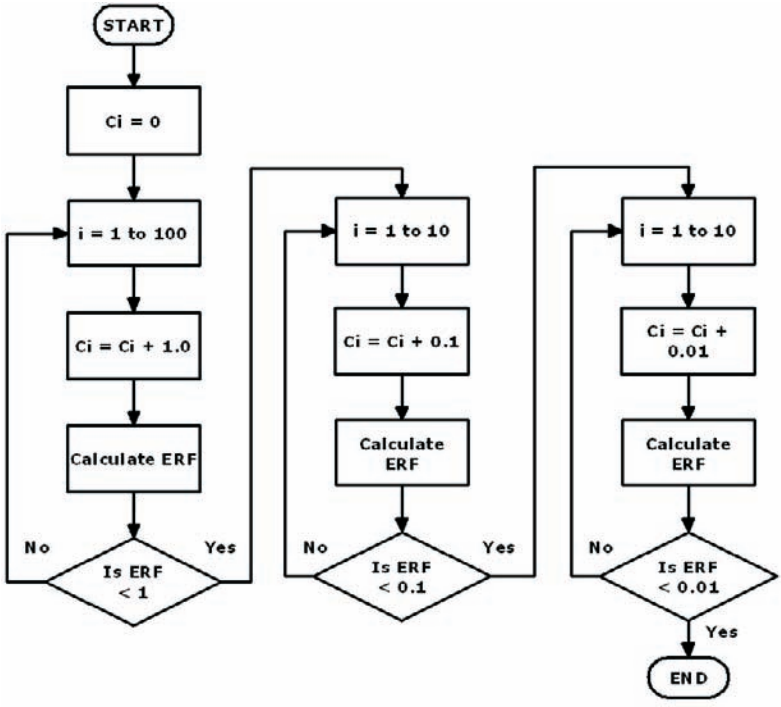

Figure 7.10 Computer software flow diagram for the program OGIVE rootfinder algorithm.

methods. The approach first increments coarse, then medium, and then fine increments in the C_i values until detecting the zero crossing of ERF to within the finest increment of C_i. In the flow diagram shown, these increments correspond to 1.0 inch, 0.1 inch, and 0.01 inch, respectively. Note that the first iteration cycle ($i = 1$ to 100) assumes that the maximum radome size is 100 inches. If your radome is larger, adjust this parameter accordingly.

Appendix 7A is a sample computer program listing that shows this particular rootfinder. This program incorporates a subroutine that models the tangent ogive radome shape discussed earlier in this chapter. The development works for tangent ogive radomes having a hemispherical shape, $L_o/D_o = 0.5$, or higher fineness ratios. Typically, this program takes from 10 to 25 cycles to find the intercept point to within an accuracy of 0.01 inch.

7.1.4 Computation of Surface Normal Vector at the Intercept Point

For any point $P(x_o, y_o, z_o)$ on the tangent ogive contour, the slope of the curve is found from:

$$m = \frac{-x_o}{r_p + B} = \frac{-x_o}{\sqrt{y_o^2 + z_o^2} + B} \tag{7.14}$$

Referring back to Figure 7.6, the slope of the normal vector is then found from

$$\tan(\psi) = \frac{-1}{m} = \frac{r_o + B}{x_o} = \frac{\sqrt{y_o^2 + z_o^2} + B}{x_o} \tag{7.15}$$

From this, the x-component of the surface normal vector is:

$$n_x = \cos\psi = \frac{1}{\sqrt{1 + \left(\dfrac{r_o + B}{x_o}\right)^2}} = \frac{1}{\sqrt{1 + \left(\dfrac{\sqrt{y_o^2 + z_o^2} + B}{x_o}\right)^2}} \tag{7.16}$$

The y- and z-components of the normal vector depicted in Figure 7.11 are

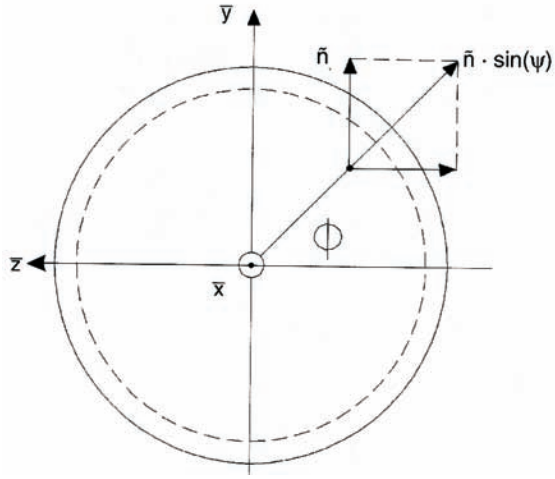

Figure 7.11 Components of the surface normal vector in the *y-z* plane.

$$n_y = \sin\psi \sin\phi = \frac{\left(\frac{r_o + B}{x_o}\right)}{\sqrt{1+\left(\frac{r_o + B}{x_o}\right)^2}} \frac{y_o}{r_o} \tag{7.17}$$

$$n_y = \frac{\left(\frac{\sqrt{y_o^2 + z_o^2} + B}{x_o}\right)}{\sqrt{1+\left(\frac{\sqrt{y_o^2 + z_o^2} + B}{x_o}\right)^2}} \frac{y_o}{\sqrt{z_o^2 + y_o^2}} \tag{7.18}$$

$$n_z = \sin\psi \cos\phi = \frac{\left(\frac{r_o + B}{x_o}\right)}{\sqrt{1+\left(\frac{r_o + B}{x_o}\right)^2}} \frac{z_o}{r_o} \tag{7.19}$$

$$n_z = \frac{\left(\frac{\sqrt{y_o^2 + z_o^2} + B}{x_o}\right)}{\sqrt{1 + \left(\frac{\sqrt{y_o^2 + z_o^2} + B}{x_o}\right)^2}} \frac{z_o}{\sqrt{z_o^2 + y_o^2}} \tag{7.20}$$

7.1.5 Determining the Ray Angle of Incidence

The transmission of a ray through the radome wall was shown earlier to be a function of the angle of incidence of the propagation vector relative to the surface normal at the intercept point, θ. This can be evaluated from simple vector relationships:

$$\cos\theta = \bar{k} \cdot \bar{n} = k_x n_x + k_y n_y + k_z n_z \tag{7.21}$$

$$\theta = \cos^{-1}\left(k_x n_x + k_y n_y + k_z + n_z\right) \tag{7.22}$$

Since most mathematical PC software does not have an inverse cosine function, this can be put into the alternate form

$$\theta = \sin^{-1}\sqrt{1 - \left(k_x n_x + k_y n_y + k_z n_z\right)^2} \tag{7.23}$$

7.2 Hemispherical Radome Shapes

The ideal radome shape is a spherically shaped radome enclosing a gimbaled antenna. It is ideal for three reasons: (1) the angle of incidence of any ray emanating from the enclosed antenna and propagating through the radome wall is relatively small and generally less than 40° permitting low loss wall designs, (2) because of the symmetry, the angles of incidence do not change with the pointing angle of the antenna and there are only very small changes in radome transmission loss with the pointing angle of the antenna, and (3) there is no boresight error (BSE) for any antenna pointing angles through the radome wall.

Spherical- or hemispherical-shaped radomes are particularly suited to terrestrial radar applications depicted in Figure 7.12 or other microwave applications as depicted in Figure 7.13. They are not suited to airborne or missile applications because of the very large aerodynamic drag. It can be shown that the hemisphere is a special case of the tangent ogive shape, but with a fineness ratio (ratio of length to base diameter) of 0.5.

Figure 7.12 Large terrestrial radar antenna in a hemispherical radome. (Photo courtesy of MFG Galileo.)

Figure 7.13 Small microwave antenna in a hemispherical radome. (Photo courtesy of MFG Galileo.)

7.3 Other Radome Shapes Having Axial Symmetry

7.3.1 Mathematical Modeling of the Radome Shape

This section discusses radomes whose shape is rotationally symmetric but not easily described mathematically in a closed form solution such as the tangent ogive radome shape. If the radius (r_p) is known as a function of distance from the radome base (x_p), then the data can be fitted to a polynomial equation using the least squares method. For instance, consider modeling the shape with a fifth-order polynomial:

$$r_p = A_o + A_1 x_p + A_2 x_p^2 + A_3 x_p^3 + A_4 x_p^4 + A_5 x_p^5 \tag{7.24}$$

The coefficients of this expression can be evaluated with a polynomial regression such as that shown in Appendix 7B by manually inputting as many data sets of r_p and x_p as practical: the computer program computes the values of each of the coefficients. The software code solves this system of equations and computes the unknown coefficients. The next section describes the procedure for using this program.

7.3.2 POLY Polynomial Regression Subroutine

This software listing in Appendix 7B is in POWERBASIC [11]. Before running the program, have a table with the $\{z_p, r_p\}$ data sets that describe the radome. The program will do the least squares fit regression analysis to insure the approximation is as close as possible over the entire range of the data. The number of data points that should be entered to get a good approximation is something of a trial-and-error process. Too few points may be insufficient for an accurate approximation, whereas too many are tedious to enter and will not significantly improve the data.

To run the program, perform the following steps:

1. Enter first the z_p, and next the r_p values for the first data pair, as you are prompted. When entering values, you may edit them with the backspace key before you press [Return]. You can abort execution at any point by pressing [Ctrl-Break].
2. Enter the rest of the data sets as the program prompts you.
3. Type "E" to exit the data entry screen after you have entered the final pair.
4. Wait for the program to run the regression analysis, ending by the display of the coefficients, A_0 through A_5, that provide the best least squares approximation to your data.

5. Enter a value of z_p when prompted, to test this approximation by allowing you to see what value of r_p results.
6. Enter Q (for quit). The program will ask if you want to try the regression analysis again with a different set of input data. Enter Y (yes) or N (no) as required.

7.3.3 Determining Intercept Point and Surface Normal Vectors

Once the coefficients are evaluated, we can find a ray intercept point and surface normal vector for a tangent ogive radome via the previously developed Method 3 of Section 7.2. Specifically, the error function ERF needed to be used to find the intercept point must be expressed in terms of these polynomial coefficients and is given by the formula:

$$ERF = r_p - r_i = \left(A_0 + A_1 x_i + A_2 x_i^2 + A_3 x_i^3 + A_4 x_i^4 + A_5 x_i^5\right) - \sqrt{y_i^2 + z_i^2} \tag{7.25}$$

To find the intercept of a propagation vector emanating from the point $P(x_o, y_o, z_o)$ and the radome wall, we need to vary the parameter C_i in (7.10), (7.12), and (7.13) adaptively until the error function ERF is zero. Once the intercept point is determined, the slope of the radome shape at the intercept point is found from

$$m = A_1 + 2A_2 x_i + 3A_3 x_i^2 + 4A_4 x_i^3 + 5A_5 x_i^4 \tag{7.26}$$

The slope of the unit normal vector is

$$\tan\psi = \frac{-1}{m} = \frac{-1}{A_1 + 2A_2 x_i + 3A_3 x_i^2 + 4A_4 x_i^3 + 5A_5 x_i^4} \tag{7.27}$$

We can resolve the three components of the normal vector following (7.16) through (7.19) and can compute the angle of incidence of an arbitrary ray and its intercept at the radome wall via (7.21).

Appendix 7C is a sample computer program listing that applies a simple rootfinder to the arbitrary shape as discussed in this section. Typically, this program takes from 10 to 25 cycles to find the intercept point to within an accuracy of 0.01 inch.

7.4 Wave Decomposition at the Intercept Point

The flat-plate voltage transmission coefficients of the radome wall must weight the incident electric field associated with each ray. The problem geometry is illustrated in Figure 7.14, which shows an arbitrarily polarized wave E^i incident on a dielectric wall at angle θ with respect to the unit surface normal at the intercept point. The assumptions are that: (1) the wave is a plane wave consistent with ray tracing, and (2) the wall will be treated as locally plane at the ray intercept point.

To apply transmission coefficients to the wave as it propagates through the wall, we must first resolve the arbitrarily polarized incident wave into components parallel and perpendicular to the plane of incidence.

Decomposition of the incident electric field into two orthogonal vector components follows from vector mathematics. First, it is necessary to determine unit vectors perpendicular and parallel to the plane formed by the surface normal vector, $\bar{n}$, and the direction of propagation vector, $\bar{k}$. The perpendicular vector is given by [12, 13]:

$$\begin{aligned}\bar{D} &= \bar{n} \times \bar{k} \\ &= \frac{\left(n_y k_z - n_z k_y\right)\bar{x} + \left(n_z k_x - n_x k_z\right)\bar{y} + \left(n_x k_y - n_y k_x\right)\bar{z}}{\sqrt{\left(n_y k_z - n_z k_y\right)^2 + \left(n_z k_x - n_x k_z\right)^2 + \left(n_z k_y - n_y k_x\right)^2}}\end{aligned} \tag{7.28}$$

or

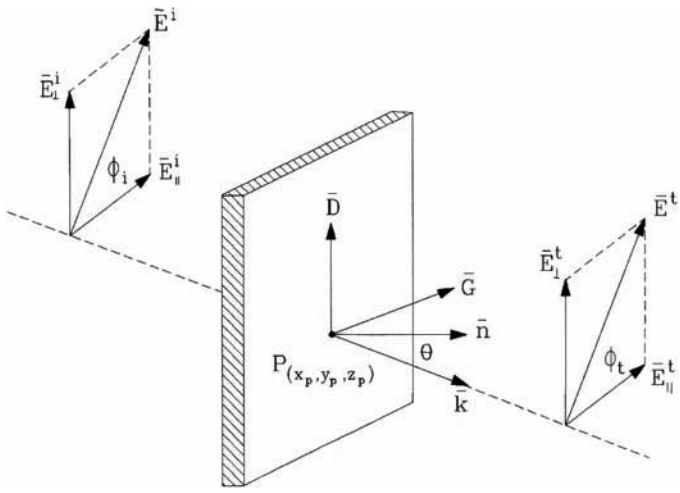

Figure 7.14 Decomposition of an incident wave into parallel and perpendicular components.

$$\overline{D} = d_x \bar{x} + d_y \bar{y} + d_z \bar{z} \tag{7.29}$$

and the parallel vector by:

$$\begin{aligned} \overline{G} &= \overline{D} \times \bar{k} \\ &= \frac{\left(d_y k_z - d_z k_y\right)\bar{x} + \left(d_z k_x - d_x k_z\right)\bar{y} + \left(d_x k_y - d_y k_x\right)\bar{z}}{\sqrt{\left(d_y k_z - d_z k_y\right)^2 + \left(d_z k_x - d_x k_z\right)^2 + \left(d_x k_y - d_y k_x\right)^2}} \end{aligned} \tag{7.30}$$

or

$$\overline{G} = g_x \bar{x} + g_y \bar{y} + g_z \bar{z} \tag{7.31}$$

We can also represent any transverse electromagnetic wave as two orthogonally polarized waves. Let $\mathbf{E}^i$ represent the electric field of a wave incident on the wall, as in Figure 7.14. Since this vector field is a complex function, we will represent the incident field in a phasor notation similar to that used by various authors [14–16].

$$\overline{E}^i \angle\gamma_i = E_x^i \angle\gamma_x \bar{x} + E_y^i \angle\gamma_y \bar{y} + E_z^i \angle\gamma_z \bar{z} \tag{7.32}$$

wherein γ_x, γ_y, γ_z represent the relative phase angle of each of the three components of $\mathbf{E}^i$.

For an example, assume that we are sufficiently into the far field of the source antenna where the phase is relatively uniform. Note also that right-hand circular polarization occurs if the *y*-component has a net 90° phase shift compared with the horizontal component. A left-hand circular wave *y*-component has a net −90° phase shift compared with the horizontal component. The Institute of Electrical and Electronic Engineers (IEEE) standards define the sense to be right-hand if the electric vector rotates in a clockwise direction for an observer looking in the direction of propagation. The sense is right-hand circular if the electric vector rotates in the opposite direction.

Also as illustrated in Figure 7.14, the incident vector field is resolved into scalar components perpendicular and parallel to the plane of incidence by vector dot products of $\mathbf{E}^i$, respectively. The result obtained is:

$$E_\perp^i \angle\gamma_\perp^i = E_x^i d_x \angle\gamma_x + E_y^i d_y \angle\gamma_y + E_z^i d_z \angle\gamma_z \tag{7.33}$$

$$E_\parallel^i \angle\gamma_\parallel^i = E_x^i g_x \angle\gamma_x + E_y^i g_y^i \angle\gamma_y + E_z^i g_z \angle\gamma_z \tag{7.34}$$

The transmitted field is expressed as the product of the incident field and the complex voltage transmission coefficients for each of the two orthogonal linear polarizations. Therefore, the magnitude and phase of each of the two components of the transmitted field are:

$$E_{\perp}^{t} \angle \gamma_{\perp}^{t} = E_{\perp}^{i} T_{w\perp} \angle \left(\gamma_{\perp}^{i} + IPD_{\perp} \right) \tag{7.35}$$

$$E_{\parallel}^{t} \angle \gamma_{\perp}^{t} = E_{\parallel}^{i} T_{w\parallel} \angle \left(\gamma_{\parallel}^{i} + IPD_{\parallel} \right) \tag{7.36}$$

where $T_{w\perp}$, $T_{w\parallel}$ are the voltage transmission coefficient for the perpendicular and parallel wave components, respectively (dimensionless), and $IPD_{\perp}$ and $IPD_{\parallel}$ are the insertion phase delays for the perpendicular and parallel wave components, respectively (radians).

We can now recombine vector components to obtain the transmitted vector field.

$$\begin{aligned} \bar{E}_{t} \angle \gamma_{t} = & \left(E_{\perp}^{t} d_{x} \angle \gamma_{\perp}^{t} + E_{\parallel}^{t} g_{x} \angle \gamma_{\parallel}^{t} \right) \bar{x} + \\ & \left(E_{\perp}^{t} d_{y} \angle \gamma_{\perp}^{t} + E_{\parallel}^{t} g_{y} \angle \gamma_{\parallel}^{t} \right) \bar{y} + \\ & \left(E_{\perp}^{t} d_{z} \angle \gamma_{\perp}^{t} + E_{\parallel}^{t} g_{z} \angle \gamma_{\parallel}^{t} \right) \bar{z} \end{aligned} \tag{7.37}$$

Subroutine COMPOSE (Appendix 7D) shows a sample computer program for an electromagnetic wave decomposition and recomposition using this approach. The program breaks the wave into parallel and perpendicular components, applies the complex, plane-wave, wall transmission coefficients, and returns a complex result for the transmitted electric field.

References

[1] Groutage, F. D., *Radome Development for a Broadband RF Missile Sensor*, Research Report NELC-TR-2023, San Diego, CA, Naval Electronics Laboratory Center, January 1977.

[2] Chin, S. S., *Missile Configuration Design*, New York: McGraw-Hill, 1981.

[3] Weckesser, L. B., "Thermal-Mechanical Design Principles," Ch. 3 in *Radome Engineering Handbook*, J. D. Walton, Jr., (ed.), New York: Marcel Dekker, 1970.

[4] Yost, D. J., L. B. Weckesser, and R. C. Mallalieu, *Technology Survey of Radomes for Anti-Air Homing Missiles*, Applied Physics Laboratory Report FS 80-022, Laurel, MD, John Hopkins University, March 1980.

[5] Crowe, B., *Air Launched Tactical Missile Radome Study*, Newport Beach, CA, Flight Systems, Inc., January 1977.

[6] Joy, E. B., and G. K. Huddleston, *Radome Effects on the Performance of Ground Mapping Radar*, Final Technical Report on Research Contract DAAH01-72-C-0598, Atlanta, GA, Georgia Institute of Technology, March 1973.

[7] Walton, J. D., (ed.), *Radome Engineering Handbook*, New York: Marcel Decker, 1970.

[8] Huddleston, G. K., and A. R. Balius, "A Generalized Ray Tracing Method for Single Valued Radome Surfaces of Revolution," *Proceedings of the 15th International Symposium on Electromagnetic Windows*, Georgia Institute of Technology, Atlanta, GA, June 1980.

[9] Joy, E. B., and D. E. Ball, "Fast Ray Tracing Algorithm for Arbitrary Monotonically Concave Three-Dimensional Radome Shapes," *Proceedings of the 17th International Symposium on Electromagnetic Windows*, Georgia Institute of Technology, Atlanta, GA, July 1984.

[10] Adams, L. J., and P. A. White, *Analytic Geometry and Calculus*, London, England: Oxford University Press, 1968, p. 542.

[11] www.powerbasic.com.

[12] Seber, G. A. F., *Linear Regression Analysis*, New York: John Wiley & Sons, 1977.

[13] Johnson, L. W., and R. D. Riess, *Introduction to Linear Algebra*, Reading, MA: Addison-Wesley Publishing Company, 1981.

[14] Kreyszig, E., *Advanced Engineering Mathematics,* New York: John Wiley & Sons, 1962.

[15] Pipes, L. A., and L. R. Harvell, *Applied Mathematics for Engineers and Physicists*, 3rd ed., New York: McGraw-Hill, 1970.

[16] Hollis, J. S., T. J. Lyon, and L. Clayton, Jr., *Microwave Antenna Measurements*, 2nd ed., Atlanta, GA: Scientific Atlanta, Inc., 1970.

Appendix 7A: Program OGIVE Software Listing

```
     #COMPILE EXE
FUNCTION PBMAIN
' PROGRAM OGIVE TO COMPUTE INTERCEPT POINT ON TANGENT OGIVE RADOME
GLOBAL L0, D0, R, B, X0, Y0, Z0, AZ, EL, DRAD, PI, AZD, ELD, Ci AS
SINGLE
GLOBAL Kx, Ky, Kz, ERF, rp, ri, Xi, Yi, Zi, Xp, Yp, Zp, ACCUM AS SINGLE
GLOBAL Nx, Ny, Nz, THETA AS SINGLE
GLOBAL COUNT AS INTEGER
PI=3.14159265
DRAD = PI/180
' L0 = length of radome (cm)
' D0 = base diameter of radome (cm)
' X0, Y0, Z0 = coordinates of initial point on antenna aperture
' Kx, Ky, Kz = propagation vector
' Xi, Yi, Zi = coordinates of tip of ray (cm)
' Xp, Yp, Zp = intercept point on radome when rp = ri
' ri = radius at tip of ray for value Xi (cm)
' rp = radius at actual radome surface for value Xi (cm)
' ERF = error function - rp - ri = distance from tip of ray to radome
```

```
' AZD, ELD = angular directions of propagation vector (degrees)
' AZ, EL = angular directions of propagation vector
' (radians)
' Note: AZ=0 EL=0 corresponds to Kx=1, Ky=0, Kz=0
' Nx, Ny, Nz are the components of the surface normal vector at the
' intercept point (cm)
' THETA is the angle of incidence between the propagation vector and
' the normal vector at the incidence point (radians)
' To demonstrate program assume:
X0=0: Y0=0: Z0=0
L0 = 100
D0 = 50
R=(4*L0^2+D0^2)/(4*D0)
B=(4*L0^2-D0^2)/(4*D0)
ELD=0
FOR AZD=0 TO 90 STEP 30
 AZ=AZD*DRAD
 EL=ELD*DRAD
 Kx=COS(AZ)*COS(EL)
 KY=SIN(AZ)
 KZ=COS(AZ)*SIN(EL)
 FOR COUNT=0 TO 100.5
 Ci=COUNT*1.0
 Xi=X0+Ci*Kx
 Yi=Y0+Ci*Ky
 Zi=Z0+Ci*Kz
 ri=SQR(Yi^2+Zi^2)
 rp=SQR(R^2-Xi^2) - B
 ERF=rp-ri
 IF ERF<0 THEN
 Ci=Ci-1
 GOTO 100
 END IF
 IF ERF<1 THEN
 GOTO 100
 END IF
 NEXT COUNT
 100 'CONTINUE
 ACCUM = Ci
 FOR COUNT=0 TO 10
 Ci = ACCUM+COUNT*0.1
 Xi=X0+Ci*Kx
 Yi=Y0+Ci*Ky
 Zi=Z0+Ci*Kz
 ri=SQR(Yi^2+Zi^2)
 rp=SQR(R^2-Xi^2) - B
 ERF=rp-ri
 IF ERF<0 THEN
 Ci=Ci-0.1
 GOTO 200
 END IF
 IF ERF<0.1 THEN
 GOTO 200
 END IF
 NEXT COUNT
 200 'CONTINUE
 ACCUM = Ci
 FOR COUNT=0 TO 10
```

```
 Ci = ACCUM+COUNT*0.01
 Xi=X0+Ci*Kx
 Yi=Y0+Ci*Ky
 Zi=Z0+Ci*Kz
 ri=SQR(Yi^2+Zi^2)
 rp=SQR(R^2-Xi^2) - B
 ERF=rp-ri
 IF ERF<0 THEN
 Ci=Ci-0.01
 Xi=X0*Ci*Kx
 Yi=Y0+Ci*Ky
 Zi=Z0+Ci*Kz
 GOTO 300
 END IF
 IF ERF<0.01 THEN
 GOTO 300
 END IF
 NEXT COUNT
 300 'CONTINUE
 'INTERCEPT POINT ON THE RADOME SURFACE IS
 Xp=Xi: Yp=Yi: Zp=Zi
 Xp=ABS(Xp)
 'NOW TO COMPUTE NORMAL VECTOR AT THE INTERCEPT POINT:
 Nx = 1/SQR(1+(rp+B/Xp)^2)
 Ny = ((Yp/rp)*((rp+B)/Xp))/SQR(1+((rp+B)/Xp)^2)
 Nz = ((Zp/rp)*((rp+B)/Xp))/SQR(1+((rp+B)/Xp)^2)
 THETA=ATN((SQR(1-(Nx*Kx+Ny*Ky+Nz*Kz)^2)/(Nx*Kx+Ny*Ky+Nz*Kz)))
 PRINT "AZ(deg)=";AZD;" EL(deg)=";ELD;" Xp=";Xp;" Yp="; Yp;" Zp="; Zp;
" THETA(deg)="; THETA/DRAD
 NEXT AZD
 PRINT "PUSH THE ENTER KEY TO END PROGRAM"
 INPUT hash$
END FUNCTION
```

Appendix 7B: Program POLY Software Listing

```
     #COMPILE EXE
FUNCTION PBMAIN ()
' ————————————————————————————-
' Program POLY is a fifth order polynomial regression code
CLS
GLOBAL RP(), XP(), X, Y, A(), MATR(), SM(), RT() AS SINGLE
GLOBAL SM(), RT(), TMP , FTR, TOT AS SINGLE
GLOBAL I, J, K, L, N, KMP, ORDER, ITMP, CNT, PNT, COUNT AS INTEGER
DIM RP(50), XP(50), A(10), MATR(10,10), SM(10), RT(10)
' ORDER = ORDER OF REGRESSION
ORDER = 5
' N = NUMBER OF DATA POINT PAIRS TO BE ENTERED
'—————————- USER INPUT DATA ——————————-
' XP = Distance from the radome base (inches)
' RP = Radome radius (inches)
 PRINT
 PRINT "MIN OF THREE DATA SETS REQUIRED"
 PRINT
 INPUT "INPUT NUMBER OF DATA SETS TO BE ENTERED = "; N
 PRINT
```

```
FOR COUNT = 1 TO N
INPUT "XP = "; XP(COUNT)
INPUT "RP = "; RP(COUNT)
PRINT
NEXT COUNT
PRINT
PRINT "WHEN READY TO BEGIN REGRESSION ANALYSIS INPUT ANY KEY"
INPUT HASH$
'BEGIN POLYNOMIAL REGRESSION ALGORITHM:
FOR I = 1 TO 2 * ORDER
SM(I) = 0
NEXT I
FOR I = 1 TO ORDER + 1
RT(I) = 0
NEXT I
FOR PNT = 1 TO N
FOR I = 1 TO ORDER * 2
SM(I) = SM(I) + XP(PNT) ^ I
NEXT I
FOR I = 1 TO ORDER + 1
IF I = 1 THEN RT(I) = RT(I) + RP(PNT)
IF I  1 THEN RT(I) = RT(I) + RP(PNT) * (XP(PNT) ^ (I - 1))
NEXT I
NEXT PNT
MATR(1, 1) = N
FOR I = 1 TO ORDER + 1
MATR(I, ORDER + 2) = RT(I)
FOR J = 1 TO ORDER + 1
IF I + J  2 THEN MATR(I, J) = SM(I + J - 2)
NEXT J
NEXT I
FOR K = 1 TO ORDER
KMP = K + 1
L = K
FOR I = KMP TO ORDER + 1
IF ABS(MATR(I, K)) > ABS(MATR(L, K)) THEN L = I
NEXT I
IF L  K THEN
FOR J = K TO ORDER + 2
TMP = MATR(K, J)
MATR(K, J) = MATR(L, J)
MATR(L, J) = TMP
NEXT J
END IF
FOR I = KMP TO ORDER + 1
FTR = MATR(I, K) / MATR(K, K)
FOR J = KMP TO ORDER + 2
MATR(I, J) = MATR(I, J) - FTR * MATR(K, J)
NEXT J
NEXT I
NEXT K
A(ORDER + 1) = MATR(ORDER + 1, ORDER + 2) / MATR(ORDER + 1, ORDER + 1)
I = ORDER
DO
ITMP = I + 1
TOT = 0
FOR J = ITMP TO ORDER + 1
TOT = TOT + MATR(I, J) * A(J)
```

```
 NEXT J
 A(I) = (MATR(I, ORDER + 2) - TOT) / MATR(I, I)
 I = I - 1
 IF I < 1 THEN EXIT DO
 LOOP

'—— DISPLAY COEFFICIENTS ————————————————
 CLS : LOCATE 1, 1
 PRINT
 PRINT "COMPUTED COEFFICIENTS"
 PRINT
 PRINT "A0 = "; A(1)
 PRINT "A1 = "; A(2)
 PRINT "A2 = "; A(3)
 PRINT "A3 = "; A(4)
 PRINT "A4 = "; A(5)
 PRINT "A5 = "; A(6)
 PRINT
 PRINT "READY TO TEST CONFORMANCE"
 PRINT
 PRINT "PUSH ANY KEY TO BEGIN"
 INPUT HASH$
'——— TEST POLYNOMIAL CONFORMANCE ————————————-
100 'CONTINUE
 PRINT
 INPUT "INPUT XP = "; X
 Y = A(1) + A(2)*X + A(3)*X^2 +A(4)*X^3 +A(5)*X^4 +A(6)*X^5
 PRINT "COMPUTED RP = "; Y
 PRINT
 PRINT
GOTO 100
200 'END OF PROGRAM
'————————————————————————————-
END FUNCTION
```

Appendix 7C: Program ARBITRARY Software Listing

```
     #COMPILE EXE
FUNCTION PBMAIN
' PROGRAM ARBITRARY TO COMPUTE INTERCEPT POINT ON AN ARBITRARY SHAPED
RADOME
' HAVING AXIAL SYMMETRY
GLOBAL X0, Y0, Z0, AZ, EL, DRAD, PI, AZD, ELD, Ci AS SINGLE
GLOBAL Kx, Ky, Kz, ERF, rp, ri, Xi, Yi, Zi, Xp, Yp, Zp, ACCUM AS SINGLE
GLOBAL Nx, Ny, Nz, Nt, THETA, PSI, ALPHA AS SINGLE
'POLYNOMIAL REGRESSION COEFFICIENTS:
GLOBAL A0, A1, A2, A3, A4, A5 AS SINGLE
GLOBAL COUNT AS INTEGER
PI=3.14159265
DRAD = PI/180
' A0 through A5 are polynomial regression coefficients for radome
shape
' obtained by use of program POLY
' X0, Y0, Z0 = coordinates of initial point on antenna aperture
' Kx, Ky, Kz = propagation vector
' Xi, Yi, Zi = coordinates of tip of ray (cm)
```

```
' Xp, Yp, Zp = intercept point on radome when rp = ri
' ri = radius at tip of ray for value Xi (cm)
' rp = radius at actual radome surface for value Xi (cm)
' ERF = error function - rp - ri = distance from tip of ray to radome
' AZD, ELD = angular directions of propagation vector (degrees)
' AZ, EL = angular directions of propagation {AU: EDIT OK?} vector
(radians)
' Note: AZ=0 EL=0 corresponds to Kx=1, Ky=0, Kz=0
' Nx, Ny, Nz are the components of the surface normal vector at the
' intercept point (cm)
' THETA is the angle of incidence between the propagation vector and
the
' normal vector at the incidence point (radians)
' PSI is the slope of the normal vector
' To demonstrate program assume:
X0=0: Y0=0: Z0=0
A0=25.00086
A1=-7.41124*10^-4
A2=-2.29406*10^-3
A3=-1.72184*10^-6
A4=+9.11312*10^-9
A5=-1.17584*10^-10
ELD=0
FOR AZD=0 TO 90 STEP 30
 AZ=AZD*DRAD
 EL=ELD*DRAD
 Kx=COS(AZ)*COS(EL)
 KY=SIN(AZ)
 KZ=COS(AZ)*SIN(EL)
 FOR COUNT=0 TO 100
 Ci=COUNT*1.0
 Xi=X0+Ci*Kx
 Yi=Y0+Ci*Ky
 Zi=Z0+Ci*Kz
 ri=SQR(Yi^2+Zi^2)
 rp=A0+A1*Xi+A2*Xi^2+A3*Xi^3+A4*Xi^4+A5*Xi^5
 ERF=rp-ri
 IF ERF<0 THEN
 Ci=Ci-1
 GOTO 100
 END IF
 IF ERF<1 THEN
 GOTO 100
 END IF
 NEXT COUNT
 100 'CONTINUE
 ACCUM = Ci
 FOR COUNT=0 TO 10
 Ci = ACCUM+COUNT*0.1
 Xi=X0+Ci*Kx
 Yi=Y0+Ci*Ky
 Zi=Z0+Ci*Kz
 ri=SQR(Yi^2+Zi^2)
 rp=A0+A1*Xi+A2*Xi^2+A3*Xi^3+A4*Xi^4+A5*Xi^5
 ERF=rp-ri
 IF ERF<0 THEN
 Ci=Ci-0.1
 GOTO 200
```

```
 END IF
 IF ERF<0.1 THEN
 GOTO 200
 END IF
 NEXT COUNT
 200 'CONTINUE
 ACCUM = Ci
 FOR COUNT=0 TO 10
 Ci = ACCUM+COUNT*0.01
 Xi=X0+Ci*Kx
 Yi=Y0+Ci*Ky
 Zi=Z0+Ci*Kz
 ri=SQR(Yi^2+Zi^2)
 rp=A0+A1*Xi+A2*Xi^2+A3*Xi^3+A4*Xi^4+A5*Xi^5
 ERF=rp-ri
 IF ERF<0 THEN
 Ci=Ci-0.01
 Xi=X0*Ci*Kx
 Yi=Y0+Ci*Ky
 Zi=Z0+Ci*Kz
 GOTO 300
 END IF
 IF ERF<0.01 THEN
 GOTO 300
 END IF
 NEXT COUNT
 300 'CONTINUE
 'INTERCEPT POINT ON THE RADOME SURFACE IS
 Xp=Xi: Yp=Yi: Zp=Zi
 Xp=ABS(Xp)
 'NOW TO COMPUTE NORMAL VECTOR AT THE INTERCEPT POINT:
 PSI=ATN(-1/(A1+2*A2*Xi+3*A3*Xi^2+4*A4*Xi^3+5*A5*Xi^4))
 Nx=COS(PSI)
 Nt=SQR(1-Nx^2)
 IF Yp=0 THEN
 Yp=10^-6
 END IF
 ALPHA=ATN(Zp/Yp)
 Ny=Nt*COS(ALPHA)
 NZ=Nt*SIN(ALPHA)
 THETA=ATN((SQR(1-(Nx*Kx+Ny*Ky+Nz*Kz)^2)/(Nx*Kx+Ny*Ky+Nz*Kz)))
 PRINT "AZ(deg)=";AZD;" EL(deg)=";ELD;" Xp=";Xp;" Yp="; Yp;" Zp="; Zp;
" THETA(deg)="; THETA/DRAD
 NEXT AZD
 PRINT "PUSH THE ENTER KEY TO END PROGRAM"
 INPUT hash$
END FUNCTION
```

Appendix 7D: Program DECOMPOSE Computer Listing

```
     #COMPILE EXE
FUNCTION PBMAIN
' Program DECOMPOSE to compute parallel and perpendicular wave to
'components at the intercept point to apply parallel and perpendicular
'transmission coefficients
GLOBAL Xp, Yp, Zp, AZ, EL, AZD, ELD, DRAD, PI, Kx, Ky, Kz AS SINGLE
```

```
GLOBAL Nx, Ny, Nz, Dt, Gt, Dy, Dz, Gx, Gy, Gz, Tpara, Tperp, Dx AS
SINGLE
GLOBAL Eix, Eiy, Eiz, Etx, Ety, Etz, THETA, Ei, Et, Eipara, Eiperp AS
SINGLE
GLOBAL Etpara, Etperp, T, TdB, Nt, Kt, Eit, Ett AS SINGLE
PI=3.14159265
DRAD = PI/180
‘Xp, Yp, Zp = coordinate of intercept point on radome surface
‘AZD, ELD = angular directions of propagation vector (degrees)
‘AZ, EL = angular directions of propagation {AU: EDIT OK?} vector
(radians)
‘Note: AZ=0, EL=0 cprres[pmds tp Lx=1, Ky=0, Kz=0
‘Nx, Ny, Nz = the components of the surface normal vector at the inter-
cept point (cm)
‘THETA is the angle of incidence between the propagation vector and
the normal
‘vector at the incidence point (radians)
‘ ———————————————————————-
‘To illustrate the procedure, assume that:
AZD=30: ELD=30
AZ = AZD*DRAD
EL = ELD*DRAD
‘Rotate aperture E vector through AZ and EL angles:
‘(Assume vertical polarization for this sample problem)
Eix = -SIN(EL)*COS(AZ)
Eiy = -SIN(EL)*SIN(AZ)
Eiz = +COS(EL)
Eit=SQR(Eix^2+Eiy^2+Eiz^2)
PRINT
PRINT “PRINT Eit TO CONFIRM THAT Eit IS A UNIT VECTOR:”
PRINT Eit
‘If horizontal polarization these expressions would be:
‘Eix = -SIN(AZ)
‘Eiy = +COS(AZ)
‘Eiz = 0
Xp=26.325: Yp=17.55: Zp=15.1974
Nx=0.05573592: Ny=0.9592745: Nz=0.2769187
Kx=0.75: Ky=0.5: Kz=0.4330127
‘Parallel and perpendicular polarization wall voltage transmission
coefficients:
Tpara = 0.8
Tperp = 0.9
‘Note: for this sample problem we will assume Tpara and Tperp totally
real
‘ ———————————————————————
‘Starting with these values {AU: EDIT OK?}, compute the components of
vector D
‘Note: D is perpendicular to the plane formed by the vectors K and N
Dx=(Ny*Kz-Nz*Ky)/SQR((Ny*Kz-Nz*Ky)^2+(Nz*Kx-Nx*Kz)^2+(Nx*Ky-Ny*Kx)^2)
Dy=(Nx*Kz-Nz*Kx)/SQR((Ny*Kz-Nz*Ky)^2+(Nz*Kx-Nx*Kz)^2+(Nx*Ky-Ny*Kx)^2)
Dz=(Nx*Ky-Ny*Kx)/SQR((Ny*Kz-Nz*Ky)^2+(Nz*Kx-Nx*Kz)^2+(Nx*Ky-Ny*Kx)^2)
PRINT
PRINT “PRINT D TO CONFIRM THAT D IS A UNIT VECTOR:”
Dt=SQR(Dx^2+Dy^2+Dz^2)
PRINT Dt
‘Note: G is in the plane formed by the vectors K and N
Gx=(Dy*Kz-Dz*Ky)/SQR((Dy*Kz-Dz*Ky)^2+(Dz*Kx-Dx*Kz)^2+(Dx*Ky-Dy*Kx)^2)
Gy=(Dx*Kz-Dz*Kx)/SQR((Dy*Kz-Dz*Ky)^2+(Dz*Kx-Dx*Kz)^2+(Dx*Ky-Dy*Kx)^2)
```

```
Gz=(Dx*Ky-Dy*Kx)/SQR((Dy*Kz-Dz*Ky)^2+(Dz*Kx-Dx*Kz)^2+(Dx*Ky-Dy*Kx)^2)
PRINT
PRINT "PRINT G TO CONFIRM THAT G IS A UNIT VECTOR:"
Gt=SQR(Gx^2+Gy^2+Gz^2)
PRINT Gt
PRINT
'The perpendicular component of Ei is
Eiperp = Eix*Dx + Eiy*Dy + Eiz*Dz
'From which
Etperp = Eiperp*Tperp
'The parallel component of Ei is
Eipara = Eix*Gx + Eiy*Gy +Eiz*Gz
'From which
Etpara = Eipara*Tpara
Ei = SQR(Eipara^2 + Eiperp^2)
Et = SQR(Etpara^2 + Etperp^2)
T = Et/Ei
TdB = 20*LOG10(T)
PRINT "TRANSMISSION LOSS FACTOR = "; T; " TRANSMISSION LOSS (dB)= ";
TdB
INPUT hash$
END FUNCTION
```

8

Radome-Enclosed Guidance Antennas

This chapter introduces computerized techniques to analyze radome-enclosed guidance antenna systems. A guidance antenna functions to detect the target location, and the currently most commonly used ones are monopulse antennas. Typically, radomes associated with these antennas are aerodynamically streamlined and have a high fineness ratio (up to 3 or greater). For specific applications, the radome materials must be chosen to simultaneously satisfy structural, environmental, and electrical requirements. The computerized analysis techniques in this chapter can determine the effect of the radome on the performance of the enclosed antenna and its electronics processing function.

A monopulse antenna is generally forward-mounted in an aircraft or missile, as depicted in Figure 8.1. The term *monopulse* refers to a signal-processing technique in which only a single radar return pulse is needed to resolve a target's location in both the elevation and azimuth planes of the antenna. Monopulse systems are typically active radar, but in certain applications they may be passive receptors as with semi-active guidance systems. In this book, the term "seeker" is used synonymously with monopulse electronics systems.

Ideally, a radome protects the monopulse antenna from the adverse flight environment while having an insignificant effect on the electrical performance of the enclosed antenna. However, in practice a radome always changes the electrical performance of the monopulse antenna because of the following factors: (1) dissipative losses within the dielectric material, (2) electrical phase shifts introduced by the presence of the radome, and (3) internal reflections. These changes produced by the radome manifest themselves as follows:

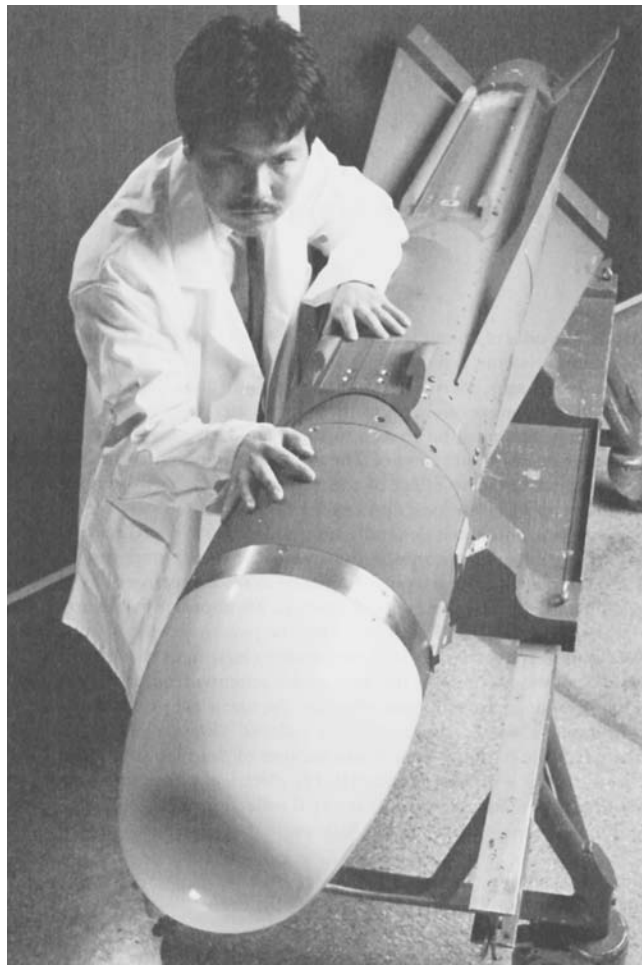

Figure 8.1 Radome-enclosed monopulse antenna used for missile guidance. (Photo courtesy of Hughes Aircraft Missile Systems Division.)

- Decreased antenna gain;
- Increased antenna beamwidth and sidelobe levels;
- Decreased monopulse null depth;
- Introduction of a boresight error and boresight error slope, which are functions of the antenna scan angle [1, 2].

In this chapter, antenna pattern calculations are made in steps, which must be performed in sequence as follows:

1. Transpose all aperture points to radome coordinates.
2. Transform all ray vectors from aperture sample points in the pattern look direction.
3. Compute the antenna pattern space phase terms.
4. Determine all ray intercept points on the radome surface.
5. Determine angles of incidence of these rays with respect to the radome surface normal at each intercept point.
6. Compute the complex voltage transmission coefficients for each ray.
7. Perform an antenna aperture integration.

Section 8.1 provides a definition of BSE and BSES. Section 8.2 discusses antenna patterns and monopulse error voltages for a monopulse antenna without a radome, whereas Section 8.3 deals with the same antenna but when it is enclosed within a dielectric radome. Finally, Section 8.4 covers radome modeling considerations, including rain erosion, aerothermal heating, and radome effects on a conscan antenna.

8.1 Definitions of Boresight Error (BSE) and Boresight Error Slope (BSES)

When used in missiles, the seeker antenna is a key part of the guidance system, which also includes the radome, receiver, autopilot, and airframe. The seeker has several functions:

- To measure the line of sight (or line-of-sight angular rates);
- To measure the range to target and the closing velocity;
- To provide steering commands to the missile autopilot and control surfaces [3–7].

Figure 8.2 shows a representative closed-loop servo control system, in which the signals received by the missile-mounted seeker antenna are used to guide the missile to the target. This guidance is accomplished in the tracking loop, which is driven by the monopulse elevation and azimuth plane guidance error voltages.

The seeker initially finds the target in angle space through the seeker antenna's beamwidth. The antenna beam is steered by one of the following methods:

- A gimbal that mechanically moves the entire antenna structure;

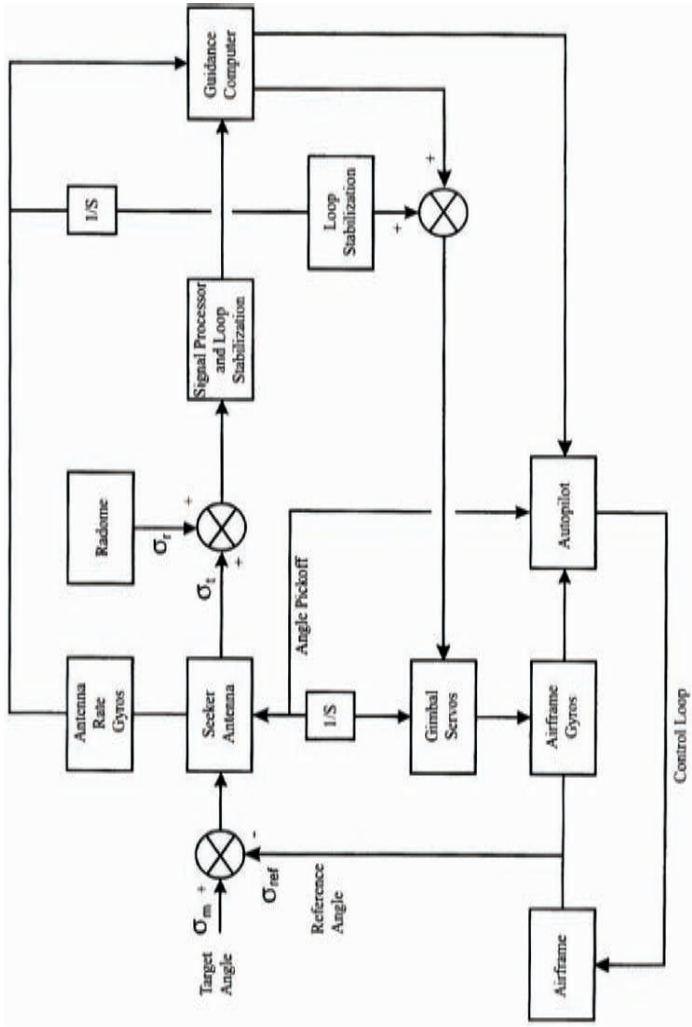

Figure 8.2 Representative guidance system block diagram.

- An electromechanical mechanism that moves only a portion of the antenna, such as a subreflector;
- An electronic steering mechanism, such as a phased-array antenna;
- Movement of the entire airframe, in the case of an antenna that is stationary and forward-looking. Fixed seeker antenna beams are used only when a pursuit navigation guidance algorithm is used. Movable seeker antenna beams are used with proportional navigation (or modern guidance law) guidance algorithms [8].

Figure 8.3 illustrates the definitions of the angles relating to the seeker-radome and missile-target geometry. In this figure, the seeker antenna is mounted on a mechanical gimbal whose pointing function is controlled by a servo loop. Because of the diffraction errors introduced by the presence of the radome, the servo system will try to keep the antenna pointed toward the apparent target direction, as opposed to the actual target direction.

The difference between the actual missile-to-target direction and the apparent missile-to-target direction is known as the radome *boresight error* (BSE). Conceptually, BSE is an angular shift in the apparent target direction and generally corresponds to difference pattern minimums in the far-field radiation patterns of the radome-enclosed guidance antenna. The *boresight error slope* (BSES) is the rate of change of the boresight error with respect to antenna scan angle.

The reference angle shown in Figure 8.3 is derived from airframe gyros. The antenna pointing angles are often determined from rate gyros mounted on

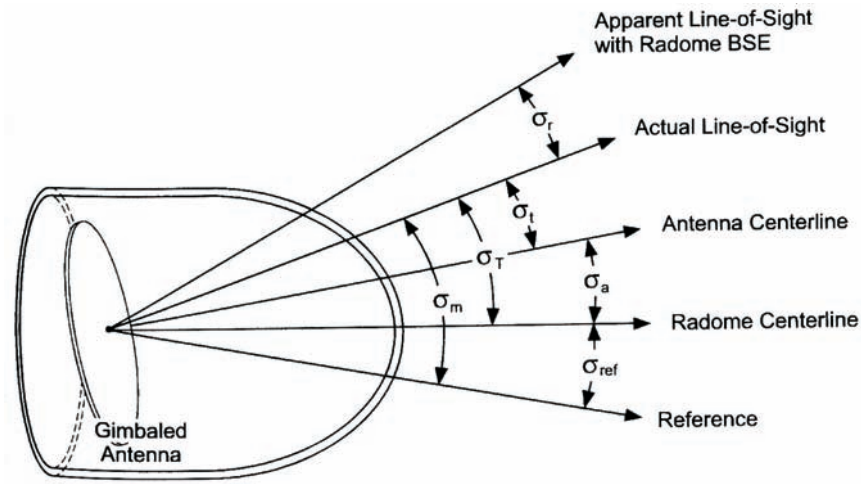

Figure 8.3 Monopulse antenna-to-target angular relationships.

the antenna gimbal. The monopulse error voltages are fed back to the autopilot. In response to the autopilot commands, the missile changes attitude, which causes the antenna to receive through an ever-changing portion of the radome. As a consequence, the response characteristics of the airframe and autopilot generate a pseudo-noise influence due to these radome-induced errors [9].

8.2 Calculation of Antenna Patterns and Monopulse Error Voltages for an Antenna Without a Radome

The physical aperture of a monopulse antenna is usually divided into four quadrants. Each of these is fed by a microwave network that resolves the signals received by each of the four quadrants into a sum channel and into elevation and azimuth plane difference channels, as illustrated in Figure 8.4. A monopulse radar receiver processes these sum and difference channel signals as complex voltages, which are resolved into in-phase (I) and out-of-phase or phase quadrature (Q) voltages prior to processing by the signal processor.

The *sum* channel antenna pattern corresponds to a single on-boresight antenna beam, with the half-power beamwidth dictated by both the antenna aperture size in wavelengths and the aperture illumination function. The elevation channel antenna pattern has a boresight null only in the elevation plane, while the azimuth channel antenna pattern has a boresight null only in the azimuth plane. The effective sum channel beamwidth obtained with a monopulse antenna is the beamwidth of the aperture, and the maximum gain of the aperture is realized.

Early monopulse systems used reflector antennas or lens antennas, with the monopulse-beam-forming network achieved with a large, complex waveguide monopulse network. Modern approaches to achieve sum and difference channel beams have very small beam-forming networks, with little or no aperture blockage [10]. These approaches include the waveguide flat-plate array and microstrip array configurations. The photograph of Figure 8.5 shows a microstrip, monopulse array antenna, utilizing square patch radiators and having the feed network on the same substrate as the patch radiators, while Figure 8.6 shows a similar circuit topology that uses circular microstrip patch elements.

From the monopulse sum and difference channel voltages, the monopulse azimuth and elevation plane error voltages are derived in the following manner [11]:

$$V_{az} = \frac{\Delta_{az}}{\Sigma} \tag{8.1}$$

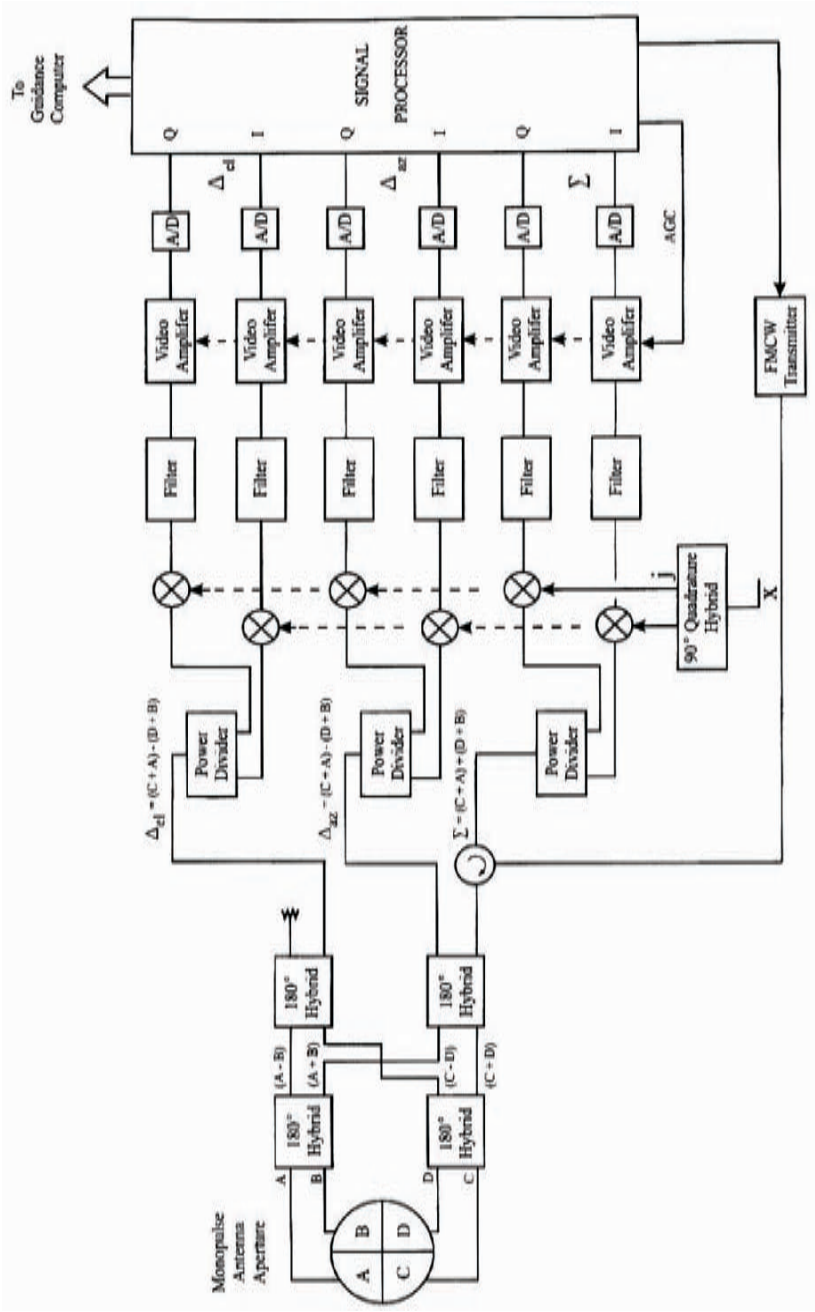

Figure 8.4 Block diagram of a typical monopulse radar.

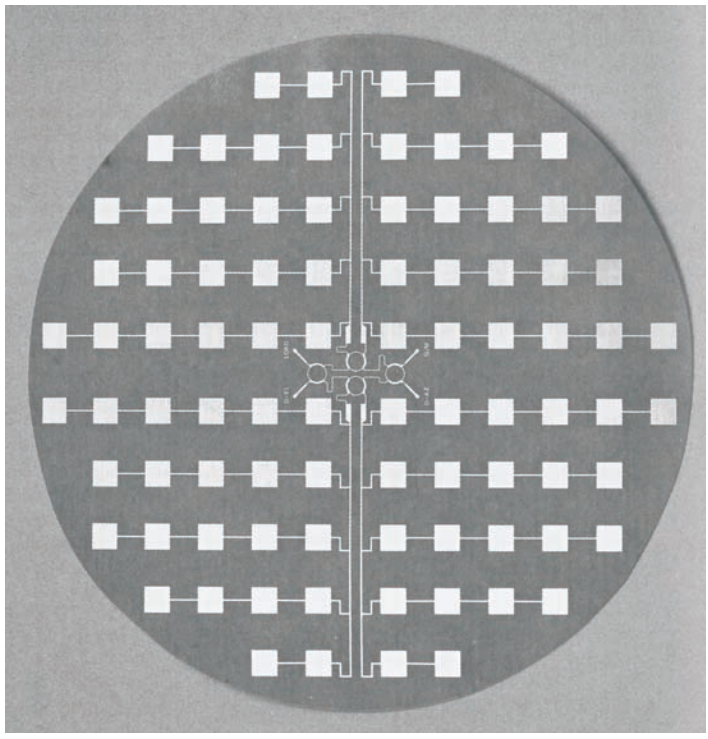

Figure 8.5 Square microstrip patch array with monopulse comparator on substrate. (Photo courtesy of Ball Corporation.)

$$V_{el} = \frac{\Delta_{el}}{\Sigma} \tag{8.2}$$

In a guidance system, these error voltages are used to guide the missile toward the target.

The array theory provides the tools to compute monopulse antenna patterns without the need to apply exact electromagnetic modeling. The following analysis introduces the modeling methodology, and we use the spherical coordinate system shown in Figure 8.7 for the calculation of antenna radiation patterns. In this system:

$P(x_o, y_o, z_o)$ = reference point at the center of the antenna aperture;

$P(x, y, z)$ = observation point at a distance R from the antenna;

$P(x_i, y_i, z_i)$ = location of the ith sample point on the antenna aperture;

r_o = unit vector in the direction from $P(x_o, y_o, z_o)$ to $P(x, y, z)$;

r_i = vector in the direction from $P(x_o, y_o, z_o)$ to $P(x_i, y_i, z_i)$.

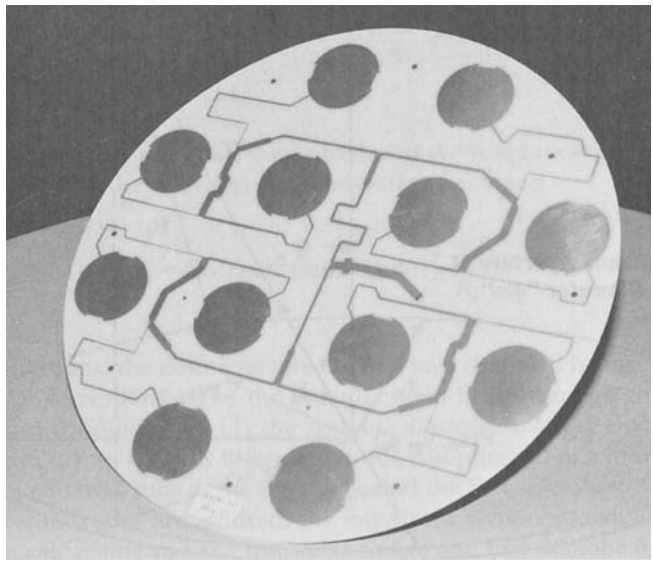

Figure 8.6 Circular microstrip patch array. (Photo courtesy of Seavey Engineering.)

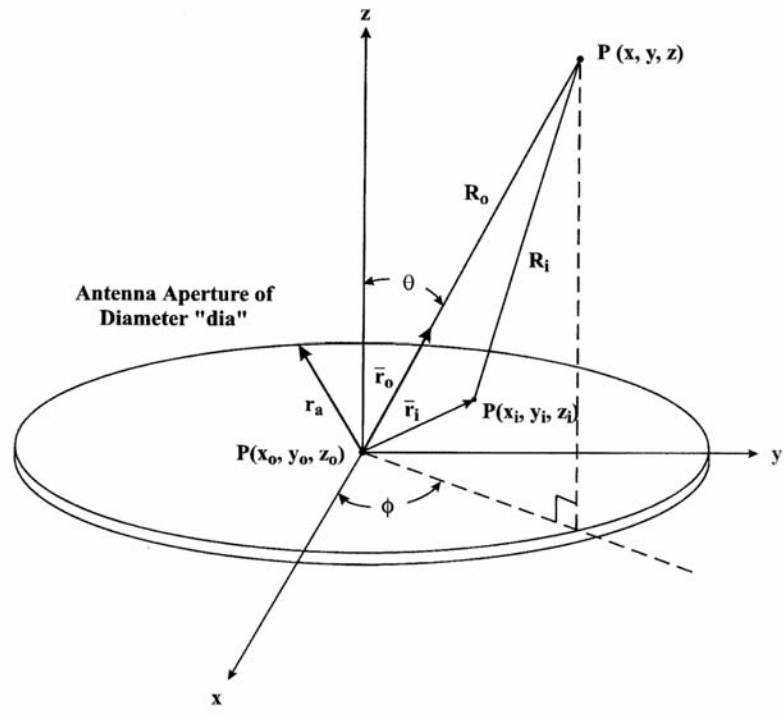

Figure 8.7 Coordinate system used in antenna pattern calculations.

The circular antenna aperture lies entirely in the *x*-*y* plane and has a radius given by the formula

$$r_a = \sqrt{(x_i - x_o)^2 + (y_i - y_o)^2 + (z_i - z_o)^2} = \frac{D_o}{2} \tag{8.3}$$

where D_a is the antenna diameter.

It is customary to obtain current sample points at spacings d_x and d_y in the *x*- and *y*-planes, respectively. If these spacings are a half-wave or less at the highest operating frequency, we guarantee that there will be no aliasing into real space to cause computational errors in the antenna pattern prediction. However, if we are only interested in the main lobe and first sidelobes of the radiation patterns, informal testing by the author shows that sample spacings up to a wavelength or more may be acceptable with only small computational errors.

In accordance with Appendix A, we will now assume that the sample point currents are an ensemble of infinitesimal dipoles, each of which is weighted in both amplitude and phase. Points on the surface of the antenna aperture are uniquely defined via the integers *m*, *n*:

$$r_i = md_y\bar{y} + nd_z\bar{z} \tag{8.4}$$

For distances relatively far from the *i*th infinitesimal dipole, its radiation pattern has an exponential phase dependence as it expands as a spherical wave and also has a sine-weighted amplitude dependence with a radiation maximum normal to the dipole. Based on the coordinate system selected, if the dipoles are *y*-directed, an appropriate coordinate transformation derives the radiation element pattern for the *i*th infinitesimal dipole as:

$$E_i = \cos\left[\tan^{-1}(\tan\theta\sin\phi)\right]\frac{e^{-jkR_i}}{R_i} \tag{8.5}$$

In this equation, *k* is the free-space wave number at the frequency of interest. If the dipoles are *x*-directed, the radiation element pattern becomes:

$$E_i = \cos\left[\tan^{-1}(\tan\theta\cos\phi)\right]\frac{e^{-jkR_i}}{R_i} \tag{8.6}$$

Under two conditions, the cosine factors in (8.5) and (8.6) will be near unity over the angle space corresponding to the antenna main beam through the first sidelobes. These conditions are:

- The antenna diameter is larger than about five wavelengths.
- We are only interested in the computation of a limited portion of the antenna patterns, such as the main lobe and the first sidelobes.

If the cosine factors are ignored, the impact on computational accuracy will be small when calculating radome transmission loss and first sidelobe degradation. However, when estimating far-out sidelobes, the cosine factors are important.

Accordingly, based on the *MN* total current sample points, the antenna array pattern can be determined from the superposition of the infinitesimal dipoles over the entire aperture.

$$E_T = \sum_{m=1}^{M} \sum_{n=1}^{N} F_{mn}^{a} \frac{e^{-jkR_{mn}}}{R_{mn}} \tag{8.7}$$

Here, the coefficients F_{mn}^{a} are the applied current element weight at the sample points induced by a received signal. In general, these weighting coefficients are complex quantities.

In (8.7), the required computational distance R_{mn} should be sufficiently into the far field of the antenna. The actual value of R_{mn} depends on the degree of fine structure desired in the antenna pattern computation. The conventional definition of antenna far field corresponds to the condition wherein

$$R_{mn} \geq \frac{2D_a^2}{\lambda} \tag{8.8}$$

A one far-field distance is adequate for main lobe and first sidelobe antenna pattern calculations. However, for antenna aperture distributions that give very low sidelobe antenna patterns, it may be necessary to use distances at least five times greater than (8.8) [12, 13]. If we let the computational distance approach infinity, the following approximation holds:

$$\frac{e^{-jkR_{mn}}}{R_{mn}} = \left[\frac{e^{-jkR_o}}{R_o}\right] e^{jk\bar{r}_{mn}\cdot\bar{r}_o} \tag{8.9}$$

Under this condition,

$$E_T = \frac{e^{-jkR_o}}{R_o} \sum_{m=1}^{M} \sum_{n=1}^{N} F_{mn}^{a} e^{jk\bar{r}_{mn}\cdot\bar{r}_o} \tag{8.10}$$

It is customary to drop out the left factor in brackets, [ ], because the antenna pattern is generally described on a sphere of a constant radius, and this term just becomes a normalizing constant [14]. This factor will have no impact on the computation of radome parameters of interest. The antenna pattern then takes the form:

$$E_T = \sum_{m=1}^{M} \sum_{n=1}^{N} F_{mn}^{a} e^{jk\bar{r}_{mn} \cdot \bar{r}_o} \tag{8.11}$$

Using vector mathematics, we note that

$$\bar{r}_{mn} = (x_{mn} - \bar{x}_o)\bar{x} + (y_{mn} - y_o)\bar{y} + (z_{mn} - z_o)\bar{z} \tag{8.12}$$

Also, the unit vector in the direction of the observation point is given in terms of the directional cosines [15]:

From these last two equations, we can simplify the dot product in (8.10):

$$\bar{r}_o = \sin\theta\cos\phi\bar{x} + \sin\theta\sin\phi\bar{y} + \cos\theta\bar{z} \tag{8.13}$$

$$\bar{r}_{mn} \cdot r_o = (x_{mn} - x_o)\sin\theta\cos\phi + (y_{mn} - y_o)\sin\theta\sin\phi + (z_{mn} - z_o)\cos\theta \tag{8.14}$$

If the center of the antenna is at the point $x_o = y_o = z_o = 0$ and we select all $z_{mn} = 0$,

$$E_T = \sum_{m=1}^{M} \sum_{n=1}^{N} F_{mn}^{a} e^{-jk(x_{mn}\sin\theta\cos\phi + y_{mn}\sin\theta\sin\phi)} \tag{8.15}$$

then the simplification on the array pattern of the antenna takes the form:

$$E_T = \sum_{m=1}^{M} \sum_{n=1}^{N} F_{mn}^{a} e^{-jk(k_x x_{mn} + k_y y_{mn})} \tag{8.16}$$

where k_x and k_y are the propagation constants in the x- and y-planes, respectively.

The monopulse sum and difference patterns should be computed by sequentially loading this equation with the proper aperture distribution functions. For example, for a monopulse antenna, these weighting factors may correspond to the following theoretical distributions.

$$F_{mn}^{a} = F_{\Sigma}^{a} = \cos\left(\frac{\pi}{2}\frac{r_{mn}}{r_a}\right) \tag{8.17}$$

or

$$F_{mn}^{a} = F_{\Delta_{el}}^{a} = \sin\left(\pi\frac{y_{mn}}{r_a}\right) \tag{8.18}$$

or

$$F_{mn}^{a} = F_{\Delta_{az}}^{a} = \sin\left(\pi\frac{r_{mn}}{r_a}\right) \tag{8.19}$$

If our computation is only interested in the relative directivity normalized with respect to the peak of the sum pattern, then the antenna array pattern is

$$E_T = \frac{\sum_{m=1}^{M}\sum_{n=1}^{N} F_{mn}^{a} e^{-jk(x_{mn}\sin\theta\cos\phi + y_{mn}\sin\theta\sin\phi)}}{\sum_{m=1}^{M}\sum_{n=1}^{N}\cos\left(\frac{\pi}{2}\frac{r_{mn}}{r_a}\right)} \tag{8.20}$$

where the F_{mn}^{a} in the numerator is one of the appropriate weighting factors from (8.17) through (8.19). The peak of the relative directivity sum pattern will then correspond to 0 dB.

Figure 8.8 shows the software flow diagram for a computer program designed to compute antenna patterns for a monopulse antenna. For angles of interest in antenna angle space, θ and φ, a surface integration over the entire antenna aperture must be performed for each of these three aperture weighting distributions. This integration will allow us to compute the antenna sum voltage and the two difference channel voltages.

Based on this flow diagram, a computer program was developed and included with this book. The operations manual shown in Appendix E clearly defines all the input and output variables, which makes it user-friendly. As configured, this code computes the principal plane sum and difference antenna pattern voltages as well as the monopulse error channel voltages in order to determine the radome boresight error.

To demonstrate the use of the program, we assumed a 15-inch circular antenna aperture at 10 GHz, having the aperture distributions of (8.17) through (8.19). Figure 8.9 shows the computed E-plane and H-plane sum patterns.

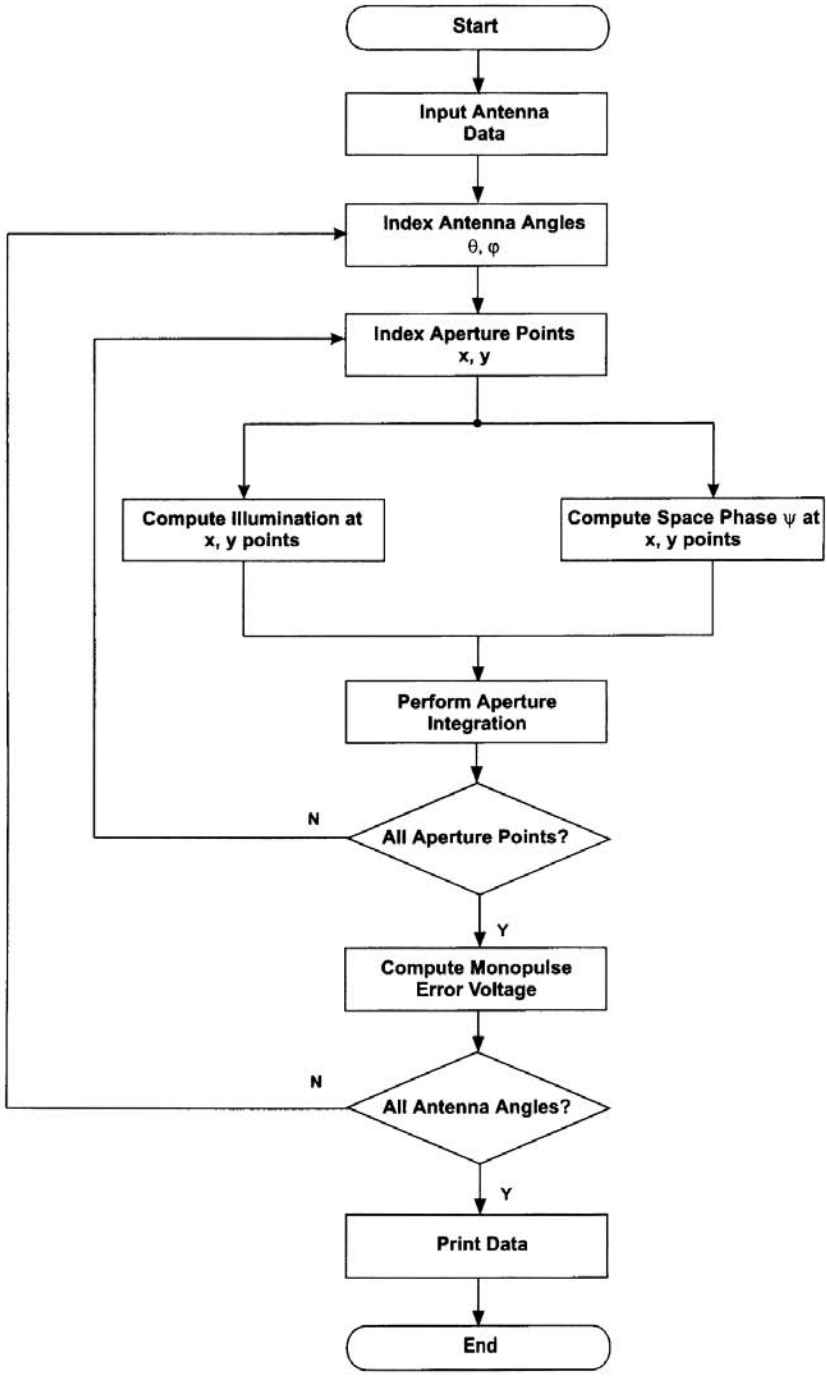

Figure 8.8 Computer program flow diagram for the program TO radome.

Figure 8.10 depicts the corresponding azimuth and elevation plane monopulse error channel voltages. Since there are no radome-induced errors, both of these functions are zero on the antenna boresight. In performing this modeling, we investigated the computational error in first sidelobe and antenna sum channel half-power beamwidth predictions versus the number of aperture sample points per wavelength. The resulting data are plotted in Figure 8.11 for sidelobe accuracy in Figure 8.12 for antenna beamwidth computational accuracy.

8.3 Calculation of Radiation Patterns and Monopulse Error Voltages for an Antenna with a Radome

8.3.1 General Approach

There are several approaches to boresight error computation:

1. Determine the shift in the difference pattern's null position, which results from a wavefront phase distortion of the signal as it propagates through the radome [16].
2. Determine the far-field sum pattern peak location [17].

This chapter uses the first method, which derives boresight error in the same way that a monopulse seeker does. This method is based on the determination of the shift in the zero crossings of the monopulse error in channel voltages

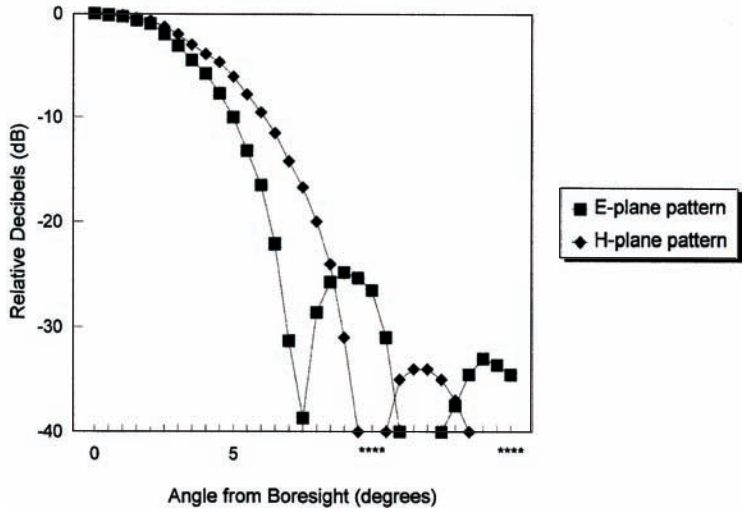

Figure 8.9 Computation of azimuth and elevation plane monopulse antenna sum pattern for a 15-inch aperture at 10 GHz.

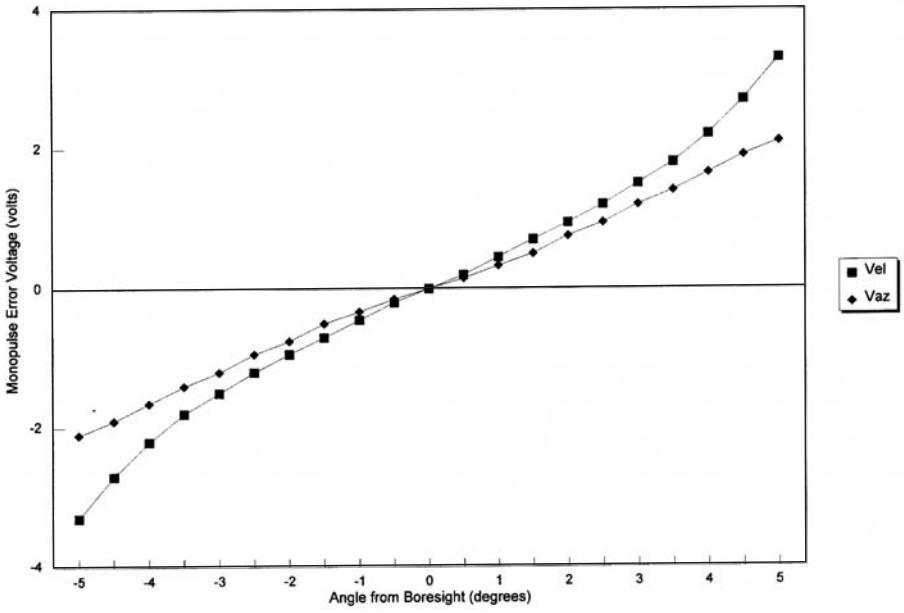

Figure 8.10 Computation of monopulse antenna azimuth and elevation plane error voltages for a 15-inch aperture at 10 GHz.

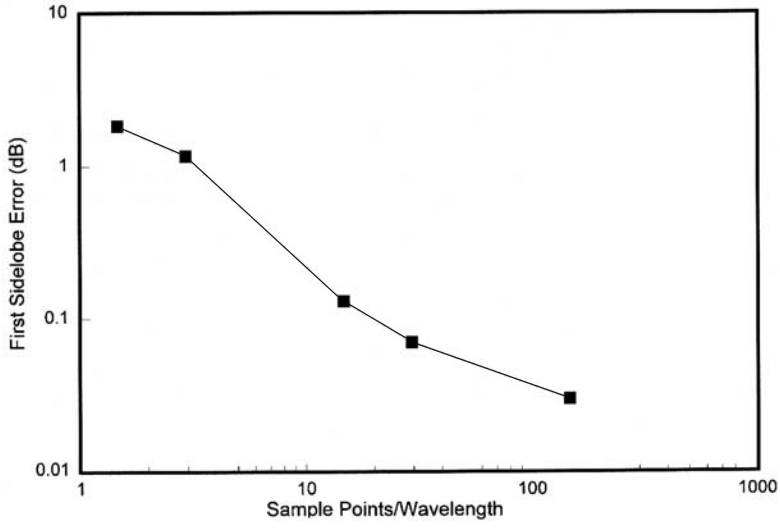

Figure 8.11 Computational error in antenna sidelobe versus sample granularity.

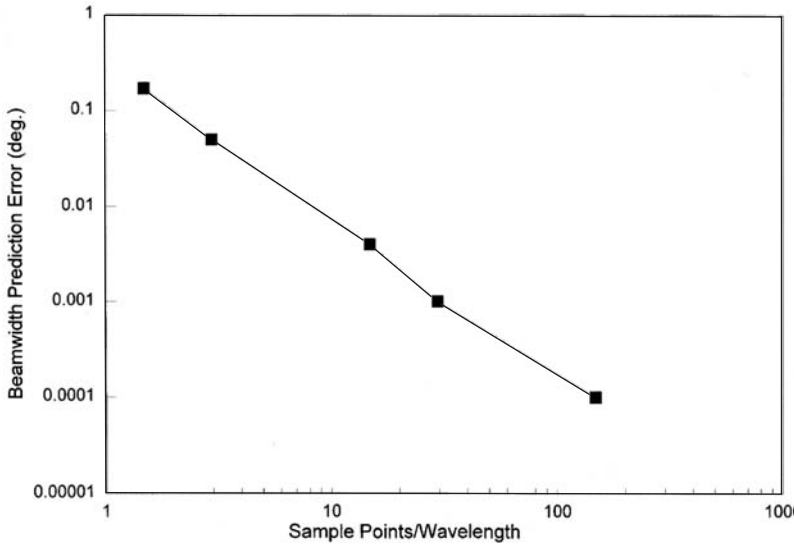

Figure 8.12 Computational error in antenna beamwidth versus sample granularity.

since the resulting wave diffraction with a radome causes a shift in the apparent direction of the target.

In (8.1) and (8.2), we showed how monopulse azimuth and elevation plane error voltages are derived from the monopulse antenna sum and difference port voltages. When no radome is present, the zero crossings in these monopulse error voltage channels correspond to the condition of a target on the antenna axis (i.e., normal to the surface of the antenna). With a radome over the antenna, as the electromagnetic signal propagates through the dielectric radome wall, the resulting wave diffraction causes a shift in the apparent direction of the target.

With the antenna physically boresighted on the target, the azimuth and elevation boresight errors are computed from the following formulas [18]:

$$BSE_{AZ} = \frac{V_{AZ}}{K_{AZ}} \tag{8.21}$$

$$BSE_{EL} = \frac{V_{EL}}{K_{EL}} \tag{8.22}$$

In these equations, the constants K_{az} and K_{el} are the azimuth and elevation difference channel monopulse antenna sensitivity constants, computed (or measured) for the no-radome condition. Usually, these constants have units of

volts-per-milliradian (mrad), and the boresight error has units of milliradians. BSE is highly influenced by antenna polarization and its implication for the azimuth and elevation plane error voltages.

The following steps summarize the modeling process for obtaining a computerized solution to a radome-enclosed monopulse antenna. In these steps, the antenna is assumed to be in a receiving mode.

8.3.2 Computation of the Antenna Pattern Space Phase Terms

Compute the antenna pattern space phase terms, based on a coordinate system centered on the antenna as illustrated in Figure 8.13. Often, in an actual aircraft or missile application, the description of a target's location is given in terms of roll, pitch, and yaw coordinates of the vehicle. To simplify our analysis, a gimbal system was selected for modeling. It describes a target's position in elevation (*EL*) and azimuth (*AZ*) angles. Both *EL*/*AZ* and *AZ*/*EL* gimbal types are possible, as discussed in Chapter 2. The following is a transformation from spherical coordinates selected to EL and AZ angles.

$$EL = \tan^{-1}(\tan\theta \sin\phi) \tag{8.23}$$

$$AZ = \tan^{-1}(\tan\theta \cos\phi) \tag{8.24}$$

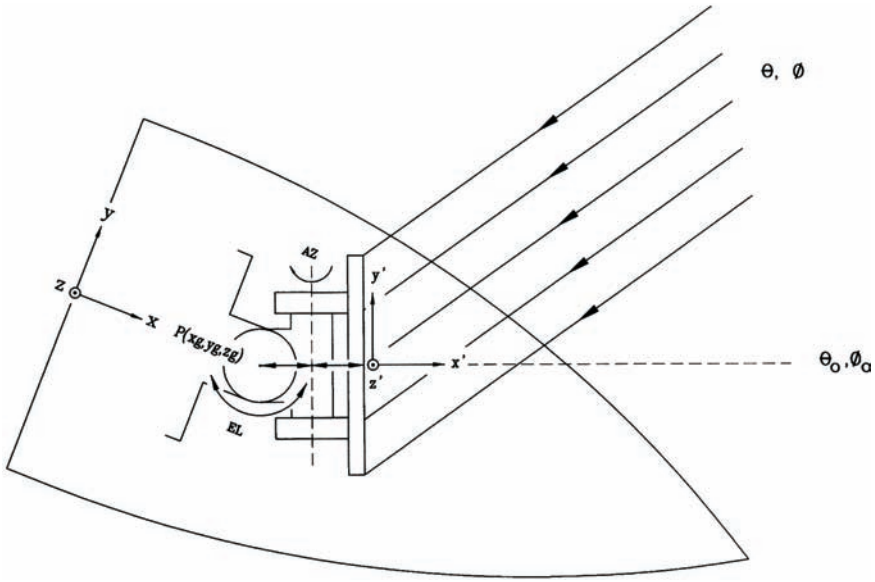

Figure 8.13 Radome and antenna coordinates used in the program TO RADOME.

8.3.3 Transformation of All Aperture Points to Radome Coordinates

For an *AZ*/*EL* gimbal system, the aperture point transformation to radome coordinates is found from [personal communication with R. Matysikiela, American Electronics Laboratories, Landsdale, Pennsylvania, 1994]:

$$\begin{bmatrix} x_i \\ y_i \\ z_i \end{bmatrix} = \begin{bmatrix} \cos AZ \cos EL & -\cos AZ \sin EL & -\sin AZ \\ \sin EL & \cos EL & 0 \\ \sin AZ \cos EL & -\sin AZ \sin EL & \cos AZ \end{bmatrix} \begin{bmatrix} \Delta_b \\ y_i' \\ z_i' \end{bmatrix} + \begin{bmatrix} \Delta_a \cos AZ \\ 0 \\ \Delta_a \sin AZ \end{bmatrix} + \begin{bmatrix} x_g \\ y_g \\ z_g \end{bmatrix} \tag{8.25}$$

Similarly, for an AZ/EL gimbal, the result, including a translation for the initial gimbal location $P(x_g, y_g, z_g)$, is

$$\begin{bmatrix} x_i \\ y_i \\ z_i \end{bmatrix} = \begin{bmatrix} \cos EL \cos AZ & -\sin EL & -\cos EL \sin AZ \\ \sin EL \cos AZ & \cos EL & \sin EL \sin AZ \\ \sin AZ & 0 & \cos AZ \end{bmatrix} \begin{bmatrix} \Delta_b \\ y_i' \\ z_i' \end{bmatrix} + \begin{bmatrix} \Delta_a \cos AZ \\ \Delta_a \sin EL \\ 0 \end{bmatrix} + \begin{bmatrix} x_g \\ y_g \\ z_g \end{bmatrix} \tag{8.26}$$

8.3.4 Transformation of All Ray Vectors from Aperture Sample Points in the Pattern Look Direction

Ray vectors described in this section are those derived from aperture sample points in the pattern look direction. Transform all these ray vectors through the antenna gimbal angles and into radome coordinates.

8.3.5 Project Rays to the Radome Surface

Determine all ray intercept points on the radome surface.

8.3.6 Compute Angle of Incidence

Determine angles of incidence of these rays with respect to the radome surface normal at each intercept point.

8.3.7 Computation of Voltage Transmission Coefficients for Each Ray

Computing each coefficient depends on:

- The angle of incidence of the ray relative to the surface normal at the point where it intercepts the radome wall;
- Radome wall parameters such as the thickness, dielectric constant, and loss tangent of each of the layers;
- The wavelength of operation;
- The polarization of the incident wave.

The WALL program developed in Chapter 5 is utilized as a subroutine in the program TO radome. The subroutine WALL makes the following assumptions: (1) the radome wall is locally plane in the vicinity of the ray intercept, and (2) the radome inner and outer walls are parallel. These approximations have produced reasonably acceptable radome electrical performance predictions in the experience of the author.

8.3.8 Perform an Antenna Aperture Integration

Perform an antenna aperture integration to determine the receive port voltage from the selected pattern look direction and for each sum and difference aperture distribution. The result gives the far-field patterns from which radome transmission loss, BSE, and BSES can be derived. The array pattern normalized to the no-radome case is given in the following formula:

$$E_T = \frac{\sum_{m=1}^{M}\sum_{n=1}^{N} F_{mn}^{a} T_{mn} e^{-jk\left(x_{mn}k_x + y_{mn}k_y + z_{mn}k_z\right)}}{\sum_{m=1}^{M}\sum_{n=1}^{N} F_{mn}^{a}} \tag{8.27}$$

where T_{mn} is the complex transmission coefficient of the radome wall for the ray associated with the mnth aperture point, and k_x, k_y, and k_z are the propagation constants in the x-, y-, and z-planes, respectively.

Figure 8.14 shows a computer software flow diagram for a program called TO RADOME, which was designed to compute the effects of a radome on a monopulse antenna. A complete listing for a Power BASIC program based on this flow diagram appears in Appendix E.

As configured, the program TO RADOME treats tangent ogive radome shapes. You can fit this program to your particular situation by making the following choices:

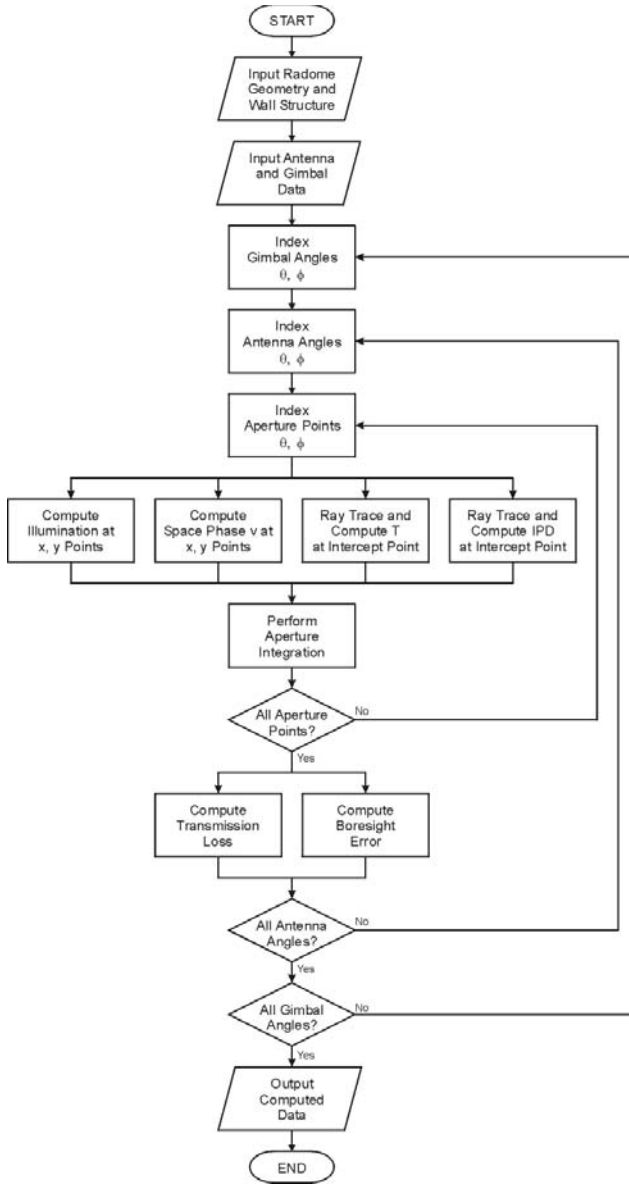

Figure 8.14 Computer software flow diagram for the program TO RADOME.

- Choose either AZ/EL or EL/AZ antenna gimbal configurations.
- Model the radome wall geometry up to 10 layers.
- Specify the thickness, dielectric constant, and loss tangent of each of these layers.

8.4 Additional Modeling Considerations

This section discusses miscellaneous factors that may be necessary to model in a given situation. The discussion that follows applies principally to radomes used on airborne vehicles such as aircraft or missiles.

8.4.1 Rain Erosion of Missile Radomes

For high-speed flight through rain, significant radome material may erode from the outer wall, particularly in ceramic radome materials. To account for the wall thickness reduction, you must modify the radome wall thickness during the modeling process. A relationship of the material eroded per unit area (T_k) for a fixed exposure time and the rain impingement angle d_r (relative to the radome surface normal) can be defined for many materials.

$$T_k = K_m \left(V \sin \gamma_r\right)^{\alpha_m - 1} \tag{8.28}$$

where V is the velocity in meters per second (m/s) and K_m and α_m are the constants for a particular material. For example, slip cast fused silica (SCFS), a popular monolithic radome material, offers excellent thermal shock resistance and electrical properties. However, it has poor rain erosion resistance above Mach 2 [19]. Balageas has published an empirical formula to calculate the material erosion rate of SCFS based on simulation test results [20].

$$\frac{dT_K}{dt} = 10^{-9}\left(3.67 - 6.78D_r + 3.94D_r^2\right)C_r V^{6.3}\left(\sin \gamma_r\right)^{5.3} \tag{8.29}$$

where

dT_k/dt = rate of material erosion (ìm/s);

D_r = diameter of rain drop (mm);

C_r = rain concentration (g/cm^3).

Equation (8.29) calculates the total erosion incurred by the radome by inputting velocity as a function of time on a flight path, and then integrating to find the total material eroded.

Equations similar to the above model require a knowledge of rain data. A computerized environmental analysis technique has been developed to permit the rapid evaluation of path-cumulative rainfall statistics. The analysis postulates a generic thunderstorm of a circular cross section and varying vertical intensity. At a selected altitude, the path-cumulative rainfall is evaluated along a path of arbitrary origin and direction. It is believed that this approach could provide a

much-needed means for quantitatively evaluating the rain environment limitations of tactical missile radomes [21].

For candidate radome materials, the erosion data can be obtained by testing small samples on a high-speed sled through a manmade (simulated) rain field. Tests reported in the technical literature have been at velocities up to approximately Mach 5 (over 1 mile per second) [22]. Silicon nitride has been sled-tested in simulated rain to determine the influence of porosity and density on the response of this material to the rain droplet impact [23]. Variations of Duroid (a glass microfiber-loaded Teflon material) have been run in sled tests [24] to determine the optimum fiber type, content, and orientation for minimum aerothermal ablation and rain erosion.

Data published in the technical literature indicate that in the special case of normal (or near-normal impact) that even with subsonic velocities it is necessary to put a rain erosion cap at the tip of the radome. This cap is usually metallic. To combine very high rain erosion resistance with good electrical properties, a dense silicon nitride cap obtained by hot pressed sintering has been employed, as described in [25]. In radome analysis modeling, an approximation of the effects of a metallic nose cap can be obtained by nulling all rays that intercept the nose cap (geometric optics approach).

8.4.2 Aerothermal Heating

For supersonic homing missiles whose mission includes the attack of supersonic maneuvering targets at a high altitude, the guidance system absolutely requires high accuracy. As a result, the guidance engineer places a stringent requirement on the allowable boresight errors (BSE) caused by the radome. For this reason, many radomes are prescription ground prior to installation on the missile airframe [26].

The effects of aerodynamic heating are:

- A decrease in dielectric permittivity;
- An increase in loss tangent.

As a result, radome BSE, BSES, and losses increase with increasing radome wall temperature.

To model aerodynamic heating of the radome wall, it is often convenient to express the temperatures over the entire surface of the radome as a function of the longitudinal position and as a function of the circumferential position.

Computer programs exist which determine temperatures of an aircraft or missile radome due to aerodynamic heating. This heating is a function of trajectory, altitude profile, velocity, and maneuvers. One such program, URLIM

[27], calculates temperatures for various points along a trajectory. It also computes the bending stresses at the base of the radome due to aerodynamic pressure and maneuver loads.

Thermal analysis theory is discussed in a report written by the Georgia Institute of Technology [27]. The approach generates temperature profiles through the radome material versus trajectory time. The model predicts the effects of temperature changes on electromagnetic windows for single- and multiple-layer windows. Temperature effects on expansion, complex permittivity, and complex permeability are included in the model. Performance factors include transmission, reflection, insertion phase delay, and absorption as functions of the angle of incidence, polarization, and temperature for a flat-plate single- or multiple-layer slab.

The philosophy followed by electromagnetic (EM) radome designers is to provide a radome having low boresight errors at ambient temperature, but not at high temperatures [28]. Because radome-induced errors increase with temperature, if the magnitude of the boresight error is large enough, an oscillatory guidance system instability can result [29]. Compensation (filtering) within the guidance loop is possible to minimize the effects of the boresight error. However, compensation decreases missile responsiveness and missile effectiveness. Missile instability may not necessarily result in significant performance degradation if the errors are confined to small regions of the radome [30].

8.4.3 Radome Effects on Conscan Antennas

Conical scan tracking systems (conscan) are generally less complex and less expensive than monopulse systems. Using conscan, a single antenna beam is offset from the antenna axis and rotated about the antenna. For instance, consider physically rotating an offset antenna reflector or antenna feed. The modulations of a received signal within the antenna beamwidth are correlated with resolvers on the scanning mechanism to determine the position of the target relative to the antenna axis. Conscan was popular for use in small missiles.

Although conscan systems have simplicity and cost advantages relative to monopulse systems, they also have performance deficiencies. For instance, because of the offset and beam nutation, the actual beamwidth of the antenna is up to 40% greater than the minimum beamwidth possible. In some cases, the crossover of the beam is at the half-power point of the two-way antenna pattern. On an antenna boresight, a net loss results in about 3 dB of receive signal gain [10].

In comparing data for conscan antennas with monopulse antennas of the same diameter and gimbal location within the same radome, the differences in computed BSE and radome transmission loss are very small. Therefore, a

conscan antenna can be approximately modeled by a monopulse antenna of the same diameter, using the techniques of this chapter.

References

[1] Dowsett, P. H., "Cross Polarization in Radomes: A Program for Its Computation," *IEEE Transactions on Aerospace Electronics Systems*, Vol. AES-9, No. 3, May 1973, pp. 421–433.

[2] Huddleston, G. K., "Radomes," Ch. 42 in *Antenna Engineering Handbook*, 3rd ed., R. C. Johnson, (ed.), New York: McGraw-Hill, 1992.

[3] Gulick, J. F., "Overview of Missile Guidance," *IEEE Eastcon Record*, September 1978, pp. 194–198.

[4] Sparks, R. A., "Systems Applications of Mechanically Scanned Slotted Array Antennas," *Microwave Journal*, Vol.31, No. 6, June 1988, pp. 26–48.

[5] Lalezari, F., T. C. Boone, and J. M. Rogers, "Planar Millimeter Wave Arrays," *Microwave Journal*, Vol. 34, No. 4, April 1991, pp. 85–92.

[6] Kelly, W., "Homing Missile Guidance—A Survey of Classical and Modern Techniques," *IEEE Southcon Technical Proceedings*, January 1981.

[7] Savage, P. G., "A Strapdown Phased Array Radar Tracker Loop Concept for a Radar Homing Missile," *AIAA Guidance Control Flight Conference*, August 1969, pp. 1–8.

[8] Schuchardt, M. J., and D. J. Kozakoff, "Seeker Antennas," Ch. 38 in *Antenna Engineering Handbook*, 3rd ed., R. C. Johnson, (ed.), New York: McGraw-Hill, 1992.

[9] Hirsch, H. L., and D. C. Grove, *Practical Simulation of Radar Antennas and Radomes*, Norwood, MA: Artech House, 1987.

[10] Skolnik, M. I., *Introduction to Radar Systems*, 2nd ed., New York: McGraw-Hill, 1970.

[11] Huddleston, G. K., "Near Field Effects on Radome Boresight Errors," *Proceedings of the 17th Symposium on Electromagnetic Windows*, Georgia Institute of Technology, Atlanta, GA, July 1984, pp. 41–55.

[12] Hacker, P. S., and H. E. Schrank, "Range Distance Requirements for Measuring Low and Ultra Low Sidelobe Antenna Patterns," *IEEE Transactions on Antennas and Propagation*, Vol. AP-30, No. 5, September 1982, pp. 956–965.

[13] Hansen, R. C., "Measurement Distance Effects on Low Sidelobe Patterns," *IEEE Transactions on Antennas and Propagation*, Vol. AP-32, No. 6, June 1984, pp. 591–594.

[14] Mailloux, R. J., *Phased Array Antenna Handbook*, Norwood, MA: Artech House, 1994.

[15] Sokolnikoff, I. S., and R. M. Redheffer, *Mathematics of Physics and Modern Engineering*, New York: McGraw-Hill, 1958.

[16] Hayward, R. A., E. L. Rope, and G. Tricoles, "Radome Boresight Error and Its Relation to Wavefront Distortion," *Proceedings of the 13th Symposium on Electromagnetic Windows*, Georgia Institute of Technology, Atlanta, GA, September 1976, pp. 87–92.

[17] Siwiak, K., T. Dowling, and L. R. Lewis, "Numerical Aspects of Radome Boresight Error Analysis," *Proceedings of the 14th Symposium on Electromagnetic Windows*, Georgia Institute of Technology, Atlanta, GA, 1978.

[18] Schuchardt, J. M., et al., "Automated Radome Performance Evaluation in the Radio Frequency Simulation System (RFSS) Facility at MICOM," *Proceedings of the 15th Symposium on Electromagnetic Windows*, Georgia Institute of Technology, Atlanta, GA, June 1980.

[19] Barta, J., "Rain and Sand Resistance of SCFS Radomes," *Proceedings of the 18th Symposium on Electromagnetic Windows*, Georgia Institute of Technology, Atlanta, GA, September 1986, pp. 131–138.

[20] Balageas, D., and A. Hivert, "Rain Erosion, a Serious Problem for Slip Cast Fused Silica," *Proceedings of the 13th Symposium on Electromagnetic Windows*, Georgia Institute of Technology, Atlanta, GA, September 1976, pp. 45–49.

[21] Crowe, B. J., "Radome Rain Damage—An Environmental Analysis Technique," *Proceedings of the 15th Symposium on Electromagnetic Windows*, Georgia Institute of Technology, Atlanta, GA, June 1980.

[22] Frazer, R. K., "Rain Erosion Tests of Full Size Slip Cast Fused Silica Radomes at M3.5 and M4.8," *Proceedings of the 17th Symposium on Electromagnetic Windows*, Georgia Institute of Technology, Atlanta, GA, July 1984.

[23] Schmitt, G. F., "Influence of Porosity and Density on the Supersonic Rain Erosion Behavior of Silicon Nitride Radome Materials," *Proceedings of the 13th Symposium on Electromagnetic Windows*, Georgia Institute of Technology, Atlanta, GA, September 1976, pp. 37–44.

[24] Bomar, S. H., et al., *Materials Evaluation*, Technical Report AFAL-TR-73-222, Wright Patterson Air Force Base, Dayton, OH; prepared by Georgia Institute of Technology, Atlanta, GA, 1973.

[25] Letson, K. N., W. G. Burleson, and R. A. Reynolds, "Influence of Angle of Incidence on the Rain Erosion Behavior of Duroid Radome Materials," *Proceedings of the 16th Symposium on Electromagnetic Windows*, Georgia Institute of Technology, Atlanta, GA, June 1982, pp. 181–186.

[26] Weckesser, L. B., et al., "Aerodynamic Heating Effects on Radome Boresight Errors," *Proceedings of the 14th Symposium on Electromagnetic Windows*, Georgia Institute of Technology, Atlanta, GA, June 1978.

[27] Frazer, R. K., "Use of the URLIM Computer Program for Radome Analysis," *Proceedings of the 14th Symposium on Electromagnetic Windows*, Georgia Institute of Technology, Atlanta, GA, June 1978, pp. 65–70.

[28] Kuehne, B. E., and D. J. Yost, "When Are Boresight Error Slopes Excessive?" *Proceedings of the 14th Symposium on Electromagnetic Windows*, Georgia Institute of Technology, Atlanta, GA, June 1978.

[29] Jefferson, F. L., "Minimizing Effects of Temperature Changes on Electromagnetic Windows," *Proceedings of the 20th Symposium on Electromagnetic Windows*, Georgia Institute of Technology, Atlanta, GA, September 1992, pp. 50–55.

[30] Weckesser, L. B., "Radome Aerodynamic Heating Effects on Boresight Error," *Proceedings of the 15th Symposium on Electromagnetic Windows*, Georgia Institute of Technology, Atlanta, GA, June 1980, pp. 97–101.

Selected Bibliography

Garnell, P., and D. J. East, *Guided Weapons Control Systems*, London, England: Pergamon Press, 1977.

Hayward, R. A., E. L. Rope, and G. Tricoles, "Accuracy of Two Methods for Numerical Analysis of Radome Electromagnetic Effects," *Proceedings of the 14th Symposium on Electromagnetic Windows*, Georgia Institute of Technology, Atlanta, GA, June 1978, pp. 53–57.

Huddleston, G. K., "Near-Field Effects on Radome Boresight Errors," *Proceedings of the 17th Symposium on Electromagnetic Windows, Georgia Institute of Technology*, Atlanta, GA, July 1984, pp. 41–55.

Letson, K. N., et al., "Rain Erosion and Aerothermal Sled Test Results on Radome Materials," *Proceedings of the 14th Symposium on Electromagnetics Windows*, Georgia Institute of Technology, Atlanta, GA, June 1978, pp. 109–116.

Pendergrass, T. S., *Radome Analysis*, Technical Report AD-A136805, Huntsville, AL, Teledyne Brown Engineering, 1983.

9

Miscellaneous Radome-Enclosed Antenna Types

Increasingly, radome-enclosed antennas are finding new applications in technology areas that include, but are not limited to, satellite navigation and communications, telecommunications, and avionics. This chapter discusses radome analysis methods for the following situations: spiral antennas, parabolas and other telecommunications antennas, air-supported radomes, metal space frame radomes, and radome-enclosed phased-array antennas.

9.1 Spiral Antennas

9.1.1 Single Mode Spiral Antennas

A planar spiral antenna as illustrated in Figures 9.1 and 9.2 is a very broadband, circularly polarized antenna element. Planar spirals are popular for use in antiradiation homing (ARH) missile guidance systems [1] or in electronics countermeasures (ECM) direction-finding systems on aircraft. A complete discussion of this category of antennas appeared in Chapter 3.

Spiral antennas typically use printed circuit technology. However, this limits their use to low-power transmit or receive applications. Thus, spirals are usually used for passive applications. Current tolerances obtained with this type of fabrication technology permit spiral electrical operation to at least Ka-band on the high end of the spectrum. Spiral antennas are available to at least L-band on the low end of the spectrum. Furthermore, certain loading techniques can reduce size or permit operation at even lower frequencies [2].

Figure 9.1 A broadband, cavity-backed, planar Archimedean spiral antenna. (Photo courtesy of Tracor Aerospace Electronic Systems.)

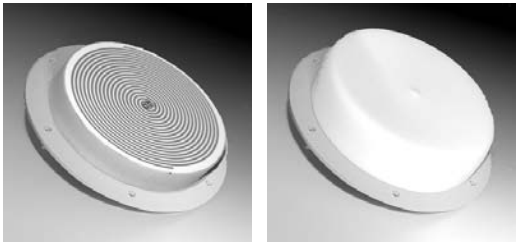

(a) (b)

Figure 9.2 Lower microwave frequency spiral antenna and plastic radome. (Photo courtesy of USDigiComm Corporation.)

The typical antenna half-power beamwidth (HPBW) is up to 90°. This wide, instantaneous field of view makes these antennas attractive for many body fixed missile guidance applications [3]. Spiral antennas can by used in arrays of two or more elements in small interferometers [4]. Missile guidance systems using these are usually fixed-mounted (nongimbaled) with pursuit navigation algorithms to obtain line-of-sight data to the target [5]. Figure 9.3 illustrates several array geometries for reference.

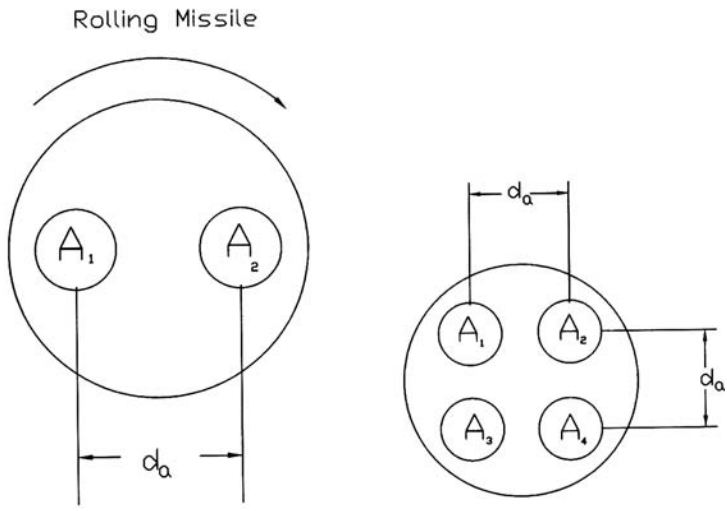

Figure 9.3 Spiral antenna array geometries.

For the no-radome condition, the principal plane sum and difference patterns for the two-element, spiral antenna array are given by the following formulas:

$$\Sigma = \cos\left(\frac{\pi d_a}{\lambda_o}\sin\theta\right)\cos\theta \tag{9.1}$$

$$\Delta = \sin\left(\frac{\pi d_a}{\lambda_o}\sin\theta\right)\cos\theta \tag{9.2}$$

where

θ = angle measured from the antenna boresight;

d_a = center-to-center spacing between the two spiral antennas;

λ_o = the operating wavelength in free space.

Figure 9.4 shows a microwave circuit to resolve the received antenna signals from a four-element spiral array into monopulse sum and difference patterns.

Placing a radome over a spiral antenna array results in an apparent boresight error (BSE) because of the wavefront phase modification over the antenna apertures. These effects need to be carefully considered during the selection of a radome design since they will influence the seeker system accuracy performance [6–8]. Broadband ARH or ECM antennas generally require

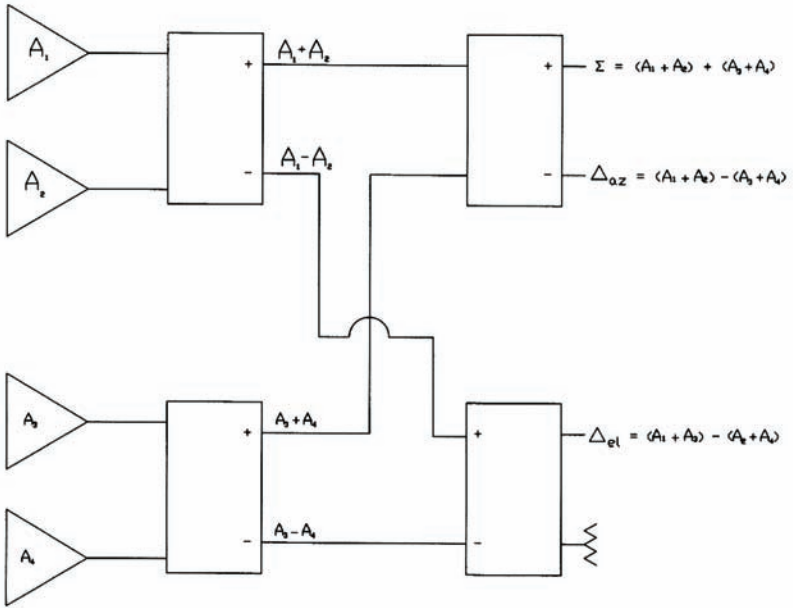

Figure 9.4 Microwave circuit to resolve the received antenna signals from a four-element spiral array into monopulse sum and difference patterns.

multilayer radome walls to obtain a required radome bandwidth commensurate with desired antenna performance. Half-wave wall radomes generally have a useful bandwidth of only 5% to 20%, depending on the dielectric constant and the radome fineness ratio. Higher-order radome walls that are integral multiples of half-wave thick walls have a considerably narrower bandwidth compared to the half-wave wall. They are limited only to very narrowband antenna applications.

When using a spiral antenna array, the relationship between BSE or boresight error slope (BSES) and the miss distance of a missile is sometimes not straightforward. We can quantify this issue only by hardware-in-the-loop (HWIL) simulation testing that takes into account a variety of scenarios and flight conditions [9, 10]. Another method is based on open-loop testing in a suitable anechoic chamber facility. This method requires a precalibration of the monopulse difference channel's sensitivity in volts per degree without the radome in place. Subsequently, the difference channel's voltage characteristics are measured with the radome placed over the antenna array. The following figures are typical for many radome types [3]:

- A boresight error requirement equal to or less than 10 mrad;
- A boresight error slope requirement equal to or less than 0.05%;
- A maximum transmission loss of −1 dB.

The following method is useful for estimating the BSE characteristics of the spiral antenna array. From Figure 9.4, rewrite the monopulse sum and difference formulas to incorporate a radome transmission coefficient associated with each antenna, based on the simple ray trace depicted in Figure 9.5.

$$\Sigma = \left(T_{w1} A_1 + T_{w2} A_2\right) + \left(T_{w3} A_3 + T_{w4} A_4\right) \tag{9.3}$$

$$\Delta_{az} = \left(T_{w1} A_1 + T_{w2} A_2\right) - \left(T_{w3} A_3 + T_{w4} A_4\right) \tag{9.4}$$

$$\Delta_{el} = \left(T_{w1} A_1 \_ T_{w3} A_3\right) - \left(T_{w2} A_2 + T_{w4} A_3\right) \tag{9.5}$$

In these equations, the signal amplitudes of each of the spiral antennas, A_i, are normally all about equal. However, the phase associated with each varies in the array. The transmission coefficients, T_{wi}, can be evaluated by the wall construction, material properties, polarization, wavelength, and the angle of incidence of a ray with respect to the surface normal at the intercept point.

A more accurate method of obtaining estimates of radome impact on the performance of the spiral array is based on equivalent transmission coefficients. Assuming a receive mode, the surface integration shown in Figure 9.6 illustrates the method. The procedure involves the physical optics (PO) method discussed

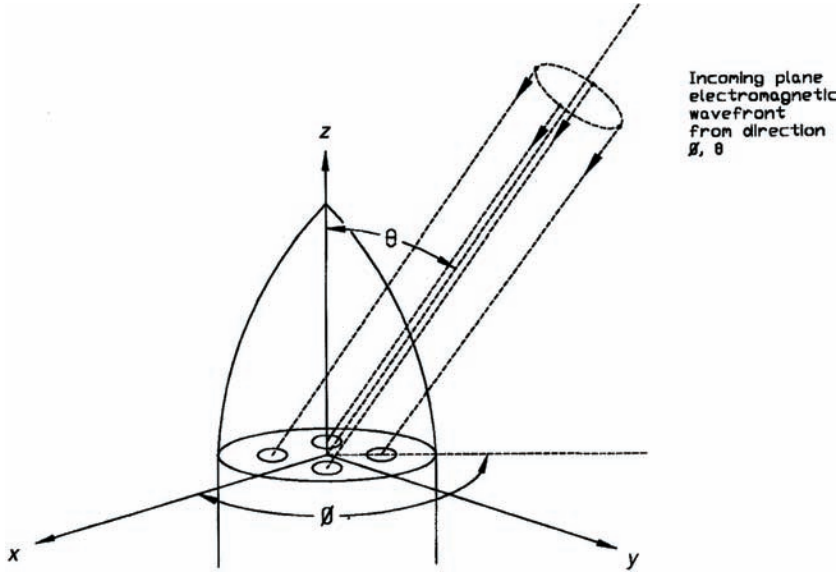

Figure 9.5 Simple ray trace.

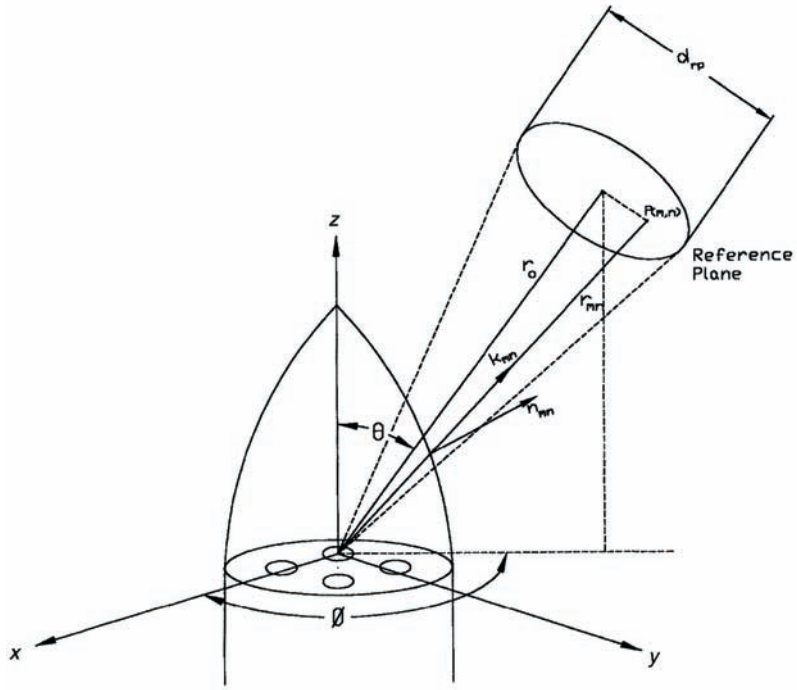

Figure 9.6 Reference plane and ray trace technique to obtain an equivalent transmission coefficient.

in Section 6.3, which models an incoming plane wavefront as an ensemble of Huygens' sources. The external reference plane is used to transform points from the ensemble of Huygens' sources to a point centered on each spiral antenna aperture [11]. In other words, we trace rays coming from points on the external reference plane, incorporating the radome transmission coefficient to modify each ray. From this process, we derive an equivalent transmission coefficient in a given look direction θ, ϕ.

$$T = \frac{1}{MN} \sum_{m=1}^{M} \sum_{n=1}^{N} \frac{T_{mn}}{\left(r_{mn} / r_o\right)} e^{-jk_0 (r_{mn} - r_o)} \tag{9.6}$$

where the m and n indices correspond to points on the external reference plane.

9.1.2 Multimode Spiral Antennas

If the diameter of a spiral antenna is sufficiently large, higher-order modes may exist. These correspond to active ring circumferences corresponding to P_λ for the Pth mode, where P is an integer. The electrical phase of the currents on these

active rings varies from 0 to $2\pi P$ as we progress around the radiating current band. All modes $P > 1$ have a radiation pattern null on boresight. Corzine and Mosko [12] present an in-depth treatment of how the first two modes might be used to generate monopulse sum and difference signals from a single antenna. A circuit for processing the first two modes of a four-arm spiral into monopulse sum and difference signals was presented and discussed in Chapter 3.

Very little technical literature exists on radiation patterns of cavity-backed, planar spiral antennas. However, Reedy et al. [13] developed a combined method of moments (MOM) and general theory of diffraction (GTD) technique.

A simplified method that is proposed here involves performing a numerical integration of the ring current band corresponding to the spiral radiation mode of interest, as illustrated in Figure 9.7. This method will yield a reasonable approximation to the spiral antenna radiation pattern when enclosed in a radome.

In this figure, for the Pth current ring, if we assume that there are a total of M sample points around the ring, the differential phase shift between current sample points is:

$$\phi_M = \frac{2\pi P}{M} \tag{9.7}$$

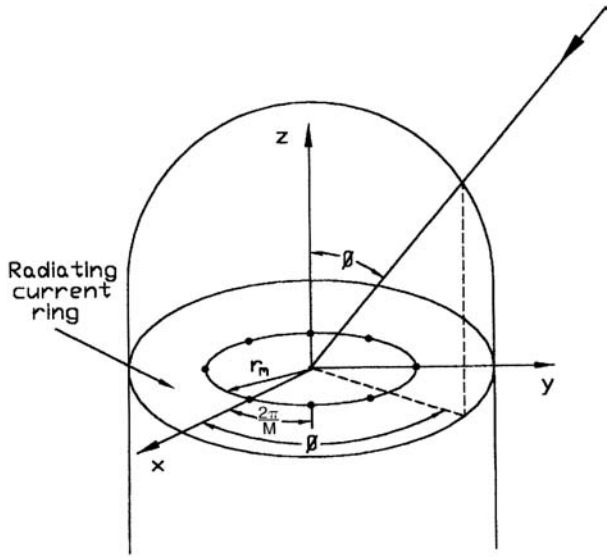

Figure 9.7 Multimode planar spiral in hemispherical radome.

and the phase shift at sample point m is:

$$\phi_m = m\phi_M = \frac{2\pi mP}{M} \tag{9.8}$$

The array factor for the Pth current ring is then broken into ϕ and θ field components:

$$E_x^{AF} = \sum_{m=0}^{N} \left(-\sin\left(\frac{2\pi m}{M}\right) e^{-j\phi_m} \right) T_m(\theta,\phi) e^{jk(x_m \sin\theta\cos\phi + y_m \sin\theta\sin\phi)} \tag{9.9}$$

$$E_y^{AF} = \sum_{m=0}^{N} \left(\cos\left(\frac{2\pi m}{M}\right) e^{-j\phi_m} \right) T_m(\theta,\phi) e^{jk(x_m \sin\theta\cos\phi + y_m \sin\theta\sin\phi)} \tag{9.10}$$

In (9.9) and (9.10), the following definitions apply.

$T_m(\theta, \phi)$ = complex radome wall voltage transmission coefficient associated with the mth sample point for a ray incident from the θ, ϕ direction;

$x_m = x$ coordinate of the mth point on the Pth current ring (m) = $r_p \cos\varphi_m$;

$Y_m = y$ coordinate of the mth point on the Pth current ring (m) = $r_p \sin\varphi_m$;

r_p = radius of Pth current ring (m) = $\dfrac{P\lambda}{2\pi}$.

9.2 Large Parabolic Antennas

Since World War II, the number of telecommunications antenna radomes has steadily increased. As the advantages of radomes become more widely recognized, the rate at which radomes are added continues to grow. To meet this growing need, it is important that specific analysis techniques be developed for telecommunications radomes.

For telecommunications antennas such as parabolas, generally a planar fabric or membrane radome is used, as illustrated in Figure 9.8. These radomes are electrically thin. The losses are held low by using a thin, low-loss material such as Teglar, a fiberglass material coated on both sides with Teflon that sheds water readily [14].

Because of their close proximity to the antenna feed, these planar radomes can introduce small increases in the antenna voltage standing wave ratio (VSWR) [15]. For a planar radome like the one shown in Figure 9.8, the VSWR increase can be reduced by tilting the radome a few degrees (moving the top further from an antenna aperture) to prevent a specular return to the feed horn [16].

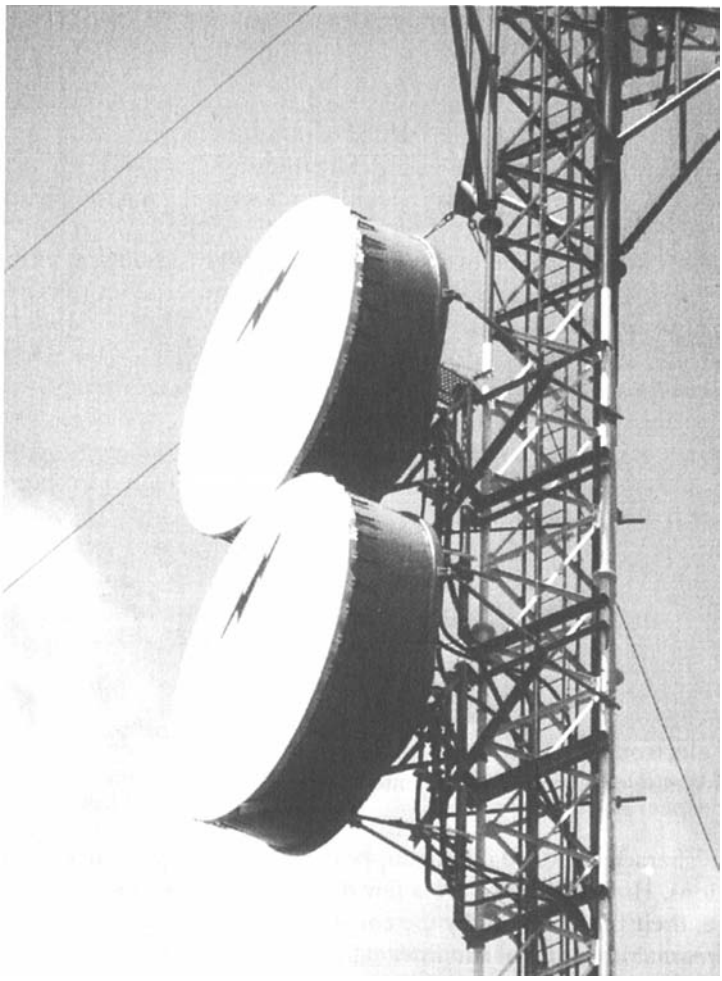

Figure 9.8 Electrically thin radome covers over parabolic antennas. (Photo courtesy of Andrew Corporation.)

9.3 Air-Supported Radomes

Many of the earliest ground-based radomes were hemispherical in shape and were supported by air pressure from within. A nonporous, waterproof dielectric fabric was placed over the antenna system, sealed around the base, and then inflated to clear the antenna. This fabric was electrically thin, and its loss tangent and thickness did not result in any significant transmission loss at the microwave frequencies where the system was used.

The hemispherical shape of these structures offers advantage in high winds. For instance, precipitation particles blow around a sphere rather than

impinge upon it. Therefore, snow, frozen precipitation, or rain is not readily deposited on the spherical surface. With these radome shapes, the incidence angles are usually less than 30°. Such radomes are called normal incidence radomes [17]. The transmission properties of wall structures commonly used in this type of radome are relatively independent on polarization and incidence angles between 0° and 30°, particularly if small tolerances on thickness variations are maintained and a narrow frequency band of operation is specified.

Early materials used for air-supported radomes were neoprene-coated nylon, hypalon-coated Dacron, and Teflon-coated fiberglass [18]. Hemispherical air-supported radomes greater that 70m in diameter are in service today [19].

The advantages of air-supported radomes are:

- Low cost;
- Good electromagnetic transparency over very wide frequency bandwidths;
- Relative ease of erection and dismantling.

These characteristics make air-supported radomes particularly suitable for mobile stations. However, there are a few disadvantages to air-supported radomes. For instance, their life is limited by the constant flexing of the material in the wind. Furthermore, maintenance of the internal pressure in high winds can be difficult. Maintenance is costly and required at frequent intervals for the overall structure and air pressure system.

Since air-supported radomes are electrically thin, monolithic wall structures, the analysis for transmission loss can readily be done using the WALL computer code discussed in Chapter 5. Other than transmission loss, these radomes generally have a negligible effect on antenna sidelobes or depolarization.

9.4 Metal Space Frame Radomes

Rigid, self-supporting, space frame radomes overcome many limitations of air-supported radomes. As illustrated in Figure 9.9, these radomes consist of a three-dimensional lattice of primary, load-bearing, metallic members, which carry the main loads or stresses. The framework is typically steel or aluminum members. This type of design is sometimes called a *geodesic dome*, in which a spherical structure is built from simple geometrical shapes. Geodesic dome design computer software is available in the form of DOME, a freeware DOS utility developed for generating the coordinates of a geodesic dome or sphere [20]. This zip archive includes DOS executable C++ source code. Of all the

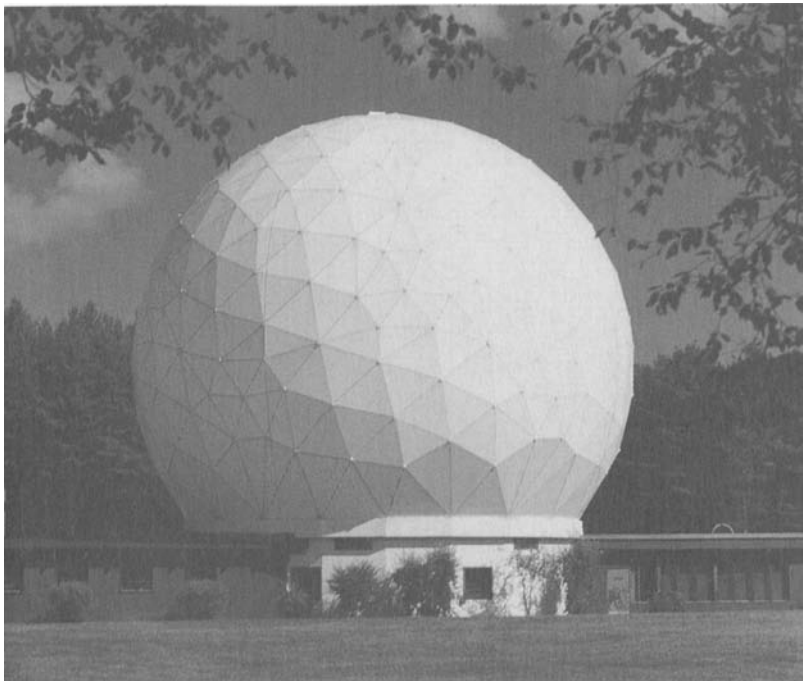

Figure 9.9 Metal space frame radome. (Photo courtesy of Antennas for Communications Inc.)

types of surface structures that have been used, the most common for large ground radomes (greater than 15m in diameter) has been the space frame radome [21].

The primary electromagnetic performance considerations to integrate into the design of a space frame radome are:

- Dielectric wall transmission loss;
- Frame blockage loss;
- Pointing errors.

These considerations are discussed in the following sections.

9.4.1 Dielectric Wall Losses

The radome transmission loss in decibels is composed of two major loss contributors.

$$L = L_w + L_B \tag{9.11}$$

The first and typically the smallest contributor, L_W, is the ordinary insertion loss associated with the signal propagation through the radome wall. In (9.11), it is expressed in decibels. The second loss contributor, L_B, comes from signals scattering off the frame structure. It is a blockage loss term, also expressed in decibels. For most frequency bands, the blockage loss component is larger than the insertion loss of the wall.

The dielectric radome material covering the walls of the dome may be an electrically thin, waterproof fabric, pulled tightly over the surface defined by the metal space frame. The electromagnetic insertion loss of the membrane is governed primarily by the dielectric properties of the membrane and the ratio of membrane thickness to operating wavelength. For the smallest possible loss, it is important to make the membrane as thin as possible.

An alternative to fabric is individual, flat, triangular panels, comprising an A-sandwich radome wall with an internal low-density foam core. The WALL program of Chapter 5 can also be applied here to compute the loss component L_W through the dielectric walls. Note that with a decreasing wavelength, the loss due to the walls generally increases, while the loss due to the radome frame remains substantially constant.

9.4.2 Frame Blockage Losses

In situations involving blockage by antenna feed supports or other obstacles, it has been customary to assume that the blocking satisfies geometric optics. This assumption leads to a simplified formula for blockage loss in decibels for a metal space frame radome [21].

$$L_B = 10\log\left(\sqrt{3}\,\frac{w_B}{L_B}\left[1+\frac{h_B}{L_B}\,\frac{\sin^{-1}\eta_A\sqrt{1-\eta_A^2}}{\eta_A^2}\right]\right) \tag{9.12}$$

where

w_B = beamwidth;

L_B = beam length;

h_B = beam dimension in radial direction;

η_A = antenna diameter to radome diameter ratio.

Equation (9.12) can be rewritten in the following manner:

$$L_B = 10\log\left(\sqrt{3}\,\frac{w_B}{L_B}\left[2+\frac{h_B}{w_B}G(\eta_A)\right]\right) \tag{9.13}$$

In (9.13), we define the optical blockage function via the next formula:

$$G(\eta_A) = \frac{\sin^{-1}\eta_A - \eta_A\sqrt{1-\eta_A^2}}{\eta_A^2} \tag{9.14}$$

This optical blockage function is plotted in Figure 9.10.

9.4.3 Pointing Errors

The pointing errors introduced by space frame radomes are extremely small, usually less than 0.1 mrad.

A uniform space frame geometry theoretically can produce no boresight error (BSE). As the geometry departs from perfect uniformity, the first significant effect is boresight error. For well-designed radomes, this appears to be the only significant effect. Boresight errors can result from: (1) imperfect uniformity of the space frame geometry as designed, and/or (2) tolerance or manufacturing variations.

To minimize the BSE pattern distortion of the main lobe and close-in sidelobes, the metallic frame geometry should have two characteristics:

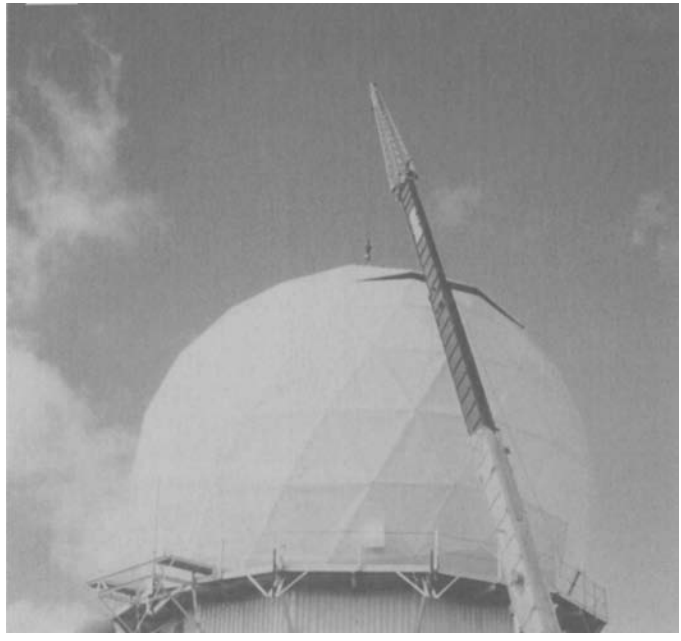

Figure 9.10 Dielectric space frame radome. (Photo courtesy of Antennas for Communications Inc.)

- Be as uniform as possible. In other words, the blocking area ratio should be the same in all parts of the radome. The blocking area geometry shown in Figure 9.11 is one that achieves the latter requirement quite effectively [22]
- Be as random as possible. The more random the space frame geometry, the less the BSE.

9.5 Dielectric Space Frame Radomes

The framework of a dielectric space frame radome typically consists of plastic, as opposed to steel or aluminum members. These radomes have several advantages over other ground-based radome types. The radome walls may be constructed as a thin membrane, a solid laminate, or a multilayer sandwich with internal foam cores. For the thin membrane wall, the radome panel flanges have dimensions capable of supporting the environmental wind loads. Often a two- or three-layer sandwich wall is used where thermal insulation or high-frequency and low-frequency loss requirements prevail.

The dielectric beams or struts act as dielectric loads. The radome engineer can add inductive elements to impedance-match a capacitive circuit load over the required bandwidth. These inductive elements might be implemented via metalized elements dispersed into the radome panel fabric or wall material. The resulting design provides reduced overall radome transmission loss, compared to what can be achieved with a metal frame radome [23]. Figure 9.12 shows typical data comparing the transmission loss of a metal space frame radome with a dielectric space frame radome of the same size and construction.

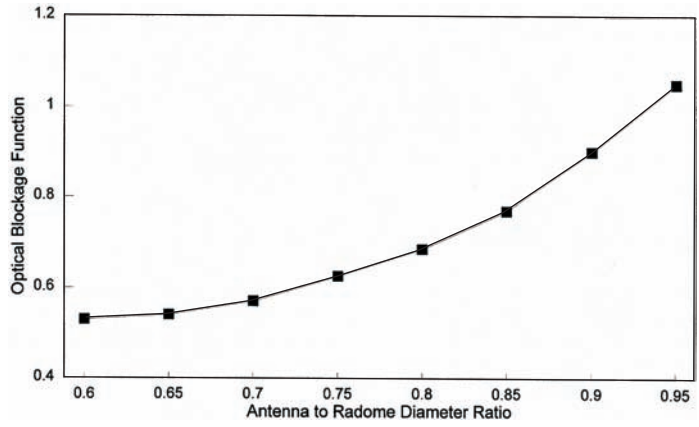

Figure 9.11 Optical blockage function versus antenna-radome diameter ratio [21].

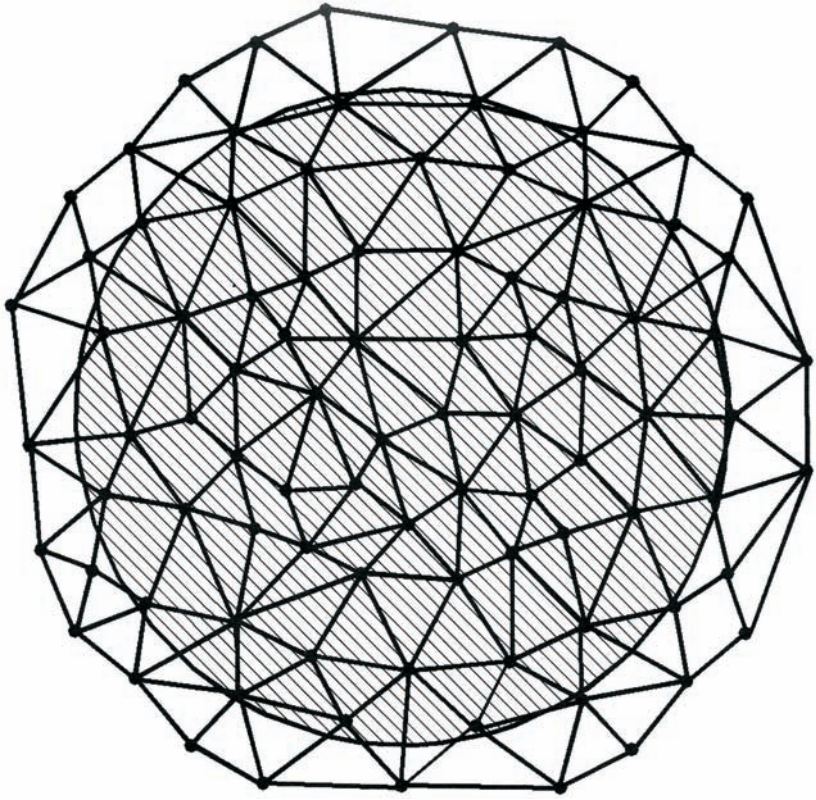

Figure 9.12 Projection of the radome frame onto the antenna aperture [22].

9.6 Radome Enclosed Phased-Array Antennas

For a phased-array antenna, the total antenna pattern can be expressed as a product of the element antenna pattern and an array factor:

$$E(\theta,\phi) = E_e(\theta,\phi)E^{AF} \tag{9.15}$$

The most commonly used element radiators for phased-array antennas are as follows:

- Dipoles;
- Slots in waveguide;
- Open-ended waveguides;
- Small horn antennas;
- Spiral antennas;

- Microstrip patch or disk radiator elements.

A corporate feed for a phased-array antenna is shown in Figure 9.13.

For a square array in the *x*-*y* plane, assume the following: (1) the index on elements in the *x*-direction is *m* and its greatest value is *M*, and (2) the index on elements in the *y*-direction is *n* and its greatest value is *N*. If the element amplitude weighting distributions, B_m and C_n, are selected independently in the principal planes of the antenna aperture, a separable amplitude distribution results so that $A_{mn} = B_m C_n$. The array factor can then be written as a product of two independent variables *u* and *v* [24]:

$$E^{AF} = \sum_{m=0}^{M} I_{mn} e^{-jk_o m d_x u} \sum_{n=0}^{N} e^{-jk_o n d_y v} \tag{9.16}$$

The following definitions for *u* and *v* apply in (9.16), where the desired phased-array beam pointing angle is èo, f$_o$:

$$u = \sin\theta_o \cos\phi_o \tag{9.17}$$

$$v = \sin\theta_o \sin\phi_o \tag{9.18}$$

Asymmetric aperture distributions are not used except for generating shaped antenna beams. For simplicity, only symmetric aperture distributions are assumed in this chapter. Specifically, an odd number of elements, *N*, along the *x*-axis and *M* elements along the *y*-axis are assumed. The center of the array is

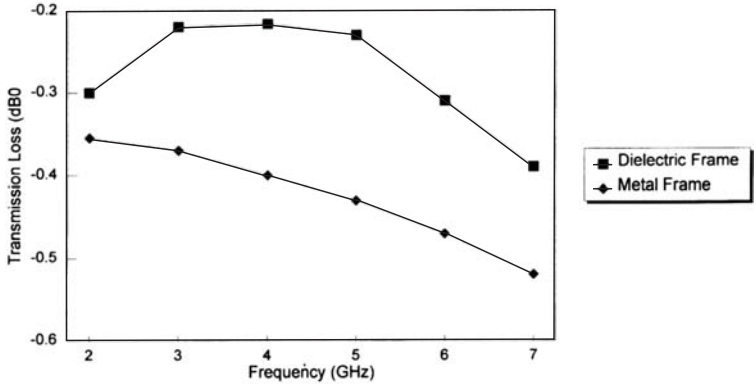

Figure 9.13 Comparison of transmission loss of a common metal space frame radome compared to a dielectric space frame radome.

always taken at $x = 0$, $y = 0$. Element spacings are assumed to meet the grating lobe criteria:

$$\frac{d}{\lambda_o} \leq \frac{1}{1 + \sin\theta_{\max}} \tag{9.19}$$

where $\theta_{\max}$ is the maximum antenna scan angle. Interelement spacing of one wavelength at the highest frequency of operation does not allow any scan. Interelement spacing of about a half wavelength allows phased-array antenna scan angles through about 80°.

Beam scanning with planar antenna arrays is accomplished by introducing a linear phase shift along both principal array coordinates, according to the above relationships. There are two types of electronic phase shifters currently being used in phased-array antennas: the ferrite and the diode phase shifter. The selection of the best type for a design depends on the frequency and RF power handling required. A comprehensive discussion appears in Tang and Burns [25].

The current excitation at the *mn*th antenna element can be expressed as:

$$I_{mn} = A_{mn} e^{jk_o\left(md_x \sin\theta_o \cos\phi_o + nd_y \sin\theta_o \sin\phi_o\right)} \tag{9.20}$$

In this form of beam steering, the required phase is the sum of a row phase and a column phase term. We can use this result to define the array factor that results with a radome in place over the phased array.

$$E^{AF} = \sum_{m=0}^{M} A_{mn} T_{mn} e^{-jk_o md_x(\sin\theta\cos\phi - \sin\theta_o\cos\phi_o)} \sum_{n=0}^{N} e^{-jk_o nd_y(\sin\theta\cos\phi - \sin\theta_o\cos\phi_o)} \tag{9.21}$$

where $T_{mn}(\theta, \phi)$ represents the complex radome voltage transmission coefficient at the *mn*th point associated with a ray incident from the θ, ϕ direction. Figure 9.14 shows a corporate fed phased array to scan a single beam.

The array factor can be computed for any arbitrary A_{mn} distribution. For instance, Figure 9.15 shows a method of achieving a simultaneous sum and difference monopulse beam for a phased-array antenna. The signals from a pair of radiating elements which are located symmetrically opposite from the centerline of the array are combined in a matched hybrid (magic T) to form the sum and difference antenna signals. The sum signals from all the pairs across the array aperture are then combined in a power combiner network to form a sum beam.

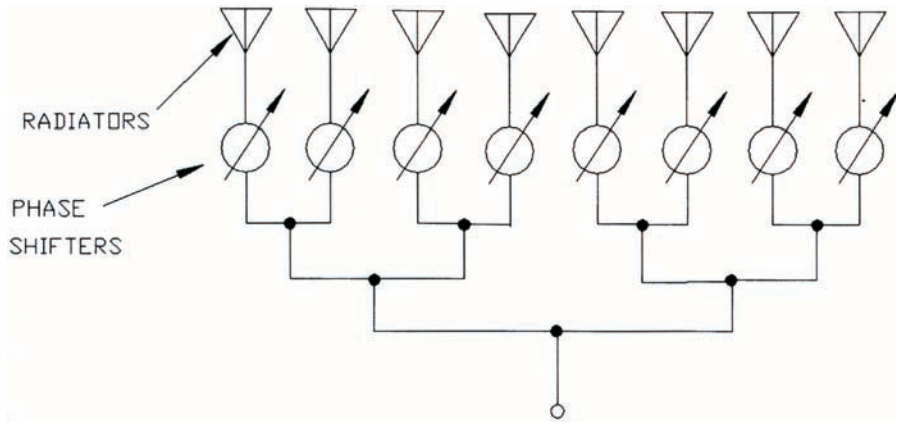

Figure 9.14 Corporate feed for a phased-array antenna.

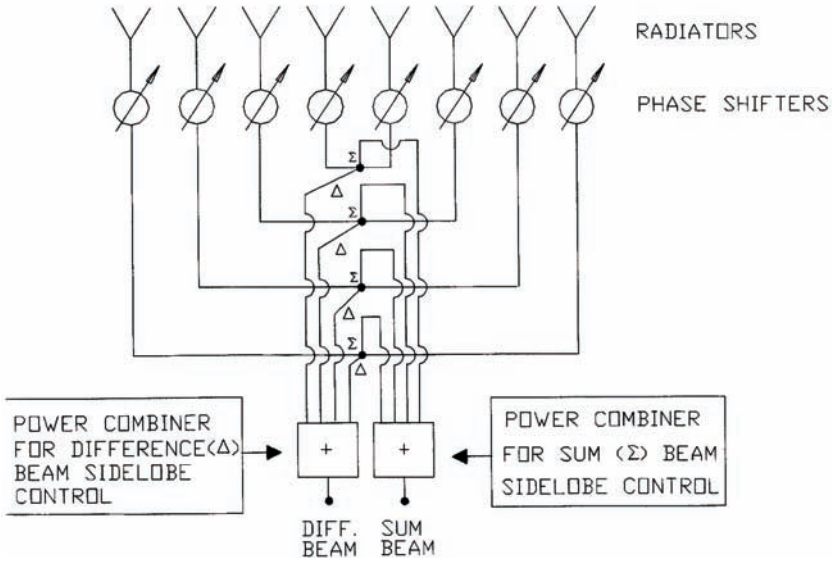

Figure 9.15 Phased-array monopulse feed.

The desired amplitude distribution for the sum beam can be achieved by proper weighting of the signals in the combiner network. The difference signals from all the pairs are combined in a separate power combiner network in order to form a difference beam. Amplitude weighting in the two combiner networks can take several forms to obtain low sidelobes for both the sum and the difference antenna beams. For instance, a Bayliss type of distribution produces low

sidelobes for a difference beam [26]. For a $\cos^q$ type of sum channel distribution, for a square array the first sidelobes correspond to −23 dB and −32 dB for q equal to 1 and 2, respectively.

References

[1] Dyson, J. D., "Multimode Logarithmic Spiral Antennas," *National Electronics Conference*, Vol. 17, October 1961, pp. 206–213.

[2] Morgan, T. E., "Reduced Size Spiral Antenna," *IEEE Ninth European Microwave Conference Proceedings*, September 1979, pp. 181–185.

[3] Schuchardt, J. M., D. J. Kozakoff, and M. Hallum, "Seeker Antennas," Ch. 38 in *Antenna Engineering Handbook*, 2nd ed., R. C. Johnson and H. Jasik, (eds.), New York: McGraw-Hill, 1988.

[4] Schuchardt, J. M., and W. O. Purcell, "A Broadband Direction Finding Receiving System," *Martin Marietta Interdivision Antenna Symposium*, Orlando, FL, August 1967, pp. 1–14.

[5] Feagler, E. R., "The Interferometer as a Sensor for Missile Guidance," *IEEE Eastcon Record*, September 1978, pp. 203–210.

[6] Marales, G., "Simulation of Electrical Design of Streamlined Radomes," *AIAA Summer Computer Simulation Conference*, Toronto, Canada, July 1979, pp. 353–354.

[7] Ossin, A., *Millimeter Wavelength Radomes*, Report AFML-TR-79-4076, Wright Patterson Air force Base, Dayton, OH, July 1979.

[8] Siwak, K., et al., "Boresight Errors Induced by Missile Radomes," *IEEE Transactions on Antennas and Propagation*, Vol. AP-27, November 1979, pp. 832–841.

[9] Russell, R. F., and S. Massey, "Radio Frequency System Simulator," *AIAA Guidance Conference*, August 1972, pp. 72–861.

[10] Sutherlin, D. W., and C.L. Phillips, "Hardware-in-the-Loop Simulation of Antiradiation Missiles," *IEEE Southeastcon Proceedings*, Clemson, SC, April 1976, pp. 43–45.

[11] Israel, M., et al., "A Reference Plane Method for Antenna Radome Analysis," *Proceedings of the 15th Symposium on Electromagnetics Windows*, Georgia Institute of Technology, Atlanta, GA, 1980.

[12] Corzine, R. G., and J. A. Mosko, *Four Arm Spiral Antennas*, Norwood, MA, Artech House, 1990.

[13] Reedy, C. J., M. D. Deshpande, and D. T. Fraleeh, *Analysis of Elliptically Polarized Cavity Backed Antennas Using a Combined FEM/MOM/GTD Technique*, NASA CR 198197, August 1995.

[14] Sellar, C. A., Jr., "Preliminary Testing of Teflon as a Hydrophobic Coating for Microwave Radomes," *IEEE Transactions on Antennas and Propagation*, Vol.AP-27, No. 4, July 1979, pp. 555–557.

[15] Redheffer, R. M., *The Interaction of Microwave Antennas with Dielectric Sheets*, Radiation Laboratory Report 484-18, Boston, MA, MIT Lincoln Laboratory, March 1946.

[16] Knop, C. M., "Microwave Relay Antennas," Ch. 30 in *Antenna Engineering Handbook*, 3rd ed., R. C. Johnson, (ed.), New York: McGraw-Hill, 1993.

[17] Huddleston, G. K., and H. H. Bassett, "Radomes," Ch. 44 in *Antenna Engineering Handbook*, 3rd ed., R. C. Johnson, (ed.), New York: McGraw-Hill, 1993.

[18] Skolnik, M. I., *Introduction to Radar Systems*, 2nd ed., New York: McGraw-Hill, 1994.

[19] Bird, W. W., "Large Air Supported Radomes for Satellite Communications Ground Stations," *Proceedings of the OSU-RTD Symposium on Electromagnetic Windows*, Ohio State University, 1964.

[20] Bono, R., "Geodesic Domes," http://www.cris.com/~rjbono/html/domes.html, 1996.

[21] D'Amato, R., "Metal Space Frame Radome Design," *International Symposium on Structures Technology for Large Radio and Radar Telescope Systems*, Massachusetts Institute of Technology, October 1967.

[22] Kay, A. L., "Electrical Design of Metal Space Frame Radomes," *IEEE Transactions on Antennas and Propagation*, Vol. AP-13, March 1965.

[23] Dielectric Space Frame (DSF) Radome Advantages, Antennas for Communication (AFC) Company, ttp://www.ocala.com/afc/imp_mat.gif, 2009.

[24] Rudge, A. W., et al., *A Handbook of Antenna Design*, London, England: Peter Peregrinus Ltd., 1986.

[25] Tang, R., and R. W. Burns, "Phased Arrays," Ch. 20 in *Antenna Engineering Handbook*, 3rd ed., R. C. Johnson, (ed.), New York: McGraw-Hill, 1993.

[26] Bayliss, E. T., "Design of Monopulse Difference Patterns with Low Sidelobes," *Bell Systems Technical Journal*, May-June 1968, pp. 623–650.

Selected Bibliography

Bird, W. W., "Large Air Supported Radomes for Satellite Communications Ground Stations," *Proceedings of the OSU-RTD Symposium on Electromagnetic Windows*, Ohio State University, 1964.

Schuchardt, J. M., et al., "Automated Radome Performance Evaluation in the RFSS Facility at MICOM," *Proceedings of the 15th Electromagnetic Windows Symposium*, Georgia Institute of Technology, Atlanta, GA, June 1980.

Webb, L. L., "Analysis of Field-of-View Versus Accuracy for a Microwave Monopulse," *IEEE Southeascon Proceedings*, April 1973, pp. 63–66.

Part IV
Radome Specifications and Environmental Degradations

10

Specifying and Testing Radome Performance

10.1 Specifying Aircraft Radomes

The RTCA document DO-213 [1] gives an interesting overview of earlier minimal operational performance requirements for aircraft radomes used to enclose Doppler weather radar antennas. Therein, radome transmission efficiency is defined as the one way that power transmission loss is expressed in percentage. For the various radome classes discussed earlier in this book, the average and minimum radome transmission efficiencies are as shown in Table 10.1.

The maximum radome BSE over the allowable scan angles of the antenna is specified as 8.72 mrad, the increase in beamwidth of the antenna is not to increase by more than 10%, and the power reflected back into the antenna by the radome is not to exceed 0.5%.

10.2 Specifying Radomes for Terrestrial and Marine SATCOM Antennas

The satellite receives uplink signals, optionally processes these signals, translates them in frequency, and amplifies and retransmits these signals to another satellite or to one or more earth terminals. Besides normal requirements for low radome loss (–0.5-dB goal), for SATCOM use there are three special problems the designer will encounter:

Table 10.1
Aircraft Radome Transmission Efficiency

Radome Class	Average Transmission Efficiency	Minimum Transmission Efficiency
a	90%	85%
b	87%	82%
c	84%	78%
d	80%	75%
e	70%	55%

- Small radome depolarization to not degrade frequency reuse performance (as small as −40- to −50-dB radome depolarization sometimes required);
- Small registration error (difference between uplink and downlink BSE) that establishes the transmit beam direction based on the direction of the arrival beam;
- Very small, far-out sidelobes to conform to sidelobe envelope specifications appearing in FCC Part 25.209 regulations, Intelsat IESS-207 and IESS-601, Eutelsat EESS500, and so forth.

The key requirements for radomes enclosing SATCOM antennas are covered in MIL-R-7705B [2], MIL-STD-188-146 [3], and by Lida [4], Kolawole [5], Tirro [6], and Evans [7].

10.3 Radome Testing Methodology

Radome electrical characterization testing is obviously required during the design and development stage of new aircraft radomes. However, electrical testing is also required for after the repair of radome defects according to International standards as well as the aircraft manufacturers' component maintenance manuals. The following sections detail testing methods and general test equipment that is required in order to accomplish these tests and that is derived from Fordham [8], Hartman [9], and Hollis et al. [10].

10.3.1 Outdoor Test Facilities

Radome tests performed on outdoor far-field ranges are normally in the very far field where

$$R \geq \frac{2D^2}{\lambda}$$

where D is the diameter of the largest antenna and λ is the free space wavelength computed at the test frequency.

In an outdoor far-field range configuration, the test antenna within the radome under test is normally installed on a test positioner located on a tower, roof, or platform outside the instrumentation control room. The microwave receiver front end is usually located at the base of this test positioner, thereby requiring only a single RF path through the positioner, greatly simplifying system design. This setup as used for BSE or radome loss measurements is illustrated in Figure 10.1.

For multiported antennas, for instance, a monopulse antenna having a sum channel and azimuth and elevation difference channels, simultaneous measurements can be made on all ports using multiplexers. The receiver front end is remotely controlled from the control console through interfaces with the receiver.

Often, the position of the radome is electronically mechanically controlled around the fixed receive antenna. The radome test positioner axes are read out

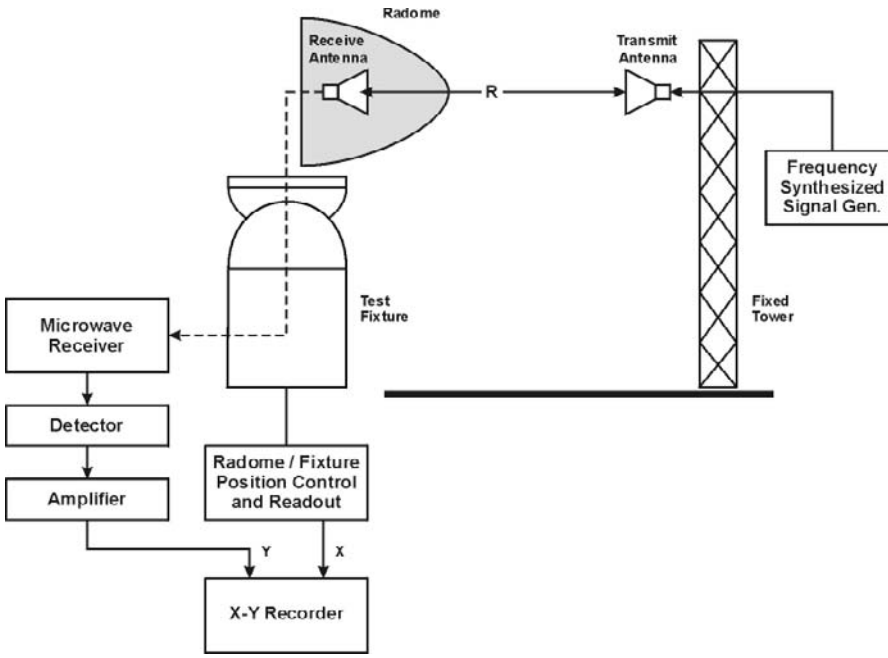

Figure 10.1 Test setup for radiation pattern and BSE measurements.

by positioner control and readout units. A typical control system consists of a control unit located in the operator's console interfaced to a power amplifier unit located near the test positioner. This configuration keeps the high power signals away from sensitive measurement instruments while providing a remote control of positioner functions from the equipment console.

The transmit antenna is normally located at the opposite end of the outdoor far-field antenna range on a tower or other supporting structure. The frequency synthesized signal source is installed near the transmit antenna to minimize signal loss. For some applications a multiplexer can be used between the signal source and a dual polarized transmit antenna allowing simultaneous copolarization and cross-polarization measurements to be performed. Utmost attention must be paid to test procedures and measurement sequences. After the measurements are completed, most modern radome test facilities will automatically generate a test report for documentation purposes.

An equipment test setup for measuring radome-induced antenna VSWR is shown in Figure 10.2. This can also be easily implemented in an outdoor facility free and clear from reflections from objects in the vicinity of the measurements.

10.3.2 Use of Indoor Anechoic Chambers

According to RTCA DO-213 [1] for indoor anechoic chambers, the minimum range distance R between the transmitting signal source and the receiving antenna as illustrated in Figure 10.3 shall be

$$R \geq \frac{D^2}{2\lambda}$$

where D is the diameter of the largest antenna and λ is the free space wavelength computed at the test frequency. This is generally not as good as what is obtainable on outdoor antenna test ranges. Indoor anechoic chamber facilities are generally extremely compact (chamber size 5-m length × 5-m width × 10-m depth) and can handle most aircraft radomes used in the industry.

The tests performed in these indoor anechoic chambers are transmission efficiency, sidelobe level increase, and radome BSE. The procedure and equipment operation using modern test equipment is most often completely automated, so that an electronics technician is normally the only skill level required to operate an indoor anechoic chamber radome test facility. For instance, in Figure 10.4 a special automated positioner is seen, which allows the radome to be moved around a fixed antenna. A photo of a radome loss measurement in process in an indoor anechoic chamber facility is shown in Figure 10.5.

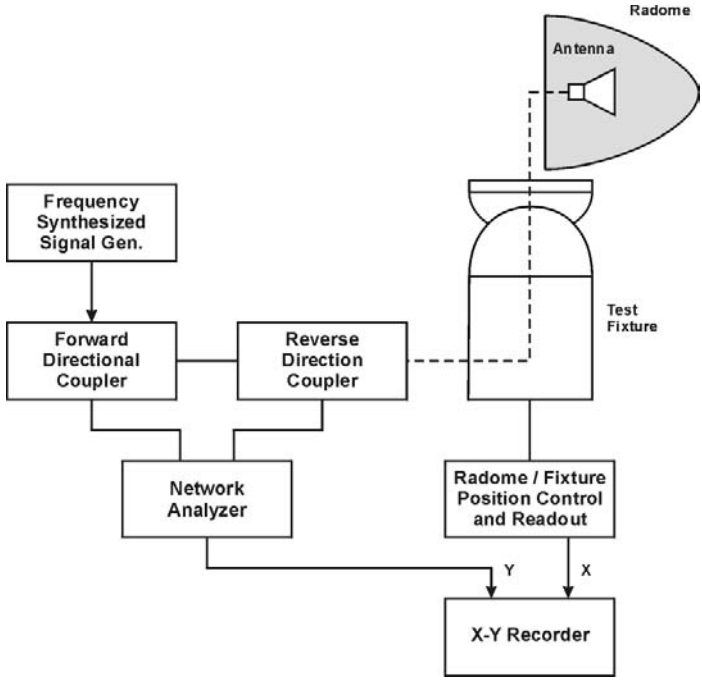

Figure 10.2 Test setup for radome-induced antenna VSWR.

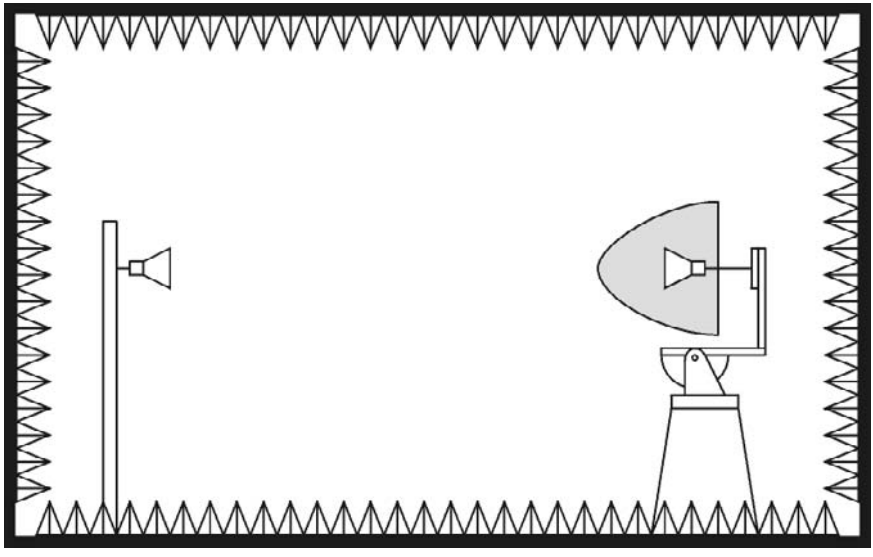

Figure 10.3 Radiation pattern measurement in indoor anechoic chamber.

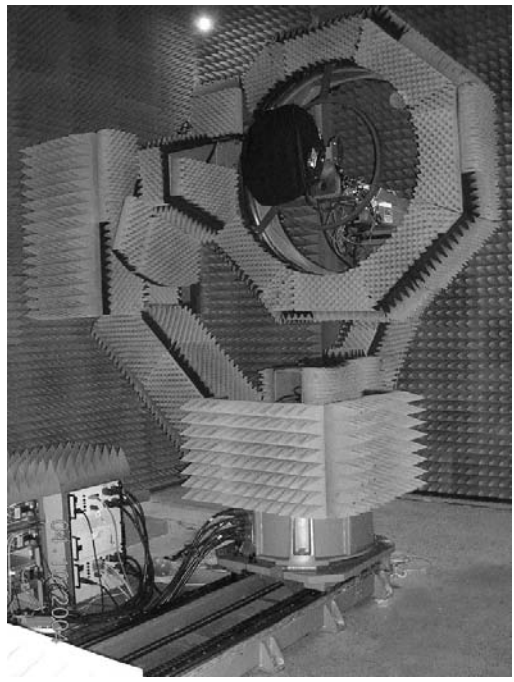

Figure 10.4 Photo of radome positioner mechanism for indoor anechoic chamber testing. (Photo courtesy of MI Technologies.)

As with outdoor testing, after the measurements are completed, most modern radome test facilities will automatically generate a test report for your documentation purposes.

10.3.3 Use of Compact Range

A compact antenna test range is a facility that is used to provide convenient testing of antenna systems at frequencies where obtaining far-field spacing to the antenna under test would be infeasible using traditional methods. The compact range mechanically collimates electromagnetic energy, thus creating a plane wave useful for testing antennas in a far-field environment. The compact range uses a source antenna that radiates a spherical wavefront and one or more secondary reflectors to collimate the radiated spherical wavefront into a planar wavefront within the desired test zone, often designated as the quiet zone. A horn feed antenna and a reflector, one typical implementation to accomplish this, are depicted in Figure 10.6 where a radome-enclosed antenna measurement is shown being tested in a compact antenna range. A photograph of such a facility can be seen in Figure 10.7.

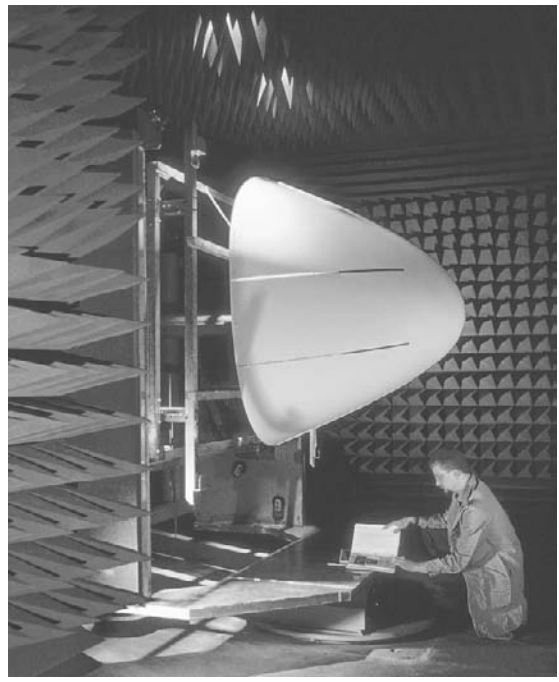

Figure 10.5 Photo of radome loss measurement in an indoor anechoic chamber. (Photo courtesy of Saint-Gobain Performance Plastics.)

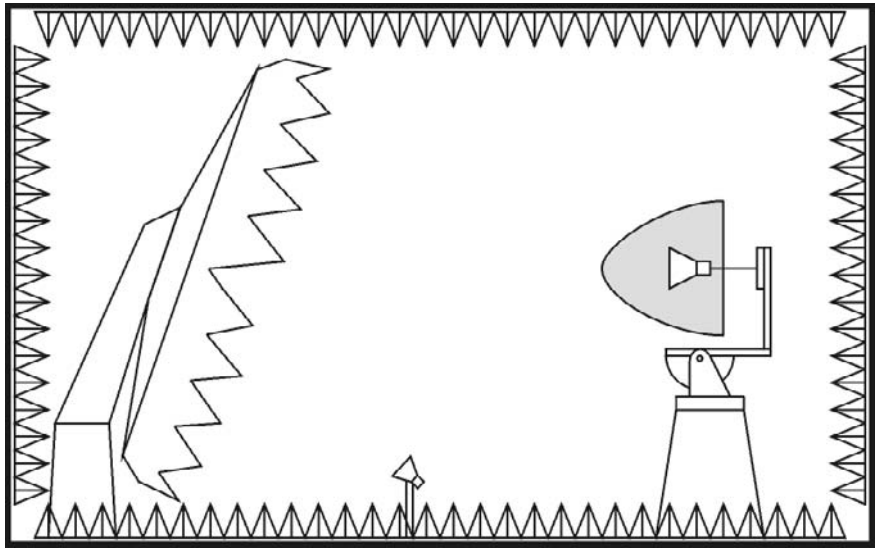

Figure 10.6 Facility for radome measurements in a compact range.

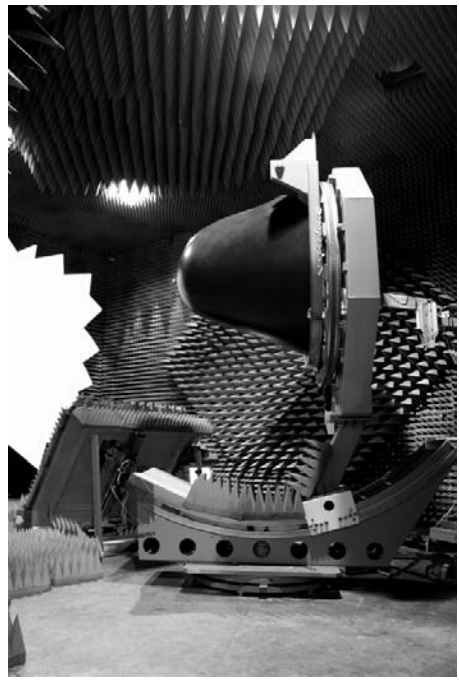

Figure 10.7 Compact antenna range with reflector. (Photo courtesy of MI Technologies.)

The physical dimensions of a compact range can be much less than the size required for a full-size, far-field anechoic chamber. However, the cost of fabrication of the specially designed reflector often can be expensive because of the need for a precision reflecting surface (typically less than ë/100 RMS surface accuracy) and the need to specially treat the edge of the reflector to avoid diffracted waves, which can interfere with the desired beam pattern.

When using a compact range to characterize radomes, the phase and amplitude variations across the antenna under test should be less than 10° and –0.5 dB, respectively.

10.3.4 Near-Field Testing Options

Near-field ranges operate by measuring the electromagnetic field near the antenna and then mathematically transforming the data to any arbitrary location. Near-field operations are a form of microwave holography. The wavefront measurements are normally made on a planar, spherical, or cylindrical surface. The foundation of near-field testing is based on Huygens' principle, which states that every point in an electromagnetic field or a wavefront can be considered the source of a secondary spherical wavelet that spreads out uniformly in all directions. The far-field angular response of an antenna can be determined by

Figure 10.8 Photo of radome test in spherical near field test facility. (Photo courtesy of Orbit FR.)

measuring the electromagnetic field distribution near the antenna and using Huygens' principle to compute the far-field response. The far-field energy is computed by summing all of the near-field spherical wavelet contributions to the desired point in the far-field region.

Spherical near-field radome test equipment designed for the indoor testing of nose-mounted radomes of commercial traffic aircraft have been designed and are marketed by a number of companies [11, 12]. Figure 10.8 shows this type of range in use.

References

[1] Minimum Operational Performance Standards for Nose Mounted Radomes, Document RTCA/DO-213, RTCA, Washington, D.C., 1993.

[2] MIL-R-7705B, *General Specification for Military Specification Radome*, January 1975.

[3] *Interoperability and Performance Standards for Satellite Communications*, MIL-STD-188-146, 1983.

[4] Lida, T., *Satellite Communications*, Fairfax, VA: IOS Press, 2002.

[5] Kolawole, M. O., *Satellite Communications Engineering*, London: Taylor and Francis, Inc., 2002

[6] Tirro, S., *Satellite Communications System Design*, New York: Springer, 1993.

[7] Evans, B. G., *Satellite Communications Systems*, London: IEEE Telecommunications Series (UK), 1999.

[8] Fordham, J. A., *An Introduction to Antenna Test Ranges, Measurements and Instrumentation*, MI-Technologies, Atlanta, GA, 2009.

[9] Hartman, R., and J. Berlekamp, "Fundamentals of Antenna Test and Evaluation," *Microwave Systems New and Communications Tracking*, June 1988.

[10] J. S. Hollis, T. J. Lyon, and L. Clayton, (eds.), *Microwave Antenna Measurements*, Atlanta, GA: Scientific-Atlanta, Inc., 1985.

[11] www.mi-technologies.com.

[12] www.orbitfr.com.

Selected Bibliography

Hudgens, J. M., and G. M. Cawthon, "Extreme Accuracy Tracking Gimbal for Radome Measurements," *Proc. of 25th Annual Meeting of the Antenna Measurement Techniques Association (AMTA '02)*, Cleveland, OH, October 2003, pp. 291–295.

Hudgens, J. M., and G. W. Cawthon, *Extremely Accurate Tracking Gimbal for Radome Measurements*, MI Technologies, Suwanee, GA, 2003.

McBride, S. T., and G. M. Cawthon, *Error Compensation for Radome Measurements*, MI Technologies, Suwanee, GA, 2003.

Product Catalog, *Microwave Measurements Systems and Product,* Microwave Instrumentation Technologies, LLC.

11

Environmental Degradations

RTCA DO-213 [1] is an interesting aircraft radome performance specification written at the advent of wind shear weather radar that established radome performance requirements for general nose mounted weather radar antennas. Although it is now obsolete, it is still useful for defining basic radome performance parameters; at the time of this writing, civil regulations establish the quantitative regulatory requirements for these parameters. This chapter discusses some of these parameters of primary interest to the radome electrical designer.

11.1 Rain Erosion

Rain erosion damage is primarily an environmental consideration for aircraft radomes that fly at relatively high speeds and rain erosion is capable of even delaminating or fracturing the walls of a radome subjected to extreme rain impact beyond its design loads. The load is a function of a maximum angle of impact that the radome will experience in flight, mean raindrop size, rainfall rate, and the aircraft velocity.

Aircraft operators are especially interested in rain erosion because of maintenance issues that may lead to the need for structural repairs. A reduction in rain erosion resistance could require more maintenance and repainting (Figure 11.1). Rain impact and erosion can have additional maintenances issues depending on the aircraft mission profile; for instance, the foundation of the MIL-R-7705B requirements [2] came from the U.S. Navy's bad aircraft radome experience in Vietnam's rainy season. Short-haul turboprops have a completely different rain erosion environment than long-range transcontinental or

Figure 11.1 Rain erosion of a typical aircraft radome. (Photo courtesy of USDigiComm Corporation.)

transoceanic aircraft. Additionally, regional jets are in an even more extreme environment than regional turboprops. General aviation and commercial pilots tend to be more fair-weather flyers, while the military are indifferent to weather.

According to RTCA DO-213, unless a radome design was previously qualified via tests or service history of the materials and radome construction applied, a sample of the radome wall with the finish coating is recommended to be tested on an approved rain erosion apparatus. The usual mechanical validation test for rain erosion is by whirling arm apparatus that uses a spinning rotor with the test coupons at the rotor tip(s). Arrays of calibrated sprinkler nozzles spray around the circumference and along the coupon width to provide the simulated rain droplet size and rate. However, the test requirement can be swayed by altering the distance that the droplet falls from the nozzle to the coupon. Some facilities use a fixed distance of a few inches, while others can be up to several feet. MIL-R-7705B had requirements at 2-mm droplets at 1 inch/hour and 500 mph. That is extreme, but representative for worst-case on-the-deck, high-speed flight.

11.1.1 Rain Erosion Paints

Aircraft maintenance crews seek to improve erosion caused by rain and reduce overall maintenance costs. One method of achieving this is with a rain erosion resistant paint such as "Caapcoat" paints that conform to AMS-C-83231 and AMS-C-83445 specifications. Both specifications are for materials that have similar properties with the exception of colors, antistatic properties, and so

forth. For higher-speed aircraft, AMS-3138 is the standard that applies to the required flouro-elastomer paints.

The rain erosion resistance of these materials is considered to be the best available for paints. However, while the simple application of these paints will greatly improve erosion resistance, the entire paint system, from substrate preparation to application of all coatings and all in-process preparations and handling, has a great influence on the end rain erosion results. Often the eventual failure of any paint system is likely due to the adhesion to the undercoats or the substrate or the cohesive failure of undercoat materials.

11.1.2 Rain Erosion Boots

Rain erosion boots fabricated from a rain erosion resistance material are quite similar to the Caapcoat paints. The explanation is simple: the film is a polyurethane of similar thickness and elastometric properties as the paint. For example, a structure applied to a severe rain field is shown in Figure 11.2; the left half, which was treated with a rain erosion material, shows negligible erosion, while the untreated right half shows extreme degradation.

3M makes a material in the form of a polyurethane tape designed for use on aircraft: 3M Polyurethane Protective Tapes and Boots. Used on the leading edges of aircraft radomes (Figure 11.3), they can help to significantly reduce the damage caused by erosion. 3M Polyurethane Protective Boots are preformed to custom fit on aircraft, so they form a continuous barrier that maintains excellent adhesion to the surface structure, including sealants and raised features. Currently, there are over 500 different custom 3M Boots available.

3M Tapes and Boots are designed to be easily handled without tearing and do not contain hazardous chemicals or volatile organic compounds (VOCs), making the installation relatively easy. A full bond occurs in 24 hours, but is ready to fly in 60 minutes.

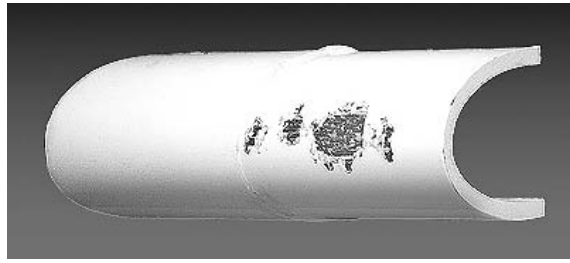

Figure 11.2 Rain erosion boot material applied to only the left half of the test article. (Photo courtesy of 3M Corporation Aerospace & Aircraft Maintenance Dept.)

Figure 11.3 Rain erosion boot applied to an aircraft radome. (Photo courtesy of 3M Corporation Aerospace.)

11.2 Atmospheric Electricity

Damage from atmospheric electricity is demonstrated in two areas: lighting strikes and static charge buildup on the surface of the radome. Some considerations for each of these conditions are discussed in the following sections.

11.2.1 Lighting Strike Damage

Lightning presents a serious, immediate, and dynamic threat to an aircraft radome (Figure 11.4). The regulatory rule states that for nonmetallic materials the lightning current shall be conducted in some manner to not endanger the aircraft.

One common type of damage caused by lighting strikes to the radome is a puncture as shown in Figure 11.5. Unless quickly repaired, a lighting puncture will promote moisture absorption and/or water ingestion into the radome walls, which will greatly deteriorate its electrical performance characteristics. Such a puncture can also cause secondary damage to RF subsystems as well as the plane's superstructure itself, potentially endangering the aircraft.

Figure 11.4 Photo of a lightning strike to an aircraft radome. (Photo courtesy of USDigiComm Corporation.)

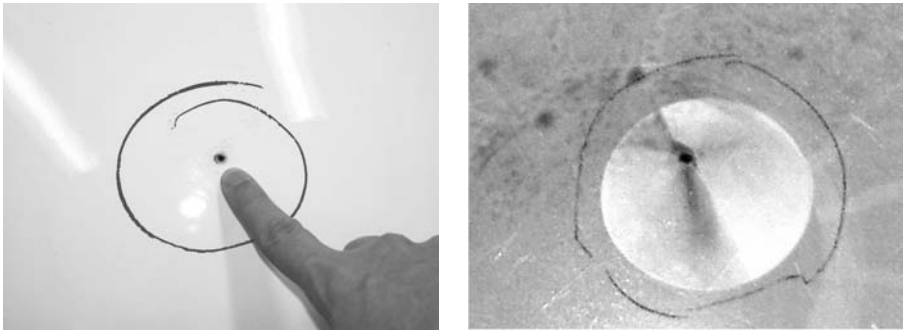

(a) (b)

Figure 11.5 Photo of actual lighting punctures through an aircraft radome. (Photo courtesy of Saint Gobain Performance Plastics.)

11.2.2 Use of Lightning Diverters

The means to meeting this requirement are usually the application of an array lightning diverters. These quasi-conductive strips, shown in Figure 11.6, perform like lightning rods on the radome's surface by diverting the lighting to the

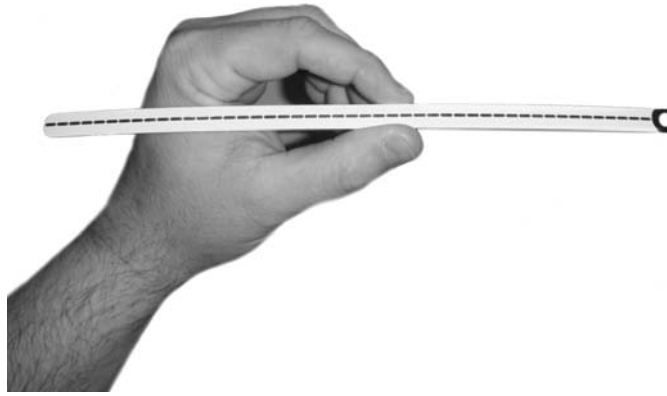

Figure 11.6 Photo of a lighting diverter strip. (Photo courtesy of USDigiComm Corporation.)

strip instead of puncturing the radome dielectric and possibly striking the antenna. The technology behind these type of strips have evolved over the past couple of decades, where lightning diverters are not necessarily solid metal elements, but differing arrangements of conductive and semiconductive materials. An aircraft radome with these types of lightning diverter strips applied is shown in Figure 11.7.

There are two aspects of the radome's lightning diverter system: (1) the diverter configuration arrayed around the radome limits the probability of puncture, and (2) the diverter construction and its grounding path limit the damage from the lightning currents.

Figure 11.7 Photo of lighting diverter strips applied to an aircraft radome. (Photo courtesy of USDigiComm Corporation.)

Because testing real lightning voltages, currents, and waveforms simultaneously is not practical, the two aspects are tested separately. The standard test specifications (SAE ARP-5416, or the less preferred DO-160 Section 23) are set up in this manner. Figure 11.8 depicts an aircraft radome subjected to lightning tests.

11.2.3 Antistatic Systems

Other static discharges, usually from precipitation (p-static) can create considerable noise on the NAV/COM systems. Today, most airborne radomes usually come with a megohm antistatic coating to bleed accrued static charge safely to the airframe. The application of the antistatic coating is straightforward. The proper coating, grounding, maintenance, and inspection and the coating's influence on rain erosion resistance are issues that are far more complicated.

The purpose of an antistatic system is to bleed off this type of electrostatic buildup. MIL-C-83231 [3] specifies a combination of antistatic and antierosion paint systems, and there are many new products on the marketplace that perform this function. In previous aircraft radome installations, antistatic coatings

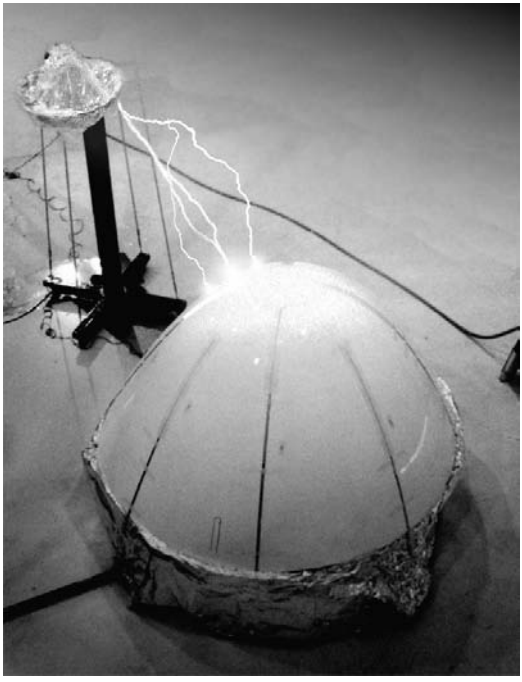

Figure 11.8 Photo of an aircraft radome with lighting diverter strips subjected to lightning tests. (Photo courtesy of USDigiComm Corporation.)

have been applied on the surface of the radome or as a layer under decorative paints.

The recommended surface resistances (ohms per unit square area) of paints currently in use range from 0.5 megohm per square up to 500 megohms per square, and to be effective the antistatic system should be terminated to the airframe.

11.2.4 Radome Wetting and Hydrophobic Materials

At microwave frequencies, even an extremely thin layer of liquid water, can result in very high radome transmission losses. One method for eliminating these losses is the application of a hydrophobic coating on the surface of the radome. Hydrophobic coatings increase surface tension, making the water beads larger so they can be blown away by an airstream or gravity more easily. Hydrophobic coatings are an important aspect of large ground-based radomes, because their sometimes stationary properties often encourage the formation of water on their surface that degrades antenna performance.

Aircraft radomes generally do not require hydrophobic coatings. There have been instances where specialized airborne radar systems have been particularly sensitive to the added reflection from small amounts of water on the radome's surface. In those instances, a material called Cytonix has been quiet successful. It is much like Rain-X, a consumer product for vehicles, but it is considerably longer lasting.

For ground-based radomes, Teflon-filled coatings are generally applied to the external surfaces. Unfortunately, these degrade over time and require frequent repainting. Other ground-based radomes are PTFE Teflon infused reinforced fibers (Saint-Gobain Raydel) that intrinsically keep the hydrophobicity properties almost indefinitely.

11.3 Radome Impact Resistance

Considerations for radome impact resistance should consider two conditions: impact to hail and impact to bird strikes.

According to RTCA DO-213 [1], all aircraft radomes should incorporate construction features to render the radome as impervious to the impact of hail as the aircraft radome designs currently in use. As an example, the A-sandwich aircraft radomes that have been constructed with three plies of 181 epoxy fiberglass or polyester laminate on each side of a low-density honeycomb or foam cores have a service history with no known hail impact fatalities. With this type of construction, damage local to the point of hail impact (including facing delamination or core crushing) has been found to be acceptable, and radomes of

this type of construction have never been known to break apart, in which case pieces of the radome might be ingested into the jet engine inlet causing other aircraft flight difficulties or failures. Radomes actually damaged in flight by small hail and large hail are shown in Figures 11.9 and 11.10, respectively.

The MIL-R-7705B & DO-213 requirements are based on 3/4-inch diameter hailstone at the cruise speed of the aircraft. In both cases, the radome can be allowed to fail, but not catastrophically, which in current terms means not to endanger the aircraft. Both specifications provide generic guidance based on experience on which laminate radome constructions are generally acceptable in lieu of a test.

There are two means of testing: Gardner impact test and the pneumatic hail gun. The Gardner test usually used a radiussed steel impactor on a flat panel. However, various plastics can be used to better simulate the mechanical characteristics of ice. The hail gun uses actual ice; however, some cotton fiber reinforcement may be added to withstand gun-firing loads.

Like rain erosion tests, the Gardner impact test is a relative measure that is difficult to equate to real service experience. The pneumatic hail gun test is quite realistic, but considerably more expensive to execute.

Radome mechanical designs for bird strike impacts are also a serious consideration as reflected in the damage shown in Figures 11.11 and 11.12.

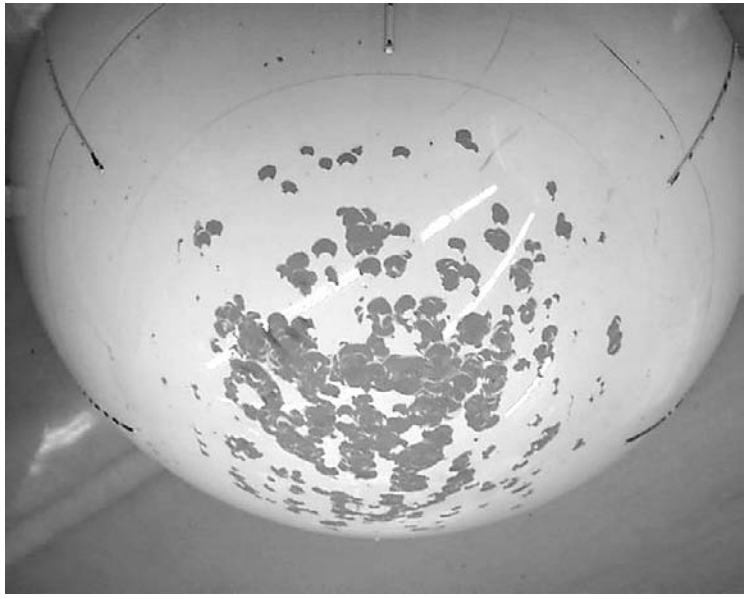

Figure 11.9 Photo of an aircraft radome subjected to small hail damage. (Photo courtesy of Saint Gobain Performance Plastics.)

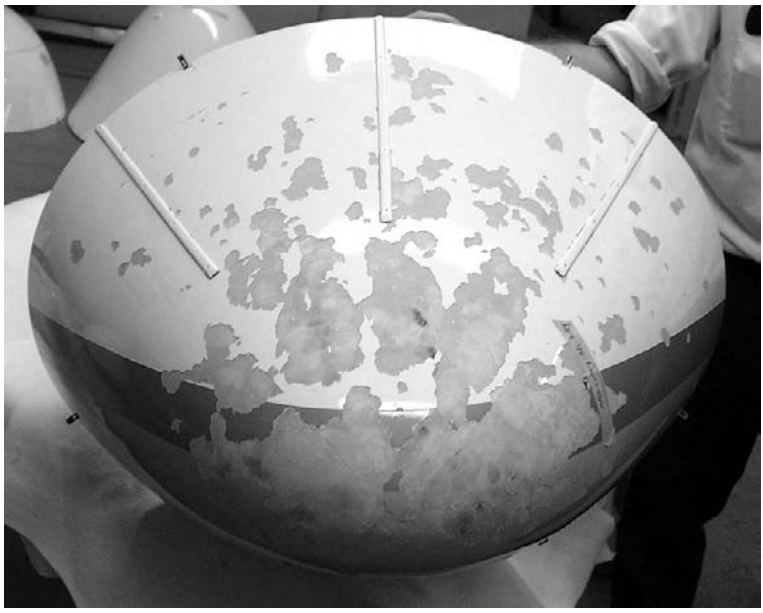

Figure 11.10 Photo of an aircraft radome subjected to small hail damage. (Photo courtesy of Saint Gobain Performance Plastics.)

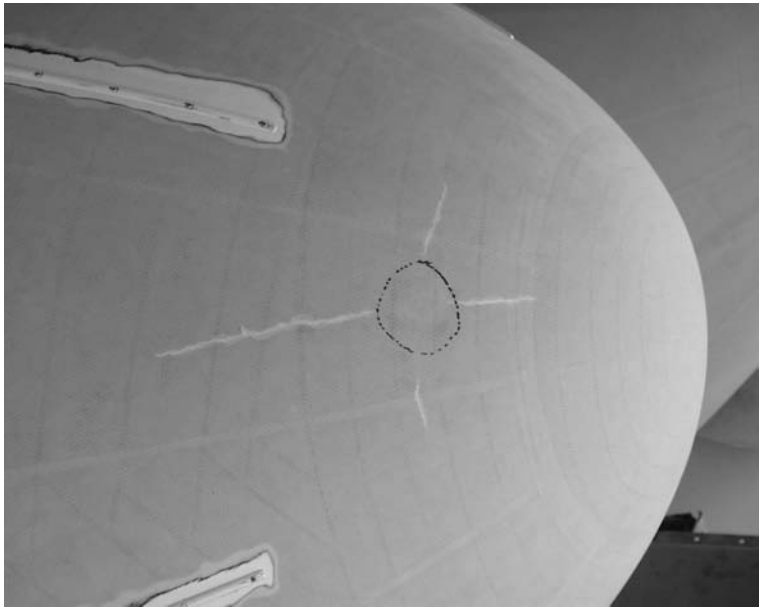

Figure 11.11 Photo of a small bird strike on aircraft radomes. (Photo courtesy of Saint Gobain Performance Plastics.)

Figure 11.12 Photo of a large bird strike on aircraft radome. (Photo courtesy of Saint Gobain Performance Plastics.)

References

[1] *Minimum Operational Performance Standards for Nose Mounted Radomes*, Document RTCA/DO-213, RTCA, Washington, D.C., 1993.

[2] MIL-R-7705B, *General Specifications for Radome*, USAF specification, 1975.

[3] Military Specification MIL-C-83231, *Coatings, Polyurethane, Rain Erosion Resistant for Exterior Aircraft and Missile Plastic Parts*, 1969.

Appendix A
Vector Operations in Various Coordinate Systems

A.1 Rectangular Coordinates

$$\nabla f = \frac{\partial f}{\partial x}\bar{x} + \frac{\partial f}{dy}\bar{y} + \frac{\partial f}{\partial z}\bar{z}$$

$$\nabla \cdot A = \frac{\partial A_x}{\partial x} + \frac{\partial A_y}{\partial y} + \frac{\partial A_z}{\partial z}$$

$$\nabla \times A = \left(\frac{\partial A_z}{\partial y} - \frac{\partial A_y}{\partial z}\right)\bar{x} + \left(\frac{\partial A_x}{\partial z} - \frac{\partial A_z}{\partial x}\right)\bar{y} + \left(\frac{\partial A_y}{\partial x} + \frac{\partial A_x}{\partial y}\right)\bar{z}$$

$$= \begin{bmatrix} \bar{x} & \bar{y} & \bar{z} \\ \dfrac{\partial}{\partial x} & \dfrac{\partial}{\partial y} & \dfrac{\partial}{\partial z} \\ A_x & A_y & Z_z \end{bmatrix}$$

A.2 Cylindrical Coordinates

$$\nabla f = \frac{\partial f}{\partial r}\bar{r} + \frac{1}{r}\frac{\partial f}{\partial \phi}\bar{\phi} + \frac{\partial f}{\partial z}\bar{z}$$

$$\nabla \cdot A = \frac{1}{r}\frac{\partial}{\partial r} rA_r + \frac{1}{r}\frac{\partial A_\phi}{\partial \phi} + \frac{\partial A_z}{\partial z}$$

$$\nabla \times A = \left(\frac{1}{r}\frac{\partial A_z}{\partial \phi} - \frac{\partial A_\phi}{\partial z}\right)\bar{r} + \left(\frac{\partial A_r}{\partial z} - \frac{\partial A_z}{\partial r}\right)\bar{\phi} + \frac{1}{r}\left(\frac{\partial}{\partial r} rA_\phi - \frac{\partial A_r}{\partial \phi}\right)\bar{z}$$

A.3 Spherical Coordinates

$$\nabla f = \frac{\partial f}{\partial r}\bar{r} + \frac{1}{r}\frac{\partial f}{\partial \theta}\bar{\theta} + \frac{1}{r\sin\theta}\frac{\partial f}{\partial \phi}\bar{\phi}$$

$$\nabla \cdot A = \frac{1}{r^2}\frac{\partial}{\partial r} r^2 A_r + \frac{1}{r\sin\theta}\frac{\partial}{\partial \theta}\left(A_\theta \sin\theta\right) + \frac{1}{r\sin\theta}\frac{\partial A_\phi}{\partial \phi}$$

$$\nabla \times A = \frac{1}{r\sin\theta}\left[\frac{\partial}{\partial \theta}\left(A_\phi \sin\theta\right) - \frac{\partial A_\theta}{\partial \phi}\right]\bar{r} + \frac{1}{r}\left(\frac{1}{\sin\theta}\frac{\partial A_r}{\partial \phi} - \frac{\partial}{\partial r} rA_\phi\right)\bar{\theta} + \frac{1}{r}\left(\frac{\partial}{\partial r} rA_\theta - \frac{\partial A_r}{\partial \theta}\right)\bar{\phi}$$

Appendix B
Propagation Constant and Wave Impedance for Arbitrary Media

In Chapter 5 we presented a boundary value problem based matrix solution for computing the electromagnetic wave transmission and insertion phase delay for a signal propagating through a multilayer dielectric radome wall. That analysis accounted for the dielectric losses in each of the dielectric layers via a loss tangent term associated with the layer. In this appendix, we consider a dielectric material that has both a loss tangent term and a conductivity term, and the electromagnetic wave behavior in such materials. As a result of the mathematical development, the reader should be able to determine the propagation constant, apparent permittivity, and wave impedance.

The assumptions made in the mathematical development that follows apply to most candidate radome materials:

- The material is nonmagnetic, therefore $\mu = \mu_o$;
- The conductivity term is totally real, that is, $\sigma = \sigma'$;
- The dielectric term is both real and imaginary, and can be modeled via $\varepsilon = \varepsilon' - j\varepsilon''$.

B.1 Wave Components in Media

We start with the time-domain form of Maxwell's curl equations:

$$\nabla \times \bar{E} = -\mu_o \frac{\partial \bar{H}}{\partial t} \tag{B.1}$$

$$\nabla \times \bar{H} = \sigma \bar{E} + \varepsilon \frac{\partial \bar{E}}{\partial t} \tag{B.2}$$

The general curl of a vector A in rectangular coordinates is:

$$\nabla \times \bar{A} = \left(\frac{\partial A_z}{\partial y} - \frac{\partial A_y}{\partial z} \right) \bar{x} + \left(\frac{\partial A_x}{\partial z} - \frac{\partial A_z}{\partial x} \right) \bar{y} + \left(\frac{\partial Ay}{\partial x} - \frac{\partial A_x}{\partial y} \right) \bar{z} \tag{B.3}$$

In the following development, we will also assume that we have a transverse electromagnetic (TEM) wave traveling in the positive z direction that has only E_x and H_y components. (For normal incidence on a dielectric surface, the reader can derive an identical result by considering a wave that has only E_y and H_x components.) Accordingly, we can write

$$\nabla \times \bar{E} = \frac{\partial E_x}{\partial z} \bar{y} - \frac{\partial E_x}{\partial y} \bar{z} \tag{B.4}$$

$$\nabla \times \bar{H} = \frac{2\partial H_y}{\partial z} \bar{x} + \frac{\partial H_y}{\partial x} \bar{z} \tag{B.5}$$

If the function is both y and x invariant, then these two expressions reduce to:

$$\nabla \times \bar{E} = \frac{\partial E_x}{\partial z} \bar{y} = -\mu_o \frac{\partial H_y}{\partial t} \bar{y} \tag{B.6}$$

or

$$\frac{\partial E_x}{\partial z} = -\mu_o \frac{\partial H_y}{\partial t} \tag{B.7}$$

Similarly,

$$\nabla \times \bar{H} = -\frac{\partial H_y}{\partial z} \bar{x} = \sigma E_x \bar{x} + \varepsilon \frac{\partial E_x}{\partial t} \bar{x} \tag{B.8}$$

or

$$-\frac{\partial H_y}{\partial z} = \sigma E_x + \varepsilon \frac{\partial E_x}{\partial t} \tag{B.9}$$

For sinusoidal ($e^{j\omega t}$) time variation, (B.7) and (B.9) reduce to

$$\frac{\partial E_x}{\partial z} = -j\omega\mu_o H_y \tag{B.10}$$

$$\frac{\partial H_y}{\partial z} = (\sigma + j\omega\varepsilon) E_x \tag{B.11}$$

Now since we propagate as

$$E_x \approx e^{-j\gamma z}; \quad H_y \approx e^{-j\gamma z} \tag{B.12}$$

then

$$\frac{\partial E_x}{\partial z} = -j\gamma E_x \tag{B.13}$$

$$\frac{\partial H_y}{\partial z} = -j\gamma H_y \tag{B.14}$$

Equations (B.10) and (B.11) can be expressed via

$$j\gamma E_x = -j\omega\mu_o H_y \tag{B.15}$$

$$j\gamma H_y = (\sigma + j\omega\varepsilon) E_x \tag{B.16}$$

From these last two equations,

$$\frac{E_x}{H_j} = \frac{\omega\mu_0}{\gamma} = \frac{-j\gamma}{(\sigma + j\omega\varepsilon)} \tag{B.17}$$

B.2 Derivation of Propagation Constant and Apparent Permittivity

The propagation constant can be derived from (B.17):

$$\gamma^2 = \omega^2 \mu\varepsilon - j\omega\mu_o\sigma \tag{B.18}$$

Or, in terms of the real and imaginary parts of the permittivity:

$$\gamma^2 = \omega^2\omega_o\varepsilon' - j\omega^2\mu_o\varepsilon'' - j\omega\mu_o\sigma = \omega^2\mu_o\varepsilon'\left[1 - j\left(\frac{\varepsilon''}{\varepsilon'} + \frac{\sigma}{\omega\varepsilon'}\right)\right] \tag{B.19}$$

From this last equation, together with the definition of loss tangent, we obtain the result:

$$\gamma = \sqrt{\omega^2\mu_o\varepsilon'}\sqrt{1 - j\left(\tan\delta + \frac{\sigma}{\omega\varepsilon'}\right)} = k\sqrt{1 - j\left(\tan\delta + \frac{\sigma}{\omega\varepsilon'}\right)} \tag{B.20}$$

Comparing this to the expression in Chapter 5 for a material without a conductivity term, we obtain the following for a complex apparent permittivity:

$$\varepsilon = \varepsilon'\left[1 - j\left(\tan\delta + \frac{\sigma}{\omega\varepsilon'}\right)\right] \tag{B.21}$$

Or, the relative apparent permittivity is

$$\varepsilon_r = \varepsilon_r'\left[1 - j\left(\tan\delta + \frac{\sigma}{\omega\varepsilon_o\varepsilon_r'}\right)\right] \tag{B.22}$$

B.3 Wave Impedance

From (B.20), we can obtain

$$\gamma = k\left[1 + \left(\tan\delta + \frac{\sigma}{\omega\varepsilon'}\right)^2\right]^{0.25} e^{-j0.5\tan^{-1}\left(\tan\delta + \frac{\sigma}{\omega\varepsilon'}\right)} \tag{B.23}$$

If we incorporate this into (B.17) and express the result in terms of the relative apparent permittivity, we obtain the wave impedance for normal incidence:

$$Z = \frac{\dfrac{120\pi}{\sqrt{\varepsilon'}} e^{j0.5\tan^{-1}\left(\tan\delta + \frac{\sigma}{\omega\varepsilon_o\varepsilon'_r}\right)}}{\left[1 + \left(\tan\delta + \dfrac{\sigma}{\omega\varepsilon_o\varepsilon'_r}\right)\right]} \tag{B.24}$$

This can be used to calculate the interfacial Fresnel reflection and transmission coefficients.

For other than normal incidence, assume the wave is propagating from one medium to a second medium. The impedance just inside the interfacial boundary in the direction of propagation is modified for perpendicular and parallel polarization via the following approximations. For perpendicular polarization:

$$Z_{\perp} = \frac{120\pi\cos\theta}{\sqrt{\varepsilon_r - \sin^2\theta}} \tag{B.25}$$

and for parallel polarization:

$$Z_{\parallel} = \frac{120\pi\sqrt{\varepsilon_r - \sin^2\theta}}{\varepsilon_r\cos\theta} \tag{B.26}$$

where θ is the angle of incidence with respect to the surface normal, and the reader should use the apparent relative permittivity given by (B.22).

Appendix C
Multilayer Propagation and Fresnel Transmission and Reflection Coefficients

This appendix deals with the matrix solution for computing the transmitted and reflected electromagnetic wave components for a multilayer dielectric wall. Specifically, for the single-layer wall depicted in Figure C.1, the reflected and transmitted wave components may be computed from the following matrix solution:

$$\begin{bmatrix} E_0^+ \\ E_0^- \end{bmatrix} = \frac{1}{T_1}\begin{bmatrix} 1 & R_1 \\ R_1 & 1 \end{bmatrix}\begin{bmatrix} e^{jk_1t_1} & 0 \\ 0 & e^{-jk_1t_1} \end{bmatrix}\frac{1}{T_2}\begin{bmatrix} 1 & R_2 \\ R_2 & 1 \end{bmatrix}\begin{bmatrix} E_2^+ \\ 0 \end{bmatrix} \tag{C.1}$$

from which

$$\begin{bmatrix} E_0^+ \\ E_0^- \end{bmatrix} = \frac{1}{T_1}\begin{bmatrix} e^{jk_1t_1} & R_1e^{-jk_1t_1} \\ R_1e^{+jk_1t_1} & e^{-jk_1t_1} \end{bmatrix}\frac{1}{T_2}\begin{bmatrix} 1 & R_2 \\ R_2 & 1 \end{bmatrix}\begin{bmatrix} E_2^+ \\ 0 \end{bmatrix} \tag{C.2}$$

In these equations, T_1 and T_2 are the front face and rear face voltage Fresnel transmission coefficients, respectively, and R_1 and R_2 are the front face and rear face voltage Fresnel reflection coefficients, respectively. The parameter k_1 is the wavenumber within dielectric material while t_1 is the thickness of the material. It is recommended that the thickness be calculated in centimeters and the wave number be calculated in units of cm^{-1}.

For a two-layer wall depicted in Figure C.2, the reflected and transmitted wave components may be computed from the following matrix solution:

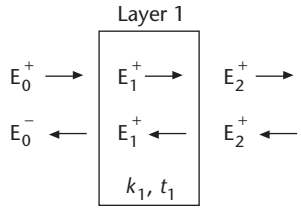

Figure C.1 Matrix solution for a single-layer dielectric wall.

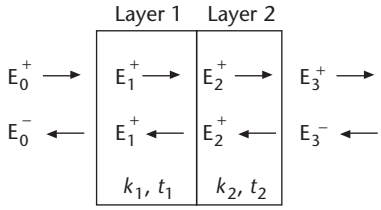

Figure C.2 Matrix solution for a two-layer dielectric wall.

$$\begin{bmatrix} E_0^+ \\ E_0^- \end{bmatrix} = \frac{1}{T_1}\begin{bmatrix} 1 & R_1 \\ R_1 & 1 \end{bmatrix}\begin{bmatrix} e^{jk_1t_1} & 0 \\ 0 & e^{-jk_1t_1} \end{bmatrix} \frac{1}{T_2}\begin{bmatrix} 1 & R_2 \\ R_2 & 1 \end{bmatrix}\begin{bmatrix} e^{jk_2t_2} & 0 \\ 0 & e^{-jk_2t_2} \end{bmatrix}\frac{1}{T_3}\begin{bmatrix} 1 & R_3 \\ R_3 & 1 \end{bmatrix}\begin{bmatrix} E_3^+ \\ 0 \end{bmatrix} \tag{C.3}$$

from which

$$\begin{bmatrix} E_0^+ \\ E_0^- \end{bmatrix} = \frac{1}{T_1}\begin{bmatrix} e^{jk_1t_1} & R_1e^{-jk_1t_1} \\ R_1e^{+jk_1t_1} & e^{-jk_1t_1} \end{bmatrix} \frac{1}{T_2}\begin{bmatrix} 1 & R_2 \\ R_2 & 1 \end{bmatrix}\begin{bmatrix} e^{jk_2t_2} & R_1e^{-jk_2t_2} \\ R_1e^{+jk_2t_2} & e^{-jk_2t_2} \end{bmatrix} \frac{1}{T_3}\begin{bmatrix} 1 & R_3 \\ R_3 & 1 \end{bmatrix}\begin{bmatrix} E_3^+ \\ 0 \end{bmatrix} \tag{C.4}$$

where T_i, R_i, t_i, and k_i are the voltage Fresnel transmission coefficient, voltage Fresnel reflection coefficient, thickness, and wave number for the ith layer, respectively, as implied in the single-layer case.

Lastly, we can generalize the result for the N-layer dielectric wall depicted in Figure C.3.

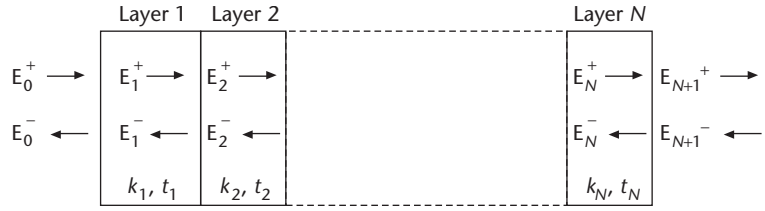

Figure C.3 Matrix solution for an *N*-layer dielectric wall.

Specifically, the front face reflected and net transmitted wave components may be computed via:

$$\begin{bmatrix} E_0^+ \\ E_0^- \end{bmatrix} = \left[\prod_{i=1}^{N} \frac{1}{T_i} \begin{pmatrix} 1 & R_i \\ R_i & 1 \end{pmatrix} \begin{pmatrix} e^{jk_i ti} & 0 \\ 0 & e^{-jk_i t_i} \end{pmatrix} \right] \frac{1}{T_{N+1}} \begin{bmatrix} 1 & R_{N+1} \\ R_{N+1} & 1 \end{bmatrix} \begin{bmatrix} E_{N+1}^+ \\ 0 \end{bmatrix} \tag{C.5}$$

from which we obtain the final result:

$$\begin{bmatrix} E_0^+ \\ E_0^- \end{bmatrix} = \left[\prod_{i=1}^{N} \frac{1}{T_i} \begin{pmatrix} e^{jk_i t_i} & R_i e^{-jk_i t_i} \\ R_i e^{+jk_i t_i} & e^{-jk_i t_i} \end{pmatrix} \right] \frac{1}{T_{N+1}} \begin{bmatrix} 1 & R_{N+1} \\ R_{N+1} & 1 \end{bmatrix} \begin{bmatrix} E_{N+1}^+ \\ 0 \end{bmatrix} \tag{C.6}$$

where all the parameters in (C.5) and (C.6) follow the implications of the single- and two-layer cases discussed previously.

C.1 Fresnel Transmission and Reflection Coefficients

The calculation of these coefficients can be accomplished by a number of different methods and are all seen to be a function of the wave polarization, angle of incidence with respect to the surface normal, wavenumbers in the respective materials, and the refractive index of the material. One approximation is to neglect the complex component of the refractive index (loss term) in which we obtain for the perpendicular polarization case:

$$R = \frac{n_i \cos\theta_i - n_t \cos\theta_t}{n_i \cos\theta_i + n_t \cos\theta_t} \tag{C.7}$$

where

n_i, n_t = the real part of the refractive indices on the left and right sides of the interface, respectively;

θ_i, θ_t = the angles of incidence with respect to the surface normal on the left side and right side of the interface, respectively, and are easily computed by Snell's law.

Likewise, one expression for the voltage transmission coefficient for the perpendicular wave component is:

$$T = \frac{2n_i \cos\theta_i}{n_i \cos\theta_i + n_t \cos\theta_t} \tag{C.8}$$

For the parallel polarization wave components, these two equations reduce to:

$$R = \frac{n_i \cos\theta_t - n_t \cos\theta_i}{n_i \cos\theta_t + n_t \cos\theta_i} \tag{C.9}$$

and

$$T = \frac{2n_i \cos\theta_i}{n_i \cos\theta_t + n_t \cos\theta_i} \tag{C.10}$$

A simplification of all these formulas may be applied; for the perpendicular polarization we obtain:

$$R = \frac{\sin(\theta_t - \theta_i)}{\sin(\theta_t + \theta_i)} \tag{C.11}$$

and for the parallel wave component,

$$R = \frac{\tan(\theta_t - \theta_i)}{\tan(\theta_t + \theta_i)} \tag{C.12}$$

and the respective transmission coefficient corresponding to each of these by applying:

$$T = \sqrt{1 - R^2} \tag{C.13}$$

Appendix D
Radiation from Elemental Currents

The purpose of this appendix is to derive expressions for both the electromagnetic field and the array factor for an ensemble of infinitesimal (dipole) current elements. Three cases are considered as illustrated in Figure D.1:

1. Current elements that are *z*-directed;
2. Current elements that are *x*-directed;
3. Current elements that are *y*-directed.

The far-field radiation pattern of an infinitesimal dipole element follows from solution of Maxwell's equations. Assuming a time harmonic field that is $e^{j\omega t}$ dependent, the fundamental relations are expressed as the curl and divergence operators:

$$\nabla \times \overline{H} = j\omega\varepsilon_0 \overline{E} + \overline{J} \tag{D.1}$$

$$\nabla \times \overline{E} = j\omega\mu_0 \overline{H} \tag{D.2}$$

where ε_o and μ_o are the permittivity and permeability of free space, $\overline{B} = \mu_0 \overline{H}$ and $\overline{D} = \varepsilon_0 \overline{E}$.

Now, define a magnetic vector potential via

$$\overline{H} = \nabla \times \overline{A}$$

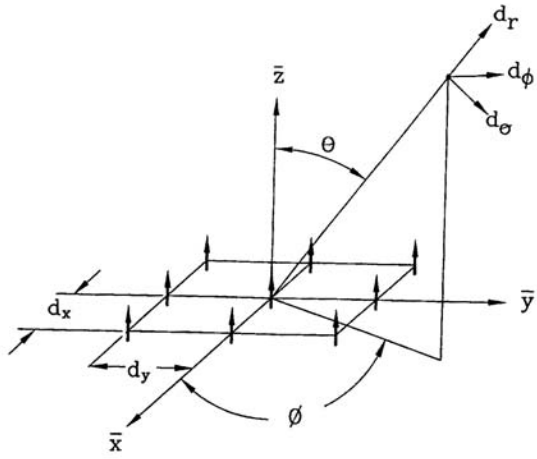

(a)

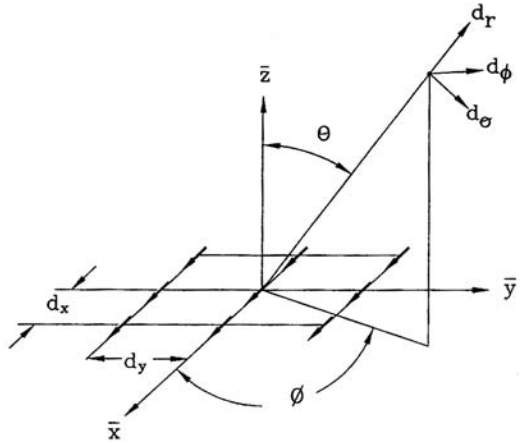

(b)

Figure D.1 Radiation from infinitesimal currents: (a) *z*-directed, (b) *x*-directed, and (c) *y*-directed.

then from (D.2) and (D.3), we obtain

$$\nabla \times \left(\bar{E} + j\omega\mu_0 \bar{A} \right) = 0$$

Because any curl-free vector can be defined as the gradient of a scalar function, one can define an electric scalar potential Φ where

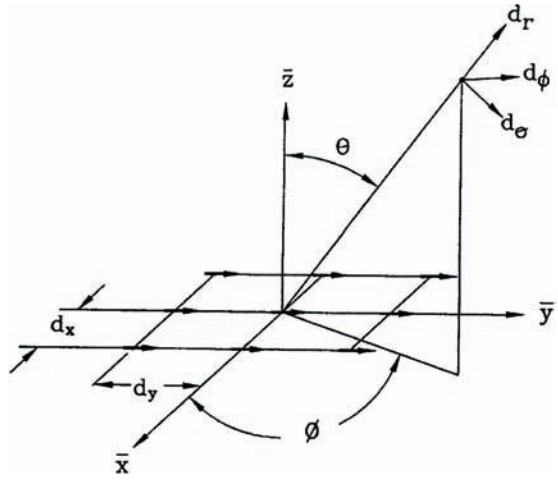

(c)

Figure D.1 (continued)

$$\bar{E} + j\omega\mu_0 \bar{A} = -\nabla\Phi \tag{D.5}$$

From (D.1), (D.3), and (D.5), we obtain

$$\nabla\left(\nabla \cdot \bar{A}\right) - \nabla^2 \bar{A} - k^2 \bar{A} = -j\omega\varepsilon_0 \nabla\Phi + \bar{J} \tag{D.6}$$

A vector is uniquely specified by both the curl and divergence. If we choose

$$\nabla\left(\nabla \cdot \bar{A}\right) = -j\omega\varepsilon_0 \nabla\Phi \tag{D.7}$$

$$\nabla^2 \bar{A} + k^2 \bar{A} = -\bar{J} \tag{D.8}$$

we obtain the well-known Helmholtz wave equation. Solutions to the field components for $\bar{A}$ follow from (D.3), (D.5), and (D.7):

$$\bar{H} = \nabla \times \bar{A} \tag{D.9}$$

$$\bar{E} = -j\omega\mu_0 \bar{A} + \frac{1}{j\omega\varepsilon_0} \nabla\left(\nabla \cdot \bar{A}\right) \tag{D.10}$$

Because rectangular components of $\overline{A}$ only have corresponding components of $\bar{J}$ as their source, the technique is first developed by assuming only a *z*-directed current element at the origin of a standard spherical coordinate system, as depicted in Figure D.1(a). We assume current of magnitude I_o and length *d*.

$$\nabla^2 A_z - k^2 A_z = I_o d \tag{D.11}$$

where *k* is the free-space wave number, *h* is the infinitesimal dipole length, and I_o is the current magnitude. Assume A_z is *r* dependent. The differential equation to be solved is

$$\frac{1}{r^2}\frac{\partial}{\partial r}\left(r^2 \frac{\partial A_z}{\partial r}\right) + k^2 A_z = I_o d \tag{D.12}$$

$$A_z = I_o \frac{e^{-jkr}}{4\pi r} \tag{D.13}$$

From (D.9)

$$\overline{H} = \nabla \times \bar{z} A_z = \frac{\partial A}{\partial r} \bar{r} \times \bar{z} \tag{D.14}$$

from which we obtain (in the far field)

$$H_\phi = jkI_o d \frac{e^{-jkr}}{4\pi r} \sin\theta \tag{D.15}$$

$$E_\theta = jk\eta I_o d \frac{-jkr}{4\pi r} \sin\theta \tag{D.16}$$

where

$$\eta = \sqrt{\frac{\mu_o}{\varepsilon_o}} = 120\pi \tag{D.17}$$

Equations (D.15) and (D.16) can be shown to be equivalent to

$$E_\theta = j\omega\varepsilon_0 \sin\theta A_z \tag{D.18}$$

$$H_\phi = \frac{1}{\eta} E_\theta \tag{D.19}$$

The relationship between far-field patterns and aperture currents follows from linear superposition of the radiated fields from each of the infinitesimal currents. For example, consider the *z*-directed current distribution shown in Figure D.1(a). The location of currents in the *x* direction is

$$x = md_x \tag{D.20}$$

and the location of currents in the *y* direction is

$$y = nd_y \tag{D.21}$$

In these last two equations, m and n are integers, where $m = 0, 1, 2, \ldots, M$ and $n = 0, 1, 2, \ldots, N$, and d_x and d_y are the current spacings in the x and y directions, respectively. The total current is given by the formula

$$I = \sum_{m=0}^{M} \sum_{n=0}^{N} I_{mn} \delta(x - md_x) \delta\left(y - nd_y\right) \delta(z) \tag{D.22}$$

where the Dirac delta functions are defined by the following relations:

$$\delta(p) \begin{cases} 0; \text{ for all } p \neq 0 & \text{(D.23)} \\ 1; \text{ for } p = 0 & \text{(D.24)} \end{cases}$$

Using this discrete current distribution in (D.13), we obtain

$$A_z = \int\int\int \frac{e^{-jkr}}{4\pi r} \delta(z) \sum_{m=0}^{M} \sum_{n=0}^{N} I_{mn} \delta(x - md_x) \delta\left(y - nd_y\right) dx\, dy\, dz \tag{D.25}$$

For a fixed distance from the antenna, r_o, this reduces to

$$A_z = \left[\frac{e^{-jkr_0}}{4\pi r_0}\right] \sum_{m=0}^{M} \sum_{n=0}^{N} Ilmn\, e^{-jk \sin\theta \left(md_x \cos\phi + nd_y \sin\phi\right)} \tag{D.26}$$

This result is sufficient to obtain far-field radiation patterns. Specifically, the far-field pattern is a simple sum of the current contributions of the

ensembles of infinitesimal current sources, that is, by incorporation of this expression into (D.18):

$$E_\theta = \sin(\theta)\left[\frac{e^{-jkr_0}}{4\pi r_0}\right]\sum_{m=0}^{M}\sum_{n=0}^{N} I_{mn}\, e^{j\psi_{mn}} \tag{D.27}$$

where the space phase term is defined via

$$\psi_{mn} = k\sin\theta\left(md_x\cos\phi + nd_y\sin\phi\right) \tag{D.28}$$

In (D.27) we can drop the term in brackets [ ] because it is a scale constant. If we do so, we obtain the following array factor:

$$E_\theta^{AF} = \sin(\theta)\sum_{m=0}^{M}\sum_{n=0}^{N} I_{mn}\, e^{j\psi_{mn}} \tag{D.29}$$

If the currents are *x*-directed, a similar development leads to the following expression for the array factor for the field component aligned with the *x*-polarization axis:

$$E_x^{AF} = \cos\left[\tan^{-1}\left(\frac{\sin\theta\cos\phi}{\sqrt{\cos^2\theta + \sin^2\theta\sin^2\phi}}\right)\right]\sum_{m=o}^{M}\sum_{n=0}^{N} I_{mn}\, e^{j\psi_{mn}} \tag{D.30}$$

If the currents are *y*-directed, the array factor for the field component aligned with the *y*-polarization axis is

$$E_y^{AF} = \cos\left[\tan^{-1}\left(\frac{\sin\theta\sin\phi}{\sqrt{\cos^2\theta + \sin^2\theta\sin^2\phi}}\right)\right]\sum_{m=o}^{M}\sum_{n=0}^{N} I_{mn}\, e^{j\psi_{mn}} \tag{D.31}$$

Appendix E
Program TORADOME Software Listing

```
#COMPILE EXE
FUNCTION PBMAIN

'———— RADOME SHAPE PARAMETERS ————————————————————
    GLOBAL x0, y0, z0, L0, D0, Adia, AZ, EL, FREQUENCY AS SINGLE
    GLOBAL DRAD, Adia, INCREMENT, RADIUS, MAGAouter() AS SINGLE
    GLOBAL PHASEAouter(), Ainner(), PI  AS SINGLE
    GLOBAL AZ, EL, EDB(),RE, IM, CNST, JACK AS SINGLE

'———— VECTOR PARAMETERS ——————————————————————————
    GLOBAL BTO, RTO, Ix, x, y, z,  xi, yi, zi, Nt, Nx,  Ny, Nz, COUNTA
AS SINGLE
    GLOBAL COUNTB, xp, yp, zp,  RE, IM, PHI, alpha, ri, rp, MATTHEW AS
SINGLE
    GLOBAL MARK, LUKE, JOHN, times, EY, EZ, VV(), CONV, theta  AS
SINGLE
    GLOBAL Kx, Ky, Kz, IZ, IY, IZZ, IYY, VH(), I, J, II, JJ, M, MM, MMM
AS SINGLE
    GLOBAL DR(), GR(), DUMB, VV(), VH(), XAZ, XEL, NAT AS SINGLE
    GLOBAL EPOL, REU, IMU, REL, IML AS SINGLE
    DIM Ainner(-50 TO 50, -50 TO 50), MAGAouter(-50 TO 50, -50 TO 50)
    DIM PHASEAouter(-50 TO 50,-50 TO 50)
    DIM EDB(-90 TO 90,-90 TO 90),  VV(3), VH(3), DR(3), GR(3)

'———— GLOBAL VARIABLES NEEDED IN SUBROUTINE WALL ————————————-
    GLOBAL wavenumber, ER(), LTAN(), THK(), gamma, Ttotmag() AS SINGLE
    GLOBAL Ttotph(), Rtotmag(), Rtotph() AS SINGLE
    GLOBAL N, K, THK(), XER(), XLTAN(), XIZ, XIY AS SINGLE
    DIM ER(10), LTAN(10), THK(10), Ttotmag(2), Ttotph(2), Rtotmag(2),
Rtotph(2)
```

```
'———— USER INPUT VARIABLES ——————————————————-
    GLOBAL IO_FREQ, IO_LAYERS, IO_N, IO_N2, IO_ERRORTIMES AS SINGLE
    GLOBAL IO_THK(), IO_ER(), IO_LTAN(), IO_cursor_y, IO_cursor_x AS
SINGLE
    GLOBAL IO_varinput IO_StartFreq, IO_StopFreq AS SINGLE
    GLOBAL IO_FILENAME, IO_keystroke, IO_vardump AS STRING
    GLOBAL IO_RadomeDiameter, IO_RadomeLength AS SINGLE
    GLOBAL IO_AntennaDiameter, IO_AntennaXo, IO_AntennaEL AS SINGLE
    GLOBAL IO_AntennaAZ AS SINGLE
    GLOBAL IO_AntennaPol AS STRING
    DIM IO_THK(10), IO_ER(10), IO_LTAN(10)

'———— ADDED TO MAKE RUN ——————————————————————
    GLOBAL keystroke AS STRING
    GLOBAL pol, BSE, NAT, XTHK(), XER(), XLTAN(), XAZ, XEL AS SINGLE
    GLOBAL StartFreq, StopFreq, xPosRad AS SINGLE
    DIM XTHK(10), XER(10), XLTAN(10)

'———— CONSTANTS ——————————————————————————
    DRAD=3.14159265/180
    PI=3.14159265
'*************************************************************************
'*                          START Subroutine                             *
'*************************************************************************
START:
    COLOR 15,1
    CLS

    COLOR 15,14
    LOCATE 1,1
    PRINT SPACE$(80);

    COLOR 0,14

    LOCATE 1,21
    PRINT "TANGENT OGIVE RADOME ANALYSIS DEMO PROGRAM"

    COLOR 15,1
    LOCATE 10,1
    PRINT "    This software computes the transmission loss through a
tangent ogive"
    PRINT
    PRINT "  shaped radome. The radome wall can be a multilayer compos-
ite with up to"
    PRINT
    PRINT "  five(5) layers of different material types and thick-
nesses."
    PRINT

    LOCATE 23,1
    COLOR 9,1
    PRINT "                          www.Radomes.net                  "
    COLOR 9,7
```

```
    LOCATE 25,1
    PRINT SPACE$(80);
    LOCATE 1,1

    COLOR 1,7
    LOCATE 25,28
    PRINT "<Press Any Key> to Continue";

    CURSOR OFF

    DO
        IO_keystroke = INKEY$
        IF IO_keystroke ><"" THEN EXIT DO
    LOOP

'*********************************************************************
'*          IO_RESTART Subroutine - Radome Geometry                  *
'*********************************************************************
IO_RESTART:

    CURSOR OFF
    COLOR 15,1
    CLS

    COLOR 15,14
    LOCATE 1,1
    PRINT SPACE$(80);

    COLOR 0,14
    LOCATE 1,28
    PRINT "RADOME GEOMETRY DESCRIPTION"

    COLOR 1,7
    LOCATE 25,1
    PRINT SPACE$(80);
    LOCATE 1,1

    COLOR 8,1
    LOCATE 22,4
    PRINT "<Arrow Keys>-Move Cursor   <Enter>-Edit Data  <F1>-Next Page
<Esc>-Exit";
    COLOR 15,1

    COLOR 9,7
    LOCATE 24,1
    PRINT SPACE$(80);
    LOCATE 25,1
    PRINT SPACE$(80);
    LOCATE 1,1

    COLOR 1,7
    LOCATE 24,2
    PRINT "NOTE: To Change Data, Use Arrow Keys to Select Desired
```

```
Field, Then Press the";
    LOCATE 25,8
    PRINT "Enter Key to Edit Data Within That Field.  Press Enter Again
When Done.";

    COLOR 15,1
    ON ERROR GOTO IO_PROGRAMERROR1

    IF IO_ERRORTIMES >= 3 THEN
        COLOR 15,0
        BEEP
        PRINT
        PRINT " UNRECOVERABLE ERROR IN PROGRAM EXECUTION!
        SLEEP 7000
        END
    END IF

    OPEN "C:\RADGEO.DAT" FOR INPUT AS #1
        '── CURSOR ──
        INPUT #1, IO_cursor_y
        INPUT #1, IO_cursor_x
        '── DATA ──
        INPUT #1, IO_StartFreq
        INPUT #1, IO_StopFreq
        INPUT #1, IO_RadomeDiameter
        INPUT #1, IO_RadomeLength
        INPUT #1, IO_AntennaDiameter
        INPUT #1, IO_AntennaEL
        INPUT #1, IO_AntennaAZ
        INPUT #1, IO_AntennaXo
        INPUT #1, IO_AntennaPol
    CLOSE #1

    COLOR 15,1
    LOCATE 3,2
    PRINT "Start Frequency(GHz)  = ";
      COLOR 15,0
      IO_vardump = USING$ (" ###.## ", IO_StartFreq)
      PRINT IO_vardump
      COLOR 15,1

    LOCATE 5,2
    PRINT "Stop Frequency(GHz)   = ";
      COLOR 15,0
      IO_vardump = USING$ (" ###.## ", IO_StopFreq)
      PRINT IO_vardump
      COLOR 15,1

    LOCATE 7,2
    PRINT "Radome Diameter       = ";
      COLOR 15,0
      IO_vardump = USING$ (" ###.## ", IO_RadomeDiameter)
      PRINT IO_vardump
      COLOR 15,1
```

```
LOCATE 9,2
PRINT "Radome Length         = ";
  COLOR 15,0
  IO_vardump = USING$ (" ###.## ", IO_RadomeLength)
  PRINT IO_vardump
  COLOR 15,1

LOCATE 11,2
PRINT "Antenna Diameter      = ";
  COLOR 15,0
  IO_vardump = USING$ (" ###.## ", IO_AntennaDiameter)
  PRINT IO_vardump
  COLOR 15,1

LOCATE 13,2
PRINT "Elevation(deg)        = ";
  COLOR 15,0
  IO_vardump = USING$ (" ###.## ", IO_AntennaEL)
  PRINT IO_vardump
  COLOR 15,1

LOCATE 15,2
PRINT "Azimuth(deg)          = ";
  COLOR 15,0
  IO_vardump = USING$ (" ###.## ", IO_AntennaAZ)
  PRINT IO_vardump
  COLOR 15,1

LOCATE 17,2
PRINT "Antenna Xo Location   = ";
  COLOR 15,0
  IO_vardump = USING$ (" ###.## ", IO_AntennaXo)
  PRINT IO_vardump
  COLOR 15,1

LOCATE 19,2
PRINT "Antenna Polarization  = ";
  COLOR 15,0
  IO_vardump = USING$ (" & ", IO_AntennaPol)
  PRINT IO_vardump
  COLOR 15,1

CURSOR OFF
LOCATE IO_cursor_y, IO_cursor_x
PRINT CHR$(16);

DO

  IO_keystroke = INKEY$

  IF IO_keystroke = CHR$(27) THEN END

  IF IO_keystroke = CHR$(0) + CHR$(72) THEN
      IF IO_cursor_y > 4 THEN
```

```
            LOCATE IO_cursor_y, IO_cursor_x: PRINT " ";
            IO_cursor_y = IO_cursor_y - 2
            LOCATE IO_cursor_y, IO_cursor_x: PRINT CHR$(16);
        END IF
    END IF

    '——— CURSOR DOWN ———
    IF IO_keystroke = CHR$(0) + CHR$(80) THEN
        IF IO_cursor_y < 19 THEN
            LOCATE IO_cursor_y, IO_cursor_x: PRINT " ";
            IO_cursor_y = IO_cursor_y + 2
            LOCATE IO_cursor_y, IO_cursor_x: PRINT CHR$(16);
        END IF
    END IF

    '======== RUN DATA ========
    IF IO_keystroke = CHR$(0)+CHR$(59) THEN GOTO IO_RESTART2

    '——— ALTER DATA <Enter> ———
    IF IO_keystroke = CHR$(13) THEN GOTO IO_ALTER_DATA

  LOOP

END
'*************************************************************************
'*                        IO_ALTER_DATA Subroutine                       *
'*************************************************************************
IO_ALTER_DATA:

'——— START FREQUENCY ———
  IF IO_cursor_y = 3 THEN
      LOCATE IO_cursor_y, 27
      COLOR 15,0
      PRINT SPACE$(7);
      LOCATE IO_cursor_y, 27

      CURSOR ON, 100
      INPUT IO_varinput
      CURSOR OFF

      IF IO_varinput >= .01 AND IO_varinput <= 100 THEN  IO_StartFreq
= IO_varinput ELSE BEEP

  END IF

'——— STOP FREQUENCY ————————————————————-
  IF IO_cursor_y = 5 THEN
      LOCATE IO_cursor_y, 27
      COLOR 15,0
      PRINT SPACE$(7);
      LOCATE IO_cursor_y, 27
```

```
        CURSOR ON, 100
        INPUT IO_varinput
        CURSOR OFF

        IF IO_varinput >= .01 AND IO_varinput <= 100 THEN  IO_StopFreq
= IO_varinput ELSE BEEP

    END IF

'———— RADOME DIAMETER ——————————————————————
    IF IO_cursor_y = 7 THEN
        LOCATE IO_cursor_y, 27
        COLOR 15,0
        PRINT SPACE$(7);
        LOCATE IO_cursor_y, 27

        CURSOR ON, 100
        INPUT IO_varinput
        CURSOR OFF

        IF IO_varinput < 999.99 AND IO_varinput >= 1 THEN
IO_RadomeDiameter = IO_varinput ELSE BEEP

    END IF

'———— RADOME LENGTH ——————————————————————
    IF IO_cursor_y = 9 THEN
        LOCATE IO_cursor_y, 27
        COLOR 15,0
        PRINT SPACE$(7);
        LOCATE IO_cursor_y, 27

        CURSOR ON, 100
        INPUT IO_varinput
        CURSOR OFF

        IF IO_varinput < 999.99 AND IO_varinput >= 1 THEN
IO_RadomeLength = IO_varinput ELSE BEEP

    END IF

'———— ANTENNA DIAMETER ———————————————————————-
    IF IO_cursor_y = 11 THEN
        LOCATE IO_cursor_y, 27
        COLOR 15,0
        PRINT SPACE$(7);
        LOCATE IO_cursor_y, 27

        CURSOR ON, 100
        INPUT IO_varinput
        CURSOR OFF
```

```
        IF IO_varinput < 999.99 AND IO_varinput >= 1 THEN
IO_AntennaDiameter = IO_varinput ELSE BEEP

    END IF

'———— ELEVATION ———————————————————————
    IF IO_cursor_y = 13 THEN
        LOCATE IO_cursor_y, 27
        COLOR 15,0
        PRINT SPACE$(7);
        LOCATE IO_cursor_y, 27

        CURSOR ON, 100
        INPUT IO_varinput
        CURSOR OFF

        IF IO_varinput >= 0 AND IO_varinput <= 90 THEN  IO_AntennaEL =
IO_varinput ELSE BEEP

    END IF


'———— AZIMUTH ———————————————————————
    IF IO_cursor_y = 15 THEN
        LOCATE IO_cursor_y, 27
        COLOR 15,0
        PRINT SPACE$(7);
        LOCATE IO_cursor_y, 27

        CURSOR ON, 100
        INPUT IO_varinput
        CURSOR OFF

        IF IO_varinput >=0 AND IO_varinput <=90 THEN  IO_AntennaAZ =
IO_varinput ELSE BEEP

    END IF

'———— ANTENNA Xo LOCATION ——————————————————
    IF IO_cursor_y = 17 THEN
        LOCATE IO_cursor_y, 27
        COLOR 15,0
        PRINT SPACE$(7);
        LOCATE IO_cursor_y, 27

        CURSOR ON, 100
        INPUT IO_varinput
        CURSOR OFF

        IF IO_varinput >= 0 AND IO_varinput <= 999.99 THEN
IO_AntennaXo = IO_varinput ELSE BEEP

    END IF
```

```
'———— ANTENNA POLARIZATION ————————————————————-
    IF IO_cursor_y = 19 THEN
        LOCATE IO_cursor_y, 27
        COLOR 15,0
        PRINT SPACE$(9);
        LOCATE IO_cursor_y, 27

        IF IO_AntennaPol = "Vertical" THEN
            IO_AntennaPol = "Horizonal"
        ELSE
            IO_AntennaPol = "Vertical"
        END IF

    END IF

    CLOSE
    OPEN "C:\RADGEO.DAT" FOR OUTPUT AS #1
        '—— CURSOR ——
        PRINT #1, IO_cursor_y
        PRINT #1, IO_cursor_x
        '—— DATA ——
        PRINT #1, IO_StartFreq
        PRINT #1, IO_StopFreq
        PRINT #1, IO_RadomeDiameter
        PRINT #1, IO_RadomeLength
        PRINT #1, IO_AntennaDiameter
        PRINT #1, IO_AntennaEL
        PRINT #1, IO_AntennaAZ
        PRINT #1, IO_AntennaXo
        PRINT #1, IO_AntennaPol
    CLOSE #1

GOTO IO_restart

'*********************************************************************
'*            IO_RESTART2 Subroutine                                 *
'*********************************************************************
IO_RESTART2:

'———— TEST FOR ANTENNA HITTING WALL ————————————————

BTO=(4*IO_RadomeLength^2-IO_RadomeDiameter^2)/(4*IO_RadomeDiameter)

RTO=(4*IO_RadomeLength^2+IO_RadomeDiameter^2)/(4*IO_RadomeDiameter)

    xPosRad = (SQR(RTO^2) - IO_AntennaXo^2) - BTO

    IF (IO_AntennaDiameter + .5) > (2 * xPosRad) THEN

        BEEP

        COLOR 15,12
        LOCATE 22,1
        PRINT SPACE$(80);
```

```
        LOCATE 22,2
        PRINT "ANTENNA EDGE HITS RADOME WALL, ALTER ANTENNA SIZE,
RADOME SIZE OR Xo-LOCATION"

        GOSUB waitforanykey
        GOTO IO_RESTART
    END IF

'———— TEST FOR LESS THAN HEMISPHERE ————————————————
    IF IO_RadomeLength < (IO_RadomeDiameter/2) THEN
        BEEP

        COLOR 15,12
        LOCATE 22,1
        PRINT SPACE$(80);

        LOCATE 22,2
        PRINT "RADOME DIMENSIONS ARE LESS THAN A HEMISPHERE, ALTER
RADOME LENGTH OR DIAMETER"

        GOSUB waitforanykey
        GOTO IO_RESTART
    END IF

    COLOR 15,1
    CLS

    COLOR 15,14
    LOCATE 1,1
    PRINT SPACE$(80);

    COLOR 0,14
    LOCATE 1,30
    PRINT "WALL LAYER DESCRIPTION"

    COLOR 8,1
    LOCATE 22,4
    PRINT "<Arrow Keys>-Move Cursor   <Enter>-Edit Data   <F1>-Run Data
<Esc>-Exit";
    COLOR 15,1

    COLOR 9,7
    LOCATE 24,1
    PRINT SPACE$(80);
    LOCATE 25,1
    PRINT SPACE$(80);
    LOCATE 1,1

    COLOR 1,7
    LOCATE 24,2
    PRINT "NOTE: To Change Data, Use Arrow Keys to Select Desired
Field, Then Press the";
    LOCATE 25,8
```

```
    PRINT "Enter Key to Edit Data Within That Field.  Press Enter Again
When Done.";

    COLOR 15,1

    ON ERROR GOTO IO_PROGRAMERROR2

    IF IO_ERRORTIMES >= 3 THEN
        COLOR 15,0
        BEEP
        PRINT
        PRINT " UNRECOVERABLE ERROR IN PROGRAM EXECUTION!
        SLEEP 7000
        END
    END IF

    OPEN "C:\WALLDSC.DAT" FOR INPUT AS #1
        '—— CURSOR —
        INPUT #1, IO_cursor_y
        INPUT #1, IO_cursor_x
        '—— LAYERS ——
        INPUT #1, IO_LAYERS
        '—— THK, ER, LTAN ——
        FOR IO_N = 1 TO 5
          INPUT #1, IO_THK(IO_N), IO_ER(IO_N), IO_LTAN(IO_N)
        NEXT IO_N
    CLOSE #1

    LOCATE 3,2
    PRINT "Number of Layers: ";
    COLOR 15,0
    IO_vardump = USING$ (" # ", IO_LAYERS)
    PRINT IO_vardump
    COLOR 15,1

'——— DIMLY PRINT ALL LAYERS ————————————————————-
    IO_N=0
    FOR IO_N2 = 1 TO 10 STEP 2

        IO_N = IO_N + 1

        COLOR 0,1
        LOCATE 4 + IO_N2,2
        PRINT "Thickness(";LTRIM$(STR$(IO_N));"): ";

        IO_vardump = USING$ (" #.### ", IO_THK(IO_N))
        PRINT IO_vardump

        LOCATE 4 + IO_N2, 27
        PRINT "Dielectric(";LTRIM$(STR$(IO_N));"): ";

        IO_vardump = USING$ (" *0.## ", IO_ER(IO_N))
        PRINT IO_vardump
```

```
        LOCATE 4 + IO_N2, 53
        PRINT "Loss Tangent(";LTRIM$(STR$(IO_N));"): ";

        IO_vardump = USING$ (" #.#### ", IO_LTAN(IO_N))
        PRINT IO_vardump

    NEXT IO_N2

'——— HIGHLIGHT SELECTED NUMBER OF LAYERS ——————————————
    IO_N = 0
    FOR IO_N2 = 1 TO IO_LAYERS * 2 STEP 2

        IO_N = IO_N+1

        COLOR 15,1
        LOCATE 4 + IO_N2,2
        PRINT "Thickness(";LTRIM$(STR$(IO_N));"): ";

        COLOR 15,0
        IO_vardump = USING$ (" #.### ", IO_THK(IO_N))
        PRINT IO_vardump
        COLOR 15,1

        LOCATE 4 + IO_N2, 27
        PRINT "Dielectric(";LTRIM$(STR$(IO_N));"): ";

        COLOR 15,0
        IO_vardump = USING$ (" *0.## ", IO_ER(IO_N))
        PRINT IO_vardump
        COLOR 15,1

        LOCATE 4 + IO_N2, 53
        PRINT "Loss Tangent(";LTRIM$(STR$(IO_N));"): ";

        COLOR 15,0
        IO_vardump = USING$ (" #.#### ", IO_LTAN(IO_N))
        PRINT IO_vardump
        COLOR 15,1

    NEXT IO_N2

    CURSOR OFF
    LOCATE IO_cursor_y, IO_cursor_x
    PRINT CHR$(16);

    DO

      IO_keystroke = INKEY$

      IF IO_keystroke = CHR$(27) THEN GOTO IO_RESTART
```

```
'——— CURSOR UP ———
IF IO_keystroke = CHR$(0) + CHR$(72) THEN
    IF IO_cursor_y > 4 THEN
        LOCATE IO_cursor_y, IO_cursor_x: PRINT " ";
        IO_cursor_y = IO_cursor_y - 2
        IF IO_cursor_y < 4 THEN IO_cursor_x = 1
        LOCATE IO_cursor_y, IO_cursor_x: PRINT CHR$(16);
    END IF
END IF

'——— CURSOR DOWN ———
IF IO_keystroke = CHR$(0) + CHR$(80) THEN
    IF IO_cursor_y < 14 AND IO_cursor_y < (IO_LAYERS*2)+2 THEN
        LOCATE IO_cursor_y, IO_cursor_x: PRINT " ";
        IO_cursor_y = IO_cursor_y + 2
        LOCATE IO_cursor_y, IO_cursor_x: PRINT CHR$(16);
    END IF
END IF

'——— CURSOR LEFT ———
IF IO_keystroke = CHR$(0) + CHR$(75) THEN
    IF IO_cursor_y >= 5 AND IO_cursor_x > 1 THEN
        IF IO_cursor_x = 26 THEN
            LOCATE IO_cursor_y, IO_cursor_x: PRINT " ";
            IO_cursor_x = 1
            LOCATE IO_cursor_y, IO_cursor_x: PRINT CHR$(16);
        END IF
        IF IO_cursor_x = 52 THEN
            LOCATE IO_cursor_y, IO_cursor_x: PRINT " ";
            IO_cursor_x = 26
            LOCATE IO_cursor_y, IO_cursor_x: PRINT CHR$(16);
        END IF
    END IF
END IF

'——— CURSOR RIGHT ———
IF IO_keystroke = CHR$(0) + CHR$(77) THEN
    IF IO_cursor_y >= 5 AND IO_cursor_x < 52 THEN
        IF IO_cursor_x = 26 THEN
            LOCATE IO_cursor_y, IO_cursor_x: PRINT " ";
            IO_cursor_x = 52
            LOCATE IO_cursor_y, IO_cursor_x: PRINT CHR$(16);
        END IF
        IF IO_cursor_x = 1 THEN
            LOCATE IO_cursor_y, IO_cursor_x: PRINT " ";
            IO_cursor_x = 26
            LOCATE IO_cursor_y, IO_cursor_x: PRINT CHR$(16);
        END IF
    END IF
END IF

'——— ALTER DATA <Enter> ———
IF IO_keystroke = CHR$(13) THEN GOTO IO_ALTER_DATA2

'======== RUN DATA ========
IF IO_keystroke = CHR$(0)+CHR$(59) THEN GOTO WALL_MODULE
```

```
    LOOP

END

'*************************************************************************
IO_ALTER_DATA2:

'———— LAYERS ———————————————————————-
    IF IO_cursor_y = 3 AND IO_cursor_x = 1 THEN
        LOCATE IO_cursor_y, 20
        COLOR 15,0
        PRINT SPACE$(3);
        LOCATE IO_cursor_y, 21

        CURSOR ON, 100
        INPUT IO_varinput
        CURSOR OFF

        IF IO_varinput => 1 AND IO_varinput <= 5 THEN IO_LAYERS =
INT(IO_varinput) ELSE BEEP

    END IF


'———— THICKNESS 1 ——————————————————————
    IF IO_cursor_y = 5 AND IO_cursor_x = 1 THEN
        LOCATE IO_cursor_y, 17
        COLOR 15,0
        PRINT SPACE$(5);
        LOCATE IO_cursor_y, 17

        CURSOR ON, 100
        INPUT IO_varinput
        CURSOR OFF

        IF IO_varinput => 0 AND IO_varinput <= 3 THEN IO_THK(1) =
IO_varinput ELSE BEEP

    END IF

'———— THICKNESS 2 ——————————————————————
    IF IO_cursor_y = 7 AND IO_cursor_x = 1 THEN
        LOCATE IO_cursor_y, 17
        COLOR 15,0
        PRINT SPACE$(5);
        LOCATE IO_cursor_y, 17

        CURSOR ON, 100
        INPUT IO_varinput
        CURSOR OFF

        IF IO_varinput => 0 AND IO_varinput <= 3 THEN IO_THK(2) =
IO_varinput ELSE BEEP
```

```
    END IF

'——— THICKNESS 3 ———————————————————————
    IF IO_cursor_y = 9 AND IO_cursor_x = 1 THEN
        LOCATE IO_cursor_y, 17
        COLOR 15,0
        PRINT SPACE$(5);
        LOCATE IO_cursor_y, 17

        CURSOR ON, 100
        INPUT IO_varinput
        CURSOR OFF

        IF IO_varinput => 0 AND IO_varinput <= 3 THEN IO_THK(3) =
IO_varinput ELSE BEEP

    END IF

'——— THICKNESS 4 ———————————————————————
    IF IO_cursor_y = 11 AND IO_cursor_x = 1 THEN
        LOCATE IO_cursor_y, 17
        COLOR 15,0
        PRINT SPACE$(5);
        LOCATE IO_cursor_y, 17

        CURSOR ON, 100
        INPUT IO_varinput
        CURSOR OFF

        IF IO_varinput => 0 AND IO_varinput <= 3 THEN IO_THK(4) =
IO_varinput ELSE BEEP

    END IF

'——— THICKNESS 5 ———————————————————————
    IF IO_cursor_y = 13 AND IO_cursor_x = 1 THEN
        LOCATE IO_cursor_y, 17
        COLOR 15,0
        PRINT SPACE$(5);
        LOCATE IO_cursor_y, 17

        CURSOR ON, 100
        INPUT IO_varinput
        CURSOR OFF

        IF IO_varinput => 0 AND IO_varinput <= 3 THEN IO_THK(5) =
IO_varinput ELSE BEEP

    END IF

'——— DIELECTRIC 1 ———————————————————————-
    IF IO_cursor_y = 5 AND IO_cursor_x = 26 THEN
        LOCATE IO_cursor_y, 43
```

```
        COLOR 15,0
        PRINT SPACE$(5);
        LOCATE IO_cursor_y, 43

        CURSOR ON, 100
        INPUT IO_varinput
        CURSOR OFF

        IF IO_varinput => .01 AND IO_varinput <= 99 THEN IO_ER(1) =
IO_varinput ELSE BEEP

    END IF

'———— DIELECTRIC 2 ——————————————————————-
    IF IO_cursor_y = 7 AND IO_cursor_x = 26 THEN
        LOCATE IO_cursor_y, 43
        COLOR 15,0
        PRINT SPACE$(5);
        LOCATE IO_cursor_y, 43

        CURSOR ON, 100
        INPUT IO_varinput
        CURSOR OFF

        IF IO_varinput => .01 AND IO_varinput <= 99 THEN IO_ER(2) =
IO_varinput ELSE BEEP

    END IF

'———— DIELECTRIC 3 ——————————————————————-
    IF IO_cursor_y = 9 AND IO_cursor_x = 26 THEN
        LOCATE IO_cursor_y, 43
        COLOR 15,0
        PRINT SPACE$(5);
        LOCATE IO_cursor_y, 43

        CURSOR ON, 100
        INPUT IO_varinput
        CURSOR OFF

        IF IO_varinput => .01 AND IO_varinput <= 99 THEN IO_ER(3) =
IO_varinput ELSE BEEP

    END IF

'———— DIELECTRIC 4 ——————————————————————-
    IF IO_cursor_y = 11 AND IO_cursor_x = 26 THEN
        LOCATE IO_cursor_y, 43
        COLOR 15,0
        PRINT SPACE$(5);
        LOCATE IO_cursor_y, 43
```

```
        CURSOR ON, 100
        INPUT IO_varinput
        CURSOR OFF

        IF IO_varinput => .01 AND IO_varinput <= 99 THEN IO_ER(4) =
IO_varinput ELSE BEEP

    END IF

'——— DIELECTRIC 5 ——————————————————————-
    IF IO_cursor_y = 13 AND IO_cursor_x = 26 THEN
        LOCATE IO_cursor_y, 43
        COLOR 15,0
        PRINT SPACE$(5);
        LOCATE IO_cursor_y, 43

        CURSOR ON, 100
        INPUT IO_varinput
        CURSOR OFF

        IF IO_varinput => .01 AND IO_varinput <= 99 THEN IO_ER(5) =
IO_varinput ELSE BEEP

    END IF

'——— LOSS TANGENT 1 ———————————————————————-
    IF IO_cursor_y = 5 AND IO_cursor_x = 52 THEN
        LOCATE IO_cursor_y, 71
        COLOR 15,0
        PRINT SPACE$(6);
        LOCATE IO_cursor_y, 71

        CURSOR ON, 100
        INPUT IO_varinput
        CURSOR OFF

        IF IO_varinput => .0001 AND IO_varinput < 1 THEN IO_LTAN(1) =
IO_varinput ELSE BEEP

    END IF

'——— LOSS TANGENT 2 ———————————————————————-
    IF IO_cursor_y = 7 AND IO_cursor_x = 52 THEN
        LOCATE IO_cursor_y, 71
        COLOR 15,0
        PRINT SPACE$(6);
        LOCATE IO_cursor_y, 71

        CURSOR ON, 100
        INPUT IO_varinput
        CURSOR OFF
```

```
        IF IO_varinput => .0001 AND IO_varinput < 1 THEN IO_LTAN(2) =
IO_varinput ELSE BEEP

    END IF

'———— LOSS TANGENT 3 ——————————————————————-
    IF IO_cursor_y = 9 AND IO_cursor_x = 52 THEN
        LOCATE IO_cursor_y, 71
        COLOR 15,0
        PRINT SPACE$(6);
        LOCATE IO_cursor_y, 71

        CURSOR ON, 100
        INPUT IO_varinput
        CURSOR OFF

        IF IO_varinput => .0001 AND IO_varinput < 1 THEN IO_LTAN(3) =
IO_varinput ELSE BEEP

    END IF

'———— LOSS TANGENT 4 ——————————————————————-
    IF IO_cursor_y = 11 AND IO_cursor_x = 52 THEN
        LOCATE IO_cursor_y, 71
        COLOR 15,0
        PRINT SPACE$(6);
        LOCATE IO_cursor_y, 71

        CURSOR ON, 100
        INPUT IO_varinput
        CURSOR OFF

        IF IO_varinput => .0001 AND IO_varinput < 1 THEN IO_LTAN(4) =
IO_varinput ELSE BEEP

    END IF

'———— LOSS TANGENT 5 ——————————————————————-
    IF IO_cursor_y = 13 AND IO_cursor_x = 52 THEN
        LOCATE IO_cursor_y, 71
        COLOR 15,0
        PRINT SPACE$(6);
        LOCATE IO_cursor_y, 71

        CURSOR ON, 100
        INPUT IO_varinput
        CURSOR OFF

        IF IO_varinput => .0001 AND IO_varinput < 1 THEN IO_LTAN(5) =
IO_varinput ELSE BEEP

    END IF
```

```
    CLOSE
    OPEN "C:\WALLDSC.DAT" FOR OUTPUT AS #1
        '-- CURSOR --
        PRINT #1, IO_cursor_y
        PRINT #1, IO_cursor_x
        '-- LAYERS --
        PRINT #1, IO_LAYERS
        '-- THK, ER, LTAN --
        FOR IO_N = 1 TO 5
          PRINT #1, IO_THK(IO_N), IO_ER(IO_N), IO_LTAN(IO_N)
        NEXT IO_N
    CLOSE #1

GOTO IO_restart2

'*********************************************************************
'*          IO_PROGRAMERROR1 Subroutine                              *
'*********************************************************************
IO_PROGRAMERROR1:

    IF ERR = 53 THEN
        CLOSE
        OPEN "C:\RADGEO.DAT" FOR OUTPUT AS #1
        '-- CURSOR --
        PRINT #1, "3"
        PRINT #1, "1"

        '-- START FREQ --
        PRINT #1, "2"
        '-- STOP FREQ --
        PRINT #1, "8"
        '-- RAD DIA --
        PRINT #1, "12"
        '-- RAD LENGTH --
        PRINT #1, "24"
        '-- ANT DIA --
        PRINT #1, "8"
        '-- EL --
        PRINT #1, "0"
        '-- AZ --
        PRINT #1, "0"
        '-- ANT LOCATION X --
        PRINT #1, "0"
        '-- ANT POL --
        PRINT #1, "Vertical"

        CLOSE #1

        GOTO IO_RESTART
    ELSE
        BEEP
        COLOR 15,9
        PRINT " ERROR IN PROGRAM EXECUTION! "
        SLEEP 5000
    END IF
```

```
END

'*************************************************************************
'*            IO_PROGRAMERROR2 Subroutine                                *
'*************************************************************************
IO_PROGRAMERROR2:

    IF ERR = 53 THEN
        CLOSE
        OPEN "C:\WALLDSC.DAT" FOR OUTPUT AS #1
        '—— CURSOR ——
        PRINT #1, "3"
        PRINT #1, "1"
        '—— LAYERS ——
        PRINT #1, "3"
        '—— THK, ER, LTAN ——
        FOR IO_N = 1 TO 5
          PRINT #1, ".05, 3, .001"
        NEXT IO_N

        CLOSE #1

        GOTO IO_RESTART
    ELSE
        BEEP
        COLOR 15,9
        PRINT " ERROR IN PROGRAM EXECUTION! "
        SLEEP 5000
    END IF

END

'*************************************************************************
'*                    WALL_MODULE Subroutine                             *
'*************************************************************************
WALL_MODULE:

    GLOBAL DRAD, PI, FREQUENCY, wavenumber, ER(), LTAN(), THK() AS
SINGLE
    GLOBAL GAMMA, GAMMADEG, TRANSMAG(), TRANSPHS() AS SINGLE
    GLOBAL FREQSTART, FREQSTOP, Rtotmag(), Rtotph(), times AS SINGLE
    GLOBAL vardump, dummy AS STRING

    COLOR 15,1
    CLS

    COLOR 15,14
    LOCATE 1,1
    PRINT SPACE$(80);

    COLOR 0,14
    LOCATE 1,30
    PRINT "CALCULATED TORADOME DATA"
```

```
    COLOR 1,7
    LOCATE 25,1
    PRINT SPACE$(80);
    LOCATE 1,1

    LOCATE 25,18
    PRINT "<Press Any Key> - Return to Data Input Screen";
    COLOR 15,1

    DIM ER(6), LTAN(6), THK(6), TRANSMAG(2), TRANSPHS(2), Rtotmag(2),
Rtotph(2)

    PI = 3.14159265
    DRAD = PI/180



    OPEN "C:\RADGEO.DAT" FOR INPUT AS #1
        '── CURSOR ──
        INPUT #1, dummy
        INPUT #1, dummy
        '── DATA ──
        INPUT #1, IO_StartFreq
            StartFreq = IO_StartFreq

        INPUT #1, IO_StopFreq
            StopFreq = IO_StopFreq

        INPUT #1, IO_RadomeDiameter
             D0 = IO_RadomeDiameter

        INPUT #1, IO_RadomeLength
             L0 = IO_RadomeLength

        INPUT #1, IO_AntennaDiameter
           Adia = IO_AntennaDiameter

        INPUT #1, IO_AntennaEL
             EL = IO_AntennaEL

        INPUT #1, IO_AntennaAZ
             AZ = IO_AntennaAZ

        INPUT #1, IO_AntennaXo
             X0 = IO_AntennaXo
             Y0 = 0
             Z0 = 0

        INPUT #1, IO_AntennaPol
            IF IO_AntennaPol = "Vertical" THEN
                EPOL = 0
            ELSE
```

```
              EPOL = 1
           END IF

    CLOSE #1

LOCATE 11,49
vardump = USING$ ("EL = ##.##", EL)
PRINT vardump

LOCATE 13,49
vardump = USING$ ("AZ = ##.##", AZ)
PRINT vardump

LOCATE 15,49
PRINT "Polarization = ";IO_AntennaPol

    LOCATE 4,9
      PRINT "Frequency(GHz)       Loss(dB)"
    LOCATE 5,9
      PRINT "————————       ————"

    LOCATE 7,1

    OPEN "C:\WALLDSC.DAT" FOR INPUT AS #1
        '—— CURSOR ——
        INPUT #1, dummy
        INPUT #1, dummy
        '—— LAYERS ——
        INPUT #1, N
        '—— THK, ER, LTAN ——
        FOR times=1 TO 5
          INPUT #1, THK(times), ER(times), LTAN(times)
        NEXT times
    CLOSE #1

'———— POLARIZATION ————————————————————————-
    IF EPOL = 0 THEN
        EZ=1
        EY=0
        'PRINT "   PROGRAM SET FOR VERTICALLY POLARIZED ANTENNA"
    END IF

    IF EPOL = 1 THEN
        EZ=0
        EY=1
        'PRINT "   PROGRAM SET FOR HORIZONTALLY POLARIZED ANTENNA"
    END IF

'———— COMPUTE TANGENT OGIVE PARAMETERS ———————————————————-

     BTO=(4*L0^2-D0^2)/(4*D0)
     RTO=(4*L0^2+D0^2)/(4*D0)
     INCREMENT=Adia/100
```

```
'——— NOW TO COMPUTE PROPAGATION VECTOR ———————————————

     Kx = COS(EL*DRAD)*COS(AZ*DRAD)
     Ky = COS(EL*DRAD)*SIN(AZ*DRAD)
     Kz = SIN(EL*DRAD)

'——— LOAD INTERNAL ANTENNA APERTURE DISTRIBUTION ——————————

        CNST=0

        FOR IZ = -50 TO 50 STEP 5
            IF IZ  0 THEN
                FOR IY = -50 TO 50 STEP 5
                    IF IY  0 THEN
                        y0=IY*INCREMENT
                        z0=IZ*INCREMENT
                        RADIUS=SQR(y0^2+z0^2)
                        IF RADIUS>=Adia/2 THEN
                            Ainner(IY, IZ)=0
                        ELSE
                            MATTHEW=((0.9*PI)*IZ)/100
                            MARK=((.8*PI)*RADIUS)/Adia
                            LUKE=((0.9*PI)*IY)/100
              Ainner(IY, IZ)
=EZ*COS(MATTHEW)+EY*COS(LUKE))*SQR(COS(MARK))
                            CNST = CNST + Ainner(IY, IZ)
                        END IF
                    END IF
                NEXT  IY
            END IF
        NEXT  IZ

   'PRINT CNST, Adia, BTO, RTO
   'input hash$
   'THIS NOW LOOKS GOOD TO HERE

'NOTE: WE ONLY NEED TO SETUP THE INITIAL APERTURE DISTRIBUTION ONCE:
'IT NEVER CHANGES

'——— FREQUENCY LOOP ——————————————————————-

    FOR FREQUENCY = StartFreq TO StopFreq STEP
((StopFreq-StartFreq)/15)

        wavenumber = 0.532 * FREQUENCY

'——— ROTATION OF POLARIZATION VECTOR ———————————————

        IF EZ=1 THEN
            VV(1) = -SIN(EL*DRAD)*COS(AZ*DRAD)
            VV(2) = -SIN(EL*DRAD)*SIN(AZ*DRAD)
            VV(3) = COS(EL*DRAD)
            VH(1) = 0
```

```
            VH(2) = 0
            VH(3) = 0
        END IF

        IF EY=1 THEN
            VV(1) = 0
            VV(2) = 0
            VV(3) = 0
            VH(1) = -SIN(AZ*DRAD)
            VH(2) = COS(AZ*DRAD)
            VH(3) = 0
        END IF

'——— LOAD EXTERNAL ARRAY TO GET A GAIN LOSS COMPUTATION ————————-

       RE=0
       IM=0

       FOR IZ = -50 TO 50 STEP 5
            IF IZ  0 THEN
                FOR IY = -50 TO 50 STEP 5
                    IF IY  0 THEN

                        y0=IY*INCREMENT
                        z0=IZ*INCREMENT

                        RADIUS=SQR(y0^2+z0^2)

                        IF RADIUS < Adia/2 THEN

                            GOSUB GIMBALROT
                            GOSUB INTERCEPT
                            GOSUB NORMAL

                            JACK = (Nx*Kx+Ny*Ky+Nz*Kz)
                            IF JACK = 0 THEN JACK = 10^-6
                            gamma = ATN(SQR(1-JACK^2)/JACK)
                            gamma = ABS(gamma)

                            GOSUB WALL_SUBROUTINE
                            GOSUB DECOMP

                            RE=RE+MAGAouter(IY, IZ)*COS(PHASEAouter(IY,
IZ))
                            IM=IM+MAGAouter(IY, IZ)*SIN(PHASEAouter(IY,
IZ))

                        END IF
                    END IF

                    IF INKEY$=CHR$(27) THEN GOTO IO_RESTART
```

```
            NEXT  IY
         END IF
      NEXT  IZ

      EDB(AZ, EL)=20*LOG10(SQR(RE^2+IM^2)/CNST)

      IF EDB(AZ,EL) >=0 THEN
         vardump = USING$("          ###.##            +##.##",
FREQUENCY, -0.001)
      ELSE
         vardump = USING$("          ###.##            +##.##",
FREQUENCY, EDB(AZ, EL))
      END IF

      PRINT vardump

   NEXT FREQUENCY

   DO
      IF INKEY$ = CHR$(27) THEN GOTO IO_RESTART
      IF INKEY$  "" THEN GOTO IO_RESTART
   LOOP

END

'*********************************************************************
'*               GIMBALROT SUBROUTINE                                *
'*********************************************************************
GIMBALROT:

'——— TRANSFORM THE APERTURE POINTS THROUGH AZ, EL ANGLES ——

   xp = -COS(AZ*DRAD) * SIN(EL*DRAD) * z0 - (SIN(AZ*DRAD) * y0)
   yp = -SIN(AZ*DRAD) * SIN(EL*DRAD) * z0 + (COS(AZ*DRAD) * y0)
   zp =  COS(EL*DRAD) * z0

RETURN



'*********************************************************************
'*                  ICEPT Subroutine                                 *
'*********************************************************************
********
INTERCEPT:

'——— FIND THE INTERCEPT OF A RAY AND THE RADOME SURFACE ———-

   MMM = 0
   CONV = 1

   FOR MM = 1 TO 100000
```

```
        MMM = MMM + CONV
        x = xp + Kx * MMM
        y = yp + Ky * MMM
        z = zp + Kz * MMM

        ri=SQR(y^2+z^2)

        rp=ABS((SQR(RTO^2-x^2))-BTO)

        IF ABS(rp-ri) <= 3   THEN CONV = .5
        IF ABS(rp-ri) <= 2   THEN CONV = .1
        IF ABS(rp-ri) <= 1   THEN CONV = .01

        IF (rp-ri) <= .1 THEN EXIT FOR

    NEXT MM

    xi = x
    yi = y
    zi = z

RETURN

'*********************************************************************
'*              NORMAL Subroutine                                    *
'*********************************************************************
NORMAL:

    Nx=1/SQR(1+((rp+BTO)/xi)^2)
    Nt=SQR(1-Nx^2)
    M=ABS(zi/yi)
    alpha=ATN(M)

    IF zi>0 AND yi>0 THEN
        Nz=Nt*SIN(alpha): Ny=Nt*COS(alpha)
    END IF

    IF zi>0 AND yi<0 THEN
        Nz=Nt*SIN(alpha): Ny=-Nt*COS(alpha)
    END IF

    IF zi<0 AND yi<0 THEN
        Nz=-Nt*SIN(alpha): Ny=-Nt*COS(alpha)
    END IF

    IF zi<0 AND yi>0 THEN
        Nz=-Nt*SIN(alpha): Ny=Nt*COS(alpha)
    END IF

RETURN
```

```
'*********************************************************************
'*     DECOMPOSE AND RECOMPOSE RAYS                                  *
'*********************************************************************
DECOMP:

    LOCAL AA, BB, CC, DD AS DOUBLE

    Nx = Nx + 10^-5
    Ny = Ny + 10^-5
    Nz = Nz + 10^-5

    DUMB = (Ny * Kz - Nz * Ky)^2
    DUMB = DUMB + (Nz * Kx - Nx * Kz)^2
    DUMB = DUMB + (Nx * Ky - Ny * Kx)^2
    DUMB = SQR(DUMB)

'———- DR() IS A VECTOR PERPENDICULAR TO THE PLANE OF INCIDENCE ———-
    DR(1) = (Ny * Kz - Nz * Ky) / DUMB
    DR(2) = (Nz * Kx - Nx * Kz) / DUMB
    DR(3) = (Nx * Ky - Ny * Kx) / DUMB

    DR(1) = DR(1)/SQR(DR(1)^2 + DR(2)^2 + DR(3)^2)
    DR(2) = DR(2)/SQR(DR(1)^2 + DR(2)^2 + DR(3)^2)
    DR(3) = DR(3)/SQR(DR(1)^2 + DR(2)^2 + DR(3)^2)

    DUMB = (DR(2) * Kz - DR(3) * Ky)^2
    DUMB = DUMB + (DR(3) * Kx - DR(1) * Kz)^2
    DUMB = DUMB + (DR(1) * Ky - DR(2) * Kx)^2
    DUMB = SQR(DUMB)

'——— GR() IS A VECTOR IN THE PLANE OF INCIDENCE ——————————-
    GR(1) = (DR(2) * Kz - DR(3) * Ky) / DUMB
    GR(2) = (DR(3) * Kx - DR(1) * Kz) / DUMB
    GR(3) = (DR(1) * Ky - DR(2) * Kx) / DUMB

    GR(1) = GR(1) / SQR(GR(1)^2 + GR(2)^2 + GR(3)^2)
    GR(2) = GR(2) / SQR(GR(1)^2 + GR(2)^2 + GR(3)^2)
    GR(3) = GR(3) / SQR(GR(1)^2 + GR(2)^2 + GR(3)^2)

'———- LOAD THE ELEMENTS OF THE EXTERNAL ARRAY Aouter(IY, IZ) ————————

    'THIS SUBROUTINE DECOMPOSES THE WAVE INTO PARALLEL AND PERP
COMPONENTS,
    'APPLIES THE RESPECTIVE TRANSMISSION COEFFICIENTS AT THE VALUES OF
AZ
    'AND EL AND RECOMPOSES THE WAVE INTO AN EQUIVALENT APERTURE OUTSIDE
RADOME

'———- FOR A VERTICALLY POLARIZED APERTURE VOLTAGE ——————————————-

    AA = (VV(1) * DR(1)) + (VV(2) * DR(2)) + (VV(3) * DR(3))
    AA = AA * Ttotmag(0)
```

```
    BB = (VV(1) * GR(1)) + (VV(2) * GR(2)) + (VV(3) * GR(3))
    BB = BB * Ttotmag(1)

'———— FOR A HORIZONTALLY POLARIZED APERTURE VOLTAGE ——————————-

    CC=(VH(1)*DR(1)+VH(2)*DR(2)+VH(3)*DR(3))*Ttotmag(0)
    DD=(VH(1)*GR(1)+VH(2)*GR(2)+VH(3)*GR(3))*Ttotmag(1)

'———— FOR VERTICAL POLARIZATION ————————————————
    IF EZ=1 THEN
        MAGAouter(IY, IZ) = Ainner(IY, IZ) * SQR(AA^2+BB^2)
        PHASEAouter(IY, IZ) = ABS(Ttotph(0)-Ttotph(1))
    END IF

'———— FOR HORIZONTAL POLARIZATION ————————————————
    IF EY=1 THEN
        MAGAouter(IY, IZ) = Ainner(IY, IZ)*SQR(CC^2+DD^2)
        PHASEAouter(IY, IZ) = ABS(Ttotph(0)-Ttotph(1))
    END IF

RETURN

'*********************************************************************
'*         WALL Subroutine                                           *
'*********************************************************************
WALL_SUBROUTINE:

    LOCAL AMW(), BMW(), CMW(), APW(), BPW(), CPW(), ANG AS SINGLE
    LOCAL IW, JW, KW AS SINGLE
    LOCAL R1, R2, E1, E2, R3, E3, tranmag, tranph, PA, corr AS SINGLE
    LOCAL zmag(), zph(), rez(), imz(), emag(), eph() AS SINGLE
    LOCAL phimag(), phiph(), rephi(), imphi(), magterm(), angterm() AS
SINGLE
    LOCAL Rmag(), Rph(), reR(), imR(), Tmag(), Tph(), reT(), imT() AS
SINGLE
    LOCAL xx, yy, MAG, ROOTMAG, ROOTANG, NUMMAG, NUMANG, DENMAG, DENANG
AS SINGLE

    DIM AMW(10), BMW(10), CMW(10), APW(10), BPW(10), CPW(10)
    DIM zmag(10), zph(10), rez(10), imz(10), emag(10), eph(10)
    DIM phimag(10), phiph(10), rephi(10), imphi(10), magterm(10),
angterm(10)
    DIM Rmag(10), Rph(10), reR(10), imR(10)
    DIM Tmag(10), Tph(10), reT(10), imT(10)

    FOR POL = 0 TO 1
        zmag(0) = 1
        zph(0) = 0
        rez(0) = 1
        imz(0) = 0

        FOR IW = 1 TO N
            xx = ER(IW)
            yy = ER(IW) * -LTAN(IW)
```

```
    GOSUB RECTPOLAR
    emag(IW) = MAG
    eph(IW) = ANG
NEXT IW

rephi(N + 1) = 0
imphi(N + 1) = 0

FOR IW = 1 TO N
    xx = ER(IW) - (SIN(GAMMA))^2
    yy = ER(IW) * -LTAN(IW)
    GOSUB RECTPOLAR
    GOSUB COMPLEXSR

    magterm(IW) = ROOTMAG:   angterm(IW) = ROOTANG

    phimag(IW) = wavenumber * magterm(IW)
    phiph(IW) = angterm(IW)

    MAG = phimag(IW)
    ANG = phiph(IW)

    GOSUB POLARRECT

    rephi(IW) = xx
    imphi(IW) = yy

    zmag(IW) = COS(GAMMA) / (magterm(IW) + 1E-12)
    zph(IW) = -angterm(IW)

    MAG = zmag(IW)
    ANG = zph(IW)

    GOSUB POLARRECT

    rez(IW) = xx
    imz(IW) = yy

    IF POL = 1 THEN
        zmag(IW) = 1 / ((emag(IW) * zmag(IW)) + 1E-12)
        zph(IW) = -(eph(IW) + zph(IW))

        MAG = zmag(IW)
        ANG = zph(IW)

        GOSUB POLARRECT

        rez(IW) = xx
        imz(IW) = yy
    END IF

NEXT IW
```

```
zmag(N + 1) = 1
zph(N + 1) = 0

rez(N + 1) = 1
imz(N + 1) = 0

FOR IW = 1 TO (N + 1)
    xx = rez(IW) - rez(IW - 1)
    yy = imz(IW) - imz(IW - 1)

    GOSUB RECTPOLAR

    NUMMAG = MAG
    NUMANG = ANG

    xx = rez(IW) + rez(IW - 1)
    yy = imz(IW) + imz(IW - 1)

    GOSUB RECTPOLAR

    DENMAG = MAG
    DENANG = ANG

    Rmag(IW) = NUMMAG / DENMAG
    Rph(IW) = NUMANG - DENANG

    MAG = Rmag(IW)
    ANG = Rph(IW)

    GOSUB POLARRECT

    reR(IW) = xx
    imR(IW) = yy

    reT(IW) = 1 + reR(IW)
    imT(IW) = imR(IW)

    xx = reT(IW)
    yy = imT(IW)

    GOSUB RECTPOLAR

    Tmag(IW) = MAG
    Tph(IW) = ANG

NEXT IW

AMW(1) = EXP(-imphi(1) * THK(1))
AMW(4) = 1 / AMW(1)
AMW(2) = Rmag(1) * AMW(4)
AMW(3) = Rmag(1) * AMW(1)
```

```
        APW(1) = rephi(1) * THK(1)
        APW(2) = Rph(1) - APW(1)
        APW(3) = Rph(1) + APW(1)
        APW(4) = -APW(1)

        FOR KW = 2 TO N

            BMW(1) = EXP(-imphi(KW) * THK(KW))
            BMW(4) = 1 / BMW(1)
            BMW(2) = Rmag(KW) * BMW(4)
            BMW(3) = Rmag(KW) * BMW(1)

            BPW(1) = rephi(KW) * THK(KW)
            BPW(2) = Rph(KW) - BPW(1)
            BPW(3) = Rph(KW) + BPW(1)
            BPW(4) = -BPW(1)

            GOSUB CMULT

        NEXT KW

        BMW(1) = 1
        BMW(4) = 1
        BMW(2) = Rmag(N + 1)
        BMW(3) = BMW(2)

        BPW(1) = 0
        BPW(2) = Rph(N + 1)
        BPW(3) = BPW(2)
        BPW(4) = 0

        GOSUB CMULT

        tranmag = 1
        tranph = 0

        FOR JW = 1 TO N + 1
            tranmag = tranmag * Tmag(JW)
            tranph = tranph + Tph(JW)
        NEXT JW

        tranmag = 1 / (tranmag + 1E-12)

        DO
            IF tranph > 2 * PI THEN tranph = tranph - 2 * PI ELSE EXIT
DO
        LOOP

        tranph = -tranph

        IF POL = 0 THEN
            Ttotmag(0) = 1 / (tranmag * AMW(1))
```

```
            Ttotph(0) = ABS(-(tranph + APW(1)))
            Rtotmag(0) = AMW(3) / AMW(1)
            Rtotph(0) = ABS(APW(3) - APW(1))
        END IF

        IF POL = 1 THEN
            Ttotmag(1)= 1 / (tranmag * AMW(1))
            Ttotph(1) = ABS(-(tranph + APW(1)))
            Rtotmag(1) = AMW(3) / AMW(1)
            Rtotph(1) = ABS(APW(3) - APW(1))
        END IF

    NEXT POL

RETURN

'*********************************************************************
'*                CMULT Subroutine                                   *
'*********************************************************************
CMULT:

    FOR IW = 1 TO 3 STEP 2
        FOR JW = 1 TO 2

            R1 = AMW(IW) * BMW(JW)
            R2 = AMW(IW + 1) * BMW(JW + 2)
            E1 = APW(IW) + BPW(JW)
            E2 = APW(IW + 1) + BPW(JW + 2)
            R3 = R1 * COS(E1) + R2 * COS(E2)
            E3 = R1 * SIN(E1) + R2 * SIN(E2)

            CMW(JW + IW - 1) = SQR(R3 * R3 + E3 * E3)

            IF (R3 > 0) AND (E3 > 0) THEN PA = 0
            IF (R3 < 0) THEN PA = PI
            IF (R3 > 0) AND (E3 < 0) THEN PA = 2 * PI

            CPW(JW + IW - 1) = (ATN(E3 / (R3 + 1E-12))) + PA

        NEXT JW
    NEXT IW

    FOR IW = 1 TO 4
        AMW(IW) = CMW(IW)
        APW(IW) = CPW(IW)
    NEXT IW

RETURN

'*********************************************************************
'*            RECTPOLAR Subroutine                                   *
 '*********************************************************************
RECTPOLAR:
```

```
    MAG = SQR(xx ^ 2 + yy ^ 2)

    IF (xx > 0) AND (yy > 0) THEN corr = 0
    IF (xx < 0) AND (yy < 0) THEN corr = PI
    IF (xx > 0) AND (yy < 0) THEN corr = 0
    IF (xx < 0) AND (yy > 0) THEN corr = PI
    IF (xx > 0) AND (yy = 0) THEN corr = 0
    IF (xx < 0) AND (yy = 0) THEN corr = PI
    IF (xx = 0) AND (yy  0) THEN corr = 0
    IF (xx = 0) AND (yy = 0) THEN ANG = 0

    ANG = ATN(yy / (xx + 1E-12)) + corr

RETURN

'*************************************************************************
'*            OLARRECT Subroutine                                        *
'*************************************************************************
POLARRECT:

    xx = MAG * COS(ANG)
    yy = MAG * SIN(ANG)

RETURN

'*************************************************************************
'*          COMPLEXSR Subroutine                                         *
'*************************************************************************
COMPLEXSR:

    ROOTMAG = SQR(MAG)
    ROOTANG = ANG / 2

RETURN

'*************************************************************************
'*      WAITFORANYKEY Subroutine                                         *
'*************************************************************************
waitforanykey:

    DO
      keystroke = INKEY$
      IF keystroke = CHR$(27) THEN END
      IF keystroke  "" THEN EXIT DO
    LOOP

RETURN

END FUNCTION
```

Appendix F
Operations Manual for Programs Provided with Book

F.1 Overview of the Programs

Two programs are included on the CD contained in this book: program "WALL" and program "TORADOME." Program WALL computes the transmission through a flat multilayer dielectric radome wall as a function of frequency and the wall layer details (thickness, dielectric constant, and loss tangent of the respective layers.) Program TORADOME computes the loss and boresight error in a wave propagating from an antenna enclosed in a tangent ogive-shaped radome. TORADOME also allows multilayer dielectric walls where the wall layer characteristics are entered by the user.

Both programs are compiled as executable code and are very user friendly. They can run off the CD or can be copied to hard drive C: on your laptop or PC.

F.2 System Requirements

The system requirements to use the programs included with this book are:

- A computer with Windows XP, Vista, or higher operating system.
- A minimum clock speed of 1.0 GHz.
- A minimum of 1 GB of system RAM.

F.3 Flat Panel Analysis (WALL)

F.3.1 Theory

The flat panel transmission analysis module (WALL) evaluates the transmission coefficients in both parallel and perpendicular components through a multilayer dielectric panel. The computations can be done as a function of frequency where the angle-of-incidence is automatically performed in five degree increments 0 through 85 degrees from the surface normal.

The mathematics was developed as a boundary value problem of both forward and reverse propagating electromagnetic waves. From this formulation, a matrix equation results and is a function of the Fresnel reflection and transmission coefficients at each dielectric boundary.

F.3.2 Operation of Program

At the resident location of the program (CD or else drive C: on your computer), click on WALL.EXE.

The program will prompt the user for the following information:

- Number of layers, N;
- Thickness of the ith layer, T(i) (inches);
- Relative dielectric constant of the ith layer, ER(i);
- Loss tangent of the ith layer, LTAN(i);
- Frequency (GHz).

When you run the program, the output will be in the form of a table of the parallel and perpendicular polarized transmission coefficients (both in dB) for angle-of-incident from 0 to 85 degrees, in 5 degree increments. The user will then be given an option to terminate the program or return to the data input screen to alter the parameters and rerun the calculations.

F.4 Tangent Ogive Radome

F.4.1 Theory

When a dielectric radome is placed over a monopulse antenna, the characteristics of the antenna's performance are altered. The radome analysis module (TORADOME) is an electromagnetic solution to resolve this problem by allowing the user to assess the effects of both a (multilayer) radome wall design and radome shape on the performance of an enclosed monopulse antenna.

The mathematics was developed via geometric optics (GO) ray trace analysis, which projects the aperture distribution through the radome wall in a desired look direction and computes the sum and difference monopulse radiation patterns from the aperture distribution, which is modified by the radome transmission effects.

F.4.2 Operation of Program

At the resident location of the program (CD or hard drive C:), click on TORADOME.EXE.

The program will prompt the user for the following information:
Radome wall description:

- Number of layers, N;
- Thickness of the ith layer, T(i) (inches);
- Relative dielectric constant of the ith layer, ER(i);
- Loss tangent of the ith layer, LTAN(i);
- Start and stop frequency (GHz).

Tangent ogive shaped radome description (see Figure F.1):

- Length of radome, Lo (inches);
- Base diameter of radome, Do (inches);
- Antenna diameter, Adia (inches);
- Location of gimbal rotations from radome base, xo (inches);
- Antenna polarization, horizontal or vertical;
- Azimuth scan angle of the antenna, AZ (degrees);
- Elevation scan angle of the antenna, EL (degrees).

When you run the program the output data screen will show the computed radome loss (in dB) as a function of frequency from the start frequency (GHz) to the stop frequency (GHz) in fifteen equal increments. The user will then be given an option to terminate the program or return to the data input screen to alter the parameters (see Figure F.1) and rerun the calculations.

This program runs for shapes ranging from a hemisphere (radome length = 0.5 radome diameter) or more pointed tangent ogive radomes (radome length > 0.5 radome diameter).

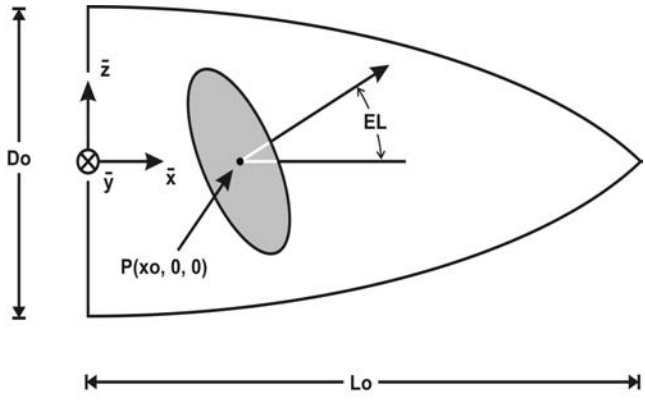

Side view

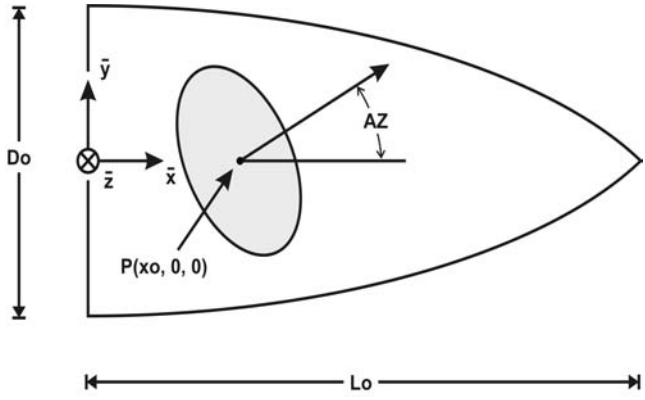

Top view

Figure F.1 Tangent ogive radome geometry parameters needed to run program TORADOME.

About the Author

Dennis J. Kozakoff is an expert and consultant in radome design and analysis. He founded the USDigiComm Corporation, a company extensively involved in electromagnetics research. Prior, he was president/CEO of Millimeter Wave Technology Inc., a high-tech manufacturer of microwave and millimeter wave sensors and instrumentation. Before that, he was a project director in the Electromagnetics Laboratory, Georgia Tech Research Institute (GTRI); a senior staff engineer at the Martin Marietta Corporation, Orlando, FL; and served engineering roles at a number of other companies. He holds a B.S.E.E. degree from the Polytechnic Institute of Brooklyn, an M.S.E. degree from the University of Florida, and a doctorate degree in engineering from Southeastern Institute of Technology. Kozakoff is a senior member of the Institute of the IEEE and a member of the IEEE Antennas and Propagation Society. Through his career, he has had extensive hands-on experience in the design and analysis of aircraft, missile, and terrestrial radomes and antennas that have gone into production. His e-mail address is dr.kozakoff@usdigicomm.com.

Index

Recent Titles in the Artech House Antennas and Propagation Series

Thomas Milligan, Series Editor

Adaptive Array Measurements in Communications, M. A. Halim

Advances in Computational Electrodynamics: The Finite-Difference Time-Domain Method, Allen Taflove, editor

Analysis Methods for Electromagnetic Wave Problems, Volume 2, Eikichi Yamashita, editor

Analysis of Radome-Enclosed Antennas, Second Edition, Dennis J. Kozakoff

Antenna Design with Fiber Optics, A. Kumar

Antenna Engineering Using Physical Optics: Practical CAD Techniques and Software, Leo Diaz and Thomas Milligan

Applications of Neural Networks in Electromagnetics, Christos Christodoulou and Michael Georgiopoulos

AWAS for Windows Version 2.0: Analysis of Wire Antennas and Scatterers, Antonije R. Djordjević, et al.

Broadband Microstrip Antennas, Girsh Kumar and K. P. Ray

Broadband Patch Antennas, Jean-François Zürcher and Fred E. Gardiol

CAD of Microstrip Antennas for Wireless Applications, Robert A. Sainati

The CG-FFT Method: Application of Signal Processing Techniques to Electromagnetics, Manuel F. Cátedra, et al.

Computational Electrodynamics: The Finite-Difference Time-Domain Method, Third Edition, Allen Taflove and Susan C. Hagness

Electromagnetic Modeling of Composite Metallic and Dielectric Structures, Branko M. Kolundzija and Antonije R. Djordjević

Electromagnetic Waves in Chiral and Bi-Isotropic Media, I. V. Lindell, et al.

Electromagnetics, Microwave Circuit and Antenna Design for Communications Engineering, Peter Russer

Engineering Applications of the Modulated Scatterer Technique, Jean-Charles Bolomey and Fred E. Gardiol

Fast and Efficient Algorithms in Computational Electromagnetics, Weng Cho Chew, et al., editors

Fresnel Zones in Wireless Links, Zone Plate Lenses and Antennas, Hristo D. Hristov

Handbook of Antennas for EMC, Thereza MacNamara

Iterative and Self-Adaptive Finite-Elements in Electromagnetic Modeling, Magdalena Salazar-Palma, et al.

Measurement of Mobile Antenna Systems, Hiroyuki Arai

Microstrip Antenna Design Handbook, Ramesh Garg, et al.

Mobile Antenna Systems Handbook, Third Edition, Kyohei Fujimoto, editor

Multiband Integrated Antennas for 4G Terminals, David A. Sánchez-Hernández, editor

Noise Temperature Theory and Applications for Deep Space Communications Antenna Systems, Tom Y. Otoshi

Phased Array Antenna Handbook, Second Edition, Robert J. Mailloux

Quick Finite Elements for Electromagnetic Waves, Giuseppe Pelosi, Roberto Coccioli, and Stefano Selleri

Radiowave Propagation and Antennas for Personal Communications, Second Edition, Kazimierz Siwiak

Solid Dielectric Horn Antennas, Carlos Salema, Carlos Fernandes, and Rama Kant Jha

Switched Parasitic Antennas for Cellular Communications, David V. Thiel and Stephanie Smith

Understanding Electromagnetic Scattering Using the Moment Method: A Practical Approach, Randy Bancroft

Wavelet Applications in Engineering Electromagnetics, Tapan Sarkar, Magdalena Salazar Palma, and Michael C. Wicks

For further information on these and other Artech House titles, including previously considered out-of-print books now available through our In-Print-Forever® (IPF®) program, contact:

Artech House
685 Canton Street
Norwood, MA 02062
Phone: 781-769-9750
Fax: 781-769-6334
e-mail: artech@artechhouse.com

Artech House
16 Sussex Street
London SW1V HRW UK
Phone: +44 (0)20 7596-8750
Fax: +44 (0)20 7630 0166
e-mail: artech-uk@artechhouse.com

Find us on the World Wide Web at: www.artechhouse.com